

A Combined Experimental and Modelling Approach to Elucidate FeCO₃ Scale Formation Kinetics

Rehan Anthony De Motte

Submitted in accordance with the requirements for the degree of
Doctor of Philosophy

The University of Leeds
Institute of Functional Surfaces, iFS
School of Mechanical Engineering

November 2016

The candidate confirms that the work submitted is his own and that appropriate credit has been given where reference has been made to the work of others.

This copy has been supplied on the understanding that it is copyright material and that no quotation from the thesis may be published without proper acknowledgement.

© 2016 The University of Leeds and Rehan Anthony De Motte

Acknowledgements

I would first and foremost like to thank my family for their continuous support and guidance throughout my life. Without them, I would not be where I am and been blessed with the opportunities they have given me. Through their advice, words of wisdom and positive attitude, they have helped me believe in myself and never let me give up when times were tough. I express my sincerest gratitude to my PhD supervisors, Professor Anne Neville and Dr. Richard Barker for patiently guiding me throughout my project. They have provided me with advice and significant knowledge without which my thesis would not be what it is today. I would also like to thank Mohammed Al-Khateeb who collaborated with me in developing the steady state corrosion rate model. His efforts and knowledge in the matter were greatly appreciated. I would like to close by thanking my sponsor BP for their continuous support and funding through the PhD.

Abstract

In CO₂ corrosion, when the local concentrations of Fe²⁺ and CO₃²⁻ ions exceed the solubility limit, precipitation of iron carbonate (FeCO₃) can occur internally within pipework, forming a protective corrosion barrier at the steel-electrolyte interface. Accurately quantifying the rate of precipitation of this film is important within the oil and gas industry as it can be implemented into corrosion prediction tools to provide a more reliable estimate of anticipated corrosion rates.

Existing precipitation rate models are based on measurements conducted in a glass cell in static conditions where the kinetics of FeCO₃ precipitation are accelerated by the addition of FeCl₂.4H₂O and correlated with bulk solution properties. They do not address the key aspects of FeCO₃ formation in real corroding systems which relate to the local surface supersaturation produced as a result of the production of Fe²⁺ ions due to the corrosion process.

In the following thesis, a combined experimental and modelling approach is carried out to investigate the development in the morphology of the FeCO₃ film under different environmental conditions and its consequent effect on the degradation rates of a pipeline. A thin channel flow cell is designed to extend the analysis to a fluid flow environment and a mechanistic model is developed to predict the nature of the near surface layer.

It is found from the experimental analysis that FeCO₃ precipitation is a simultaneous nucleation and growth process and the characteristics of the surface film significantly changes under varying parameters. Results show that the existing precipitation models based on measuring the dissolved ferrous ions in the bulk solution overestimate the precipitation of iron carbonate by a large margin and the precipitation model developed through the direct weight change approach is limited to the experimental conditions in which it was carried out. The models are correlated with bulk solution properties and it has been clearly demonstrated within this work that the precipitation of FeCO₃ is directly related to the conditions at the steel surface which can be very different from that in the bulk. A combined model and experimental analysis shows that a higher initial surface saturation ratio indicates a more protective film formation over time.

Table of Contents

Acknowledgements	i
Abstract	ii
Table of Contents	iii
List of Tables	vii
List of Figures	viii
List of Abbreviations/ Symbols	xvi
Chapter 1 Introduction and Research Project Background	1
1.1 Project Background	1
1.1 Objectives	2
1.2 Structure of Thesis	3
Chapter 2 Introduction to Corrosion in the Oil and Gas Industry	6
2.1 The Petroleum Industry	6
2.2 Pipeline Corrosion and its Significance.....	8
2.3 The Basics of Corrosion in an Electrochemical Cell	11
2.3.1 Electrochemical Cell	11
2.3.2 Thermodynamics of Aqueous Corrosion Reactions	13
2.3.3 Electrical Double Layer (EDL)	15
2.3.4 Corrosion Kinetics.....	16
Chapter 3 CO₂ Corrosion and FeCO₃ Scale Formation	20
3.1 CO ₂ Corrosion Chemistry	20
3.2 FeCO ₃ Crystallisation	24
3.3 Key Parameters affecting CO ₂ Corrosion Rate	27
3.3.1 Water Chemistry and Content.....	27
3.3.2 CO ₂ Corrosion Products	28
3.3.3 Operating Temperature	28
3.3.4 pH	29
3.3.5 Partial Pressure	30
3.3.6 FeCO ₃ Film Growth over Time.....	31
3.3.7 Effect of Flow	32
Chapter 4 Assessment of CO₂ Corrosion Prediction Models	35
4.1 Empirical Models	35
4.2 Semi-Empirical Models	37

4.3 Mechanistic Models	40
4.3.1 Theory behind Mechanistic Modelling	41
4.3.1.1 Electrochemical Reactions at the Surface	42
4.3.1.2 Transport Based Electrochemical Models	44
4.3.1.3 Incorporating FeCO ₃ Film Development	45
Chapter 5 Precipitation Models – Review & Analysis	49
5.1 FeCO ₃ Precipitation Models	49
5.2 Sun and Nescic Precipitation Model	54
5.2.1 S&N Experimental Procedure	56
5.2.2 Existing Precipitation Model Analysis.	57
5.2.3 Scale Retention Rate and Corrosion Rate over Time	59
5.2.4 Experiments Conducted at Constant Supersaturation	60
5.3 Solubility Product (K _{sp}) Calculation	61
5.4 Literature Review – Key Findings and Limitations	64
Chapter 6 Static Experimental Theory and Methodology.....	67
6.1 Static Experimental Set-Up.....	69
6.1.1 Sample Preparation	70
6.1.2 Solution Preparation	71
6.1.3 Corrosion Measurement	71
6.2 Weight Change Method	75
6.3 Method of Fe ²⁺ Addition	77
6.4 Solution Analysis - ([Fe ²⁺ (aq)] Calculation	78
6.5 Post Experimental Analysis Techniques	81
6.5.1 Scanning Electron Microscopy (SEM)	81
6.5.2 X-ray Diffraction (XRD).....	82
Chapter 7 Development of Thin Channel Flow Cell.....	85
7.1 Flow Cell Design and Manufacture	85
7.2 Flow Analysis through TCFC	87
7.4 Experimental Methodology	91
7.4.1 Solution Preparation	91
7.4.2 Sample Preparation	91
7.4.3 Laboratory Flow Loop Set-Up	92
7.4.4 In-Situ Electrochemical Measurements	92
7.4.5 Post-Experimental Analysis	93

Chapter 8 Static Experimental Results	95
8.1 Parametric Analysis of CO ₂ Corrosion of Carbon Steel.....	95
8.1.1 Effect of Temperature.....	96
8.1.2 Effect of Salinity	96
8.1.3 Effect of Surface Roughness	98
8.1.4 Effect of pH	99
8.2 Nucleation and Growth of FeCO ₃ over Time	101
8.2.1 Quantitative Analysis of FeCO ₃ Precipitation.....	102
8.2.2 SEM images of Sample Surface	103
8.2.3 Corrosion Rate Analysis	110
8.2.4 Precipitation Rate and Bulk Saturation Ratio Analysis	113
8.2.5 Comparison of Precipitation Rate to Corrosion Rate	115
8.2.6 XRD Surface Analysis	116
8.3 Accelerating FeCO ₃ Precipitation Kinetics.....	117
8.3.1 Effect of FeCl ₂ .4H ₂ O Addition	118
8.3.2 Effect of Adding FeCl ₂ .4H ₂ O on Results over Time.....	120
8.3.3 Later Stages of FeCO ₃ Nucleation and Growth	121
Chapter 9 Flow Cell Experimental Results	124
9.1 Comparison between Results in Same Flow Channel	124
9.2 Effect of Flow Velocity.....	128
9.2.1 Effect of Flow on Solution Resistance for TCFC	128
9.2.2 Effect of Flow on Tafel Plot for TCFC	129
9.2.3 Effect of Flow on Corrosion Rate for TCFC	129
9.3 Summary of Experimental Results	133
Chapter 10 Development of Corrosion Rate Model	136
10.1 Modelling Framework.....	137
10.1.1 Equilibrium Chemical Reactions in Bulk.....	138
10.1.2 Transport of Species between Steel Surface and Bulk ...	141
10.1.3 Electrochemical Reactions at Surface.....	143
10.2 Step-wise Implementation of MATLAB Model	147
10.3 Steady State Corrosion Rate Model Results	148
10.3.1 Model Validation with Literature.....	148
10.3.2 Model Sensitivity Analysis	150
10.3.3 Model Validation with Experimental Results	152

Chapter 11 Modelling Near Surface Region for CO₂ Corrosion	153
11.1 COMSOL Model Development.....	153
11.2 Mesh Sensitivity Analysis	157
11.3 Model Validation with Literature	159
11.4 Comparison of Model with Experimental Observations	164
11.5 Summary of Modelling Analysis	166
Chapter 12 Discussion of Experimental and Modelling Results	167
12.1 Nucleation and Growth of FeCO ₃ Film Formation.....	167
12.1.1 Precipitation Rate and Film Protectiveness	172
12.1.2 Scaling Tendency	174
12.1.3 Surface Coverage and Crystal Size	175
12.1.4 Quantifying Saturation Ratio	178
12.1.5 Limitation of Modelling Static System	180
12.2 Accelerating Kinetics of FeCO ₃ Film Formation	181
12.3 Later Stages of FeCO ₃ Film Development	185
12.4 Effect of Flow on FeCO ₃ Film Development.....	187
Chapter 13 Final Conclusion and Future Consideration	190
13.1 Limitation of this Study and Future Work	192
Bibliography	194

List of Tables

Table 2.1 Current sources of world energy, 2005 [11]	6
Table 2.2 Analysis of selected number of pipeline failures in petroleum related industries [17]	8
Table 2.3 Causes of corrosion related failures in petroleum related industries [17].....	9
Table 2.4 Standard electrode reduction potentials versus a standard hydrogen electrode (SHE) [25, 26].	14
Table 5.1 Greenberg and Tomson (G&T) Precipitation Model [4, 5]	49
Table 5.2 Johnson and Tomson (J&T) Precipitation Model [6, 7].....	49
Table 5.3 Van Hunnik at al. (vP&H) Precipitation Model [8]	50
Table 5.4 Sun and Nescic (S&N) Precipitation Model [9, 10]	50
Table 5.5 Model variations for pre-exponential constant A_p , activation energy, E_a and saturation ratio expression, $\sigma(SR)$ [36].....	51
Table 5.6 Summary of attributing factor to significant difference in precipitation models as a result of employed experimental technique [36].	54
Table 5.7 Experimental matrix for S&N model development.	56
Table 5.8 Chemical composition of X65 (wt%) (Fe is the balance)	57
Table 6.1 Steel surface properties upon polishing with SiC abrasive papers.	70
Table 7.1 Flow configuration through thin channel flow cell.	88
Table 8.1 Experimental matrix	95
Table 8.2 Experimental Matrix	118
Table 10.1 Chemical reactions accounted for in the model and their equilibrium constants.....	138
Table 10.2 Equilibrium (K), forward (k_f) and backward (k_b) reaction rate coefficients ($K=k_f/k_b$) where T_f is temperature in degrees Fahrenheit, T_K is absolute temperature in Kelvin, T_c is temperature in degrees Celsius, I is ionic strength in molar and p is the total pressure in psi) [69].	139
Table 10.3 Reference molecular diffusion coefficient, D_{ref} [69].	142
Table 10.4 Electrochemical reactions at steel surface	143
Table 10.5 Electrochemical parameters for the reactions included in the model which fit the general rate Equation (10.23) and exchange current density Equation (10.25) [69].	146

List of Figures

Figure 1.1 Thesis and research structure	5
Figure 2.1 A map of world oil reserves according to OPEC, January 2014 [13]	7
Figure 2.2 Oil and gas industry [14]	8
Figure 2.3 Typical corrosion cell [22]	11
Figure 2.4 Corrosion on a steel surface [22]	12
Figure 2.5 Simplified view of a double-layer of negative ions in the electrode and solvated positive ions in the liquid electrolyte, separated by a layer of polarised solvent molecules [28].	15
Figure 2.6 Theoretical potential-current density for a single redox reaction on a metal surface [19].	18
Figure 3.1 Regions of Crystal Growth [36].....	23
Figure 3.2 The effect of supersaturation and temperature on the growth of FeCO_3 [38].....	29
Figure 3.3 Quantity of Fe^{2+} needed to be produced by corrosion to reach FeCO_3 saturation plotted as a function of pH. The brine pH is the pH before corrosion has started [38]	30
Figure 3.4 Corrosion rate over time for static experiment at high temperature (80°C), pCO_2 ranging from 10 to 80 bar and autogeneous pH [34].	31
Figure 3.5 Cross-sectional and surface morphologies of corrosion product films formed at different times at 75°C : 108h (a and b), 144h (c and d), 240h (e and f), $\text{pH}=6.5$, $\text{pCO}_2 = 10$ bar [52].....	32
Figure 3.6 LPR corrosion rates at 120°C , pH 4.0, 1 wt% NaCl and rotating speeds of 0,100, 500 and 1000 rpm (equivalent to 0, 0.1, 0.5 and 1 m/s respectively) [53].....	34
Figure 4.1 De Waard and Milliams nomogram for CO_2 Corrosion [34].....	38
Figure 4.2 Sketch of the calculation domain; δ_f is the surface film thickness, $\delta-\delta_f$ is the liquid boundary layer thickness. The curve on the top represents a typical variation of a single species concentration expected from theory [41].	42
Figure 4.3 Pictorial representation of under deposit corrosion, also known as "film undermining".	46
Figure 5.1 Comparison of precipitation rates ($\text{mol/m}^2/\text{s}$) determined by different precipitation models at varying SR and $T=80^\circ\text{C}$	52
Figure 5.2 Comparison of precipitation rates ($\text{mol/m}^2/\text{s}$) determined by different precipitation models at varying temperature and $\text{SR}=10$	52

Figure 5.3 Schematic of the experimental test cell [9, 10]: 1. Bubbler; 2. Temperature probe; 3. Rubber cork with nylon cord; 4. Steel substrate; 5. Hot plate; 6. Condenser; 7. Cole-Parmer AgCl pH probe; 8. Glass cell.....	56
Figure 5.4 Experimental and calculated (using kinetics expression given by van Hunnik et al.) scale retention rates of iron carbonate under a saturation ratio of 12 to 250 at a temperature of 80°C [9, 10].....	58
Figure 5.5 The comparison of differential scale retention rate (DSRR) of iron carbonate scale (DSRR) and differential corrosion rate of X65 carbon steel (DCR) in pure CO ₂ corrosion under the conditions of initial Fe ²⁺ concentration 50 ppm (which then drifted down), pH 6.6, T=80°C [9, 10].	59
Figure 5.6 The comparison of differential scale retention rate of iron carbonate scale in pure CO ₂ corrosion for constant Fe ²⁺ concentration 50 ppm, pH 6.6, T 60°C, 70°C, and 80°C.....	60
Figure 5.7 The comparison of the experimental scale retention rate by weight change method and the calculated scale retention rate using kinetic expressions given by Johnson and Tomson, van Hunnik et al., and the present expression, under a saturation ratio of 24 to 200 and T = 80°C.....	61
Figure 5.8 Comparison of pK _{sp} for temperature ranges 0-100°C	62
Figure 5.9 Effect of ionic strength on pK _{sp} , solubility product for a varying temperature.	63
Figure 5.10 Effect of ionic strength on S&N precipitation rate equation for varying temperature.	64
Figure 5.11 Main literature findings and work carried out to address the identified limitations.	66
Figure 6.1 Summary of static experimental work done.....	68
Figure 6.2 Labelled 3D CAD model of static experimental set-up.	69
Figure 6.3 Typical LPR plot that demonstrates the linear potential-current relationship at low applied over potential. The gradient is used to obtain the polarisation resistance R _p	72
Figure 6.4 SEM image of carbon steel sample before and after film removal using Clarke's solution. Sample was exposed to a CO ₂ saturated environment at 80°C, pH 6.8 for 20 hours. (a) Before removal. (b) After film removal.....	76
Figure 6.5 (a) Hach Fe ²⁺ ion cuvettes used in analysis of solution. (b) Image representation of working principle behind spectrophotometer used in determining Fe ²⁺ ion concentration in sample solution [83].	79
Figure 6.6 Image of a) SEM used in study and b) TM3030 Benchtop SEM [86]	82

Figure 6.7 a) Image of in-house XRD facility. b) Schematic representation of the XRD Technique and Bragg Diffraction [88],	83
Figure 6.8 XRD pattern results for carbon steel samples [90].	84
Figure 7.1 Exploded and labelled 3D CAD model of designed flow cell. Top right hand corner depicts flow cell with all components fitted together.	86
Figure 7.2 (a) 3D constructed geometry of flow cell imported into COMSOL Multiphysics. (b) Defined mesh distribution across geometry of fluid flow.	89
Figure 7.3 (a) – (d) Computational results showing the velocity fields in (m/s) for each indicated flow setting. Scale is used to determine and indicate, using dotted line, location of three samples. (e) Indicates wall shear stress across surface.	90
Figure 7.4 Test sample fitted into cable gland and screwed into flow cell base.	92
Figure 7.5 Labelled 3D CAD drawing of laboratory flow loop set-up. 1) CO ₂ feed. 2) Temperature probe. 3) Hot plate. 4) Condenser. 5) Glass beaker. 6) Pump. 7) Tubing. 8) X65 Carbon Steel Samples. 9) Reference/ counter electrode. 10) Flow cell. 11) Pump stand. 12) Flow cell stand.....	94
Figure 8.1 Effect of temperature on CO ₂ corrosion of X65 carbon steel. (Working Conditions: 3.5 wt% NaCl, pH 6.8, 0.54 pCO ₂ , 600 grit).	96
Figure 8.2 Effect of salinity on CO ₂ corrosion of X65 carbon steel. (Working Conditions: 80°C, pH 6.8, 0.54 pCO ₂ , 600 grit)	97
Figure 8.3 Effect of salinity on CO ₂ corrosion of X65 carbon steel, logarithmic plot. (Working Conditions: 80°C, pH 6.8, 0.54 pCO ₂ , 600 grit)	98
Figure 8.4 Effect of surface roughness on CO ₂ corrosion of X65 carbon steel, logarithmic plot. (Working Conditions: 80°C, pH 6.8, 0.54 pCO ₂ , 3.5 wt% NaCl)	99
Figure 8.5 Effect of pH on CO ₂ corrosion of X65 carbon steel, logarithmic plot. (Working Conditions: 80°C, 0.54 pCO ₂ , 3.5 wt% NaCl, 600 grit).....	100
Figure 8.6 SEM Imaging of X65 carbon steel surface at varying pH. (Working Conditions: 80°C, 0.54 pCO ₂ , 3.5 wt% NaCl, 600 grit)	101
Figure 8.7 Mass gain due to FeCO ₃ precipitation at pH 6.3 and pH 6.8 over variable time periods (Working Conditions: 80°C, 0.54 pCO ₂ , 3.5 wt% NaCl, 600 grit).	102
Figure 8.8 Mass loss due to FeCO ₃ precipitation at pH 6.3 and pH 6.8 over variable time periods (Working Conditions: 80°C, 0.54 pCO ₂ , 3.5 wt% NaCl, 600 grit).	103

Figure 8.9 SEM images illustrating FeCO ₃ crystal formation at different time periods for pH 6.3 and pH 6.8. Images are also annotated to indicate average crystal size, average mass gain and corrosion at these time steps.....	105
Figure 8.10 Analysis of SEM images over time to determine average crystal size for pH 6.3 and pH 6.8.	106
Figure 8.11 Image analysis using MATLAB to determine surface coverage. a) Image as attained from SEM for 80°C, 6.3 pH, 5 hours. b) Image corrected for contrast and brightness. c) Matlab correction into black and white pixels.....	106
Figure 8.12 SEM images illustrating FeCO ₃ crystal formation at different time periods for pH 6.3. Images are also annotated to indicate surface coverage at these time steps.....	108
Figure 8.13 SEM images illustrating FeCO ₃ crystal formation at different time periods for pH 6.8. Images are also annotated to indicate surface coverage at these time steps.....	109
Figure 8.14 Analysis of SEM images over time to determine average surface coverage for pH 6.3 and pH 6.8.	110
Figure 8.15 Corrosion rate (mm/year) calculated over time from mass loss measurements.	111
Figure 8.16. Comparison of weight loss measurements with corrected LPR measurements for pH 6.3 and pH 6.8.	112
Figure 8.17 Precipitation rate (mol/m ² .s) calculated over time from mass gain measurements.	113
Figure 8.18 Bulk saturation ratio over time determined through spectroscopy for pH 6.3 and pH 6.8.	114
Figure 8.19 Comparison of bulk Fe ²⁺ ion concentration at pH 6.3 and pH 6.8.	115
Figure 8.20 % Fe ²⁺ ions lost from surface that precipitates as FeCO ₃ determined from weight change results.	116
Figure 8.21 XRD patterns of X65 carbon steel exposed to a CO ₂ saturated environment at 80°C, pH 6.3 and pCO ₂ 0.54 bar for 20 hours.	117
Figure 8.22 XRD patterns of X65 carbon steel exposed to a CO ₂ saturated environment at 80°C, pH 6.3 and pCO ₂ 0.54 bar for 20 hours.	117
Figure 8.23 Effect of initial SR on corrosion rate and precipitation rate over 2 hour period. (Working Conditions: 80°C, pH 6.8, 0.54 pCO ₂ , 3.5 wt% NaCl).....	119
Figure 8.24 Precipitation rate vs. bulk saturation ratio for varying amounts of FeCl ₂ .4H ₂ O added over 2 hour period. (Working Conditions: 80°C, pH 6.8, 0.54 pCO ₂ , 3.5 wt% NaCl).....	119

Figure 8.25 Effect of initial SR on precipitation rate and corrosion rate over time. (Working Conditions: 80°C, pH 6.8, 0.54 pCO ₂ , 3.5 wt% NaCl, 50 ppm FeCl ₂ .4H ₂ O)	120
Figure 8.26 Precipitation rate as a function of the bulk saturation ratio. Arrow indicated direction with time. (Working Conditions: 80°C, pH 6.8, 0.54 pCO ₂ , 3.5 wt% NaCl, 50 ppm FeCl ₂ .4H ₂ O)	121
Figure 8.27 Change in mass gain and mass loss measurements testing the effect of turbulence and adding FeCl ₂ .4H ₂ O on a pre-formed protective film.	123
Figure 8.28 Calculated precipitation rate and corrosion rate testing the effect of turbulence and adding FeCl ₂ .4H ₂ O on a pre-formed protective film.	123
Figure 9.1 Nyquist plot indicating solution resistance and charge transfer resistance. Working conditions (80°C, pH 6.8, 3.5 wt% NaCl and velocity of 1 m/s)	124
Figure 9.2 Tafel plot for 80°C, pH 6.8, 3.5 wt% NaCl and velocity of 1 m/s across sample surface.	125
Figure 9.3 Overall analysis of electrochemical measurements of X65 carbon steel at 80°C, pH 6.8, 3.5 wt % NaCl and a flow velocity of 1 m/s. (a) 3D representation of flow cell identifying samples and their corresponding redox electrode. (b) Nyquist plot. (c) Tafel plot. (d) Corrected corrosion rate over time for each sample.	127
Figure 9.4 Nyquist plot showing solution resistance for variable flow velocities at 80°C, pH 6.8, pCO ₂ 0.54 bar and 3.5 wt % NaCl.....	129
Figure 9.5 Tafel plot, effect of velocity at 80°C, pH 6.8, pCO ₂ 0.54 bar and 3.5 wt % NaCl.	129
Figure 9.6 Effect of velocity on corrosion rate for working conditions 80°C, pH 6.8, pCO ₂ 0.54 bar and 3.5 wt % NaCl.	130
Figure 9.7 Precipitation rate determined from mass gain measurements at the end of 20 hours for variable flow velocity and working conditions 80°C, pH 6.8, pCO ₂ 0.54 bar and 3.5 wt % NaCl.	131
Figure 9.8 SEM images of the surface of the sample at variable flow velocities (a) 0.95 m/s (b) 0.63 m/s (c) 0.31 m/s (d) 0.12 m/s.	132
Figure 9.9 XRD patterns of X65 carbon steel exposed to a CO ₂ saturated environment at 80°C, pH 6.8, pCO ₂ 0.54 bar and flow velocity 0.12 m/s for 20 hours.	132
Figure 9.10 XRD patterns of X65 carbon steel exposed to a CO ₂ saturated environment at 80°C, pH 6.8, pCO ₂ 0.54 bar and flow velocity 0.95 m/s for 20 hours.	133
Figure 10.1 Stages of corrosion model.	136
Figure 10.2 Illustration of computation domain for CO ₂ corrosion rate model.....	138

Figure 10.3 Equilibrium distribution of species concentration in bulk solution as a function of pH at T=80°C, pCO ₂ = 0.54 bar	141
Figure 10.4 Comparisons between model predictions results at 1 bar CO ₂ , 20°C, pH 4 and 1wt% NaCl.	149
Figure 10.5 Comparisons between model predictions results at 1 bar CO ₂ , 20°C, pH 6 and 1wt% NaCl.	150
Figure 10.6 Effect of pH on predicted steady state corrosion rate using developed model.	151
Figure 10.7 Effect of temperature on predicted steady state corrosion rate using developed model.	151
Figure 10.8 Comparison of experimental results with model output for variable velocity at 80°C, pH 6.8, pCO ₂ 0.54 bar and 3.5 wt% NaCl.	152
Figure 11.1 Schematic diagram describing COMSOL analysis	154
Figure 11.2 Simplified sketch of computational grid and control volumes used for discretisation of the computational domain in COMSOL. δ - δ_f represents the liquid boundary layer thickness.....	155
Figure 11.3 Saturation ratio trend for varying number of mesh elements.....	158
Figure 11.4 Flow velocity profile across channel height at different sections of the flow channel.	158
Figure 11.5 Flow velocity across height of channel at centre of geometry.	159
Figure 11.6 Deviation of dissolved species concentration from the bulk values as a function of distance from the steel surface; 20°C, pipe diameter 0.1 m, flow velocity 1 m/s and pH 6, pCO ₂ = 1 bar.	160
Figure 11.7 COMSOL model output for deviation of dissolved species concentration from the bulk values as a function of distance from the steel surface; 20°C, 3mm channel height, flow velocity 0.47 m/s and pH 6, pCO ₂ = 1 bar.....	162
Figure 11.8 Supersaturation as a function of distance from the steel surface at conditions: 20°C, pipe diameter 0.1 m, flow velocity 1 m/s, varying pH, pCO ₂ = 1 bar and [Fe ²⁺] = 1 ppm [35].	163
Figure 11.9 COMSOL model output for saturation ratio as a function of distance from the steel surface at conditions: 20°C, 3mm channel height, flow velocity 1 m/s, varying pH, pCO ₂ = 1 bar and [Fe ²⁺] = 1ppm.	163
Figure 11.10 Saturation ratio as a function of distance from the surface for variable flow velocities operated within thin channel flow cell at 80°C, pH 6.8 and pCO ₂ 0.54 bar.	164
Figure 11.11 Steady state corrosion rate model output for variable velocity at 80°C, pH 6.8, pCO ₂ 0.54 bar and 3.5 wt% NaCl.....	165

Figure 11.12 pH as a function of distance from the surface for variable flow velocities operated within thin channel flow cell at 80°C, pH 6.8 and pCO ₂ 0.54 bar.	166
Figure 12.1 Representation of typical corrosion rate graph based on experimental observations for a pH 6.3 and pH 6.8.	168
Figure 12.2 Pictorial representation of development of FeCO ₃ film over time for pH 6.3 and pH 6.8.	169
Figure 12.3 Effect of pH on saturation ratio as a function of distance from the metal surface for parameters of 80°C, pCO ₂ 0.54 bar, 3.5 wt % and a velocity of 0.1 m/s.	170
Figure 12.4 Effect of pH on saturation ratio as a function of distance from the metal surface for parameters of 80°C, pCO ₂ 0.54 bar, 3.5 wt %, 0.1 m/s and corrosion rate of 0.45 and 0.09 for pH 6.3 and pH 6.8 respectively.	171
Figure 12.5 Parameters investigated and observed to have an effect on FeCO ₃ precipitation rate.	172
Figure 12.6 Corrosion rate as a function of surface coverage for pH 6.3 and pH 6.8 at 80°C, 3.5 wt% NaCl, pCO ₂ 0.54 bar.	173
Figure 12.7 Precipitation as a function of corrosion rate for pH 6.3 and pH 6.8 at 80°C, 3.5 wt% NaCl, pCO ₂ 0.54 bar.	175
Figure 12.8 Sequence carried out to determine precipitation rate from surface coverage and crystal size.	176
Figure 12.9 Comparison of the precipitation rate determined from mass gain measurements and a combined analysis of surface coverage and crystal size at 80°C, pH 6.3, 3.5 wt% NaCl, pCO ₂ 0.54 bar.	177
Figure 12.10 Comparison of the precipitation rate determined from mass gain measurements and a combined analysis of surface coverage and crystal size at 80°C, pH 6.8, 3.5 wt% NaCl, pCO ₂ 0.54 bar.	178
Figure 12.11 Effect of pH and temperature on CO ₃ ²⁻ ion concentration. ...	179
Figure 12.12 Saturation ratio and corrosion rate as a function of velocity from developed model for thin channel flow cell. Working Conditions (80°C, pH 6.8 and pCO ₂ 0.54 bar).	180
Figure 12.13 Surface saturation ratio as a function of distance from metal surface for varying concentration of Fe ²⁺ added at 80°C, pH 6.8, 0.54 bar, 3.5 wt% NaCl and 0.1 m/s.	182
Figure 12.14 Corrosion rate vs. time compared for a freely corroding system and 50 ppm Fe ²⁺ ions added for experiments conducted at 80°C, pH 6.8, 0.54 bar and 3.5 wt% NaCl.	183

Figure 12.15 Comparison of experimental data with precipitation models for a series of test done over initial time period of 2 hours and varying initial $\text{FeCl}_2 \cdot 4\text{H}_2\text{O}$. (Working Conditions: 80°C , pH 6.8, 0.54 pCO_2 , 3.5 wt% NaCl).	184
Figure 12.16 Precipitation rate as a function of supersaturation in comparison to S&N model. (Working Conditions: 80°C , pH 6.8, 0.54 pCO_2 , 3.5 wt% NaCl, 50 ppm $\text{FeCl}_2 \cdot 4\text{H}_2\text{O}$).	185
Figure 12.17 Precipitation rate as a function of surface saturation ratio for a thin channel flow cell at variable flow velocities in comparison to S&N precipitation model. (Working Conditions: 80°C , pH 6.8, 0.54 pCO_2 , 3.5 wt% NaCl).....	188
Figure 13.1 Schematic for once-through flow system for future work.	193

List of Abbreviations/ Symbols

AV	Surface Area/Volume Ratio
AC	Alternate Current
A_p	Pre-exponential Constant
bbI	Oil Barrel
CAD	Computer Aided Design
CE	Counter Electrode
c_i	Concentration of different species i
CR	Corrosion Rate
CRA	Corrosion Resistant Alloys
D	Diffusion Coefficient
DC	Direct Current
DCR	Differential Corrosion Rate
D_{ref}	Reference molecular diffusion coefficient
DSRR	Differential Scale Retention Rate
E	Potential difference
E°	Potential difference at standard conditions
E_a	Activation Energy
E_{anodic}	Reduction potential of anodic reaction
E_{cathodic}	Reduction potential of cathodic reaction
E_{cell}	Cell potential in volts
E_{corr}	Free Corrosion Potential
EDL	Electrical Double Layer
EIS	Electrochemical Impedance Spectroscopy
F	Faraday's Constant
f_{CO₂}	Fugacity of CO ₂
G&T	Greenberg and Tomson [4, 5]
I	Ionic Strength

i_{corr}	Corrosion Current Density
IFE	Institute of Energy Technology
IHP	Inner Helmholtz Plane
J&T	Johnson and Tomson [6, 7]
k	Boltzman Constant
K	Equilibrium Constant
K_b	Backward Reaction Rate Coefficient
K_{CG}	Crystal Growth Rate Constant
K_f	Forward Reaction Rate Coefficient
k_m	Mass Transfer Coefficient
K_{sp}	Solubility Product
LPG	Liquefied Petroleum Gas
LPR	Linear Polarisation Resistance
MW	Molecular Weight
n	Number of electrons exchanged
N_i	Flux of species, i
NN	Neural Network
OCP	Open Circuit Potential
OHP	Outer Helmholtz Plane
OPEC	Organisation of Petroleum Exporting Countries
ORP	Oxidation-Reduction Potential
OTC	Offshore Technology Conference
p	Total pressure
p_{CO_2}	Partial pressure of carbon dioxide
PDE	Partial differential equation
PDP	Potentiodynamic polarisation
P_{FeCO_3}	Precipitation rate of FeCO_3
ppm	Parts per million (mg/L)
PR	Precipitation Rate

Q	Volumetric Flow Rate
R	Ideal gas constant
r_c	Critical Nucleus Size
R_c	Rate of Crystal Nucleation
R_{CT}	Charge Transfer Resistance
Re	Reynold's number
RE	Reference Electrode
R_{FeCO₃}	Precipitation rate of FeCO ₃
R_i	Rate of reaction of species i
R_p	Polarisation Resistance
R_s	Solution Resistance
S&N	Sun and Nestic [9, 10]
Sc	Schmidt Number
SEM	Scanning Electron Microscopy
Sh	Sherwood number
SHE	Standard Hydrogen Electrode
SR	Saturation Ratio
SS	Super-saturation
ST	Scaling Tendency
T_c	Temperature in degrees Celcius
TCFC	Thin Channel Flow Cell
T_f	Temperature in degrees Farenheit
T_K	Temperature in Kelvin
V_m	Mass transfer Processes
vP&H	van Hunnik et al [8].
V_r	Electrochemical Processes
WE	Working Electrode
wt%	Weight Percentage
XRD	X-Ray Diffraction

z_i	Species charge
α_k	Charge transfer coefficient
β_a	Anodic tafel slope
β_c	Cathodic tafel slope
γ	Interfacial tension
ΔG	Gibbs free energy change
ΔG°	Gibbs free energy change at standard conditions
ε	Volumetric Porosity
η	Over-potential
λ	Wavelength of beam
ρ	Density
$\sigma(S)$	Expression for Saturation Ratio
σ_f	Surface film thickness
T_{ind}	Induction time
Φ	Electric potential of solution in volts

Chapter 1

Introduction and Research Project Background

1.1 Project Background

The Oil and Gas industry is a multi-billion dollar industry responsible for the production of petroleum products that accounts for a large percentage of the world's energy consumption. The production of oil and gas, its transportation, refining and its subsequent use as fuel and raw materials constitute a complex and demanding process. One of the various problems encountered in this process that has a significant economic and environmental impact on the oil and gas industry is carbon dioxide (CO₂) corrosion of pipelines [1].

Despite the fact that high cost Corrosion Resistant Alloys (CRAs) were developed to resist internal corrosion, carbon steel is still the most widely used material in oil and gas production. The industry dependence on the use of carbon steel as pipework materials is based on their vast availability and ability to fulfil many of the mechanical, structural, fabrication and cost requirements. However, their poor corrosion performance has led to corrosion being widely investigated to optimise the use of carbon steel in corrosive conditions and ensure the operational integrity of equipment and facilities. Over the past several decades, corrosion models have been developed to predict the corrosion rate of carbon steel under their specific working conditions. Reliable estimation of the corrosion rate is a key consideration in the design of pipelines and their related infrastructure. Whilst these models have been extensively used, their proper application is limited to the specific conditions in which the models are built which mean that unplanned failures and unexpectedly high corrosion rates are experienced in some cases without proper explanation [2, 3]. In more recent years, advancements in the mechanistic understanding of the underlying processes in CO₂ corrosion have provided opportunities for more robust calculations and flexibility required to include various conditions and processes in corrosion rate prediction.

One area of critical importance in the CO₂ corrosion of mild steel and the main focus of this thesis is the precipitation of ferrous carbonate (FeCO₃) films on the surface of X65 carbon steel. The layer forms on the corroding surface preventing the underlying steel from further dissolution and acting as

a barrier stifling the corrosion rate. However, if there is any damage of the protective FeCO_3 film, it may lead to serious localised corrosion problems by exposing the underlying metal to the aggressive corrosive environment resulting in catastrophic failure and significant economic cost.

FeCO_3 film growth depends primarily on the kinetics of scale formation. Therefore, understanding the factors governing the rate of precipitation and formation of FeCO_3 layer on the corroding surface is an important step in predicting and controlling the CO_2 corrosion of carbon steel. In literature, there are four models reported for calculating the rate of FeCO_3 precipitation. In each case, the rate of precipitation is a function of iron carbonate super saturation, the solubility limit, temperature and surface area-to-volume ratio. The precipitation rate is measured by either the consumption of Fe^{2+} from the bulk solution in models by Greenberg and Tomson (G&T) [4, 5], Johnson and Tomson (J&T) [6, 7] and van Hunnik et al. (vP&H) [8] or the accumulation of FeCO_3 on the steel sample in model by Sun and Netic (S&N) [9, 10]. However, both of these test methods are based on measurements conducted in a glass cell in static conditions where the kinetics of FeCO_3 precipitation are accelerated by the addition of $\text{FeCl}_2 \cdot 4\text{H}_2\text{O}$ and correlated with bulk solution properties. They do not address the key aspects of FeCO_3 formation in real corroding systems which relate to the local surface supersaturation produced as a result of the production of Fe^{2+} ions due to the corrosion process. In the following work, the developed FeCO_3 precipitation models are critically analysed. The identified limitations of these models when accounting for FeCO_3 is the key driver for this research.

1.1 Objectives

In order to address the gaps and limitations outlined previously, the focus of the PhD is to investigate the formation of corrosion films, particularly the early stages of initiation and propagation in a combined experimental and modelling approach.

The following objectives are defined:

- To understand the development in the morphology of the FeCO_3 film under different environmental conditions and its consequent effect on the degradation rates of a pipeline.

- To understand the nature of the near surface region and in particular the flow characteristics (and associated mass transfer) and the distribution of the ionic species (electro-kinetics).
- To assess the validity of the existing FeCO_3 precipitation models highlighting their confines and applicability.
- To design and develop a flow cell to understand the experimental significance of transition from static to flow induced corrosion and the effect on the kinetics of iron carbonate scale formation.
- To develop a mechanistic model to assess the local, near-surface concentration boundary layer to determine the local saturation ratio. Assess the fundamental link between FeCO_3 growth and the saturation ratio.

1.2 Structure of Thesis

This thesis contributes to literature by providing further understanding of the kinetics of FeCO_3 nucleation and growth on the surface of X65 carbon steel. It demonstrates the ability of laboratory apparatus to investigate the characteristics of the formation of FeCO_3 film and prediction models, based on a purely theoretical understanding of the physics behind the process, to provide information where experimental techniques are limited. The combined experimental and modelling approach provides a complementary analysis and defines the structure of the thesis.

Chapter 2 presents an initial introduction to corrosion in the oil and gas industry expressing its economic and environmental significance to the industry, the existing preventative measures and the different types of corrosion failure. It also provides a fundamental understanding on the chemistry of corrosion. The literature review is presented in three chapters. **Chapter 3** provides a literature review on CO_2 corrosion and the varying parameters investigated to further its understanding and that of its by-product, FeCO_3 film formation. **Chapter 4** and **Chapter 5** consist of a full analysis of the existing CO_2 corrosion models over the last few decades and the FeCO_3 precipitation models respectively. The later chapters present the experimental, design and modelling work conducted throughout this project. **Chapter 6** presents the experimental methods and techniques developed in order to investigate the formation of FeCO_3 films. **Chapter 7** presents the design and development of a flow cell to incorporate flow characteristics within the analysis. **Chapter 8** and **Chapter 9** are the experimental results chapters and systematically provide an analysis of the obtained data from

experiments conducted in static and flowing conditions respectively. **Chapter 10** and **Chapter 11** comprise the modelling work. They are divided into two chapters based on their individual predicted outputs and the two different modelling software used, MATLAB and COMSOL. A final discussion highlighting the main findings, along with a comparison of literature and experimental studies is presented in **Chapter 12**. The final **Chapter 13** provides the limitations of this study, future work and overall conclusions. Figure 1.1 demonstrates a brief overview of the thesis structure sequentially illustrating the different phases of research, measurements carried out or parametric values input, output and relationship between the two segments.

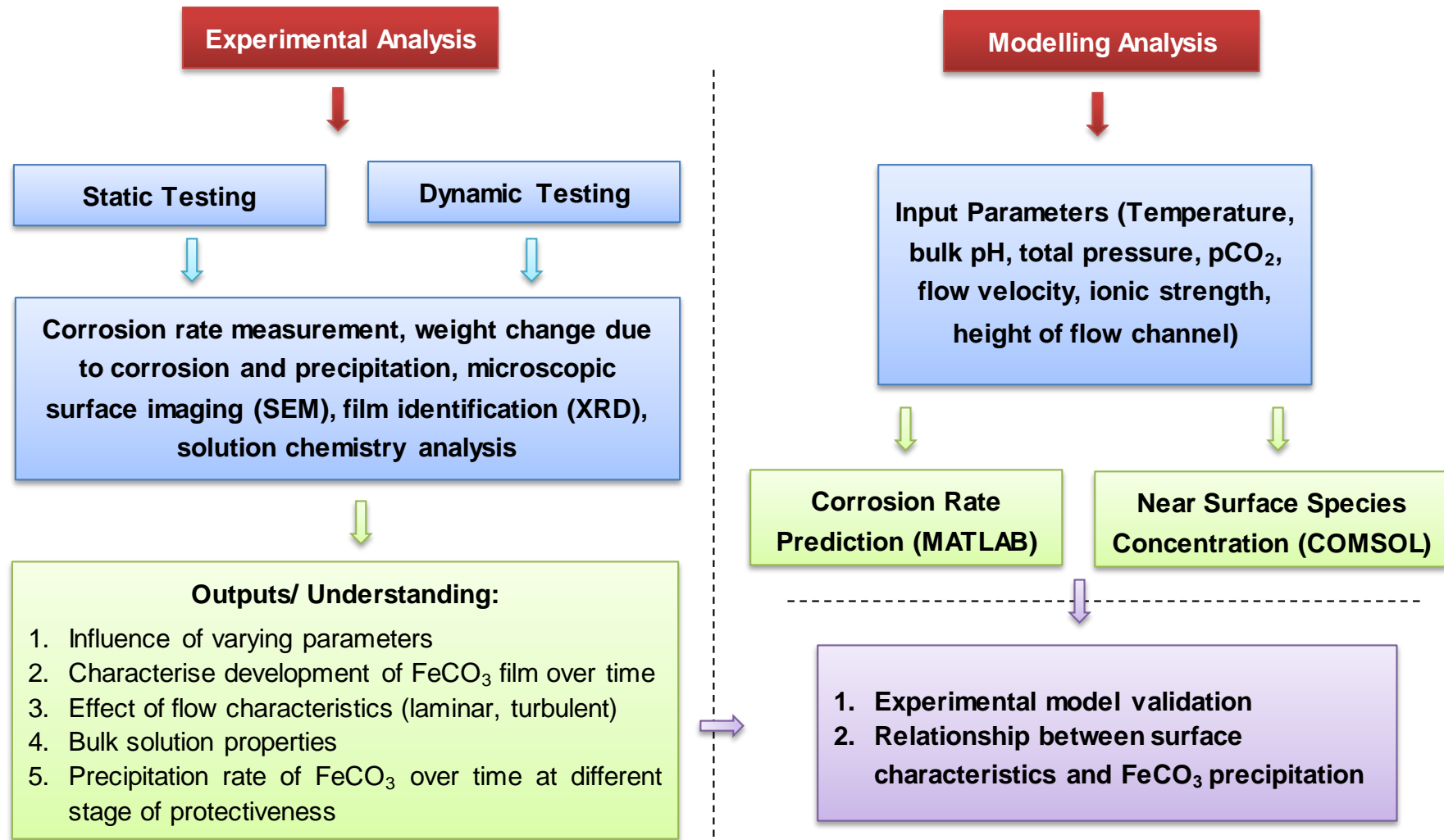


Figure 1.1 Thesis and research structure

Chapter 2

Introduction to Corrosion in the Oil and Gas Industry

This chapter provides a birds-eye view of the oil and gas industry. It discusses the importance of the industry and its demand, the industry network from extraction to consumption, the impact of corrosion on the industry and an understanding of the corrosion process.

2.1 The Petroleum Industry

Over the past two centuries, civilisation has depended on energy derived from crude oil, natural gas, coal, nuclear reaction and renewable sources such as wind, sun, biofuels, etc. Oil and gas is a multi-billion dollar industry responsible for the production of petroleum products that accounts for a large percentage of the world's energy consumption as shown in Table 2.1

Table 2.1 Current sources of world energy, 2005 [11]

Energy Source	Supply Percentage
Crude oil	38
Natural gas	23
Coal	23
Nuclear	7
Renewables	9

It is approximated that the total worldwide oil consumption is 93 million bbl/day as per the International Energy agency [12] and the approximate location and intensity of the oil reserves around the world is shown in Figure 2.1.

This energy, that is so fundamental in our day to day life, comes from hydrocarbons that occur naturally in the earth. According to the most widely accepted theory, hydrocarbons were formed when organic matter, such as the remains of plants or animals, was compressed under the earth, at very high pressure and temperature for a very long time. They may occur in the earth either as liquid or gas. Liquid hydrocarbon is commonly known as

crude oil or petroleum and gaseous hydrocarbon is commonly known as natural gas.

At relatively lower temperatures, more crude oil is formed and at higher temperatures more gas is formed. As we go further beneath the earth's crust, the temperature increases. For this reason, gas is usually associated with oil in wells that are within one or two miles from the earth's crust. Wells deeper than two miles primarily produce natural gas. Together, they consist of more than 60% of the current world energy consumption [11].

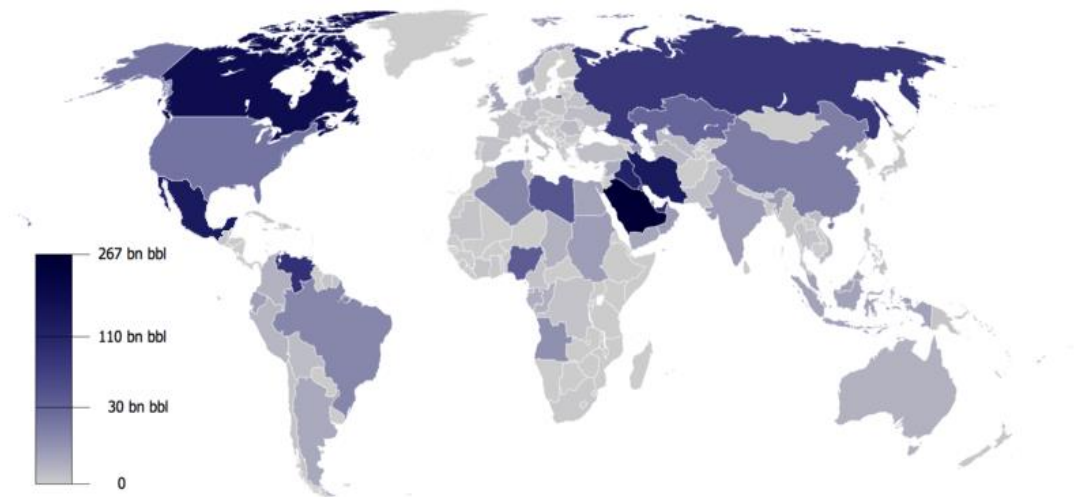


Figure 2.1 A map of world oil reserves according to OPEC, January 2014 [13]

Petroleum products in their crude form are of little use to consumers. The Oil and Gas industry is a multitude of complex processes that essentially has the ultimate goal of transforming crude oil into marketable products. Figure 2.2 illustrates the four essential processes. The initial process is the exploration and extraction. Seismic data and reservoir technology is used to discover the location of potential oil and gas reserves prior to drilling either on land or offshore. Once oil has been brought to the surface, it is cleaned and separated to meet the specific standards of refineries. This generally takes place onsite where extracted well mixed oil, gas, and saltwater are separated out in settling tanks. The third stage is the transportation of crude oil to refineries that are usually near oil consumption markets. This is done mainly via pipeline. For longer distances, oil is put in tanker trucks or moved by sea in oil tankers. After transportation, much of the crude oil is placed in storage facilities or tank farms until the refinery is ready to process it. Finally the last stage is the refining and delivery. In the refinery, petroleum is

physically, thermally and chemically separated into fractions and then converted into finished products. About 90% of these products are fuels such as gasoline, aviation fuels, distillate and residual oil, liquefied petroleum gas (LPG), and kerosene. Refineries also produce non-fuel products, including petrochemicals, asphalt, road oil, lubricants, solvents and wax. Petrochemicals (ethylene, propylene, benzene and others) are shipped to chemical plants, where they are used to manufacture chemicals and plastics [14-16].

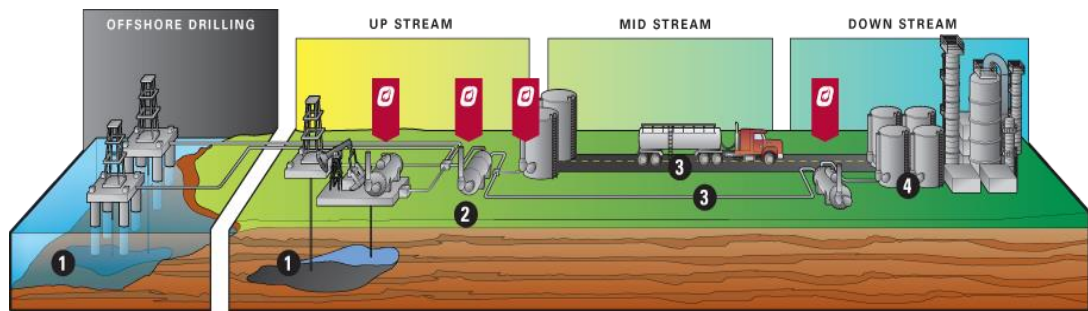


Figure 2.2 Oil and gas industry [14]

2.2 Pipeline Corrosion and its Significance

At the source of petroleum production, when an oil company pumps crude oil out of the ground, it also pumps out a hot mixture of water, carbon dioxide, sulfur, microorganisms and solid particles. The exposure of these chemicals on the internal walls of the pipelines is what causes the corrosion of the pipe wall. Corrosion degrades the useful properties of material and structures including strength, appearance and permeability to liquids and gases. The nature and extent of the damage caused depends on the concentration and particular combinations of these various elements within the pipe as well as of the operating conditions within the pipeline [2, 14].

Table 2.2 Analysis of selected number of pipeline failures in petroleum related industries [17]

Type of Failure	Frequency (%)
Corrosion (all types)	33
Fatigue	18
Mechanical damage/ overload	14
Brittle fracture	9
Fabrication defects (excluding weld defects)	9

Welding defects	7
Others	10

The wide-ranging environmental conditions present in the oil and gas industry provide a plethora of different degradation phenomena causing failures, with corrosion being the most recurrent form of attack. An analysis of the types of petroleum industry related failures and corrosion related failures were published in Kermani et al. [17] and reproduced in Table 2.2 and Table 2.3.

Table 2.3 Causes of corrosion related failures in petroleum related industries [17]

Type of Failure	Frequency (%)
CO ₂ related	28
H ₂ S related	18
Preferential weld	18
Pitting	12
Erosion corrosion	9
Galvanic	6
Crevice	3
Impingement	3
Stress corrosion	3

Despite the development of high cost Corrosion Resistant Alloys (CRAs), the industry continues its dependency on the use of carbon steel as pipework materials due to their vast availability and ability to fulfil many of the mechanical, structural and cost requirements. Their poor corrosion performance; however, has led to corrosion being widely investigated to optimize the use of carbon steel in a corrosive environment. A stringent corrosion management strategy is essential to not only reduce cost, but to prevent serious safety and environmental implications [1].

According to Table 2.2 and Table 2.3, approximately 33% of pipeline failures in the oil and gas industry are corrosion-related, and about half of these come about under CO₂ (sweet) and H₂S (sour) aqueous environments. Extracted oilfield brines pass through wellheads, tubing strings, flowlines and

risers under variable temperatures (from 5°C to 300°C (downhole)) and pressures (0.1 MPa to 100 MPa (downhole)) [18, 19] and internal corrosion of equipment under these conditions can become quite problematic.

According to an Offshore Technology Conference (OTC) presentation in 2008, the total annual cost of corrosion in the oil and gas production industry is estimated to be \$1.372 billion [20]. These costs include preventative and maintenance measures taken to prevent the occurrence of a pipeline rupture and the major financial and economic losses that result from a pipeline failure. As the years have progressed, more and more preventative measures are taken when a pipeline is built in an attempt to ensure the optimal and secure operation of pipelines.

Field devices such as flow, pressure and temperature gauges/transmitters and other devices are installed along pipelines to measure required data to maintain its remote operation. Furthermore, pipelines are also kept clean to ensure the integrity of its contents flowing through using a bullet shaped instrument called a pig that scrubs the wall of pipelines. More technologically advanced pigs, called smart pigs, use cameras to monitor the pipe for flaws and detect anomalies in the pipe that need to be addressed, such as corrosion, pipeline deformation, cracking and other abnormal features. Pipe manufacturers also employ many preventative measures such as preventative coatings, cathodic protection, inhibitors, etc. to safeguard the pipe and pipeline welds from corrosion [17, 21].

Despite the high costs of maintaining these measures, the costs caused by plant failure are significantly larger than the cost of prevention. The financial impact of a plant failure includes lost revenue, lost product (from spills, fires, replacements etc.) and efficiency, contamination of product, delays and lawsuits [17, 21].

The costly impact of corrosion on industry and the environment places a great demand on the importance of managing corrosion effectively and efficiently. This makes it imperative that research is sustained in the field of corrosion mitigation. Researchers are presented with the challenge of reducing unavoidable costs through advancements in technology whilst searching for more environmentally friendly products for industry to use. With the growing environmental awareness and imposed international legislation, corrosion issues in the oil and gas industry are much under scrutiny, highlighting the necessity for intensive research.

2.3 The Basics of Corrosion in an Electrochemical Cell

Recognising corrosion when it does occur and understanding the mechanisms involved is an instrumental initial step in corrosion mitigation and management.

2.3.1 Electrochemical Cell

The basic corrosion mechanism follows the principle of an electrochemical cell which is capable of either generating electrical energy from chemical reactions or facilitating chemical reactions through the introduction of electrical energy. A typical cell consists of two half cells, each containing an electrode immersed in an electrolyte. All metals have a tendency to dissolve or corrode to a greater or lesser degree. In this case, the metal with the greater tendency to corrode forms the negative pole and is called the anode. When the two are connected, the other metal forms the positive pole, or cathode as shown in Figure 2.3. Loss of positive metal ions from the anode causes a release of free electrons in a process called oxidation. The build-up of electrons generates an electrical potential, causing them to flow through the conductor to the cathode. At the cathode, excess electrons are neutralised or taken up by ions in the electrolyte in a process called reduction. The anode will continue to corrode as long as the electric circuit is maintained and the metal ions are removed from solution [19, 22].

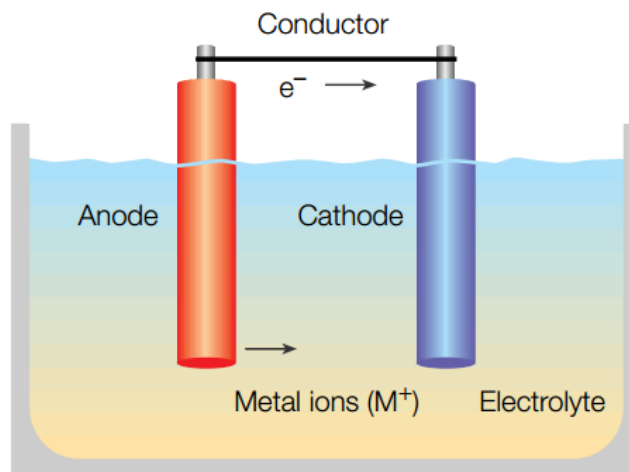


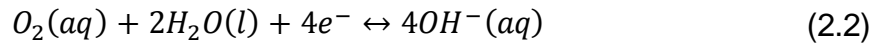
Figure 2.3 Typical corrosion cell [22]

In the case of carbon steel or a real metal surface, the anode and cathode form on the single piece of metal made of small crystals of slightly different

compositions. In other words, different regions of the same metal surface, can represent the anodes and cathodes on of an electrochemical cell. The iron (Fe) in the steel has a tendency to dissolve into the solution as Fe^{2+} leaving two electrons behind and giving that area of the metal a small negative charge.



If nothing happens to remove Fe^{2+} ions around the anodic site, the tendency to dissolve will diminish. In oil production, Fe^{2+} ions are commonly removed by reacting with oxygen (O_2), hydrogen sulphide (H_2S) or carbon dioxide (CO_2) as shown in Figure 2.4. Excess electrons flow away from the anodic region to a site where they form a cathode and where the reduction occurs. Reduction of oxygenated water forms hydroxyl ions $[OH^-]$.



If oxygen is not present, but CO_2 or H_2S is, then the dominant cathodic reaction is the reduction of hydrogen ions to produce hydrogen gas.



In more complex cases, the metal ions combine with other species in the solution and precipitate compounds such as rust (Fe_2O_3), iron sulphides (FeS) or iron carbonate ($FeCO_3$) [19, 22, 23].

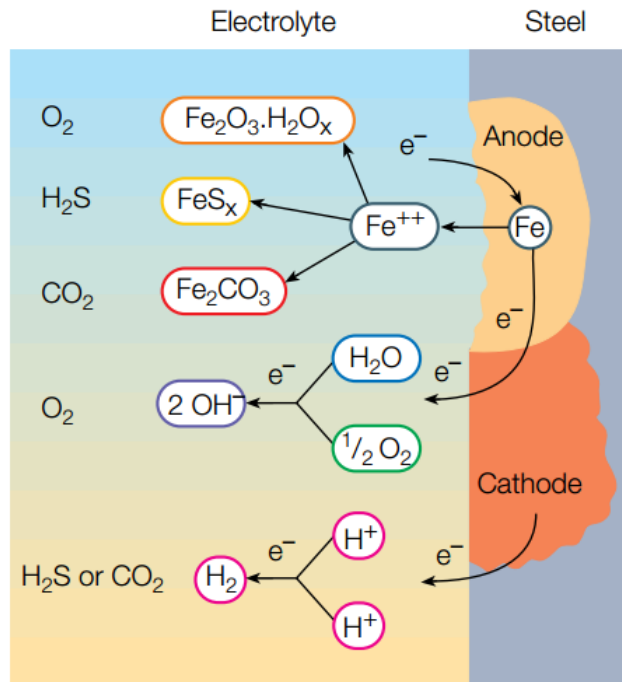


Figure 2.4 Corrosion on a steel surface [22]

2.3.2 Thermodynamics of Aqueous Corrosion Reactions

Engineering metals are unstable and given the opportunity, they will corrode as discussed in the previous section. Metals try to lower their energy by spontaneously reacting to form solutions or compounds with greater thermodynamic stability [24]. The following section looks at the driving force for metallic corrosion which is the Gibbs free energy change (ΔG).

Gibbs free energy is the change in free energy of the metal and environment combination brought about by corrosion. If a reaction is spontaneous, then ΔG must be negative. The term ΔG is only the difference between the Gibbs energies of the final and initial states of the reaction process, making it independent of the various intermediate stages [3, 25].

A metal surface immersed in any aqueous solution will develop an electrode potential. Faraday derived an equation which relates potential difference and charge transported with the Gibbs free energy change of the corrosion process [25].

$$\Delta G = (-nF)E \quad (2.4)$$

Where ΔG is the free energy change for the corrosion reaction in kJ/mol, n is the number of electrons exchanged in the corrosion reaction, F is Faraday's constant in Coulombs/mole and E is the potential difference at non-standard conditions in Volts.

By using the superscript ($^\circ$), the equation can be rewritten to represent standard conditions at a temperature of 273.15 K and a pressure of 1 atmosphere [25].

$$\Delta G^\circ = (-nF)E^\circ \quad (2.5)$$

Values of E° are available for all metals as well as many other half cell redox reactions and examples of some standard half-cell potentials are provided in Table 2.4. An absolute measurement of this standard electrode potential is not possible. It can however be measured against a reference system. By convention, standard electrode potential for electrochemical reaction are measured against a standard hydrogen electrode (SHE). This half-cell reference is given an E° of 0.00 V. Metals at the negative end corrode readily and tend to be anodes [25, 26].

The Gibbs free energy of a chemical reaction is related to the temperature and composition of the reaction mixture. By using thermodynamic principles, the value of ΔG at any given temperature or concentration can be defined as.

$$\Delta G = \Delta G^\circ - RT \ln \frac{[a_{products}]}{[a_{reactants}]} \quad (2.6)$$

Where R is the ideal gas constant (8.314 J/mol.K), T is the absolute temperature in Kelvin (K) and $[a_{products}]$ or $[a_{reactants}]$ are the concentrations or pressures of all the product or reactant species multiplied together in moles or atm [23, 25].

Table 2.4 Standard electrode reduction potentials versus a standard hydrogen electrode (SHE) [25, 26].

Electrode	Standard Electrode Potential E° (V)
$Au^{3+}(aq) + 3e^- \rightarrow Au$	+1.50
$\frac{1}{2}O_2 + 2H^+(aq) + 2e^- \rightarrow H_2O$	+1.228
$Fe^{3+}(aq) + e^- \rightarrow Fe^{2+}$	+0.771
$2H^+(aq) + 2e^- \rightarrow H_2(g)$	0.00
$Ni^{2+}(aq) + 2e^- \rightarrow Ni$	-0.250
$Fe^{2+}(aq) + 2e^- \rightarrow Fe$	-0.440
$Cr^{3+}(aq) + 3e^- \rightarrow Cr$	-0.740
$Zn^{2+}(aq) + 2e^- \rightarrow Zn$	-0.763

By combining Equation (2.6) with Faraday's law (Equation (2.5)), the Nernst equation can be created, which allows for the correction of standard reduction potentials based on the environmental concentrations.

$$E = E^\circ - \frac{RT}{nF} \ln \frac{[a_{products}]}{[a_{reactants}]} \quad (2.7)$$

Electrode potentials can be combined arithmetically to give cell potentials consisting of both anodic and cathodic reactions. Knowledge of standard electrode potentials of metals can reveal their corrosion tendencies to each other. A spontaneous reaction such as the corrosion must result in a reduction in Gibbs energy, so ΔG must be negative. Therefore E_{cell} must be positive for corrosion to occur and is calculated as follows [23, 25].

$$E_{cell} = E_{cathodic} - E_{anodic} \quad (2.8)$$

Where E_{cell} is the cell potential in Volts, $E_{cathodic}$ is the reduction potential of the cathodic reaction and E_{anodic} is the reduction potential of the anodic reaction.

Nernst equation provides an idea of the thermodynamic driving force that could sustain the oxidation (corrosion) in a given solution. However, it is unknown how quickly the metal corrodes in a solution containing these oxidising agents. The rate of material corrosion is understood from the principles of corrosion kinetics [19].

2.3.3 Electrical Double Layer (EDL)

Initially, the focus is brought to the electrical double layer to understand the nature of the electrode/ electrolyte interface when a metal is immersed into an aqueous solution. Local anodic and cathodic regions are generated instantaneously at the solid/liquid interface as a result of differences in free energy states between reacting sites.

As previously discussed, when a metal corrodes, ions depart their lattice, leaving behind their electrons. Water molecules then surround the metal ions as they escape the lattice, hydrating them. The hydrated ions are then free to diffuse away from the metal. The surface of the metal becomes negatively charged due to excess electrons and tends to attract some of the positively charged ions. This means that a certain percentage of ions remain near the surface, instead of diffusing into the bulk electrolyte. The water layer around the ions helps prevent them from making contact with the excess surface electrons and subsequently being reduced to metal atoms. Positive ions already in the electrolyte are also attracted to the negatively charged surface [25, 27].

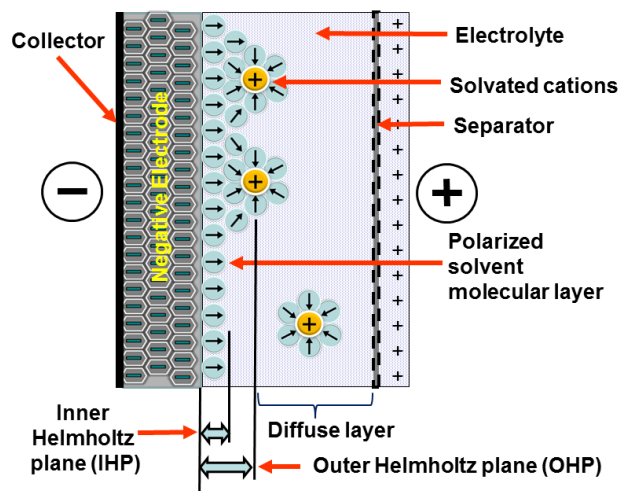


Figure 2.5 Simplified view of a double-layer of negative ions in the electrode and solvated positive ions in the liquid electrolyte, separated by a layer of polarised solvent molecules [28].

Figure 2.5 shows a schematic of the Electrical Double Layer (EDL) at a metal-solution interface. The electrolyte layer adjacent to an electrode surface contains water molecules and ions from both the metal and bulk electrolyte providing it with a distinctly different chemical composition than the bulk solution. This layer of specifically adsorbed ions forms the inner Helmholtz plane (IHP) balancing the associated electron charge at the surface. A layer of solvated ions, which are free to diffuse into the bulk solution forms the adjacent region known as the Outer Helmholtz Plane (OHP). The negatively charged surface and the adjacent electrolyte layer are collectively referred to as the electrical double layer (EDL) [28].

The physical separation of two oppositely charged planes created by the EDL causes it to produce capacitor-like behaviour, with the level of capacitance being determined by the metal and electrolyte composition. The metal also resists transferring excess electrons to the electrochemically active ions, which allows the EDL to also behave as a resistor [25, 27].

The charge separation in an EDL going from the metal surface (electrode) to the OHP (solution), undoubtedly creates an electrical potential that changes with the properties of the solution. The existence of a measurable electrical potential difference and the involvement of electron transfer in corrosion suggest there is a relationship between the EDL chemical composition, voltage and electric current [25, 27].

2.3.4 Corrosion Kinetics

Thermodynamic principles can explain a corrosion situation in terms of the solubility of chemical species and reactions associated with the corrosion process. Revisiting Section 2.3.1, when an electrode is immersed in an aqueous solution, both an oxidation and reduction may occur. The thermodynamically favourable reaction that takes place is determined from the reduction potential using Nernst equation for certain environmental concentrations.

An equilibrium potential is associated with each reaction and is the potential at which the sum of the anodic and cathodic reaction rates are equal to zero. It is termed the free corrosion potential (E_{corr}) which is dependent on the metal and the nature of the solution. The corresponding current density is called the corrosion current density (i_{corr}) [29]. Faraday proposed that the magnitude of current density indicates the rate of oxidation/ reduction.

E_{corr} values change when EDL composition changes and applied voltages change EDL composition. The Nernst equation mathematically relates EDL behaviour to electrical potential:

$$E = E^{\circ} - \frac{RT}{nF} \ln \frac{[a_{products}]}{[a_{reactants}]} \quad (2.9)$$

The measured potential is dependent upon the concentrations of both the metal ions and electrochemically active species in the EDL. The magnitude of a measured potential will therefore change with EDL chemical composition. Hence, E_{corr} will change if the bulk electrolyte composition is changed in such a way that it alters the EDL composition [25, 27].

The Nernst equation does not express a relationship for electrical current. Rather the Nernst equation expresses the tendency of a material to corrode, not the rate at which the material will deteriorate as mentioned previously.

When a current is applied to the electrode surface, the electrode potential changes and the electrode is said to be polarised. The difference between this resultant potential (E) and each electrode's reaction equilibrium potential (E_{eq}) is called polarisation or over-potential (η) and is modelled as [30]:

$$\eta = E - E_{eq} \quad (2.10)$$

The electrode potential, E is determined using the Butler-Volmer equation for an applied current for corroding electrodes in the absence of competing reduction-oxidation reactions [31].

$$i = i_{corr} \left[e^{\left(\frac{(1-\alpha)nF(E-E_{corr})}{RT} \right)} - e^{\left(\frac{-\alpha nF(E-E_{corr})}{RT} \right)} \right] \quad (2.11)$$

where E_{corr} is the free corrosion potential in Volts, i is the external current in Amps/cm² flowing to or from the electrode because of an applied potential, i_{corr} is the corrosion current density in Amps/cm² that occurs when the electrode is at E_{corr} , E is the applied potential in Volts, α is a coefficient ranging from 0 to 1 and R , T , n and F have been defined previously. The first term in Butler-Volmer equation describes the forward, anodic (metal dissolution) reaction while the second term describes the backward, cathodic reaction [25, 30].

Alternatively, the equation can be expressed in term of Tafel slopes (β_a and β_c) which are given by the gradients of the polarisation curves in the anodic and cathodic regions for a plot of E vs $\log(i)$ i.e. ($dE/d\log(i)$). Figure 2.6 shows a theoretical potential-log current density of polarisation curve for a

single electrochemical reaction on a metal surface under standard conditions.

$$i = i_{corr} \left[e^{\left(\frac{2.303(E-E_{corr})}{\beta_a} \right)} - e^{\left(\frac{-2.303(E-E_{corr})}{\beta_c} \right)} \right] \quad (2.12)$$

This relationship provides the basis for the electrochemical polarisation technique for a corroding electrode at its free corrosion potential [32].

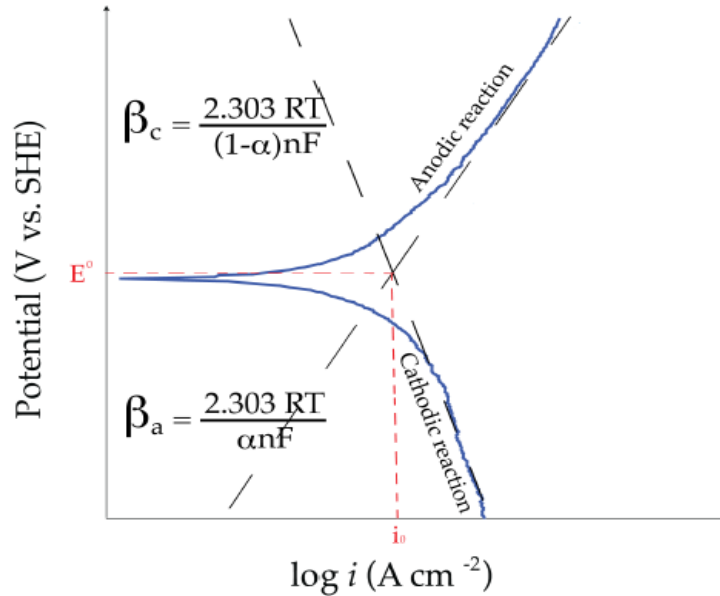


Figure 2.6 Theoretical potential-current density for a single redox reaction on a metal surface [19].

Applying a few millivolts of polarisation from E_{corr} has been well-known to produce a linear relationship between applied voltage and current. The Butler-Voltmer equation was simplified by Stern and Geary [33] for the case of small over-potentials with respect to E_{corr} . The kinetic expression has the following form.

$$R_p = \left[\frac{\Delta E}{\Delta i} \right]_{(E-E_{corr}) \rightarrow 0} = \frac{1}{2.303 i_{corr}} \left[\frac{\beta_a \beta_c}{\beta_a + \beta_c} \right] = \frac{B}{R_p} \quad (2.13)$$

Where R_p is the polarisation resistance (Ohm.cm^2) given by the gradient of the polarisation plot as small over-potentials (dE/di) for a plot of E vs i .

This theory links to the electrochemical measurement technique, commonly known as Linear Polarisation Resistance (LPR) technique that was used in determining the corrosion rate in experimental work in Chapter 6 and 7. Knowledge of R_p , β_a and β_c enables direct determination of the corrosion rate at any instant in time.

The above theory provides a basic understanding of the corrosion process which is essential first step in its mitigation and development of novel techniques. CO₂ corrosion has been recognised as one of the most prevalent corrosive agents in upstream production and transport operations. One important feature is the formation of iron carbonate or siderite corrosion product scales (FeCO₃) that is complementary to the CO₂ corrosion of steel and is the focus of the work done in this thesis. The next chapter centres on an overall literature understanding of CO₂ corrosion and FeCO₃ film formation and the parameters that effect its kinetics.

Chapter 3

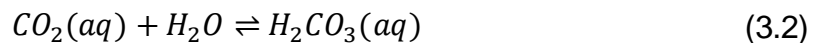
CO₂ Corrosion and FeCO₃ Scale Formation

Corrosion is a key hindrance to successful operation in the oil and gas industry. Its occurrence degrades the properties of a pipeline and has a major financial and environmental impact as discussed in the previous chapter. One of the most frequent and major internal corrosion problems experienced in pipelines is carbon dioxide corrosion which is also known as sweet corrosion (as shown in Table 2.3 in Chapter 2). In order to fully assess its impact, it is essential to first understand the governing processes that occur. This chapter outlines the current understanding of CO₂ corrosion mechanisms for carbon and low-alloy steels in hydrocarbon production and highlights key parameters which influence CO₂ corrosion behaviour and the rate of FeCO₃ film formation.

3.1 CO₂ Corrosion Chemistry

CO₂ corrosion is the chemical reaction of the pipeline material in the presence of water and CO₂. It is a complex process in which a number of chemical reactions, electrochemical reactions and transport processes occur simultaneously which can be divided into both anodic and cathodic reactions. The presence of CO₂ in an aqueous solution promotes the hydrogen evolution reaction, increasing the rate of corrosion of iron [34].

The chemical process of CO₂ corrosion commences by the dissolution of CO₂ in water. Depending on the conditions within the flow, a percentage of the carbon dioxide gas dissolves in the produced water and results in the formation of weak carbonic acid as shown in the Equations (3.1) and (3.2) [34, 35].



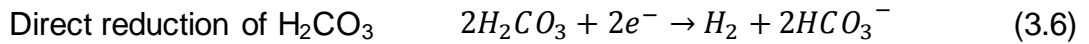
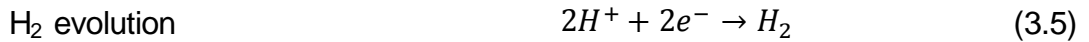
Carbonic acid is considered a weak acid as it does not fully dissociate. It is diprotic and partially dissociates in two steps to form bicarbonate (HCO₃⁻) and carbonate (CO₃²⁻) providing H⁺ ions. This separation provides the necessary H⁺ ions to enable the corrosion reaction.



According to the leading mechanism for CO₂ corrosion of carbon steel developed by De Waard and Milliams (1975) [34], the reduction of the un-dissociated acid molecule (H₂CO₃) occurs after it is absorbed onto the metal surface. This is therefore the rate-determining step of the process, so therefore the corrosion rate of the metal surface is directly related to the concentration of the un-dissociated acid in the solution.

Corrosion is an electrochemical process and involves the transfer of electrons at the metal-solution interface. For CO₂ corrosion of carbon steel, there are two possible cathodic reactions shown in Equation (3.5) and (3.6) [2, 34, 35].

Cathodic Reactions

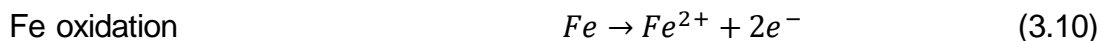


Whether or not the direct reduction of carbonic acid (Equation 3.6) actually occurs on the metal surface is debated in literature since it could be argued that carbonic acid would dissociate into a hydrogen ion faster than it could diffuse to the surface of the steel. If carbonic acid dissociated in the boundary layer, then it would only act as an additional source of hydrogen ions and the only cathodic reaction in the corrosion process is Equation (3.5).

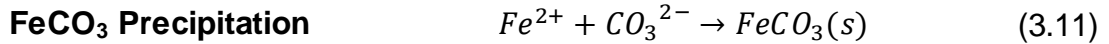
De Waard and Milliams [34] also found that the anodic dissolution of iron is determined by Equations (3.7), (3.8) and (3.9). The overall reaction is shown in Equation (3.10).



Anodic Reaction



A direct result of the CO₂ corrosion process is the increase in the presence of Fe²⁺ ions. At a certain instant in time, depending on the conditions, when the product of the concentrations of Fe²⁺ and CO₃²⁻ ions in the solution exceed the solubility limit (K_{sp}), they precipitate on the pipeline surface to form a protective film on the steel surface called FeCO₃(s) as shown in Equation (3.11) [35].



FeCO₃ acts as a diffusion barrier for corrosive species and has a surface covering effect which therefore reduces the corrosion rate of the pipeline. However, if there is any damage of the protective FeCO₃ film, it may lead to serious localized corrosion problems, also known as mesa attack, by exposing the underlying metal to the aggressive corrosive environment. This can result in catastrophic failure and significant economic cost. The integrity of the FeCO₃ film depends on the characteristics of the film formed (porosity, thickness, etc). Two non-dimensional parameters that are used to identify the protectiveness of FeCO₃ in literature are the Scaling Tendency and Saturation Ratio [2, 34, 35]

Saturation Ratio $SR_{FeCO_3} = \frac{[Fe^{2+}][CO_3^{2-}]}{K_{sp}}$ (3.12)

Scaling Tendency $ST = \frac{FeCO_3 \text{ Precipitation Rate}}{Corrosion Rate}$ (3.13)

If the rate of precipitation is faster than the rate of corrosion, the scaling tendency will be high. Thus the FeCO₃ forms as a dense and protective scale on the steel surface. On the other hand, if the corrosion rate is faster than the precipitation rate the scaling tendency is low, a porous and non-protective corrosion product layer will form.

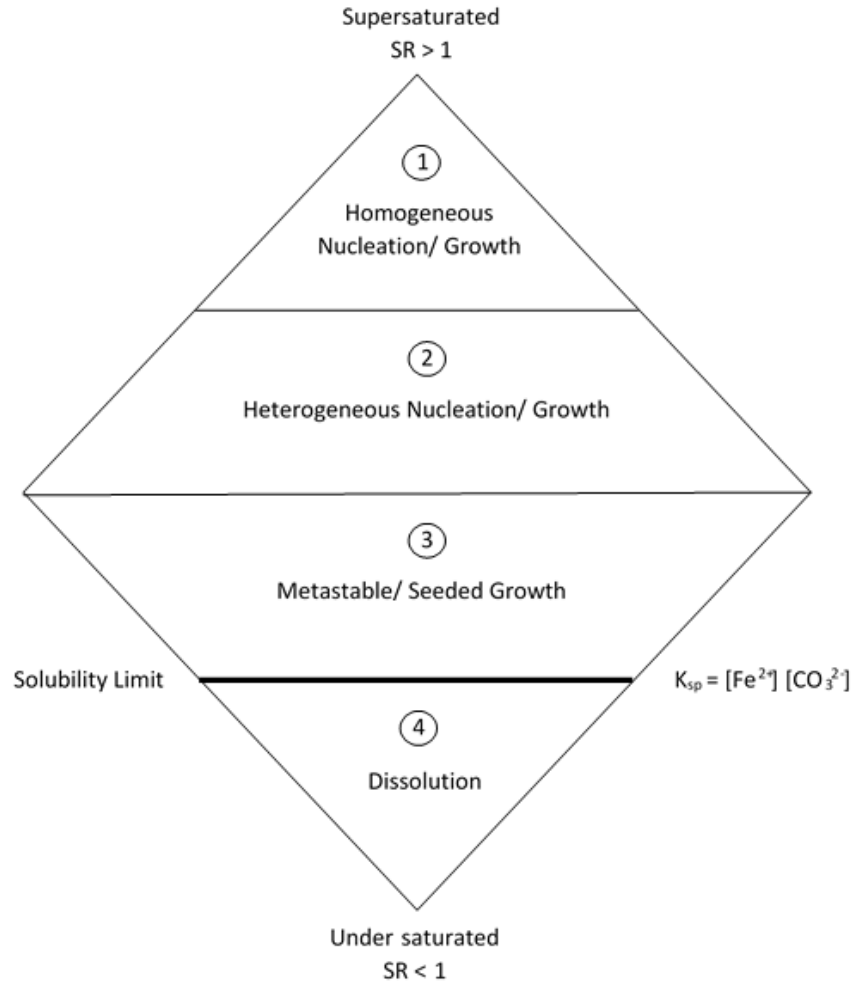


Figure 3.1 Regions of Crystal Growth [36]

In terms of the saturation ratio, Figure 3.1 shows the different regions of crystal growth as a function of the concentrations of the ions [36]. For precipitation to take place, supersaturation of ions is needed. Region 1 is under-saturated ($SR < 1$).

At this point the ions are dissolved in the solution (dissolution of the crystal). When the concentration of the ions reaches the solubility product, $FeCO_3$ can form and the protectiveness of the layer depends on how high the saturation ratio is [36]. At a high supersaturation, $FeCO_3$ crystals may rapidly nucleate in a large number of locations and grow fast to form a thin tight surface film with small crystal size. These films are very protective. At a low supersaturation, nucleation happens in significantly smaller number of locations. The crystal growth proceeds slowly and the crystals become very large. Furthermore, the large crystals form a much thicker and looser surface layer that is less protective and is more easily damaged or swept away by the flow [35, 36].

3.2 FeCO₃ Crystallisation

As discussed in the previous section, the rate of FeCO₃ precipitation from the solution is governed to a large extent by the saturation ratio. The ratio is quantified by the effusion of iron ions from the metal surface and infusion of carbonate ions from the bulk solution and is favourable only when the ratio is much greater than one. However, it is noted that the saturation ratio is a driving force and not a kinetic parameter of FeCO₃ precipitation. The crystal precipitates on to the surface via nucleation and crystal growth and the competition between these two processes determines the morphology of the scale in terms of volumetric porosity. The corrosion product films would be less porous and compact if the nucleation rate is higher than the growth rate [37, 38].

Nucleation is the first step in forming iron carbonate crystals and is followed by crystal growth. According to classical theory, if the nucleating phase is a sphere with radius r , the overall Gibbs free energy change, ΔG associated with nucleation from the solution is given by Equation (3.14) [39].

$$\Delta G = \left(\frac{4}{3} \pi r^3 \Delta G_{\text{volume}} \right) + 4\pi r^2 \gamma \quad (3.14)$$

Where ΔG_{volume} is the free energy change involved during the transformation of a crystallising solute to a large crystal of infinite volume and γ is the interfacial tension. Taking the first derivative of Equation (3.14), gives

$$\frac{d\Delta G}{dr} = 0 = (4\pi r^2 \Delta G_{\text{volume}}) + 8\pi r \gamma \quad (3.15)$$

And rearranging provides the value for the critical nucleus size, r_c [39].

$$r_c = \frac{-2\gamma}{\Delta G_{\text{volume}}} \quad (3.16)$$

For the nucleation of crystals from solution, the Ostwald-Freundlich equation [40] relates the solution saturation ratio to the size of the nucleating particle.

$$\ln SR = \frac{2\gamma v}{kT r} \quad (3.17)$$

Where SR is the saturation ratio, v is the volume of the aggregate, k is the Boltzman constant ($1.38 \times 10^{-23} \text{ m}^2 \cdot \text{kg/s}^2 \text{K}$), T_i is temperature (K), γ is the interfacial tension and r is the size of the aggregate. By combining Equation (3.16) and (3.17), it is observed that the critical cluster size (r_c) is inversely proportional to the saturation ratio.

$$-\Delta G_{volume} = \frac{2\gamma}{r_c} = \frac{kT \ln SR}{v} \quad (3.18)$$

Finally, substituting the expression for ΔG_{volume} in Equation (3.18) and the expression for critical nucleus size, r_c in Equation (3.16) into the general equation for Gibbs free energy, ΔG for nucleation in Equation (3.14), provides an expression that shows how the saturation ratio can be related to the height of the free energy barrier for critical nucleus formation, ΔG_c as shown in Equation (3.19).

$$\Delta G_c = \frac{16\pi\gamma^3}{3\left(-\frac{kT \ln SR}{v}\right)^2} = \frac{16\pi\gamma^3 v^2}{3(-kT \ln SR)^2} \quad (3.19)$$

ΔG_c is the Gibbs free energy at critical nucleus size, R_c and is also known as the nucleation barrier. The height of the free energy barrier ΔG_c is inversely proportional to the square of the saturation ratio. Thus, the critical nucleus size and the critical free energy requirement decrease with the saturation ratio [19, 40, 41].

For FeCO_3 crystals to nucleate homogeneously in a solution, the crystallising solute particles need to interact, organise themselves in a structural order and grow beyond a critical size simultaneously. This is energetically demanding because FeCO_3 aggregates would need to collide with each other in solution, overcome high interfacial tension during growth, and counteract intermolecular repulsion forces. Figure 3.1 shows spontaneous homogeneous nucleation to occur at the top of the triangle at the highest levels of supersaturation. In practice, the process of nucleation is observed more typically as heterogeneous nucleation which is aided by the rough steel surface which acts as preferential nucleation sites. This offers adsorption sites to developing FeCO_3 nuclei, which decreases the interfacial tension term, and thus the overall Gibbs free energy of nucleation. Properties of the surface such as its structure, composition and 'wettability', are important variables that influence crystal nucleation. Wettability refers to the interaction between fluid and solid phases. This means that the Gibbs free energy for heterogeneous crystal nucleation is lower (and thus more favourable) compared to the required free energy for homogeneous nucleation [19, 37, 42].

So, from the above thermodynamic consideration, it may be generalised that smaller critical cluster sizes and lower ΔG are obtained at higher supersaturation implying that an increasing supersaturation leads to a higher nucleation rate [19].

For a corroding metal-solution interface in a sweet solution, as the ferrous and carbonate ion concentrations increase, an originally under-saturated solution passes through the equilibrium saturation line ($SR=1$). In the under-saturated solution, it is thermodynamically unfavourable for $FeCO_3$ crystals to form and existing crystals should dissolve away. Above $SR=1$, the solution is supersaturated and crystallisation is favourable. The time delay between exceeding supersaturation and the onset of nucleation is known as the induction time (τ_{ind}). Ostwald recognised that a metastable zone exists at low supersaturation values as shown in Figure 3.1, where some crystallisation is possible but it can be difficult for nucleation events to take place due to long induction times [19]. Above some critical supersaturation (SR_{crit}), nucleation events are likely to proceed. The influence and range of this metastable zone can be a rate-limiting factor in crystal nucleation [19, 42].

Precipitated nuclei are deemed to be nano-crystalline or amorphous (without a clearly defined shape or form). As the nucleated phase begins to incorporate incoming $FeCO_3$ growth onto a lattice, it begins to develop into a crystal. The nuclei grows only after reaching its critical size, r_c , the nucleus is stable and at that instant the nuclei has overcome its free energy barrier, ΔG [37].

The number of crystallising aggregates over time passing through the thermodynamically determined energy barrier, ΔG_c in order to become $FeCO_3$ crystals provides the rate of nucleation. Dugstad et al. [43] reported that the rate of nucleation is believed to increase exponentially with relative supersaturation whereas the rate of particle growth bears an approximate linear relationship to this parameter. Crystal growth should therefore predominate at low relative supersaturation. When the supersaturation is high, the exponential dependency of nucleation rate may cause this nucleation process to occur to the near exclusion of particle growth.

The Arrhenius equation relates the rate constant of a chemical reaction to temperature.

$$k = [A] \exp \left[-\frac{E_a}{kT} \right] \quad (3.20)$$

[A] is the pre-exponential factor related to the frequency of molecular collisions and E_a is the activation energy. The rate of crystal nucleation, R_{Nuc} , defined as the number of aggregates overcoming ΔG_c to form a pre-crystal nucleus with time is formed, according to Arumugam et al. [44], using the Arrhenius expression where ΔG_c replaces E_a .

$$R_{Nuc} = P[A] \exp \left[-\frac{16\pi\gamma^3 v^2}{3(kT)^3 \ln(SR)^2} \right] \quad (3.21)$$

P is the probability that [A] number of crystallising solute nuclei will grow into crystals. Nucleation relies on the interfacial tension, γ of the nucleated phase-solution boundary, the solution temperature, T and the saturation ratio, SR [19, 41, 42].

The growth rate of a crystal is defined as the rate of change of a dimension of the crystal with time. According to Dugstad et al [43], the growth rate is observed to have a linear relationship with the relative saturation ratio and can be expressed according to Equation (3.22).

$$R_{CG} = k_{CG}(SR - 1)^y \quad (3.22)$$

Where k_{CG} is the crystal growth rate constant and exponent y is the growth order that represents the growth mechanism of the crystal.

3.3 Key Parameters affecting CO₂ Corrosion Rate

The rate at which carbon steel corrodes in a CO₂ environment is affected by a number of different factors. These parameters include water chemistry, CO₂ content, temperature and fluid dynamics. The following section provides an overview of the existing literature describing observed results of the effect of these parameters on the corrosion rate and the formation of FeCO₃ film.

3.3.1 Water Chemistry and Content

Solution chemistry plays an important role in CO₂ corrosion rates. The solution composition can vary from simple to very complex with numerous species in the solution such as formation water accompanied by the presence of crude oil. This can be further complicated by the species which partition into the water from the oil phase [45].

CO₂ corrosion occurs as a result of water being present in the system which wets the steel surface. The intensity of the CO₂ attack increases with the time during which the water phase is in contact with the steel surface. Therefore the water content and the notion of water wetting is an important consideration when examining CO₂ corrosion. In cases where a water-in-oil emulsion is created and the water is held in the emulsion, then the water wetting of steel is significantly reduced, lowering the corrosion rate. Crude oil has been shown to help reduce CO₂ corrosion through its interaction with the steel surface, as well as it reducing the surface wettability [45, 46].

A complete understanding of brine chemistry and the effect this can have on CO₂ corrosion rate is an important concept. However, in the following thesis, the area of concern is restricted to brine saturated with CO₂ in order to maintain a controlled environment and identify specific causes.

3.3.2 CO₂ Corrosion Products

CO₂ corrosion of carbon steel is strongly dependant on the surface films formed during the corrosion process. The protectiveness, rate of precipitation and stability of the film dictate the corrosion rate and its nature. The corrosion rate will depend on the protectiveness of this porous scale, which is determined by the nature of the base alloy in terms of its composition and microstructure, the properties of the environment such as temperature, CO₂ partial pressure, pH, etc. and the mechanical forces within the flow. The rate of precipitation heavily influences the properties of the FeCO₃ film [47].

The formation of iron carbonate films is governed by many factors but two of the most influential aspects are the solution pH and operating temperature. As mentioned previously, the super saturation with respect to iron carbonate needs to be exceeded in order to obtain appreciable enough levels of precipitation to form a dense protective scale and achieve successful protection.

3.3.3 Operating Temperature

Research and experiments have shown that the CO₂ corrosion rate and the precipitation of FeCO₃ have equally high dependence on the operating temperature. At room temperature, precipitation is slow and even at high supersaturation, an un-protective film containing voids and grain boundaries will be produced unless pH is very high. Increasing the temperature of the electrolyte accelerates all processes involved in corrosion including chemical reactions in the bulk, electrochemical reactions at the metal surface and mass transport. The rate of corrosion steadily increases with temperature at low pH when the precipitation of iron carbonate and other protective scales do not form. The situation changes significantly when the conditions mean the solubility of iron carbonate (or other salts) is exceeded, which typically occurs at a higher pH. In these conditions, increasing temperature accelerates the kinetics of precipitation and protective scale formation, decreasing the corrosion rate [47-49].

Studies by Ikeda et al. [50] show that at lower temperatures (<60°C) the film struggles to adhere to the surface and therefore offers little protection. At

temperature above 60°C, film protectiveness is seen to increase with temperature. Peaks in corrosion rate are usually seen between 60°C and 80°C depending upon the solution chemistry and flow behaviour and this is referred to as the 'scaling' temperature [45]. Figure 3.2 shows the growth rate of FeCO₃ film at different levels of supersaturation.

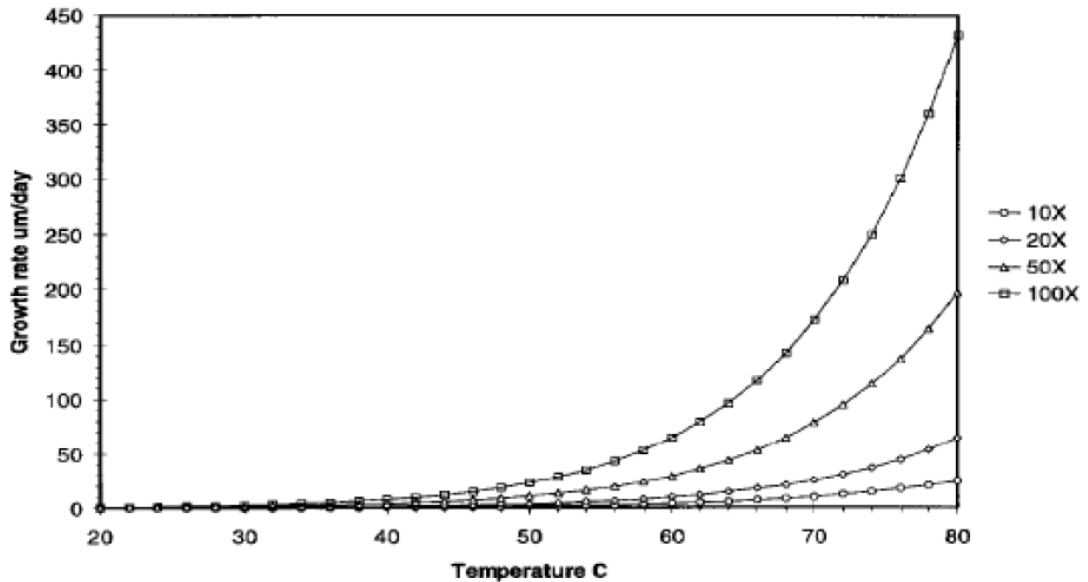


Figure 3.2 The effect of supersaturation and temperature on the growth of FeCO₃ [38]

However, the precipitation of FeCO₃ in itself does not necessarily result in the formation of a protective film. At higher temperatures, the film becomes different in texture, more crystalline and generally more protective. At lower temperatures (below 60°C), the corrosion product has a smudge-like texture and is easily removed by flowing fluid [51].

In reality, high supersaturation cannot be sustained for long periods at high temperature as the accelerated precipitation process will tend to rapidly return the solution to thermodynamic equilibrium. All investigations agree that increasing the temperature improves the protectiveness of the film, however, there is little agreement on a practical threshold temperature [48].

3.3.4 pH

With regard to solution pH, Nestic et al. [49] showed experimentally and computationally that pH has a strong influence on the formation of iron carbonate scale and henceforth the corrosion rate. A lower pH results in a more corrosive system. At high pH, the solubility of FeCO₃ decreases leading to a high precipitation rate and scaling tendency.

Figure 3.3 shows the influence that CO₂ partial pressure and pH have on the level at which FeCO₃ saturation is attained [38].

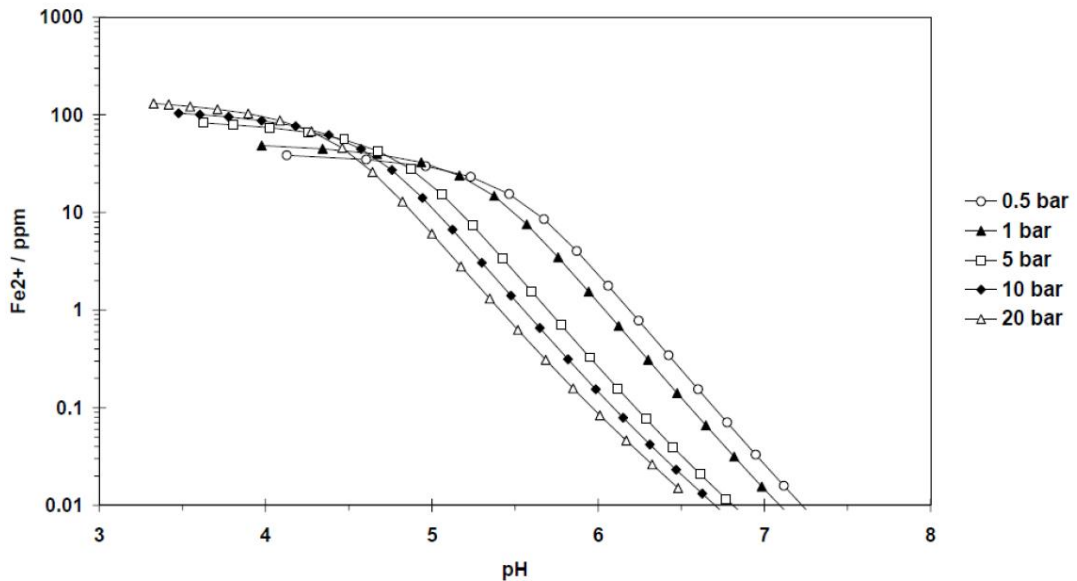


Figure 3.3 Quantity of Fe²⁺ needed to be produced by corrosion to reach FeCO₃ saturation plotted as a function of pH. The brine pH is the pH before corrosion has started [38]

The study has shown that increasing the pH of a solution from 4 to 5 reduces the solubility of Fe²⁺ by approximately a factor of 5. A further increase in pH from 5 to 6 reduces solubility 100 times. A low solubility can correspond to higher supersaturation, which accelerates the precipitation and formation of FeCO₃ films. Therefore, for pH > 5, as is the case with most CO₂ saturated brines, the probability of film formation is increased, which can contribute to a lower corrosion rate [38].

3.3.5 Partial Pressure

In the case of scale-free CO₂ corrosion, an increase of CO₂ partial pressure (pCO₂) tends to result in a rise in corrosion rate. It is generally considered that with increasing pCO₂, the concentration of H₂CO₃ increases, accelerating the cathodic reaction, and ultimately the corrosion rate. However, when conditions are favourable for the formation of iron carbonate scales, increasing pCO₂ can have a beneficial effect. At high pH, high pCO₂ can accelerate precipitation and scale formation by increasing the bicarbonate and carbonate ion concentration [2, 34].

These findings are supported in Figure 3.4. The figure shows the result of a study by Suhor et al. [34] on the effect of high partial pressure on the corrosion rate over a period of 25 hours. The experiment was conducted in a 20 litre autoclave at 80°C and autogeneous pH.

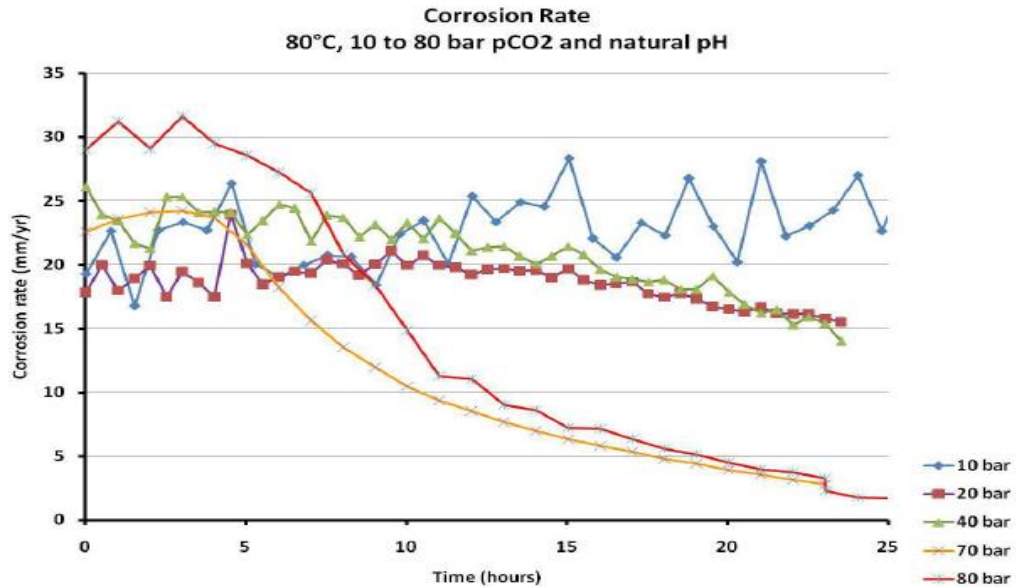


Figure 3.4 Corrosion rate over time for static experiment at high temperature (80°C), pCO₂ ranging from 10 to 80 bar and autogeneous pH [34].

3.3.6 FeCO₃ Film Growth over Time

The following section focuses primarily on the kinetics of scale formation. There are two phases which iron carbonate film growth goes through: nucleation and growth. In the nucleation phase, crystals form on the imperfections of the steel surface and in the growth phase crystals grow from a large number of discrete nuclei into dendritic structures forming a porous film. As more iron carbonate precipitates, the film grows in density as well as thickness. Corrosion can occur under the film, creating a gap between the film and the steel surface; however, this is filled up by ongoing precipitation [36, 38].

In a study by Gao et al. [52], ex-situ glass cell experiments were performed to explore the initiation and growth of iron carbonate films over time. The paper focussed specifically on the relationship between the growth of the iron carbonate crystals and the structure of the corrosion product films. Linear polarisation resistance (LPR) was used to monitor the corrosion rate and Scanning Electron Microscopy (SEM) was used to observe the formation of corrosion product films produced after different lengths of time. The conditions of the experiment are stated in the caption of Figure 3.5.

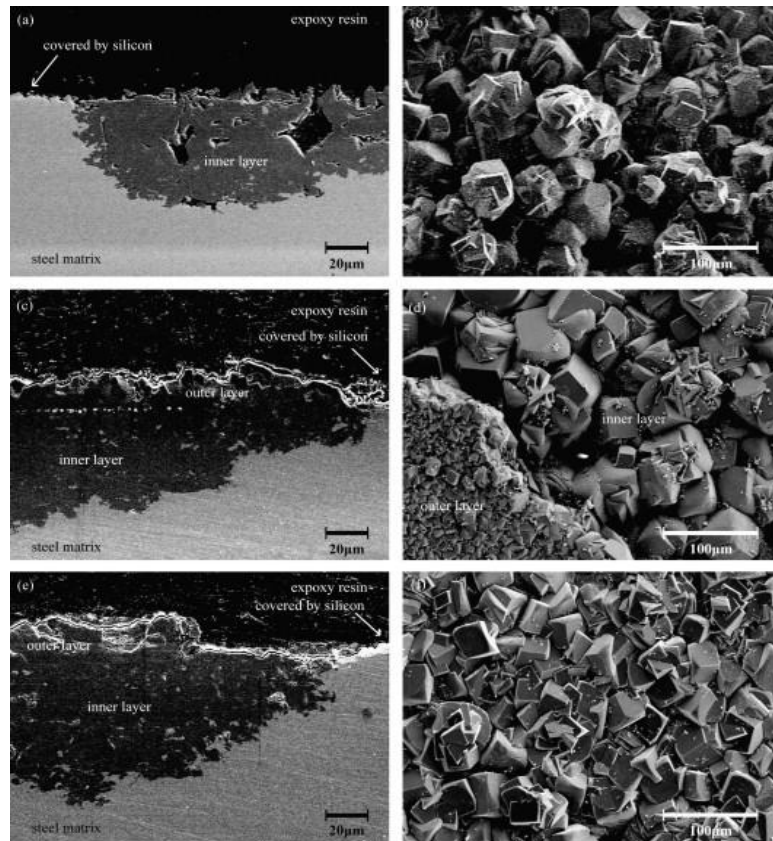


Figure 3.5 Cross-sectional and surface morphologies of corrosion product films formed at different times at 75°C: 108h (a and b), 144h (c and d), 240h (e and f), pH=6.5, $p\text{CO}_2 = 10$ bar [52].

The figure shows the SEM images of the corrosion product films formed after 108, 144 and 240 hours. Silicone rubber was used in the experiments to prevent parts of the steel coupons from corroding in order to see the thickness and morphology of the corrosion films relative to the original uncorroded steel surface. After 108 hours, a single layer can be seen on the steel, which is beneath the original steel surface. At 144 hours, the critical time, an outer layer corrosion film above the original steel surface forms. After the critical point, the thickness of the inner and outer layer increases with time. The surface morphologies also exhibit differences between the iron carbonate structures formed before and after the critical point. Before the critical point, the size of the iron carbonate grains is disordered and large, resulting in long distances between the crystal grains, increasing the porosity of the layer. A new compact crystal layer is shown to form over the steel surface or among the voids of the inner film soon after the critical point, creating a dense protective film [52].

3.3.7 Effect of Flow

Corrosion can be affected by flow differently depending on the mechanism governing the corrosion process. There are two cases to consider: the effect

of flow on corrosion when no surface films are present and the effect of flow on corrosion in the presence of surface films [45].

In the absence of films, the primary effect of flow on corrosion is through mass transfer of the species involved in the corrosion reaction at the metal surface. For mass transfer in turbulent liquid flow, all the concentration changes occur in a very narrow layer adjacent to the metal surface known as the mass-transfer boundary layer. The thickness of this layer is a function of the flow rate and flow geometry [45, 53].

When surface films are present, a high flow rate can reduce the corrosion rate by hindering the transport of species involved in the electrochemical reactions at the metal surface. The surface films can be removed locally or globally by chemical dissolution or by mechanical forces, both of which lead to very high corrosion rates. Both mechanisms of film removal are related to flow and the transfer processes within. Chemical dissolution of surface deposits is related to mass transfer and to water chemistry. Mechanical removal of films is related to momentum transfer and often is encountered in single- and multiphase flows. In multiphase flow, film removal can be caused by the impact of solid particles present in the liquid, by the impact of droplets present in the gas flow (erosion), or by pressure and shear stress fluctuations due to slugging, etc. In single-phase flow, mechanical film removal often is seen particularly at geometrical irregularities (e.g., weld beads, grooves, and areas of sudden diameter changes) [53-55].

The effect of flow on CO₂ corrosion behaviour at 120°C was studied using a RCE in a study by Nestic et al. [53]. Figure 3.6 shows the observed corrosion rate from LPR at 120°C over time. The corrosion rates decreased with time for all rotating speeds due to the formation of corrosion product layers. However, the corrosion rates at 100 rpm were the lowest. By visual comparison of SEM images from each test, it was seen that the FeCO₃ crystals appeared damaged at 1000 rpm. Considering that the main corrosion product was FeCO₃, the surface pH must have been higher than the bulk pH. Without flow, the concentration of Fe²⁺ with corrosion will increase the pH, but, with flow, mass transfer of species reduces the difference in pH between the surface and the bulk conditions. In other words, the value of surface pH was close to bulk pH, and then the condition becomes under-saturated for the FeCO₃ formation. Thus, the FeCO₃ crystals dissolved back or were chemically damaged resulting in the increase in the corrosion rate at higher flow rate [53-55].

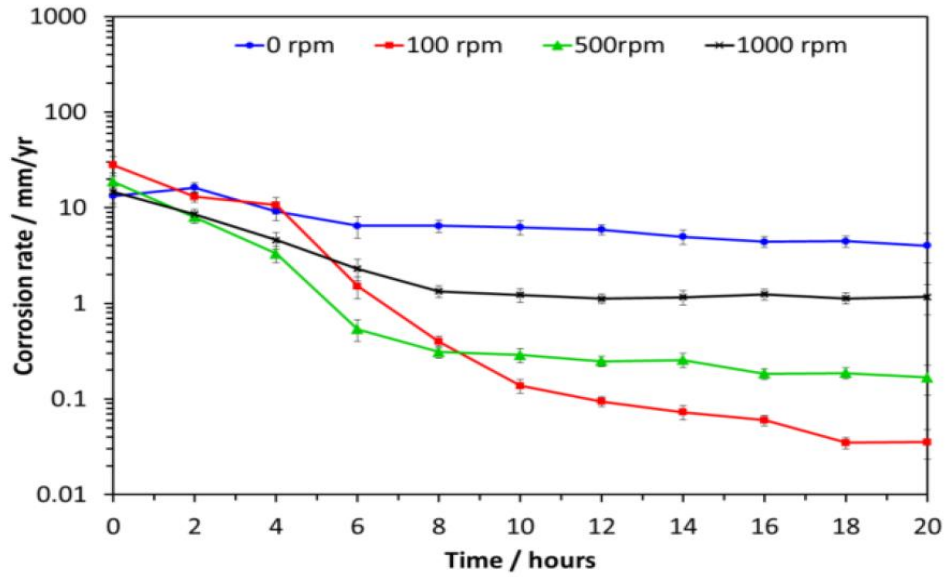


Figure 3.6 LPR corrosion rates at 120°C, pH 4.0, 1 wt% NaCl and rotating speeds of 0,100, 500 and 1000 rpm (equivalent to 0, 0.1, 0.5 and 1 m/s respectively) [53]

Chapter 4

Assessment of CO₂ Corrosion Prediction Models

In recent years, many research papers have been published that describe an integrated approach, based on corrosion modelling and laboratory testing, to optimise the use of carbon steel in corrosive service. A similar approach will be carried out in the following PhD. To be most effective, the models should account for relevant chemistry and physics of the corrosion process and for variations in conditions and flow characteristics along the length of the pipeline.

The following chapter focuses on providing a review of the many different mathematical models for CO₂ corrosion that are used nowadays by engineers in the oil and gas industry. Different models have been developed for the past several decades since 1970. They provide engineers quick and economical corrosion predictions that provide essential information on the material degradation of pipelines under different environmental conditions. The models available offer a large scatter in the prediction due to different theories, assumptions and modelling strategies. However, the following review is limited primarily to the models described in the open literature as the majority are patented models. The latter are typically a variation of publicly available models or are empirical correlations based on practical experience [45, 56].

The models considered here have been chosen either because they are well known and widely used by industry or reflect the variety of different categories of models available. These CO₂ corrosion models have been divided into three categories: empirical, semi-empirical and mechanistic models. They differ from one another by the level of experimental influence on the model and how firmly they are grounded in theory.

4.1 Empirical Models

Empirical corrosion predictive models are purely data driven and require a large amount of corrosion data that are either obtained from actual plant operations or from laboratory experiments. They provide reasonable predictions inside of their validation range. However, the drawbacks of this type of model are that they require a large set of data for various operating conditions that affect the corrosion rate and they extrapolate poorly outside the conditions present in their database [56, 57].

Dugstad et al. model

The model by Dugstad et al. [58, 59] was first introduced in 1992. Their approach was to determine a temperature-dependent best-fit polynomial function and then multiply it by correction factors for pCO₂, pH, velocity (shear stress) and steel Cr content. The model correlation is at the core of the NORSOK model and is based on the same experimental database as the model of de Waard et al. [34]. Equation (4.1) is the model correlation.

$$CR_T = K_T f_{CO_2}^{0.6} \left(\frac{S}{19} \right)^{0.15+0.03 \log(f_{CO_2})} f(pH)_T \quad (4.1)$$

where CR_T is the corrosion rate at a specific temperature in mm/year, K_T is a temperature constant, f_{CO₂} is the fugacity of CO₂ in bar, S is the wall shear stress in Pa and f(pH)_T is a constant dependent upon pH. Values for K_T and f(pH)_T are determined from an experimental database and can be found using tables such as those provided by Halvorsen and Søntvedt [60].

Mishra et al. model

In 1997, Mishra et al. [61] developed an empirical corrosion prediction equation based on reaction kinetic principles where the corrosion rate is expressed as a function of temperature, pH and CO₂ partial pressure as shown in Equation (4.2).

$$CR = C [H^+]^{1.33} pCO_2^{0.67} e^{-Q/kT} \quad (4.2)$$

Where CR is the corrosion rate (mmpy), C is a constant, [H⁺] is the concentration of hydrogen ions (kmol/m³), pCO₂ is the partial pressure of CO₂ in (N/m²), Q is the instantaneous reaction rate constant of CO₂ dissolution in water, k is the Boltzman constant (J/K) and T is the temperature (K).

Nesic et al. model

In 1999, Nesic et al. [62, 63] presented a highly nonlinear empirical CO₂ corrosion model based on neural networks (NN) using the experimental database of Dugstad et al. [59] for calibration. The correlation was developed by using a “back propagation” neural network combined with a genetic algorithm. The NN model was cited to have demonstrated superior performance when compared to the empirical model of Dugstad et al. [59], the semi-empirical model of de Waard et al. [34] and the mechanistic electrochemical model of Nesic et al. [62, 63].

The key problem with the NN and other fully empirical models is that they are considered “black boxes” meaning their prediction algorithms offer limited insight into the nature of the predictions they offer and cannot be used with confidence outside their calibration range. Adding new knowledge is a difficult process as it requires recalibration of the entire model with all the data.

4.2 Semi-Empirical Models

Semi empirical models are of two parts: an empirical correlation for base corrosion rate and correction factors that are based on theoretical hypotheses. The empirical correlation is derived from the corrosion data from either plant operations or experiments. Its correction factors are represented by parameters from physical or chemical phenomena involved in corrosion processes, such as FeCO_3 film formation, flow velocity, pH, and/or the presence of inhibitors. Hence, semi-empirical models can be used to predict the corrosion rate outside the variable ranges used during model development with higher confidence than the empirical model [56, 57].

This type of model is less time consuming and simpler to develop than purely theory-driven mechanistic models. Calibrated with a sufficiently large and reliable experimental database these models can extrapolate better than empirical models and enable good interpolation predictions. However, its drawbacks are similar to that of empirical models with respect to extrapolation and data requirements. Extrapolation can lead to unreliable and sometimes physically unrealistic results.

By far the most commonly used and the best-known semi-empirical model of CO_2 corrosion are the models by De Waard and collaborators. Other semi-empirical models can be found in the literature; however, they can be seen most often as variations of the De Waard models, where the experimental database is different, and the curve fitting strategy is more or less advanced.

The first semi-empirical model was proposed by de Waard and Milliams in 1975 [34], based on the assumption of the direct reduction of H_2CO_3 . The authors presented a correlation for the corrosion rate as a function of temperature and CO_2 partial pressure derived from gravimetric and linear polarisation measurements. Assuming a charge-transfer-controlled reaction between carbon steel and carbonic acid, an Arrhenius relationship was formulated along with an associated nomogram provided in Figure 4.1.

$$\log V_{corr} = 7.96 - \frac{2320}{T + 273} - 5.55 \times 10^{-3}T + 0.67 \log P_{CO_2} \quad (4.3)$$

where V_{corr} is the corrosion rate in mm/year, T is the temperature in °C and pCO_2 is the partial pressure of CO_2 in bar.

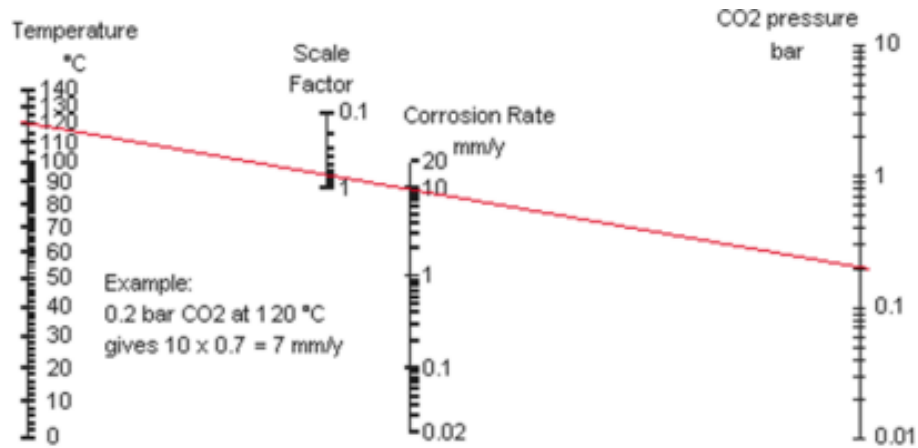


Figure 4.1 De Waard and Milliams nomogram for CO_2 Corrosion [34]

The model has been revised several times since, where different factors have been added to the original equation through the early 1990's by essentially recalibrating the constants against more reliable experiments and introducing various correction factors to quantify the influence of physical and environmental properties under various conditions. In 1991, De Waard et al. [48] introduced correction factors for pH and corrosion product scale [64].

In 1993, De Waard et al. [64] took into account the effect of mass transport, fluid velocity and steel composition. The model represents a best fit to a large number of corrosion flow loop data generated at Institute for Energy Technology (IFE). It was stated that every corrosion reaction consists of two consecutive steps; the transport of the corrosive species through a hydrodynamic or concentration boundary layer to the metal surface (mass transfer coefficient), and the reaction of the species at the metal's surface (reaction rate constant). This theory was used to develop a parallel resistance model to determine the effect of velocity on corrosion rate in the absence of surface scales. The model essentially combined the flow-independent kinetics of the corrosion reaction with the flow-dependent mechanism relating to mass transfer of dissolved CO_2 .

$$\frac{1}{V_{cor}} = \frac{1}{V_r} + \frac{1}{V_m} \quad (4.4)$$

where V_r represents the rate of the electrochemical processes and V_m denotes mass transfer.

In 1995, De Waard et al. [58] further refined the model from 1993 to provide the following values for V_r and V_m according to Equation (4.5) and (4.6) respectively.

$$\log V_r = 5.8 - \frac{1710}{T + 273} + 0.67 \log f_{CO_2} \quad (4.5)$$

$$V_m = 2.45 \frac{U^{0.8}}{d^{0.2}} P_{CO_2} \quad (4.6)$$

where T is the temperature in °C, pCO_2 is the partial pressure in bar and pH actual and pH_{CO_2} are the pH values of the aerated solution in the presence of dissolved salts and with dissolved CO_2 , respectively, U is the flow velocity in m/s and d is the pipe diameter in m. The results used to develop the 1993 and 1995 models were the first set of substantial data to become available pertaining to the effect of velocity on CO_2 corrosion under well-defined turbulent conditions. Tests were performed using coupons mounted within pipes and the environmental conditions were not influenced by the accumulation of corrosion products.

In 2001 and 2003, De Waard et al. [65, 66] updated the original de Waard and Lotz empirical correction for water wetting and proposed the introduction of a new factor based on the emulsion breakpoint approach. The new empirical correction took into account the API gravity, emulsion stability and water wetting of steel by an oil-water mixture. Unfortunately, this model does not take into account pipe diameter, oil density, oil viscosity or operating temperature on the critical velocity of the flowing oil phase required for entrainment.

Over the years, the De Waard and Milliams model of 1975 has been revised on several occasions, extending its validity into areas where protective scales are involved and to account for changes in high pH in brines, velocity, water wetting etc. Despite certain theoretical shortcomings, De Waard and Milliams' work has marked one of the important reference points for CO_2 corrosion research over the past three decades, and its most recently revised form is still used informally by industries today. However, these models are only helpful in the oil and gas industry for estimating corrosion rates if the applied material properties and environmental parameters are very similar to those in the study [25].

4.3 Mechanistic Models

Mechanistic corrosion models differ from the empirical and semi-empirical models in that they are built purely on theory of corrosion processes and do not require any corrosion data for model development. All calculations are purely predictive. These models have good extrapolation capacity within the limitations of the theory and can be modified to simulate other systems. However, the drawbacks of such a model are the work required to implement the models and the specialised knowledge needed in order to extend the model to new systems. They require an understanding of fundamental science relating to kinetics, thermodynamics, heat transfer, mass transfer, and many different fields of engineering and science. The time consuming nature of the development of such models indicate that the majority of models were developed by groups within universities. There is no guarantee that the models reproduce measured corrosion rate data but the models may be evaluated against experimental data in order to assess the validity [56, 57].

Following the initial landmark study by De Waard and Milliams in 1975 which resulted in a mechanistic model, it took until almost two decades later before Gray et al. [67] presented a more complete electrochemical model as part of their experimental study of CO₂ mechanisms. A number of mechanisms for the electrochemical reactions occurring at the metal surface were adopted from literature and included into an overall model [56].

In 1999, Anderko and Young [68] developed a mechanistic corrosion model composed of thermodynamic and electrochemical components to provide realistic speciation of aqueous system, as well as anodic and cathodic processes at the metal surface. The model was validated against experimental results and used to analyse parametric effects on corrosion rate, such as temperature, CO₂ partial pressure, solution composition and flow velocity.

Since early in the 21st century, the development of mechanistic models was dominated by Nescic et al. In 2001, Nescic et al. [69] developed their first mechanistic CO₂ corrosion model at the University of Ohio. This model incorporated electrochemical reactions at the metal surface, diffusion of chemical species between bulk and metal surface, diffusion of chemical species across porous FeCO₃ films, electro-migration of ions under the influence of the established potential gradients, and the chemical reactions

taking place in the bulk solution. The model allows users to specify FeCO_3 film thickness and study its effect on corrosion rate.

Later in 2003, Netic and Lee [49] improved the previous model by incorporating the growth of FeCO_3 films mechanistically into the model. The FeCO_3 precipitation starts when the solution is supersaturated with Fe^{2+} and CO_3^{2-} ions and it was found from the simulation results that FeCO_3 films formed at high pH, high temperature, high CO_2 partial pressure and high Fe^{2+} concentration.

In 2009, Netic et al. [70] developed a mechanistic model, FREECORP that uses species transport equations to solve for speciation. This model includes the effects of H_2S , O_2 and organic acid on corrosion rates. Transport equations were written using Fick's first and second laws, and electro neutrality was added as a constraint to solve for speciation. The model could predict corrosion rates at various CO_2 partial pressures, temperatures, velocities, FeCO_3 film thicknesses and flow velocities.

However, a limitation of CO_2 corrosion mechanistic modelling to date is that although aqueous CO_2 corrosion environments can cause pitting corrosion, mesa attack, flow induced corrosion and uniform corrosion, due to the predominance of uniform corrosion and the complexity of model development for localized corrosion, all corrosion prediction models for aqueous CO_2 environments to date were developed for uniform corrosion [25, 56].

In the following sections, the theory behind the mechanistic models discussed above shall be presented.

4.3.1 Theory behind Mechanistic Modelling

The core of all mechanistic models is their governing electrochemical kinetic equations. The models are based on the fact that CO_2 dissolves into the liquid phase, is hydrated and dissociates to create HCO_3^- and CO_3^{2-} which produces an acidic solution. H_2CO_3 then diffuses to the pipe surface and participates in cathodic reactions leading to the production of H_2 . These reactions only proceed if electrons are supplied by other reactions, namely, the anodic reaction involving the dissolution of iron. The relevant process was expressed in detail in Chapter 3.

Furthermore, the produced species diffuse away from the surface and depending upon the environmental conditions, FeCO_3 may precipitate on the pipe wall, forming a protective scale. The presence of this carbonate film can act as a diffusion barrier, meaning electron transfer is smaller and the rate of

dissolution of iron is reduced. Figure 4.2 shows a representation of the modelling domain behind the mechanistic models by Nescic et al. [49, 62, 70] and the following section covers the underlying theory behind their model development.

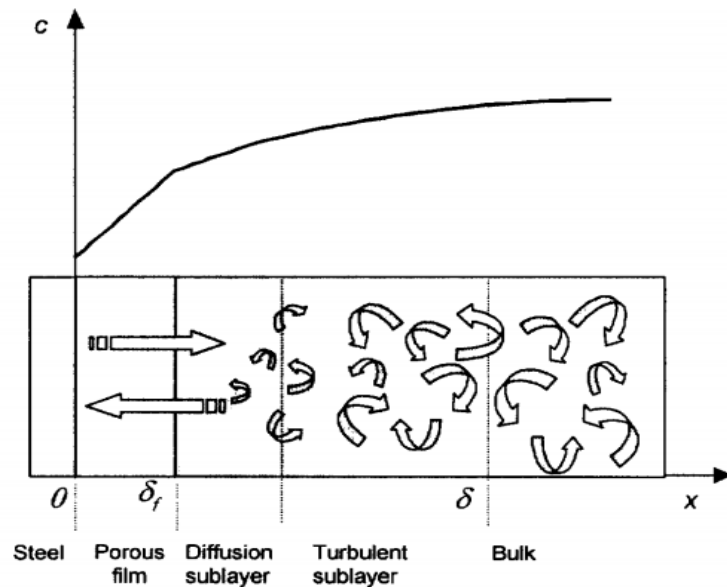


Figure 4.2 Sketch of the calculation domain; δ_f is the surface film thickness, $\delta - \delta_f$ is the liquid boundary layer thickness. The curve on the top represents a typical variation of a single species concentration expected from theory [41].

4.3.1.1 Electrochemical Reactions at the Surface

The general structure of the electrochemical kinetic reactions at the surface are typically formulated from the Volmer-Butler Equation (4.7).

$$i_{net} = \sum_k i_{0,k} \left(\exp \left(\frac{(1 - \alpha_k) n_k F (E - E_k^\circ)}{RT} \right) - \exp \left(\frac{-\alpha_k n_k F (E - E_k^\circ)}{RT} \right) \right) \quad (4.7)$$

Where $i_{0,k}$ is the exchange current density of the k'th electrochemical surface reaction, α_k is the charge transfer coefficient and n_k is the number of electrons transferred by reaction k. A table summary of the parametric constants in Equation (4.5) for the main electrochemical reactions in CO_2 corrosion are found in all relevant publications by Nescic et al [49, 69, 71]. This leaves the equation with an unknown potential, E that it is solved for and the surface concentration of the relevant species. The surface

concentration differs greatly from that at the bulk solution and brings about the main challenge in mechanistic models. Some models aim to solve this using diffusion theory and shall be analysed in the following section.

Upon determining the surface concentration of the species, the equation is solved for the unknown potential, E. When E is calculated, the corrosion current is calculated and converted to mm/year using Faraday's law according to Equation (4.8) [49]. The equation was derived by the combination of Faraday's 1st and 2nd law and then expressed in terms of Current Density (i) which has units (A/cm²) [49].

$$CR = \frac{ai}{nF} \text{ or } CR = 0.00327 \frac{ai}{nD} \quad (4.8)$$

Where CR (corrosion rate) is determined in mm per year, D is the density of the metal, a is the atomic weight, n is the valency (which is the number of valence bonds a given atom has formed, or can form, with one or more other atoms) and F is Faraday's Constant (F=96485 C/mol).

The model developed by Nescic et al. [72], in 1996, couples four cathodic reactions with a single anodic reaction representing the dissolution of iron according to Equation (4.9). The model is based on purely electrochemical reactions at the surface.

$$i_{H^+} + i_{H_2CO_3} + i_{H_2O} + i_{O_2} = i_{Fe} \quad (4.9)$$

The model required the user to input parameters such as temperature, pH, pCO₂, oxygen concentration, steel type and flow geometry. 'Pipe flow' requires inputs of velocity and pipe diameter, while 'RCE' requires the rotating speed and cylinder diameter.

Once the input parameters are determined, the program generates anodic and cathodic Tafel curves. The intersection of the curves gives the corrosion potential which is found by solving Equation (4.10). The program calculates i_{corr} based on the known E_{corr} and the anodic curve and subsequently the corrosion rate.

$$i = i_{corr} \left[e^{\left(\frac{2.303(E-E_{corr})}{\beta_a} \right)} - e^{\left(\frac{-2.303(E-E_{corr})}{\beta_c} \right)} \right] \quad (4.10)$$

This approach was similarly used by Anderrko et al. [68] and George et al. [73] All models that are solely based on electrochemical principles have a limitation in that although they can adequately describe the electrochemical processes occurring on the metal surface, the treatment of the transport processes in the boundary layer are not taken into consideration. This is

particularly crucial when a reliable prediction of protective scale is sought [25].

4.3.1.2 Transport Based Electrochemical Models

In corrosion, Fe^{2+} ions are created at the steel surface and H^+ ions are depleted by the electrochemical reactions. This process inevitably leads to concentration gradients and diffusion of species to and from the corroding material surface. The challenge of mechanistic models lies in the calculation of surface concentrations as discussed. This in literature is attempted by diffusion theory. The relatively new approach of coupling transport and electrochemical behaviour has long been established in other areas of electrochemistry and crevice corrosion, but Turgoose et al. [74] were the first to pave the way for a more realistic way of interpreting the transport process in the boundary layer for the case of CO_2 corrosion.

The calculation of the diffusion process is performed by setting up a discretized partial differential equation (PDE) mass balance as shown in Equation (4.11) [69].

$$\frac{\partial c_i}{\partial t} = -\frac{\partial N_i}{\partial z} + R_i \quad (4.11)$$

Where $\partial c_i/\partial t$ is the accumulation term and $\partial N_i/\partial z$ is the flux term. C_i is the concentration of species i , N_i is the flux of species i , R_j is source or sink of species "i" in kmol/m^3 due to all the chemical reactions in which the particular species is involved, t is time and z is spatial coordinate in m.

The molar flux N was calculated by either Fick's Law (Equation (4.12)) or the Nernst Planck Equation (Equation (4.13)) depending on the model [49, 66].

Ficks Law
$$N_i = -D_i \frac{\partial c_i}{\partial z} \quad (4.12)$$

Nernst Planck Equation
$$N_i = -D_i \frac{\partial c_i}{\partial z} - z_i u_i F c_i \frac{\partial \phi}{\partial z} + c_i v \quad (4.13)$$

Where D_i is the molecular diffusion coefficient of species in m^2/s , z_i is the electrical charge of species j in C, u_j is the mobility of species, F is Faradays constant, ϕ is the electric potential in the solution in V and v is the instantaneous velocity in m/s.

Once the transport equation in Equation (4.11) was written for each species in the solution, the resulting set of equations is solved by numerical methods simultaneously in space and time. The boundary conditions for this set of partial differential equations are the flux of species as determined from the rate of the electrochemical reactions and the equilibrium concentrations of

species obtained based on chemical reactions of species based on their equilibrium constants.

As the transport equation is transient, initial conditions are typically defined as a bare metal surface with the solution in chemical equilibrium and is used as the initial condition. Once the set of equations is solved for any given time step, the corrosion rate was calculated as the flux of Fe^{2+} ions at the metal surface [69].

4.3.1.3 Incorporating $FeCO_3$ Film Development

A variety of chemical reactions accompany the CO_2 corrosion process. By affecting the surface concentrations of species, chemical reactions can significantly alter the rate of electrochemical processes at the steel surface and the rate of corrosion. This is particularly true when, due to high local concentrations of species, the solubility limit is exceeded and precipitation of surface scales occur [56, 69].

The rate of precipitation of iron carbonate $FeCO_3(s)$ in literature is predicted as a function of temperature and the saturation ratio and is discussed in detail in Chapter 5. The general form of the equation is:

$$R_{FeCO_3(s)} = \frac{A}{V} \times f(T) \times K_{sp} \times f(SR) \quad (4.14)$$

Where A/V is the surface area to volume ratio in m^{-1} , T is the absolute temperature in K, K_{sp} is the solubility limit and SR is the saturation ratio as shown in Equation (4.15).

$$SR_{FeCO_3} = \frac{[Fe^{2+}][CO_3^{2-}]}{K_{sp}} \quad (4.15)$$

In 2001, Netic et al [69] was the first to incorporate the growth of $FeCO_3$ films into their model. However, the corrosion film thickness and porosity could not be predicted mechanistically and were correlated empirically with results from corrosion loop experiments. Upon comparison with experimental data, the predicted corrosion rates were higher than the measured ones and it was concluded that improved models are needed to describe formation of protective corrosion films.

In 2003, Netic and Lee [49] developed the model where the iron carbonate film depends primarily on the precipitation rate, R_{FeCO_3} as well as the rate of under deposit corrosion governed by the corrosion rate. The model was developed on the principle that initially, the surface water chemistry and the corrosion potential of the steel were obtained from the electrochemical

model described in the previous section. If the calculation of surface concentrations suggests that the solubility is exceeded a corrosion product layer is modelled on the steel surface and if not, the corrosion model proceeds unimpeded.

As iron carbonate precipitates, the film grows in density as well as thickness. However, the steel surface corrodes under the film, continuously creating a "void" between the film and the steel surface. This process is referred to as "film undermining" by Nescic et al. and a pictorial representation has been shown in Figure 4.3. The void fills up by ongoing precipitation and the surface conditions and relative corrosion rate define whether the film is protective or not.

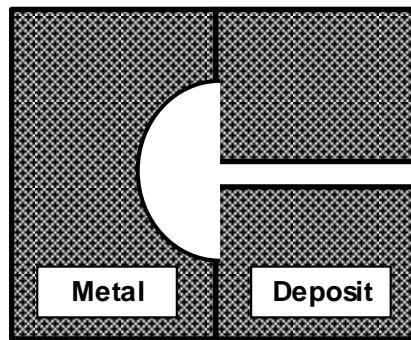


Figure 4.3 Pictorial representation of under deposit corrosion, also known as "film undermining".

The formation of iron carbonate affects the fluxes and thereby the concentration of species at the steel surface which in turn changes the kinetics of the electrochemical processes and corrosion. To reflect this the mass conservation reaction, flux of species between the bulk and the steel surface, diffusion through the porous corrosion product layer, flux of species as a result of electrochemical reactions at the steel surface are all modified to account for the porosity of the corrosion product layer, ϵ .

Volumetric porosity, ϵ is defined as:

$$\begin{aligned} \epsilon &= \frac{V_{void}}{V_{total}} = \frac{(V_{total} - V_{FeCO_3(s)})}{V_{total}} = 1 - \frac{V_{FeCO_3(s)}}{V_{total}} \\ &= 1 - \frac{c_{FeCO_3(s)} M_{FeCO_3(s)}}{\rho_{FeCO_3(s)}} \end{aligned} \quad (4.16)$$

where $M_{FeCO_3(s)}$ is the molecular mass of $FeCO_3$ and is 115.95 g/mole and $\rho_{FeCO_3(s)}$ is the density of iron carbonate and is 3,900 kg/m³.

The amount (concentration) of solid iron carbonate found in any volume, $c_{FeCO_3(s)}$ is determined by the $FeCO_3$ precipitation rate (R_{FeCO_3}) model

developed by van Hunnik et al. [8] and the film undermining effect that represents the corrosion process that removes the steel under the film and is described by Equation (4.17).

$$\frac{\partial c_{FeCO_3(s)}}{\partial t} = R_{FeCO_3(s)} - CR \frac{\partial c_{FeCO_3(s)}}{\partial x} \quad (4.17)$$

The equation is rearranged and the proposed equation describing film growth kinetics is in the form of Equation (4.18).

$$\frac{\partial \varepsilon}{\partial t} = \frac{M_{FeCO_3(s)}}{\rho_{FeCO_3(s)}} (R_{FeCO_3(s)}) - CR \frac{\partial \varepsilon}{\partial x} \quad (4.18)$$

film porosity change = precipitation – undermining

Where M_{FeCO_3} is the molar mass in g/mol, ρ_{FeCO_3} is the density in kg/m³ and CR is the corrosion rate.

The precipitation rate model developed by van Hunnik et al. is shown by Equation (4.19).

$$R_{FeCO_3} = A_p e^{-\frac{E_a}{RT_K}} \left(\frac{A}{V}\right) K_{sp} (SR - 1) \left(1 - \frac{1}{SR}\right) \quad (4.19)$$

Where A_p is the pre-exponential constant, E_a is the activation energy, T_K is the temperature in Kelvin, R is the universal gas constant, A/V is the area of volume ratio, K_{sp} is the solubility product and SR is the saturation ratio.

The model solves for Equation (4.18) simultaneously with the transport Equation (4.11) and the electrochemical Equation (4.7) all considered for calculations of porosity and thickness of iron carbonate scale. The model predicts the kinetics of iron carbonate film growth, the change in morphology of the film with respect to space and time as well as the resulting corrosion rate as a function of time [49]. It was concluded that the model was successfully calibrated against limited experimental data; however, further adjustment of the model would be needed as more accurate data on CO₂ corrosion in the presence of iron carbonate films emerge.

In 2009 [70], the model was developed to incorporate the effects of H₂S corrosion and the FeCO₃ precipitation prediction model was modified for the Sun and Netic (S&N) precipitation model [9, 10]. It was concluded that the performance of model was favourably compared to the performance of other similar models.

FeCO₃ film growth is a complex process and in the models developed by Netic [49, 70], detailed information of the film is lost as the process is simplified into a one-dimensional control volume approach. In each

publication, the models are observed and concluded to correlate with experimental data however only for select working conditions. The main limitation of these models is the incorporated FeCO_3 precipitation rate models that shall be discussed in detail in Chapter 5. There is a contradiction in the underlying theory as the corrosion rate models are developed for turbulent pipe flow whereas the precipitation rate models are based on a static system and correlated with bulk solution properties. The main limitations of these precipitation models shall be expressed in the following chapter and shall be investigated in the work carried out in this PhD.

Chapter 5 Precipitation Models – Review & Analysis

FeCO₃ precipitation is essential to the understanding of CO₂ corrosion of mild steel due to its influence on the corrosion rate and the link then that the corrosion rate has on subsequent FeCO₃ precipitation. The layer formed on the corroding surface acts as a barrier, stifling the corrosion rate by hindering the transport of species involved in the electrochemical reactions at the metal surface. The protectiveness, rate of precipitation and stability of the film dictate the corrosion rate and its nature.

5.1 FeCO₃ Precipitation Models

Corrosion literature reports four FeCO₃ precipitation models. A summary of the experimental methods used to develop the models, the resulting precipitation rate equations and the K_{sp} (solubility product) correlation associated with each precipitation is given in Table 5.1 to Table 5.4.

Table 5.1 Greenberg and Tomson (G&T) Precipitation Model [4, 5]

Model	$P_{FeCO_3} = A_p e^{-\frac{E_a}{RTK}} \left(\frac{A}{V}\right) K_{sp} (SR^{1/2} - 1)^2$
Experimental Method	Based on experiments following the change in [Fe ²⁺] concentration with time as precipitation occurs from a solution of relatively low super-saturation onto well characterised FeCO ₃ seed crystals.
K_{sp}	$\log_{10} K_{sp} = -59.2385 - 0.041377T - \frac{2.1963}{T} + 24.5724 \log_{10}(T)$

Table 5.2 Johnson and Tomson (J&T) Precipitation Model [6, 7]

Model	$P_{FeCO_3} = A_p e^{-\frac{E_a}{RTK}} \left(\frac{A}{V}\right) K_{sp} (SR^{1/2} - 1)^2$
Experimental Method	Based on experiments following the change in [Fe ²⁺] concentration with time as precipitation occurs from a solution of relatively low super-saturation onto well characterised FeCO ₃ seed crystals.
K_{sp}	$\log_{10} K_{sp} = -0.4343 \left(\frac{-30140}{8.314(T_c + 273.15)} \right) + 36.22$

Table 5.3 Van Hunnik et al. (vP&H) Precipitation Model [8]

Model	$P_{FeCO_3} = A_p e^{-\frac{E_a}{RT_K}} \left(\frac{A}{V}\right) K_{sp} (SR - 1) \left(1 - \frac{1}{SR}\right)$
Experimental Method	Based on experiments following the change in slope of the $[Fe^{2+}]$ concentration as the system passes through the pH at which the product of $[Fe^{2+}]$ and $[CO_3^{2-}]$ exceeds the solubility limit, K_{sp} . This work was intended to extend the range of validity of the J&T to levels of $S \approx 1000$.
K_{sp}	No correlation identified – assumed same as S&N

Table 5.4 Sun and Nescic (S&N) Precipitation Model [9, 10]

Model	$P_{FeCO_3} = A_p e^{-\frac{E_a}{RT_K}} \left(\frac{A}{V}\right) K_{sp} (SR - 1)$
Experimental Method	Based on experiments following the direct measurements of $FeCO_3$ amount which precipitates on a corroding steel surface by determining the difference in weight of a $FeCO_3$ covered steel sample and the sample without the $FeCO_3$ layer.
K_{sp}	$\log_{10} K_{sp} = -59.3498 - 0.041337T_K - \frac{2.1963}{T_K} + 24.5724 \log_{10}(T_K)$

A review of these models enables gaps in research to be identified which the thesis will address. The first precipitation model was established by Greenberg and Tomson [4, 5] in 1987 and was later developed in 1991 by Johnson and Tomson [6, 7]. They both developed semi empirical growth rate expressions that fitted their experimental results for a solution of a very low levels of supersaturation onto well characterised $FeCO_3$ seed crystals. Their precipitation rate expression is the same and only differ in their kinetic and K_{sp} constants shown in Table 5.5. Figure 5.1 shows that the predicted precipitation rates by Greenberg and Tomson’s model [4, 5] have very similar values to that of Johnson and Tomson’s model with slight variations attributing to the differences in the values of the constants.

In 1996, Van Hunnik et al. [8] developed a $FeCO_3$ precipitation model that was intended to extend the validity of J&T’s model for higher levels of super-

saturation. They believed that J&T's model over estimates the precipitation rate particularly at higher values of super-saturation. The information regarding the model by Van Hunnik et al. [8] is limited as the description of the experimental procedure is incomplete in literature. However, there is a close relationship between vP&H and J&T model as shown in Figure 5.1.

In 2006, Sun and Netic [9, 10] developed a precipitation model based on the direct measurements of FeCO_3 which precipitated on a corroding steel surface by weight gain. This technique produced precipitation rates that differ from the other models by 1-3 orders of magnitude as shown in Figure 5.1.

The expression for the saturation ratio, $\sigma(\text{SR})$, the values of the pre-exponential constant, A_p and activation energy, E_a are different in the various equations as shown in Table 5.5. The comparison between the predictions made by these models are shown in Figure 5.1 and Figure 5.2. There is a broad consistency between the predictions from G&T, J&T and vP&H models, and this group differs substantially from the results of S&N model by a factor of between 10 and 100. Also, as would be expected from general kinetic theory, there is an increase in precipitation rate with temperature and saturation level for all models.

Table 5.5 Model variations for pre-exponential constant A_p , activation energy, E_a and saturation ratio expression, $\sigma(\text{SR})$ [36]

Author	P_{FeCO_3}	A/V	$\ln A_p$	E_a (kJ mol)	$\sigma(S)$
G&T	$\frac{\text{mol}}{\text{kg s}}$	$\frac{\text{m}^2}{\text{kg}}$	44.4	95.8	$(\text{SR}^{1/2} - 1)^2$
J&T	$\frac{\text{mol}}{\text{kg s}}$	$\frac{\text{m}^2}{\text{kg}}$	56.3	127.3	$(\text{SR}^{1/2} - 1)^2$
vP&H	$\frac{\text{mol}}{\text{kg s}}$	$\frac{\text{m}^2}{\text{kg}}$	52.4	119.8	$(\text{SR} - 1) \left(1 - \frac{1}{\text{SR}}\right)$
S&N	$\frac{\text{mol}}{\text{m}^3 \text{ s}}$	$\frac{\text{m}^2}{\text{m}^3}$	28.2	64.9	$(\text{SR} - 1)$

A comparative analysis of the four precipitation models was made in a review paper by Woollam et al. [36] investigating the reasoning behind the significant difference in values between the S&N's model and the rest of the models. The main distinction made is that on one side the rate equation was determined based on precipitation on well-characterised seed crystals (G&T

and J&T model) whereas on the other side, the rate equation was determined by precipitation on an actively corroding iron substrate (S&N model).

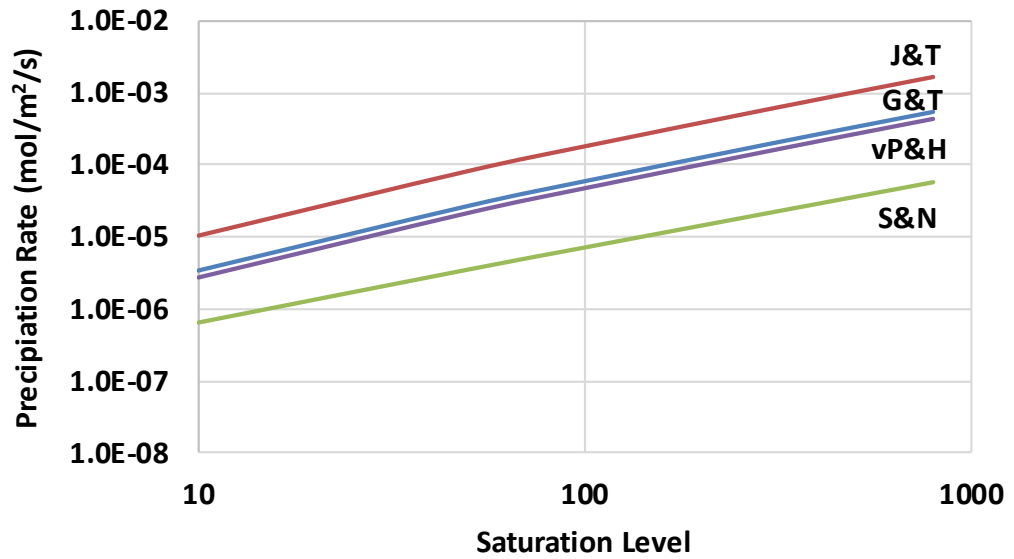


Figure 5.1 Comparison of precipitation rates (mol/m²/s) determined by different precipitation models at varying SR and T=80°C.

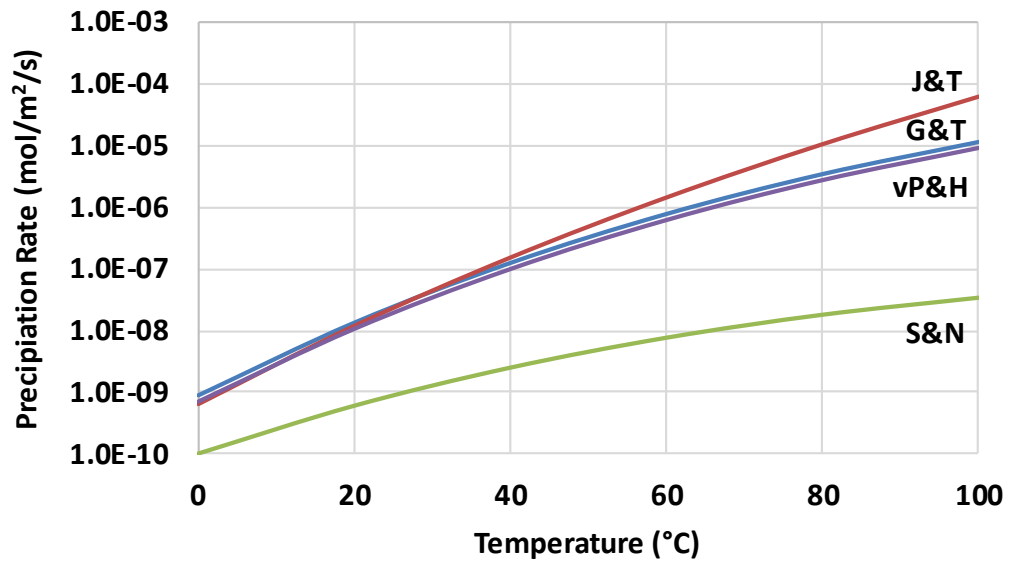


Figure 5.2 Comparison of precipitation rates (mol/m²/s) determined by different precipitation models at varying temperature and SR=10.

Therefore, it is the experimental variation that is the root cause of the large difference in predicted precipitation rates between the two classes of the

models. A possible theory behind the significant difference in the two classes of models expressed by Woollam et al [36] is discussed below.

FeCO₃ crystal growth proceeds in two sequential steps, aqueous transport of species from the bulk to the crystal surface and then a surface process which results in the ions becoming part of the crystal lattice. The rate of the precipitation process is directly dependant on the rate determining step; the slowest step in the overall reaction.

According to the mass transfer coefficient to a spherical particle under forced convection, the mass transfer coefficient is inversely proportional to the square root of the characteristic dimension of the particle or in this case the size of the crystal [75]. As the particle size increases, the mass transfer coefficient decreases in alignment with the following equation:

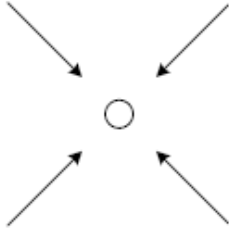
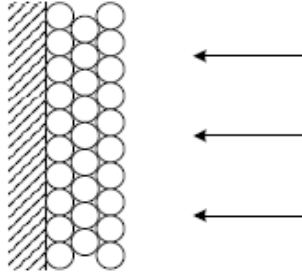
$$k_m \propto \frac{D^{2/3} u^{1/2} \rho^{1/6}}{R_p^{1/2} \mu^{1/6}} \quad (5.1)$$

Therefore, the mass-transfer coefficient to the well characterised seed crystals is generally greater than the mass-transfer coefficient to a corroding surface because of the change in characteristic lengths. In the experimental procedure for G&T [4, 5] and J&T [6, 7], the well characterised crystals are $\approx 1 \mu\text{m}$ in size while the corroding surface in the S&N [9, 10] experiments considered is $\approx 0.01 \text{ m}$, which is 4 orders of magnitude difference resulting in a difference in mass-transfer coefficient of about 100.

In the experiments of Sun and Nescic [9, 10], the surface was initially clean as there were no crystals present. This indicates that as the FeCO₃ layer develops, the surface area available for the surface reactions increases, whereas the mass-transfer rate to the surface decreases. It is then possible for the rate of the surface reaction to become greater than the mass-transfer rate and therefore the mass transfer reaction becomes the rate-determining step.

The differences in the precipitation rates is believed to be attributed to the differences in the rate-determining step in the precipitation reaction. In the seeded crystal work (G&T and J&T), the surface reactions dominate and for the corrosion surface work (S&N), the diffusion process dominates, hence there is a significant difference in the predicted precipitation rates. Table 5.6 provides a summary of the theory behind the difference in the models.

Table 5.6 Summary of attributing factor to significant difference in precipitation models as a result of employed experimental technique [36].

Class1: G&T // J&T Model	Class 2: S&N Model
Based on precipitation onto well characterised seed crystals.	Based on precipitation on an actively corroding iron substrate
	
Single crystal	Film formation
seed crystal $\approx 1 \mu\text{m}$	corroding surface $\approx 0.01\text{m}$
$4 \times \text{Characteristic Length}_{\text{class1}} \approx \text{Characteristic Length}_{\text{class2}}$	
Mass transfer coefficient $_{\text{class1}} \approx 100 \times \text{Mass transfer coefficient}_{\text{class}}$	
$R_{\text{Diffusion}} \gg R_{\text{Surface}}$	$R_{\text{Surface}} \gg R_{\text{Diffusion}}$
Surface dominant	Mass transfer dominant

5.2 Sun and Nescic Precipitation Model

In the following work, focus is given to the development of the more recent Sun and Nescic (S&N) [9, 10] model. The model is developed based on a more direct technique, weight change method, to investigate the scale retention rate of FeCO_3 on the steel surface in comparison to the other developed models. The following section consists of a summary of S&N published analysis of the previously developed models and the experimental procedure and theory behind the developed S&N model [9, 10].

Scale growth depends primarily on the kinetics of scale formation and the previous authors developed semi-empirical growth rate expressions based on the following iron carbonate precipitation rate PR equation:

$$PR = k_r \frac{A}{V} \sigma^r \quad (5.2)$$

Where k_r is kinetic constant, A/V is surface area-to-volume ratio, σ is the driving force and r is the reaction order. The driving force for crystallisation is

described in terms of the saturation ratio, SR. SR is defined as the ratio of species concentrations and the solubility limit K_{sp} . The equation is defined previously in Equation (4.15) (page 43).

Several equations were fitted with their experimental data using a temperature ramp method in order to obtain an iron carbonate precipitation rate equation. For example, Johnson and Tomson [6, 7] fitted equations such as Equation (5.3) to (5.5) with their experimental data and found that Equation (5.4) fit best with their data and hence developed the iron carbonate precipitation rate Equation (5.6).

$$\sigma = \left(([Fe^{2+}][CO_3^{2-}])^{0.5} - K_{sp}^{0.5} \right) \quad (5.3)$$

$$\sigma = \left(\frac{([Fe^{2+}][CO_3^{2-}])^{0.5} - K_{sp}^{0.5}}{K_{sp}^{0.5}} \right) = ((SR)^{0.5} - 1) \quad (5.4)$$

$$\sigma = \ln \left(\frac{[Fe^{2+}][CO_3^{2-}]}{K_{sp}} \right) = \ln(SR) \quad (5.5)$$

$$PR = k_r \frac{S}{V} K_{sp} ((SR)^{0.5} - 1)^2 \quad (5.6)$$

The models by Johnson and Tomson [6, 7] and Van Hunnik et al. [8] were based on an indirect experimental technique, ferrous ion concentration measurement, which is based on measuring the decrease of ferrous ion concentration in the bulk of the solution. Their assumption was that the entire amount of ferrous ion lost in the solution ends up as a deposited iron carbonate scale on the steel surface. However, it is noted by S&N that iron carbonate not only deposits on the steel surface, but also precipitates elsewhere in the glass cell. Therefore, the assumption may lead to an overestimation of the deposition rate of iron carbonate on the steel surface, which is the main parameter affecting the corrosion rate [9, 10].

There are three parts to the experiments carried out by Sun and Netic in the published work. The initial set of experiments were performed to critically analyse the previously developed models. Then, experiments were carried out under varying conditions determining the weight change over time and bulk SS through spectroscopy. The final set of experiments were performed at a controlled super saturation to test its validity as the controlling factor. These results then led to the development of the model. Each experimental procedure and the summarised analysis and conclusion has been broken down in the following sub sections with the first sub section providing a summary of the overall experimental procedure.

5.2.1 S&N Experimental Procedure

The experimental method behind Sun and Nestic's developed model is based on static tests in a bubble cell. Figure 5.3 depicts the experimental setup used and Table 5.7 summarises the experimental conditions.

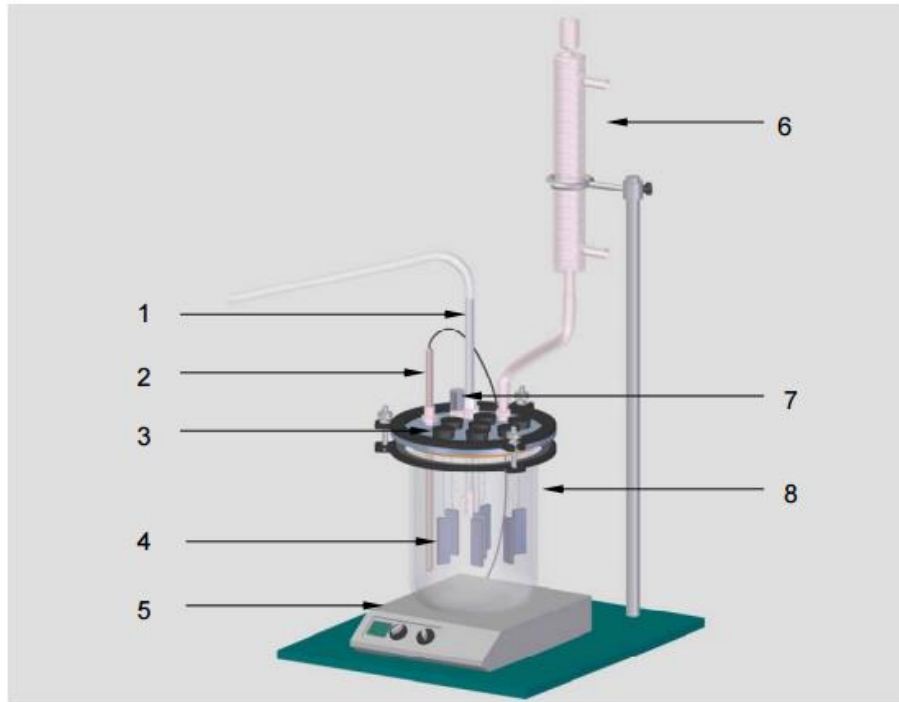


Figure 5.3 Schematic of the experimental test cell [9, 10]: 1. Bubbler; 2. Temperature probe; 3. Rubber cork with nylon cord; 4. Steel substrate; 5. Hot plate; 6. Condenser; 7. Cole-Parmer AgCl pH probe; 8. Glass cell.

Table 5.7 Experimental matrix for S&N model development.

Parameter	Value
Brine	De-ionised water, 1 wt% NaCl purged with CO ₂ gas
Temperature	60°C - 90°C
pH	6.6
Total pressure	1 bar
Volume	2 litres
SR	10 - 300

The saturation ratio of iron carbonate in the solution was controlled through adding Fe²⁺ in the form of deoxygenated ferrous chloride salt (FeCl₂.4H₂O)

solution and the samples were X65 carbon steel polished to 600 grit using SiC paper. The defined composition of the carbon steel samples is shown in Table 5.8. Time-averaged scale retention rate of iron carbonate was obtained by subtracting the weight of the coupons which had iron carbonate scale and those after the scale was removed using Clarke's solution. Time-averaged corrosion rate was calculated by subtracting the weight of the coupons prior to running the experiments and after removing the iron carbonate scale. The indirect ferrous ion concentration measurements were also used to obtain the iron carbonate scale retention rate. A spectrophotometer was used to measure ferrous ion concentration in the solution [9, 10].

Table 5.8 Chemical composition of X65 (wt%) (Fe is the balance)

C	Mn	Si	P	S	Cr	Cu	Ni	Mo	Al
0.050	1.32	0.31	0.013	0.002	0.042	0.019	0.039	0.031	0.032

5.2.2 Existing Precipitation Model Analysis.

Sun and Nestic [9, 10] conducted three sets of experiments to verify the previous iron carbonate scale retention rate expressions/ models. The experiments were carried out with different surface areas at pH 6.6, temperature of 80°C and initial Fe^{2+} 50 ppm. The first set of experiments was conducted using one specimen with a surface area of 5.4 cm². The second set of experiments was conducted using thirty specimens each having a surface area of 2 cm² (total of 60 cm²). During these experiments, six specimens were taken out of the solution every two and a half hours. In the third set of experiments, twelve specimens, each having a surface area of 21 cm² (total of 252 cm²), were inserted in the solution and three specimens were taken out every two and a half hours. Results were taken in the form of direct weight change method and to compare with the previous models, ferrous ion concentrations were measured at different times.

The results showed that the change of ferrous ion concentration in the solution with time was found to be similar irrespective of the very different surface areas of the substrates. As the surface area of the substrate decreased, the scale retention rate measured by the weight change method decreased while the results measured by the Fe^{2+} method did not. These results were used to disprove the Johnson and Tomson [6, 7] and Van Hunnik et al. [8] model expressions, as the scale retention rate on the steel surface should be proportional to the surface area-to-volume ratio (A/V).

However, it was also observed that for large AV , most of the iron carbonate deposits on the steel substrate and the Fe^{2+} method used by these models appears to be valid. For a small AV , most of the precipitated iron carbonate does not end up on the steel surface and the Fe^{2+} method is found to be in gross error.

This observation expresses the limitation in the previous models. Sun and Nestic [9, 10] described it being impossible to directly reproduce the original experiments of Johnson and Tomson and van Hunnik et al [8] due to insufficient details published. However, large discrepancies were found upon comparing with their measurements of the scale retention rate with the experimental data obtained by weight change method being up to two orders of magnitude lower. The analysis and possible theory behind the difference in the models based on experimental procedure was discussed previously. They concluded in their published work that the Johnson and Tomson [6, 7] and van Hunnik et al. [8] model overestimates the actual scale retention rate by a large margin because the experimental data used to derive them were based on the Fe^{2+} method in which the assumption of Fe^{2+} lost in the bulk of the solution becoming $FeCO_3$ scale on the steel surface is unreliable. Figure 5.4 provides S&N's published graph showing the comparative analysis of the previous models and S&N experimental results.

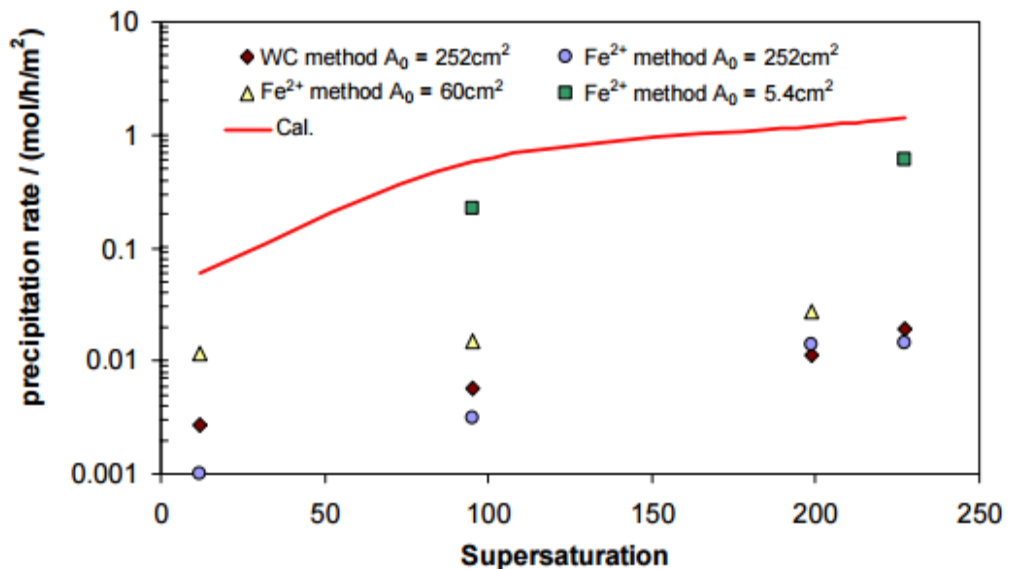


Figure 5.4 Experimental and calculated (using kinetics expression given by van Hunnik et al.) scale retention rates of iron carbonate under a saturation ratio of 12 to 250 at a temperature of 80°C [9, 10].

From Figure 5.4, it is observed, as previously discussed, that for a lower surface area, the precipitation rate is closer to the calculated curve for the

van Hunnik model. However, for a larger surface area, the results are in par with the weight loss measurements which are orders of magnitude smaller in comparison.

5.2.3 Scale Retention Rate and Corrosion Rate over Time

These experiments were conducted by Sun and Nescic (S&N) [9, 10] in static solution with initial Fe^{2+} of 50 ppm, pH of 6.6 and range of temperatures was used which varied from 60°C to 90°C. The surface area and quantity of the X65 carbon steel samples used in the experiments were not mentioned. The ferrous ion concentration was measured with time in addition to the weight change method in order to determine the bulk saturation ratio. Results showed that the ferrous ion concentration decreased steadily with time and decreased with the increase in temperature. In all conditions, the scale retention rate by the weight change method is seen to follow the saturation ratio in the bulk of the solution [9, 10].

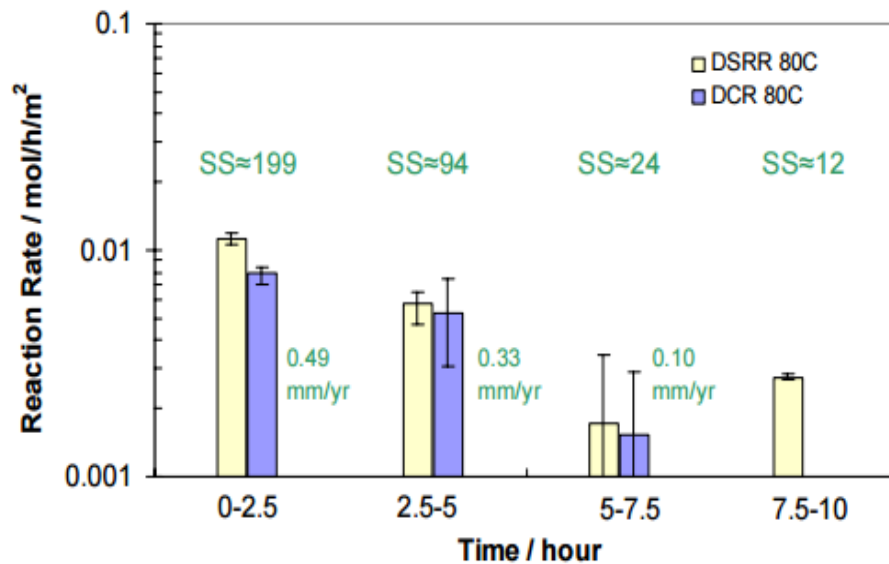


Figure 5.5 The comparison of differential scale retention rate (DSRR) of iron carbonate scale (DSRR) and differential corrosion rate of X65 carbon steel (DCR) in pure CO_2 corrosion under the conditions of initial Fe^{2+} concentration 50 ppm (which then drifted down), pH 6.6, $T=80^\circ\text{C}$ [9, 10].

At 80°C, the scale retention rate decreased steadily with time because of the decrease of the saturation ratio in the bulk of the solution. Since iron carbonate scale formed faster at higher temperature and was more protective, the corrosion rate was observed by S&N to decrease more with the increase of temperature. The scale retention rate was also found to be higher than the corrosion rate at any time in the experiments proving that the

bulk Fe^{2+} is a more significant source of ferrous ions forming iron carbonate scale at 80°C than at lower temperatures. The published bar graph based on the obtained results for a temperature of 80°C is shown in Figure 5.5.

5.2.4 Experiments Conducted at Constant Supersaturation

The following experiments were conducted by Sun and Netic (S&N) [9, 10] at a controlled constant supersaturation in static solution with Fe^{2+} concentrations of 50 ppm and 10 ppm, pH 6.6, and temperatures of 60°C , 70°C , and 80°C . The controlled constant supersaturation was achieved by continuously dosing a deoxygenated ferrous chloride solution to the glass cell to compensate for the Fe^{2+} ions lost by precipitation. Again in the following case, the surface area and quantity of the X65 carbon steel samples used in the experiments were not mentioned. The results from these experiments concluded that by controlling the key parameters stable and reproducible results for the kinetics of iron carbonate scale formation can be obtained. Figure 5.6 shows the published results showing that maintaining the supersaturation results in repeatable data observed by Sun and Netic [9, 10].

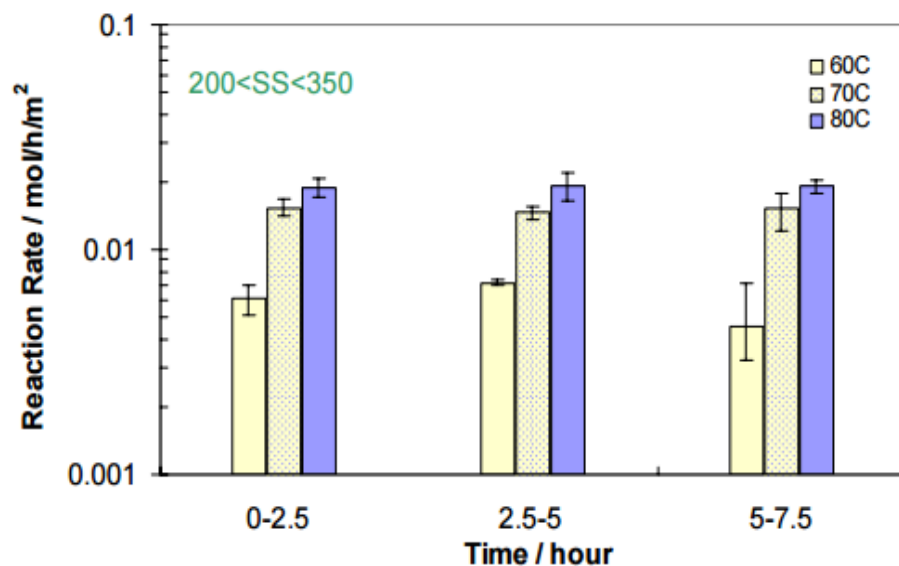


Figure 5.6 The comparison of differential scale retention rate of iron carbonate scale in pure CO_2 corrosion for constant Fe^{2+} concentration 50 ppm, pH 6.6, T 60°C , 70°C , and 80°C .

As a result of the work done, Sun and Netic concluded from their results that the indirect dissolved ferrous ion concentration method leads to an error in calculating how much iron carbonate deposits on the steel surface because iron carbonate at high supersaturation not only deposits on the steel surface, but also precipitates elsewhere in the solution. They then developed a semi

empirical scale retention rate expression for corrosion engineering applications using the experimental data obtained by the direct weight change method.

The experimental data similarly were employed to fit several empirical scale retention rate expressions including the previous models by Johnson and Tompson [6, 7] and van Hunnik et al. [8]. Equation (5.7) was found to fit the experimental data better than the other models.

$$PR = k_r \frac{S}{V} K_{sp} (SR - 1) \quad (5.7)$$

The kinetic constant, k_r was derived from experimental scale retention rates via the scale retention rate equation and Arrhenius's law with temperature and is expressed in Table 5.5. The iron carbonate solubility limit K_{sp} is a function of temperature (T) in Kelvin and ionic strength (I) in mol/L which shall be discussed in further detail in the following section. Figure 5.7 shows the comparison between the different models and the experimental data attained by Nesic et al.

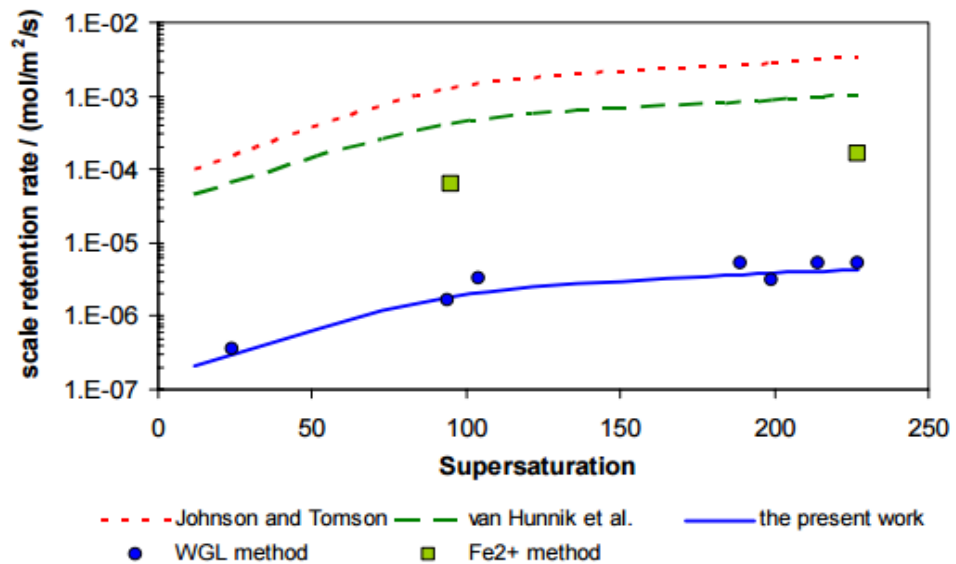


Figure 5.7 The comparison of the experimental scale retention rate by weight change method and the calculated scale retention rate using kinetic expressions given by Johnson and Tomson, van Hunnik et al., and the present expression, under a saturation ratio of 24 to 200 and $T = 80^{\circ}\text{C}$.

5.3 Solubility Product (K_{sp}) Calculation

The following section expands on the equations used to determine the K_{sp} for the different precipitation models and analyses the importance of the

parameter. The K_{sp} equation used in each model is previously described in Table 5.1 to Table 5.4.

It is important to have a reliable estimate of the solubility limit in order to predict the deposition of FeCO_3 on the steel surface. The saturation ratio has been discussed previously to be the controlling factor in the development of the precipitation models and according to Equation (5.3), the value of SR is directly dependant on the K_{sp} value and hence directly effecting the predicted precipitation rate.

Figure 5.8 shows the results of the comparison of solubility product, pK_{sp} values used by the different models. Each of the curves show an increasing trend with temperature, as would be expected, with divergence at the lower end of the temperature range. Overall, the differences in the K_{sp} values are small and are not a major source of the discrepancies in the precipitation rate predictions discussed previously.

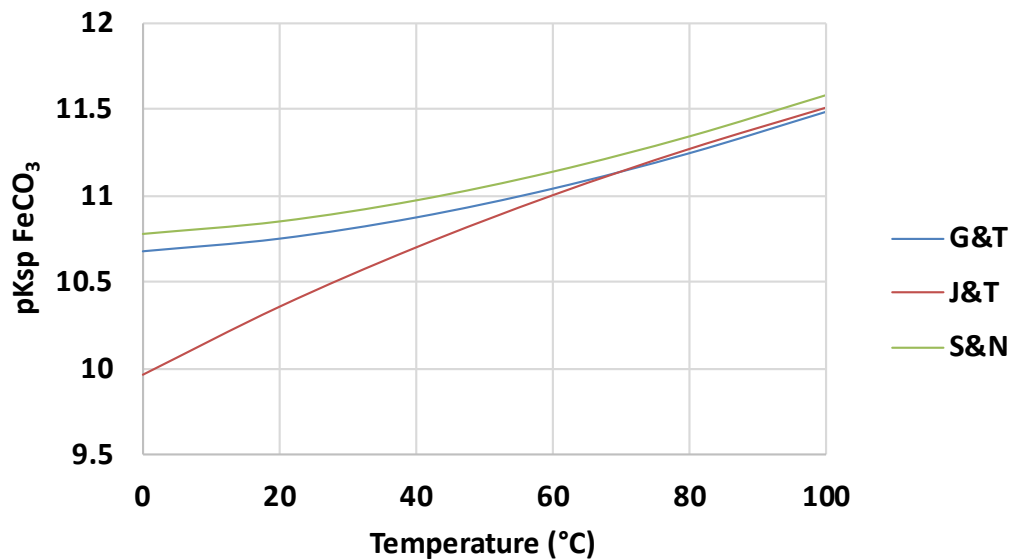


Figure 5.8 Comparison of pK_{sp} for temperature ranges 0-100°C

However, the models below do not account for ionic strength. In a recent review, Sun et al [9] proposed a more complete correlation which accounted for both the effect of temperature as well as ionic strength on FeCO_3 solubility product, developed based on literature data. The Equation (5.8) [9] is listed and the predictions made has been supported to agree well with published experimental data.

$$\log K_{sp} = -59.3498 - 0.041377T_k - \frac{2.1963}{T_K} + 24.5724 \log_{10}(T_K) + 2.518I^{0.5} - 0.657I \quad (5.8)$$

Where the ionic strength [9] is defined as:

$$I = \frac{1}{2} \sum_i c_i z_i^2 \quad (5.9)$$

And c_i is the concentration of different species in the aqueous solution in mol/L, and z_i is the species charge.

The solution chemistry is slightly different between the two groups of experiments, J&T [6, 7] did their experiments in the absence of sodium chloride (NaCl) while S&N [9] experiments were done in a 1 w.t. % NaCl solution. Figure 5.9 and Figure 5.10 shows the differences due to the effect the ionic strength has on the solubility product, K_{sp} . Using the correlation of Sun et al, the change in ionic strength resulting from the presence of 1 w.t. % NaCl results in an increase in the precipitation kinetics by a factor of approximately 10. However, S&N experimental results which included 1 w.t. % NaCl are much lower than those of Greenberg and Johnson done without NaCl, indicating that this is not a reason for the significant differences between the models. It has been generalised in literature that taking into account ionic strength provides a more accurate estimation of the K_{sp} and therefore a more accurate prediction of FeCO_3 . [9]

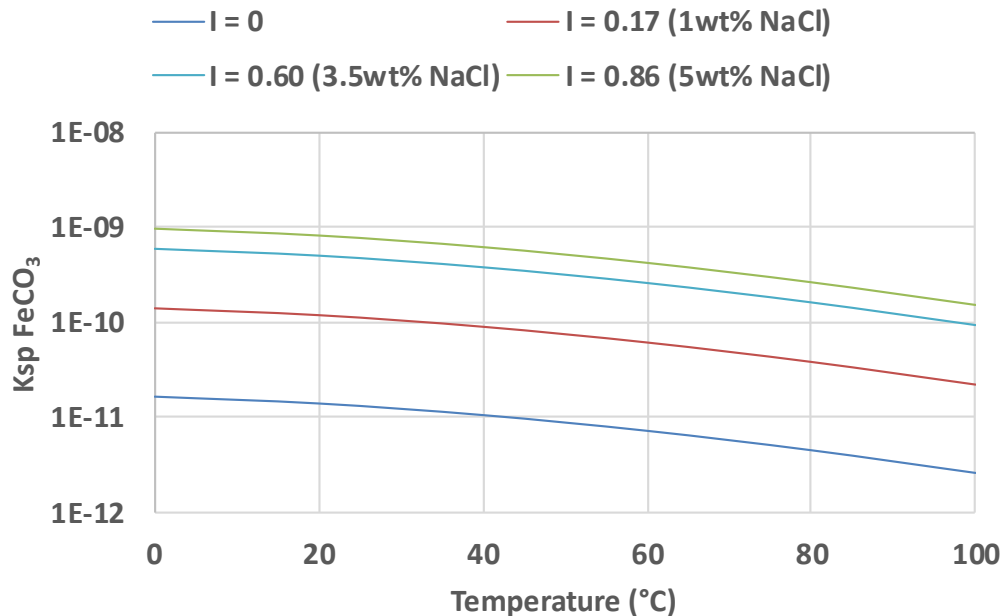


Figure 5.9 Effect of ionic strength on $\text{p}K_{sp}$, solubility product for a varying temperature.

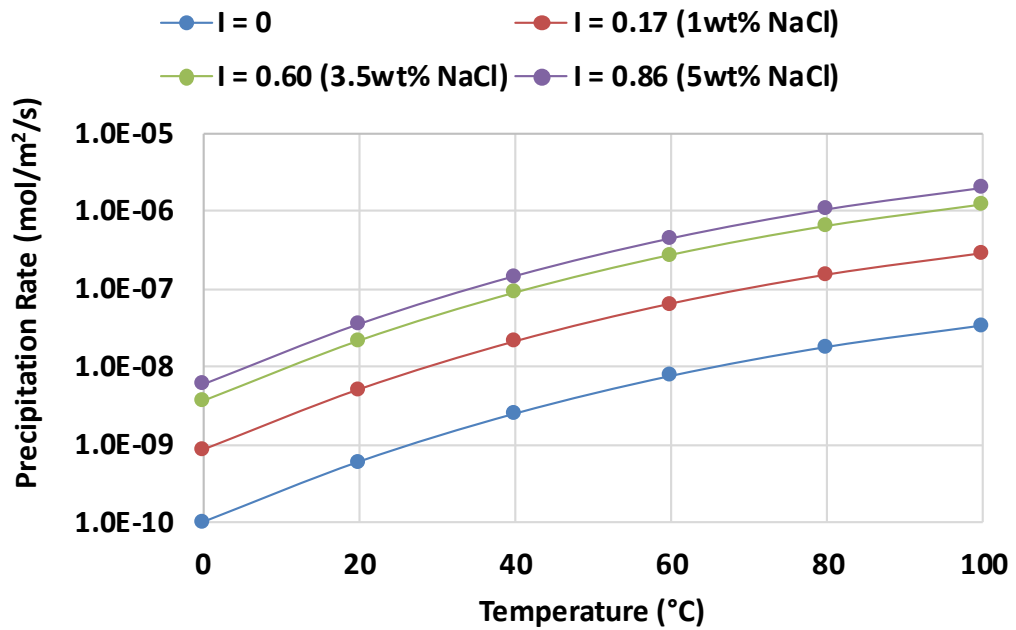


Figure 5.10 Effect of ionic strength on S&N precipitation rate equation for varying temperature.

5.4 Literature Review – Key Findings and Limitations

The mechanisms of carbon steel corrosion in CO₂-containing environments have been studied and debated for many years. A great deal of literature has been published with a number of different corrosion rates and mechanisms being reported. The understanding of CO₂ corrosion has come a considerable way over the past many years; however challenges still exist in this field. The above literature review has intensively discussed different attributes that effect CO₂ corrosion in industry and the different techniques that have been developed to understand and predict its process. The following summary highlights the important aspects of the literature review and identifies the gaps that shall form the subject of this thesis.

The electrochemistry of steel dissolution in CO₂ solutions has been largely understood. The conditions that lead to the formation of protective and un-protective FeCO₃ scales have been identified and the influence of various parameters on this phenomenon has been studied. All investigations in literature agree that increasing the temperature and pH improves the protectiveness of the film, however the sensitivity of the environment plays a

vital role and there is little agreement on a particular threshold temperature and pH. A parametric analysis of different variables that may play a role on the rate of FeCO_3 film formation is observed in Chapter 8.

The exact characteristics and morphology of the FeCO_3 film formed on the surface layer over time is understudied in literature and is an area of interest to the following thesis. This is addressed through applying different techniques to help understand the factors that control or dictate the nucleation and growth of FeCO_3 and the protectiveness of the film formed.

A main area of interest in this thesis is in advancing the mechanistic understanding of FeCO_3 formation. A number of models (mechanistic, semi-empirical and empirical) exist to predict CO_2 corrosion in literature. They all consist of different levels of complexity and different theoretical bases leading to a potentially inconsistent assessment of CO_2 corrosion risk. Sometimes the basis and applicability limits of these prediction models are misunderstood which lead to incorrect prediction. Review papers of existing models show that the majority of mechanistic models assume ideality of the non-ideal electrolyte mixtures. A review paper by Sun et al. [45] concluded that improving the results by incorporating a semi-empirical activity coefficient in the mechanistic diffusion calculations may improve model predictions.

There are very few existing models in literature that focus on the effect of hydrodynamics on FeCO_3 film formation. The precipitation models discussed in Chapter 5 have all been derived from static conditions where the kinetics of FeCO_3 precipitation are accelerated by the addition of $\text{FeCl}_2 \cdot 4\text{H}_2\text{O}$ and correlated with bulk solution properties. They do not address the key aspects of FeCO_3 formation in real corroding systems which relate to the local surface supersaturation produced as a result of the production of Fe^{2+} ions due to the corrosion process. Furthermore, CO_2 corrosion models that account for FeCO_3 film formation in prediction of the corrosion rate over time are developed for pipe flow and the precipitation model incorporated is developed based on static conditions and bulk solution properties which results in an inconsistency in the underlying theory. A large part of the following thesis is focussed in addressing this gap in a combined modelling and experimental approach. Figure 5.11 illustrates a flow chart highlighting the main gaps that are identified in the following literature review and the work carried out in this thesis to further the understanding of FeCO_3 film formation.

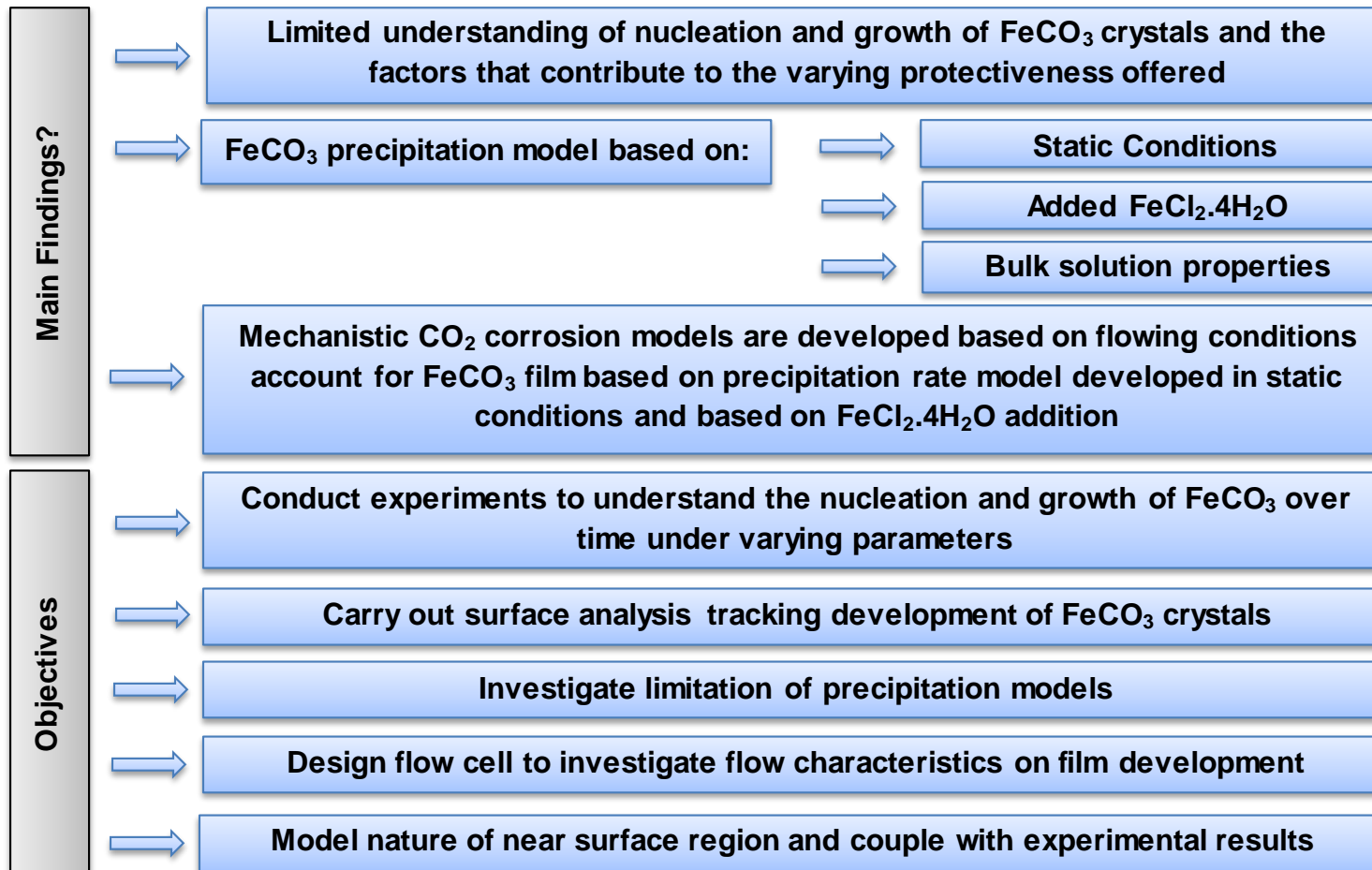


Figure 5.11 Main literature findings and work carried out to address the identified limitations.

Chapter 6

Static Experimental Theory and Methodology

This chapter provides a theoretical understanding of the practical techniques used to investigate carbon dioxide (CO₂) corrosion of X65 carbon steel in a static environment. This work contributes to furthering the understanding of the formation of FeCO₃ under varying parameters, its effect on the corrosion rate and the characteristics of the film.

The experimental analysis is divided into three stages. Initially, the effect of varying parameters on the corrosion rate is tested. The results from this analysis are compared with existing published data and theory in order to validate the experimental procedure and observations. Furthermore, the results provide an understanding of the different parameters that can cause an effect on the CO₂ corrosion rate of X65 carbon steel in a static environment emphasising the sensitivity of this process. In the second stage, two different conditions are decided on from the previous analysis; one where a protective film is formed and the other where the film is less protective. Under these conditions, the nucleation and growth of the FeCO₃ crystals are tracked with time through scanning electron microscopy, weight change due to corrosion and film precipitation through mass measurements and spectroscopy to determine the bulk Fe²⁺ ion concentration. This stage of experiments is performed to understand the factors that contribute to making a film protective through observing the development of the film over time. A series of different analysis techniques are used to compare the two different conditions and highlight the limiting components in the spontaneous nucleation and growth of FeCO₃ crystals. The final stage of the static tests was carried out with the addition of hydrated FeCl₂.4H₂O where the precipitation rate is determined from the weight gain due to FeCO₃ crystal formation on a corroding steel surface and pre-formed protective FeCO₃ film. Figure 6.1 provides an overview of the tests done under static conditions and the subsequent analysis. The following chapter covers a detailed overview of the experimental procedure along with the theory behind the practical applications applied.

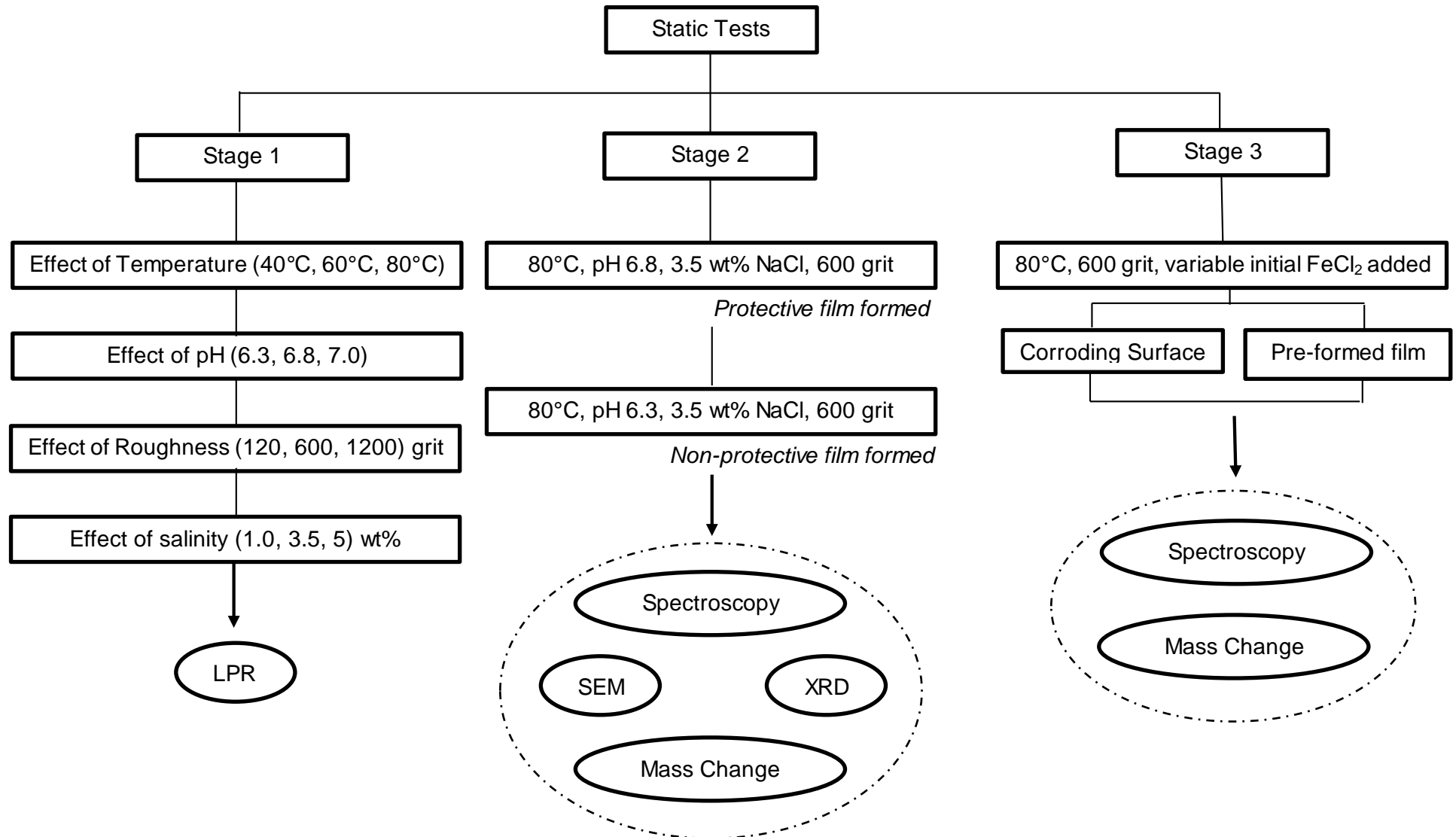


Figure 6.1 Summary of static experimental work done.

6.1 Static Experimental Set-Up

The true mechanism behind corrosion is the actual atomic, molecular, or ionic transport process that occur at the material interface. These processes cannot be directly observed on an atomic scale, making it necessary to infer possible mechanisms based on indirect measurements and observations such as mass loss, rate of corrosion product formation or changes in surface appearance. When electrochemical corrosion is occurring, mechanisms can be identified through the implementation of an electrical potential and/ or current measurements [3].

In the following study, as in most electrochemical techniques, a 'three-electrode configuration' is used. The setup comprises a working electrode (WE), a reference electrode (RE) and a counter electrode (CE). Figure 6.2 depicts a 3D model of the experimental apparatus used to carry out the static experiments. The figure is clearly labelled identifying the different components used in the study.

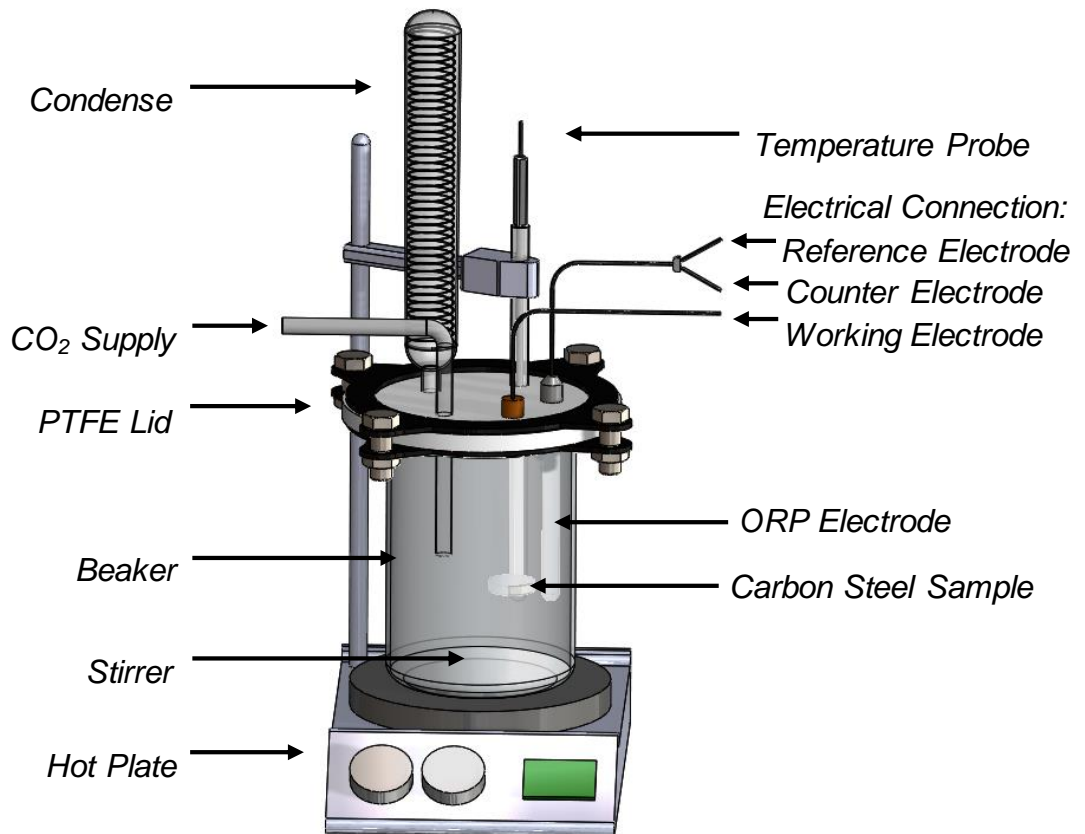


Figure 6.2 Labelled 3D CAD model of static experimental set-up.

The working electrode is an X65 carbon steel sample and is the electrode under study. A combined ORP (oxidation-reduction potential) electrode is used as the reference/ counter electrode. The reference electrode allows measurement of the working electrode potential without passing current through it while the counter (auxiliary) electrode is an inert electrode with a 'current-carrying function' (allows current to pass through WE) to study WE kinetics [19]. The three electrodes are electrically connected to a potentiostat which controls the potential of the working electrode and measures the resulting current. The following three sub-sections highlight the step-wise procedure to starting and running a static test and collecting electrochemical measurements.

6.1.1 Sample Preparation

Carbon steel samples were cut from the pipework and machined down to 25 mm diameter pieces. The exposed area of each specimen to the test solution was 4.9 cm². X65 carbon steel was the material used as it is commonly used to manufacture oil and gas pipelines due to its availability and ability to fulfil many of the mechanical, structural and cost requirements [1].

Its chemical composition as shown in Table 5.8 (page 54). The machined coupons were initially soldered to a wire approximately 20 cm in length before being embedded in to a non-conductive resin. The resin mixture was prepared by mixing VariDur10 powder with VariDur10 liquid solvent hardener and then poured into the resin moulds over the soldered coupons. After the resin had set, the coupons were removed from the moulds and were then polished. SiC abrasive paper is used within the University of Leeds for polishing metallic specimens. SiC abrasive papers are available in all common grit sizes ranging from 120 to 1200 grit.

Table 6.1 Steel surface properties upon polishing with SiC abrasive papers.

Standard ANSI grit	European (P-Grade)	Median Diameter (microns)	Surface Roughness on Steel, (Ra – nm)
120	P120	106	1050
320	P360	40.5	230
600	P1200	15.3	15.3
800	P2400	6.5	6.5

1200	P4000	2.5	2.5
------	-------	-----	-----

Table 6.1 shows different representations of the surface finish of the polished samples. The samples were then degreased with ethanol and rinsed with distilled water to completely clean them of any leftover residue and then dried with compressed air.

6.1.2 Solution Preparation

A glass cell was filled up with 1L of electrolyte that was prepared by dissolving 3.5 wt% (35 g) of NaCl in distilled water. Initially, the solution was deaerated with CO₂ gas for about 1h before starting the test as well as throughout the experiment to ensure complete saturation. The cell was sealed apart from a small outlet to prevent O₂ contamination while the CO₂ gas was bubbling. A hot plate was used to heat the temperature to required operating temperature and it was maintained at $\pm 1^\circ\text{C}$ with the use of the temperature probe forming a feedback loop. The cell was operating at atmospheric pressure. A pH meter was calibrated using three different buffer solutions and then the solution pH was adjusted to the desired value of pH by adding sodium bicarbonate to the solution. A magnetic stirrer rotating at a speed of 200 rpm was used continuously throughout the experiment to promote chemical consistency throughout the fluid.

6.1.3 Corrosion Measurement

Once the setup was at the desired operating conditions, the electrodes were immersed into the test solution. They were then connected electrically to the potentiostat for electrochemical measurements to be taken. The electrochemistry in the following study was carried out by means of the DC linear polarisation technique using a computer controlled Potentiostat (ACM Gill).

The experiment is run and the corrosion rate of the metal working electrode is directly measured every 15 minutes using Linear Polarisation Resistance (LPR) electrochemical technique. The technique works by first measuring the Open Circuit Potential (OCP). The OCP is the equilibrium potential assumed by the steel specimen in contact with the electrolyte and is required prior to carrying out reliable electrochemical corrosion kinetics assessments through Potentiodynamic Polarisation (PDP), Linear Polarisation Resistance (LPR) and Electrochemical Impedance Spectroscopy (EIS).

Assuming no external polarisation, oxidation and reduction reactions take place at the same rate on an immersed electrode surface, meaning that opposing anodic and cathodic current densities are equal in magnitude and there is zero net current. Under such conditions, measuring the WE potential with respect to that of the RE gives the OCP. When the OCP values (as a function of time) become stable, the electrode is assumed to have reached a 'steady state'. The change of OCP with time can be informative about the reactions occurring on the electrode surface. For example, an OCP shift to a more negative potential can indicate a change in the corrosion kinetics to one either favouring the anodic reaction or suppressing the cathodic reaction [19]. In this work, electrodes were left to corrode at their open circuit potential for all periods outside of electrochemical measurements. The OCP for carbon steel is typically around -0.7V vs. Ag/AgCl for a pH of 6.

Polarisation measurements were then subsequently started. Polarization resistance measurements were conducted by polarising the working electrode $\pm 15\text{mV}$ from OCP and scanning at a rate of 0.25 mV/s . For such small potential perturbations, the WE surface is not altered/damaged [32, 33]. A typical plot obtained of current density vs. potential is shown in Figure 6.3 which shows that the measured current density is linearly proportional to the applied potential.

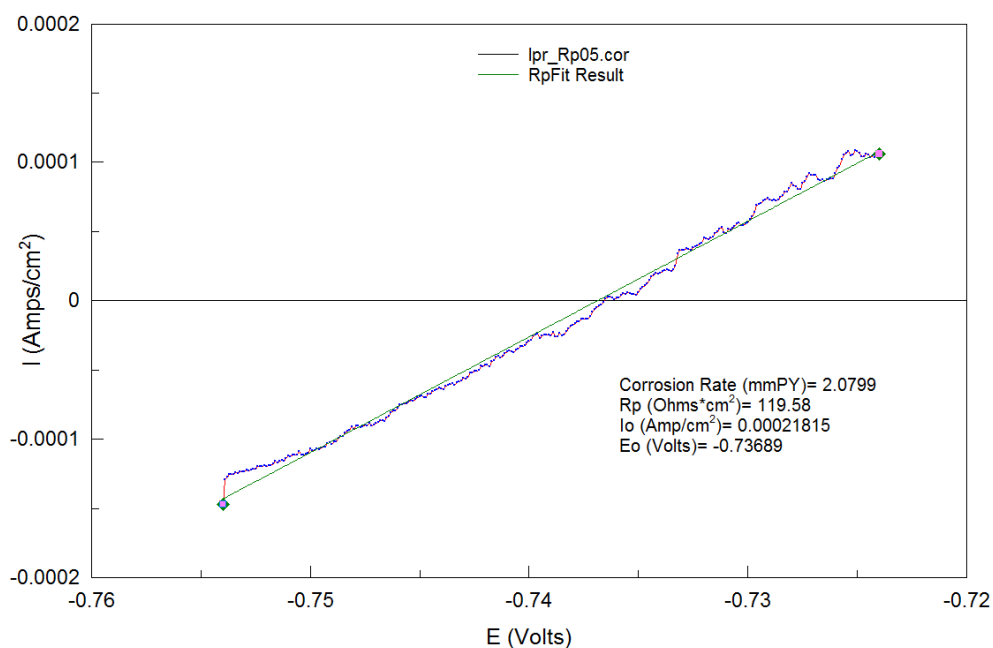


Figure 6.3 Typical LPR plot that demonstrates the linear potential-current relationship at low applied potential. The gradient is used to obtain the polarisation resistance R_p .

The gradient of the linear section, attained from numerical fit of the curve, yields the value for Polarisation Resistance, R_p of the electrode [19]. This potential-current gradient around OCP is the uncompensated for the solution resistance between the WE and RE, i.e.

$$R_p = R_{ct} + R_s \quad (6.1)$$

R_p is the measured gradient, which contains the electrode's true Faradaic corrosion resistance (R_{ct}) and the solution resistance (R_s). The solution resistance term for a static cell at 80°C in 3.5 wt% NaCl is recorded to be quite small (approximately 1 Ohm.cm²) and is assumed negligible in the experiments in the following chapter. A number of research groups working in static conditions have taken a similar approach [19, 76-80]. However, it may be significant in some cases such as in the following chapter. In such a case, R_s is subtracted from the polarisation resistance (R_p) obtained from linear data curve fitting. The true R_{ct} is considered to be proportional to the rate of the corrosion reactions taking place at the electrode surface. Solution resistance (R_s) was measured from AC impedance spectroscopy.

R_{ct} is inversely proportional to the corrosion rate and can be related to the corrosion current density (i_{corr}) by the Stern-Geary Equation [47].

$$R_{ct} = \frac{B}{i_{corr}} = \frac{(\Delta E)}{(\Delta i)_{\Delta E \rightarrow 0}} \quad (6.2)$$

Where R_{ct} is the charge transfer resistance (Ohms.cm²), i_{corr} the corrosion current density (A/cm²) and B is the proportionality constant and is known as the Stern-Geary coefficient 'B' (in V decade⁻¹). B can be calculated from β_a and β_c , the slopes of the anodic and cathodic tafel as shown in the Equation (6.3) [47].

$$B = \frac{\beta_a \beta_c}{2.303(\beta_a + \beta_c)} \quad (6.3)$$

The value of B for an electrode immersed in an electrolyte, in a given system, is often a topic of controversy since selecting a straight line in a polarisation curve is subjective. Furthermore, the B parameter varies over time as surface conditions on the electrode change and reported values from literature are never specific to the exact practical conditions under study (i.e. solution chemistry, flow, material, microstructure, electrode geometry are all different) [19].

Stern et al. [81] described β_a and β_c as a function of temperature.

$$\beta_a = \frac{2.303RT}{\alpha_a F} \quad (6.4)$$

$$\beta_c = \frac{2.303RT}{\alpha_c F} \quad (6.5)$$

Where T is the absolute temperature in K, R is the universal gas constant (8.314 J/mol K), and α_a and α_c are the symmetry factors for anodic and cathodic reaction. The values of α_a and α_c are 1.5 and 0.5 as explained by the Bockris mechanism. F is the Faraday's constant (96,496 Coulombs/mole).

For the corrosion rate calculations under static conditions in this work, B was maintained as 26 mV decade⁻¹ so that all presented corrosion rates become comparable with each other, as done in [80]. A number of research groups have used B = 26 mV decade⁻¹ when presenting their corrosion rate data [19, 76-80]. The corrosion rate data in those works, and indeed this thesis, have been used predominantly as an indicator of the progress of scale development and the protective effect that scaling imparts over time. Even though B = 26 mV decade⁻¹ may not be entirely accurate, it only provides a systematic error and therefore its usage in this work is justifiable as a 'conversion' factor [19].

The corrosion rate, CR is then finally quantified using Equations (6.6, 6.7).

$$CR \left(\frac{mm}{y} \right) = \frac{i_{corr} \left(\frac{A}{cm^2} \right) \times 10 \left(\frac{mm}{cm} \right) \times 31,556,926 \left(\frac{s}{yr} \right) \times M \left(\frac{g}{mol} \right)}{n (e^-) \times F \left(\frac{C}{mol} \right) \times \rho \left(\frac{g}{cm^3} \right)} \quad (6.6)$$

$$CR \left(\frac{mm}{y} \right) = 1.17 \times 10^4 (i_{corr}) \quad (6.7)$$

Where i_{corr} is the corrosion current density (A/cm²), M is the atomic weight of the metal (55.85 g/mol), ρ is the density (7.8 g/cm³), n is the charge number (2^{e-}) which indicates the number of electrons exchanged in the dissolution reaction and F is Faraday's constant (96,485 C/mol).

At the end of each experiment, the specimen was removed and immediately rinsed with distilled water and then flushed with ethanol until it was cooled to room temperature. This was done in order to reduce oxidation of wet films at an elevated temperature and remove any unwanted salts that may have formed on the surface. Any remaining alcohol was then blown away from the surface using a compressed air gun. The samples were freed from the resin and the wire attached to the samples by carefully breaking the resin. The

specimen was then placed in a desiccator under a low humidity atmosphere for storage prior to further surface analysis.

6.2 Weight Change Method

The following experimental technique was used in the second and third stage of the static experimental work done in order to directly infer the weight loss of an X65 carbon steel sample due to corrosion and the weight gained due to FeCO_3 precipitation during the duration of exposure in a CO_2 environment. The technique was used previously by Sun et al. [9, 10] and the experimental set-up is similar to discussed previously. The experiments were performed in a static solution with 1 bar total pressure. The glass cell was filled with 1 litre of distilled water and 3.5 wt % NaCl, which was heated and purged with CO_2 gas four hours prior to and throughout the experiment. The pH was increased to the desired pH by adding sodium bicarbonate. Once the solution had reached the required conditions, the X65 carbon steel sample was inserted into the solution.

The difference in the following technique lies in the sample preparation. The sample was still 25 mm in diameter and the exposed area was 4.9 cm^2 . However, in these experiments, the sample surface was initially polished with 120, 320 and 600 grit SiC paper, rinsed with ethanol, distilled water and then dried with compressed air. The initial mass of the sample was then measured using a sensitive micro balance (Mettler XP26). The sample was similarly embedded in non-conductive resin. The surface of the sample was protected using tape preventing any of the resin hardening on the surface to be exposed. The sample was not soldered to a wire as electrochemical measurements were not required. However, a wire of similar length is fixed on to the sample in the resin in order to drop the sample into the solution and hold it in place. After the resin had set, the coupons were removed from the moulds and tape. It was then rinsed with ethanol, distilled water and dried with compressed air before being immersed in the prepared solution.

At the end of each experiment, the sample was similarly removed and rinsed with ethanol, distilled water and then dried with compressed air. The resin was then cracked and the sample weight was once again measured determining the mass of the sample with the FeCO_3 film formed. The scale was then removed using Clarke's solution. Clarke's solution was prepared using 20g antimony trioxide and 50 g stannous chloride in 1 litre hydrochloric acid at room temperature for up to 25 minutes. A thin layer of the solution

was placed on the exposed surface of the sample and a cotton swab was used to remove the film.

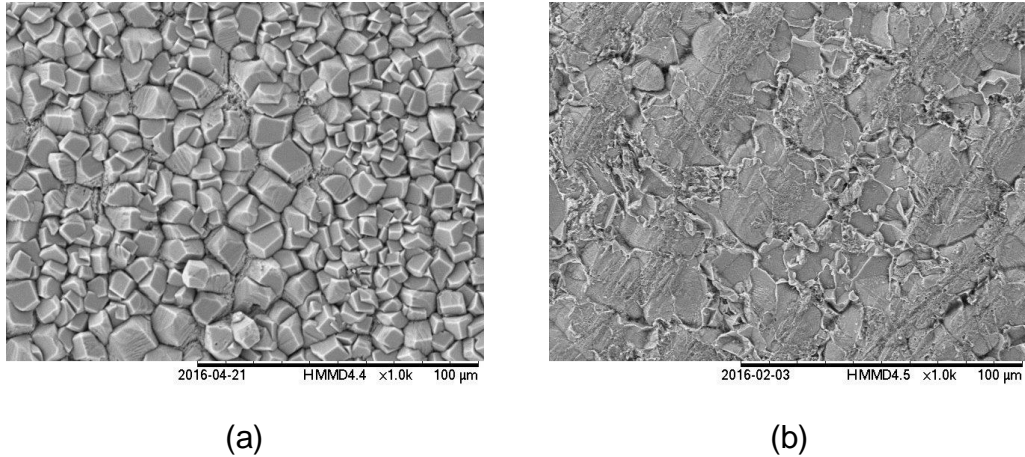


Figure 6.4 SEM image of carbon steel sample before and after film removal using Clarke's solution. Sample was exposed to a CO₂ saturated environment at 80°C, pH 6.8 for 20 hours. (a) Before removal. (b) After film removal.

This technique was used by Sun et al. [9, 10] however was initially tested in order to ensure that it was effective and the complete FeCO₃ film was removed. Scanned electron microscopy (SEM) images of the surface of the samples with a complete film and after rubbing with Clarke's solution was observed. Multiple images were taken across the surface and the technique used was found to be effective. Figure 6.4 shows an SEM image of the sample before and after removal of the film.

Another test was performed in order to ensure that the technique used did not remove more than just the FeCO₃ film. This was performed by polishing a few samples, determining their initial mass and then rubbing the surface with Clarke solution. The mass of the samples were then measured in order to determine if there was a mass loss due to the Clarke solution possibly effecting a clean sample. The mass loss was found to be approximately on average 4μg supporting the use of the technique.

After removal of the film, a third measurement of the sample mass was taken. This measurement represented the post experimental mass of the sample of the sample without a film present. The time-averaged corrosion rate was calculated by subtracting the weight of the samples prior to running the experiments and after removing the iron carbonate scale. The time-averaged precipitation rate of iron carbonate was obtained by subtracting the weight of the sample which had iron carbonate and those after the scale was

removed. The equations used to calculate the two terms are expressed below.

$$CR\left(\frac{mol}{m^2s}\right) = \frac{m_1(g) - m_3(g)}{MW_{Fe} \left(\frac{g}{mol}\right) \times t (hr) \times S (m^2) \times 3600 \left(\frac{s}{hr}\right)} \quad (6.8)$$

$$CR\left(\frac{mm}{yr}\right) = CR\left(\frac{mol}{m^2s}\right) \times \frac{365 \left(\frac{days}{yr}\right) \times 86400 \left(\frac{s}{day}\right) \times MW_{Fe} \left(\frac{g}{mol}\right)}{\rho \left(\frac{kg}{m^3}\right)} \quad (6.9)$$

$$PR\left(\frac{mol}{m^2s}\right) = \frac{m_2(g) - m_3(g)}{MW_{FeCO_3} \left(\frac{g}{mol}\right) \times t (hr) \times S (m^2) \times 3600 \left(\frac{s}{hr}\right)} \quad (6.10)$$

Where CR is the corrosion rate (mm/year), PR is the precipitation rate (mol/m²s), m₁ is the weight of the coupon prior to running experiments (g), m₂ is the weight of the sample which has scale on it after the experiments (g), m₃ is the weight of the sample after removing the scale (g), MW_{Fe} is the molecular weight of iron (g/mol), MW_{FeCO₃} is the molecular weight of iron carbonate, t is the exposed time (hours), S is the exposed sample area (m²) and ρ is the density of the sample (kg/m³).

6.3 Method of Fe²⁺ Addition

In the third stage of experiments, the weight change technique was applied to observe the effect of a variable bulk super saturation on the iron carbonate scale retention rate on the steel surface. The required amounts of Fe²⁺ were added in the form of deoxygenated ferrous chloride salt (FeCl₂.4H₂O) solution. The procedure used for the addition of FeCl₂ was applied previously by Nafday et al [82].

A gram of FeCl₂.4H₂O was weighed in a weighing dish and was added to 10 ml of deoxygenated distilled water in a small vessel. After the FeCl₂ was dissolved, the required amount of solution was removed out of the glass vessel using a pipette and added to the test solution. The amount of iron chloride solution added to the test solution to achieve a required concentration of Fe²⁺ (ppm), when 1 gram of FeCl₂.4H₂O is dissolved in 10 ml of deoxygenated solution is given by Equation (6.11).

$$V(ml) = \frac{Fe^{2+}(ppm)}{MW_{Fe^{2+}}(\frac{g}{mol}) \times 1000} \times \frac{V_{total}(l) \times V_{FeCl_2.4H_2O}(ml)}{\left(\frac{W(g)}{MW(\frac{g}{mol})}\right)_{FeCl_2.4H_2O}} \quad (6.11)$$

Where V is the volume needed to be added to the test (ml), V_{total} is the total volume of the test solution in litres (l), W is the weight of $FeCl_2.4H_2O$ added (1 g), MW is the molecular weight of $FeCl_2.4H_2O$ (198 g/ mol) and $V_{FeCl_2.4H_2O}$ is the volume of $FeCl_2$ solution in ml (10 ml).

6.4 Solution Analysis - ($[Fe^{2+}(aq)]$) Calculation

Determining the Fe^{2+} ion concentration was of specific interest in this study because it could indicate the degree to which the bulk solution was supersaturated with respect to $FeCO_3$ at the time of sample removal. The solution saturation ratio can be determined using Equation (6.12) as discussed previously. The unitless parameter indicated whether the bulk of the solution is under saturated (< 1) or supersaturated (> 1).

$$SR = \frac{c_{Fe^{2+}} c_{CO_3^{2-}}}{K_{sp}} \quad (6.12)$$

A spectrophotometer was used to measure ferrous ion concentration in the solution. The technique involved removing 2ml of the test solution at a given time instant using a calibrated pipette. This volume is added to a Fe^{2+} ion cuvette (Hach Iron (II/III) cuvette test 0.2 – 6.0 mg/l Fe) as shown in Figure 6.5. The solution mixes with a chemical reagent and after 5 minutes, the cuvette is placed in the spectrophotometer (DR3900) that provides a reading of the concentration of Fe^{2+} ions in mg/l. The device measures how much the chemical substance absorbs light by measuring the intensity of light as a beam of light passes through sample solution. The intensity of the colour of a solution is proportional to the concentration of the absorbing species and a comparison of the intensity of the colour of solutions of known concentration with the intensity of an unknown permits identification of the concentration of the unknown solution.



Figure 6.5 (a) Hach Fe^{2+} ion cuvettes used in analysis of solution. (b) Image representation of working principle behind spectrophotometer used in determining Fe^{2+} ion concentration in sample solution [83].

The solubility limit for FeCO_3 is determined based on the knowledge of solution temperature and ionic strength using the empirical expression proposed by Sun et al. [9, 10] discussed previously. The equation has been reiterated below.

$$\log K_{sp} = -59.3498 - 0.041377T_k - \frac{2.1963}{T_K} + 24.5724 \log_{10}(T_K) + 2.518I^{0.5} - 0.657I \quad (6.13)$$

Where T_K is the temperature in degrees Kelvin (K), and I is the solution ionic strength. For a system of CO_2 saturated distilled water at 80°C and 3.5 wt% NaCl, the K_{sp} (FeCO_3) can be calculated to be 1.62×10^{-10} according to Equation (6.13).

The final term in determining the solution saturation ratio is the CO_3^{2-} ion concentration. For a specific solution temperature, ionic strength and pH, this can be calculated through knowledge of the equilibrium bulk concentrations for a CO_2 saturated solution. Oddo and Tomson [84] proposed the following empirical expressions, which were republished by Sun and Nescic in Shreir's Corrosion Handbook (Corrosion in Acid Gas solutions) [34].

In order to estimate the dissolved CO_2 concentration ($[\text{CO}_2(\text{aq})]$), Henry's Law can be used, through determining the CO_2 gas solubility constant ($K_{sol}(\text{CO}_2)$) in the aqueous solution and knowing the partial pressure of CO_2 gas (bar). This is expressed in Equation (6.14).

$$K_{sol} = [\text{CO}_2]/p_{\text{CO}_2} \quad (6.14)$$

The CO₂ gas solubility constant ((K_{sol}) [34] depends upon solution temperature (in degrees Fahrenheit) and ionic strength according to Equation (6.15).

$$K_{sol} = \frac{14.5}{1.00258} \times 10^{[-(2.27+5.65 \times 10^{-3}T_f - 8.06 \times 10^{-6}T_f^2 + 0.075I)]} \text{ molar/bar} \quad (6.15)$$

The product of K_{sol} and p_{CO2} (bar) will provide the aqueous dissolved concentration of CO₂.

A proportion of dissolved CO₂ hydrates to form carbonic acid (H₂CO₃ (aq)). The equilibrium hydration constant (K_{hy}) is taken as ~ 2.58 x 10⁻³ from the literature, and does not vary significantly from 20 – 100°C.

$$K_{hy} = [H_2CO_3]/[CO_2] \quad (6.16)$$

The dissolved H₂CO₃ concentration can be calculated as the product of the dissolved CO₂ concentration ([CO₂ (aq)]) and the equilibrium hydration constant (K_{hy}) according to Equation (6.16).

Furthermore, carbonic acid dissociates into hydronium (H⁺) and bicarbonate (HCO₃⁻) ions. The equilibrium constant for this reaction is known as the carbonic acid dissociation constant denoted by K_{ca}, as Equation (6.17) shows [34, 84, 85].

$$K_{ca} = [H^+][HCO_3^-]/[H_2CO_3] \quad (6.17)$$

The equilibrium first dissociation constant is a function of the solution temperature (degrees Fahrenheit) and ionic strength, and can be calculated using Equation (6.18).

$$\begin{aligned} K_{ca} &= 387.6 \\ &\times 10^{[-(6.41-1.59 \times 10^{-3}T_f + 8.52 \times 10^{-6}T_f^2 - 3.07 \times 10^{-5}p - 0.4772I^{1/2} + 0.1180I)]} \text{ molar} \end{aligned} \quad (6.18)$$

The dissociation constant depends upon solution temperature (in degrees Fahrenheit), ionic strength and total pressure in pounds per square inch (psi). Therefore, [HCO₃⁻(aq)] is determined as K_{ca} and [H₂CO₃ (aq)] is calculated. The [H⁺ (aq)] is determined from solution pH.

Finally, the [CO₃²⁻ (aq)] can be calculated. Similar to carbonic acid, bicarbonate ions dissociate into hydronium (H⁺) and carbonate (HCO₃⁻) ions, according to Equation (6.19).

$$K_{bi} = [H^+][CO_3^{2-}]/[HCO_3^-] \quad (6.19)$$

The equilibrium constant for this reaction is known as the bicarbonate dissociation constant and is denoted by K_{bi} [34, 84].

$$K_{bi} = 10^{[-(10.61 - 4.97 \times 10^{-3} T_f + 1.331 \times 10^{-5} T_f^2 - 2.624 \times 10^{-5} p - 1.166 I^{1/2} + 0.3466 I)]} \text{ molar} \quad (6.20)$$

$[\text{CO}_3^{2-}]_{(\text{aq})}$ can be calculated as $[\text{HCO}_3^-]_{(\text{aq})}$, solution pH ($[\text{H}^+]_{(\text{aq})}$) and K_{bi} are known. From this, we have all the necessary values to estimate the bulk SS according to Equation (6.20).

This technique was used in both stage 2 and stage 3 of the experimental tests and provided an understanding of the change in bulk SS with time and its relation to the observed precipitation rate determined through the weight change method. The calculations discussed will be revisited in more detail in future chapters where all the bulk species concentrations are determined and a model is implemented to calculate the values more efficiently.

6.5 Post Experimental Analysis Techniques

The focus of this analysis is to develop a further understanding for the mechanism of scale formation. This includes the characterisation of the morphology, structure and chemical composition of the film. After the performed experiments, the samples are analysed using specialised surface analysis techniques. The techniques carried out are explained in the following sections.

6.5.1 Scanning Electron Microscopy (SEM)

SEM is a qualitative surface analysis technique used to observe the surface of the carbon steel sample exposed to a CO_2 environment under varying conditions. The instrument provides high resolution imaging and the machines available in-house is the Carl Zeiss Evo MA15 and the TM3030 as shown in Figure 6.6. The EVO MA15 requires sample preparation prior to analysis under the electron microscope. The carbon steel samples were attached to specimen mounts using double sided carbon tape and painted around the edges with graphite paint to form a conductive bridge between the top surface of the specimen and specimen holder. The samples were then coated with a 50 nm layer of gold to prevent the samples from charging during SEM analysis. After sample preparation, the Carl Zeiss Evo machine was initially vented and opened. The samples were then loaded into the machine and secured on to the stage. The SEM machine was closed and pumped down to a vacuum of about 1.3×10^{-6} torrs. Images were then taken at a working distance of 8 mm and several areas of the samples were analysed and scanned [34].



(a)



(b)

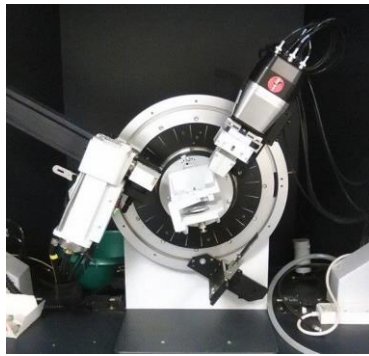
Figure 6.6 Image of a) SEM used in study and b) TM3030 Benchtop SEM [86]

The TM3030 was used more frequently in the following study due to its availability and ease of use. It is operated under a low vacuum environment and allows for quick image observation without specimen preparation. The sample is mounted on a base and connected to the required set height. It is fixed inside the SEM chamber, as shown in Figure 6.6 (b), and then closed. The chamber was then pumped into vacuum. The device upon start-up automatically turns on the beam, adjusts focus, brightness and contrast displaying the image at a starting magnification of $\times 100$. The images were recorded at an accelerating voltage of 5keV in comparison to the 20keV of the EVO MA15 [86, 87].

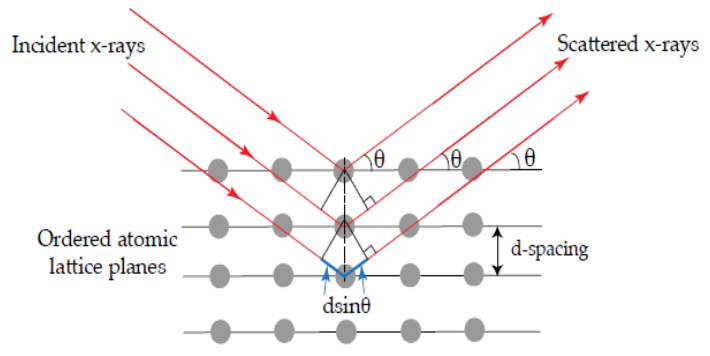
6.5.2 X-ray Diffraction (XRD)

Another essential surface analysis technique that provides vital information to the following work is X-Ray diffraction (XRD). It is a commonly used technique in the identification of the phases which constitute the film at an instant in time.

The in-house XRD Machine at the University of Leeds is the Siemens Bruker D8 Advance XRD machine capable of using either copper or silver source tubes.



(a)



(b)

Figure 6.7 a) Image of in-house XRD facility. b) Schematic representation of the XRD Technique and Bragg Diffraction [88],

In the following analysis, copper source tube was used as it results in higher resolution and therefore more visible peaks with less noise. The sample was placed on the metal ring shown in Figure 6.7 (a) and was positioned against the three sample leveller pins in the sample holder stage within the XRD machine so that the sample is in line with the rim of the holder and x-rays impinge only upon the sample surface. Scattered x-rays are detected using a point detector that scans the range $20^\circ < 2\theta < 70^\circ$ to capture the main FeCO_3 peaks. When the sample is bombarded with radiation, X-rays are typically diffracted from the surface via the electron in the material according to Bragg's Diffraction law (Equation (6.20)) where d is the spacing between the diffracting planes or lattice, θ is the incident angle, n is any integer and λ is the wavelength of the beam [88, 89].

$$2d \sin \theta = n\lambda \quad (6.20)$$

The diffracted X-ray beams are picked up by a detector scanning at this angle and the positions of these reflections inform the user about the inter-layer spacing of atoms in the crystal structure. Peak intensities give information about how much X-ray scattering is contributing to that reflection in terms of where particular atoms lie in the structure, or how much of a phase is present in a sample. The diffraction pattern is analysed using X-Pert Analysis software that allows the identification of phases within a given sample [88].

Figure 6.8 shows a typical result of XRD analysis of a carbon steel sample at variable times of exposure to experimental conditions 70°C , pH 6.5, 3.5 wt% NaCl and 0.54 bar pCO_2 . X-Pert High Score Plus Software is used to label the peaks produced by comparing with the standard. The Figure shows that

there was a general FeCO_3 film increase with time while the Fe peak intensity decreases.

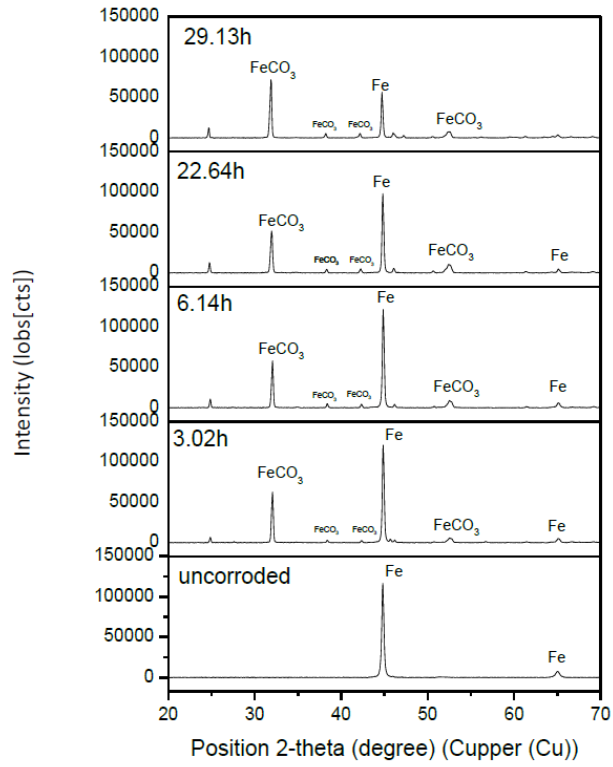


Figure 6.8 XRD pattern results for carbon steel samples [90].

Chapter 7

Development of Thin Channel Flow Cell

An integral part of the experimental aspects of this thesis is the design, manufacture and development of a thin channel flow cell for examining the effects of single phase fluid flow on CO₂ corrosion and the formation of FeCO₃.

The CO₂ corrosion process has been seen to accelerate significantly under extreme environmental conditions such as high temperature, high pressure, and turbulent fluid flow [91]. To further the understanding of these field corrosion problems, researchers have attempted to reproduce the same or similar conditions in controlled settings in a laboratory environment. Well-known laboratory equipment for temperature and pressure control are the bubble cell and autoclave systems. They are widely used, readily available and referenced in a multitude of literature. However, their primary drawback is that they are limited to static conditions. In Chapter 6, a variety of test methodologies were discussed for experiments conducted in a glass cell. In the following chapter, the work is extended to introduce a fluid flow condition. Corrosion is a surface-related degradation process and the flow of fluid media over a metal surface could increase or decrease the corrosion rate of the metal. A commonly-used laboratory system to incorporate flow into a testing environment is a Rotating Cylinder Electrode (RCE) [53, 92] where a metal sample is rotated with respect to the fluid. In the following work; however, the fluid is moved across the sample in the form of a designed thin channel flow cell which is believed to represent pipe flow more accurately and eliminates the effect of the centrifugal force encountered in the rotating cylinder electrode system.

7.1 Flow Cell Design and Manufacture

The study on the effect of flow on corrosion requires that the flow apparatus has a well-defined hydrodynamic and mass transfer behaviour. This is important in establishing that the observed flow-sensitive corrosion is due to mass transfer control and not due to hydrodynamic shear stress. The thin channel flow cell, shown in Figure 7.1, was designed to study the effect of a fully developed single phase laminar and turbulent flow on corrosion and the kinetics of FeCO₃ film formation. The width of the channel (15 mm) is 5 times larger than its thickness (3 mm) so as to ensure that there will be no edge effect and the velocity gradient will be only in the height direction therefore

mass transport will only be one dimensional. The entrance length is set at 105 mm which ensures that the hydrodynamic and the diffusion boundary layer will be uniform over the sample surface.

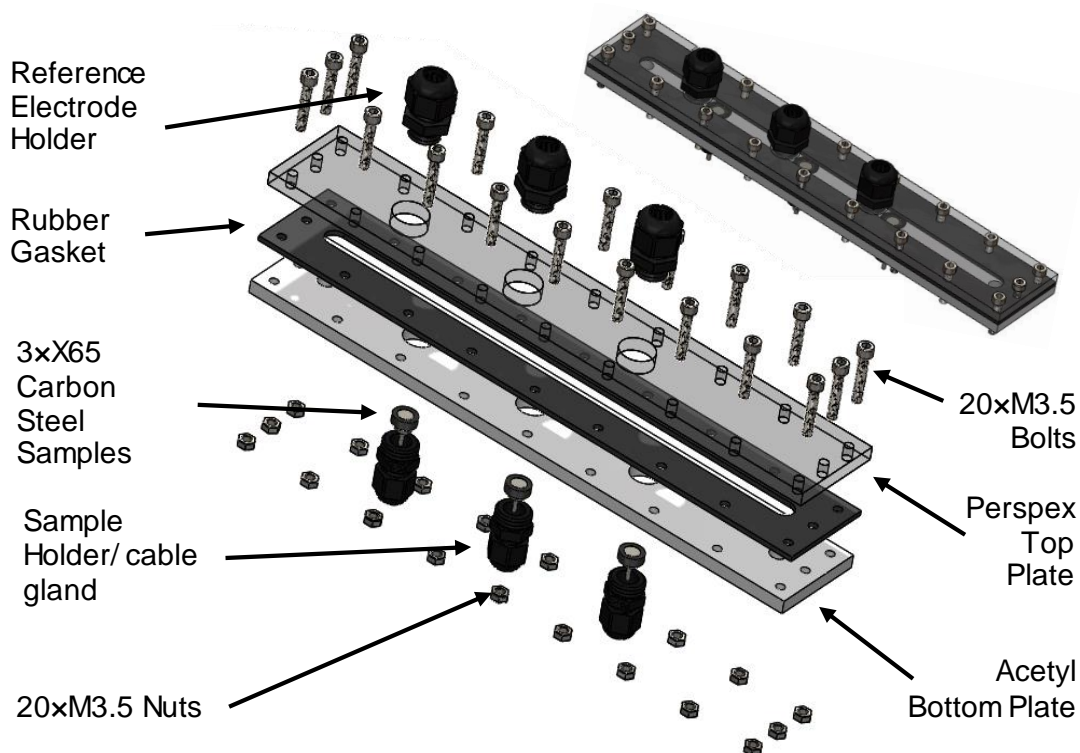


Figure 7.1 Exploded and labelled 3D CAD model of designed flow cell. Top right hand corner depicts flow cell with all components fitted together.

The exploded view is used to show the individual components of the cell which consist of three main parts, a Perspex top plate providing a visual view of the flow across the sample, a Viton rubber gasket which controls the flow path across the sample surface and offers sealing properties between the two plates and the acetyl bottom plate which houses three X65 carbon steel samples. The three components are tightly sealed/ bolted together preventing any leakages or oxygen contamination. The top plate is also modelled to accommodate three cable glands to house three reference/ counter electrodes. Each reference/ counter electrode is connected with its respective working electrode to provide LPR measurements. The carbon steel samples are flush mounted with a total exposed surface area of 0.79 cm^2 each. The flow channel across the sample is determined through the use of a gasket where the flow velocity is determined according to its shape. The thickness of the gasket is 3 mm and COMSOL computational fluid dynamic (CFD) analysis is performed to identify the flow velocity across the sample and shall be further discussed in the following section.

The configuration of the flow cell to accommodate three samples and three corresponding reference and counter electrodes was initially designed to vary the flow across each sample by altering the width of the flow channel across each sample. Each redox electrode would then be exposed to the same flow velocity as its corresponding sample and the distance between the sample and its redox electrode was kept at the minimum to reduce solution resistance. The straight gasket shown in Figure 7.1 was then intended to be used to determine the effect of each of the samples on each other. However, initial testing and analysis showed that altering the channel width across each sample was limited by the size of the flow cell and achievable change in velocity across the sample did not have a significant effect on the corrosion rate results obtained through LPR measurements. The design of the tests were then modified to facilitate the use of the straight gasket where the width of the flow channel across each of the samples was the same and the main distinction in velocity was achieved through different pump flow rates.

7.2 Flow Analysis through TCFC

An essential component of the analysis of the thin channel flow cell (TCFC) is determining the flow across each of the samples for a given configuration. An initial decision was made that the flow cell shall be analysed for four different velocities determined by the pump settings of 400, 1000, 2000 and 3000 ml/min. The flow was calibrated to determine the flow rate through the flow cell for each pump setting and Table 7.1 shows the results.

$$Q(m^3/s) = V(m/s) \times A(m^2) \quad (7.1)$$

The flow velocity across the surface of the sample was initially determined analytically for each flow rate (Q) according to Equation (7.1). The area of the flow channel across the sample is defined by the gasket and was 15mm×3mm. The calculated flow velocities are shown in Table 7.1.

The type of flow for each pump setting is determined by Reynolds number, Re and is calculated according to Equation (7.2) for a thin channel flow cell.

$$Re_T = \frac{V \times h}{\nu} \quad (7.2)$$

Where V is the velocity across the surface of the sample in m/s, h is the height of the thin channel flow cell in m and ν is the kinematic viscosity of water in m^2/s . The Reynolds number for each flow velocity is shown in Table

7.1 and flow is found to be laminar for a flow velocity of 0.12 m/s and turbulent for 0.31, 0.62 and 0.95 m/s across the surface of the sample.

Table 7.1 Flow configuration through thin channel flow cell.

Pump Setting (ml/min)	Calibrated Flow Rate, Q (ml/min)	Velocity COMSOL (m/s)	Velocity Analytical (m/s)	Re #
400	304.2	0.12	0.11	986.30
1000	775.2	0.31	0.29	2547.95
2000	1562.4	0.62	0.58	5095.89
3000	2376.2	0.95	0.88	7808.22

The analytically calculated velocity values are a simple approximation of the flow characteristics. The technique does not take into account the inconsistency of the flow and possible stagnation points or boundary layer separation that may occur. A more complete analysis of the fluid flow through the flow cell was studied with COMSOL Multiphysics. The software provides the ability to simulate a more accurate representation of the flow characteristics through the flow cell and determine the flow efficiency. The geometry of the fluid is 3-dimensionally modelled in Solid Works and imported into COMSOL as shown in Figure 7.2. The water fluid parameters, boundary conditions, inlet flow rate and mesh are defined and the simulation is run for a stationary solver. The turbulent flow, k- ω model interface is used for simulating the flow at high Reynold's number while a laminar flow interface is used for a flow velocity of 0.1 m/s. The defined mesh is illustrated in Figure 7.2 and comprises of 71,547 elements. It was determined by progressively creating a finer mesh until a robust, mesh independent solution was obtained.

COMSOL flow analysis results for each of the pump settings are shown in Figure 7.3. The colour panel identifies the flow velocities across the thin channel flow path showing a uniform flow across the surface of the samples with the uniform velocity across all three samples indicated in Table 7.1. The dark blue region indicates stagnation points in the flow and are found to be minimal at all flow settings and form at the very far end of the inlet and outlet walls. Figure 7.3 (e) shows the wall shear stress in (N/m²) at the highest flow velocity considered (0.95 m/s). It was found to be minimal across the

surface of the sample and the noted maximum shear stress was 2.4 N/m^2 . Further investigation into the wall shear stress has been neglected as according to Yang et al. [93], stresses of the order of 10^6 pascals are needed to detach a protective FeCO_3 layer [94].

Overall, the results show that the designed flow path created by the gasket provides a uniform flow velocity across the surface of the samples and justifies its use in the flow cell design.

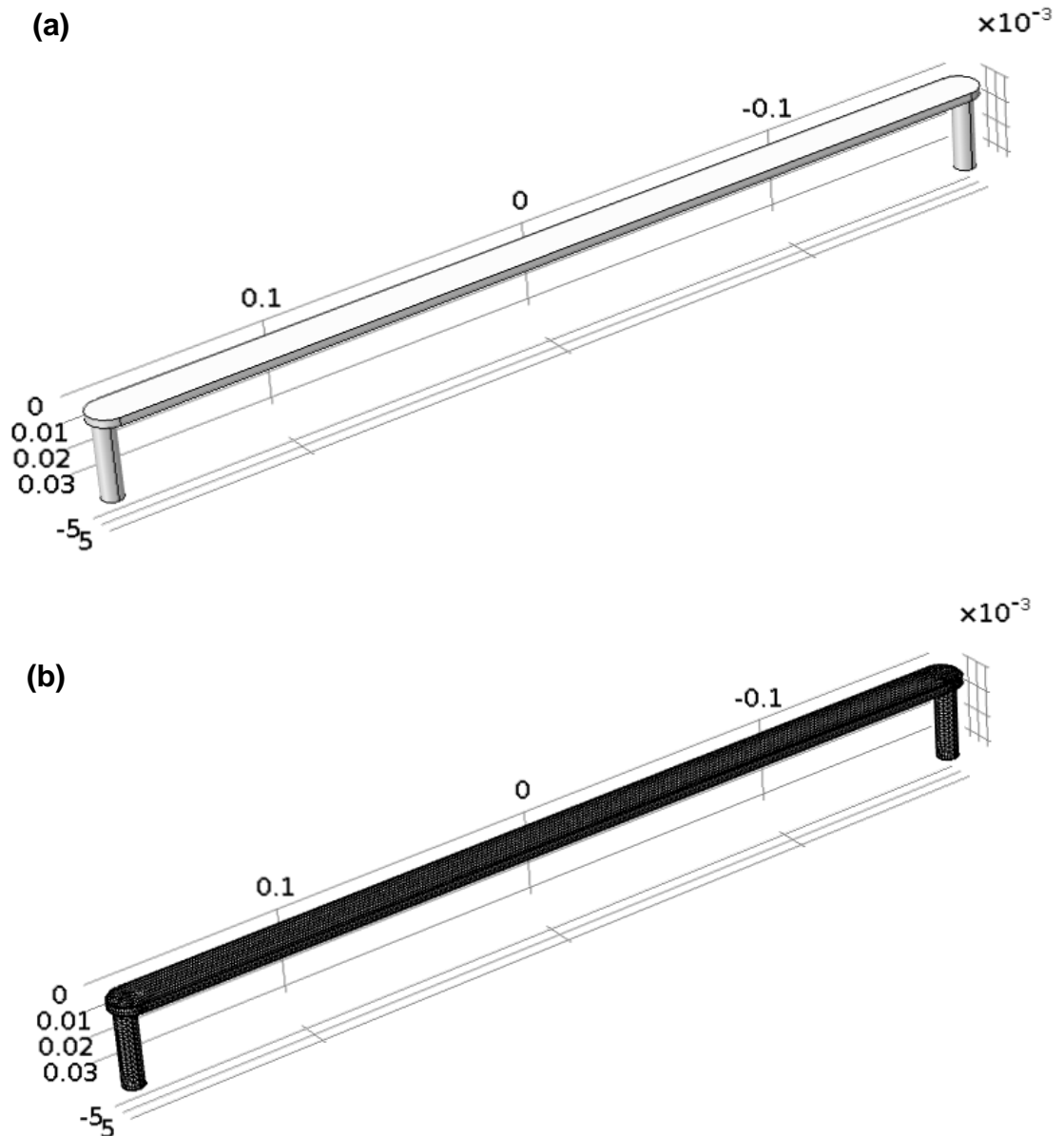


Figure 7.2 (a) 3D constructed geometry of flow cell imported into COMSOL Multiphysics. (b) Defined mesh distribution across geometry of fluid flow.

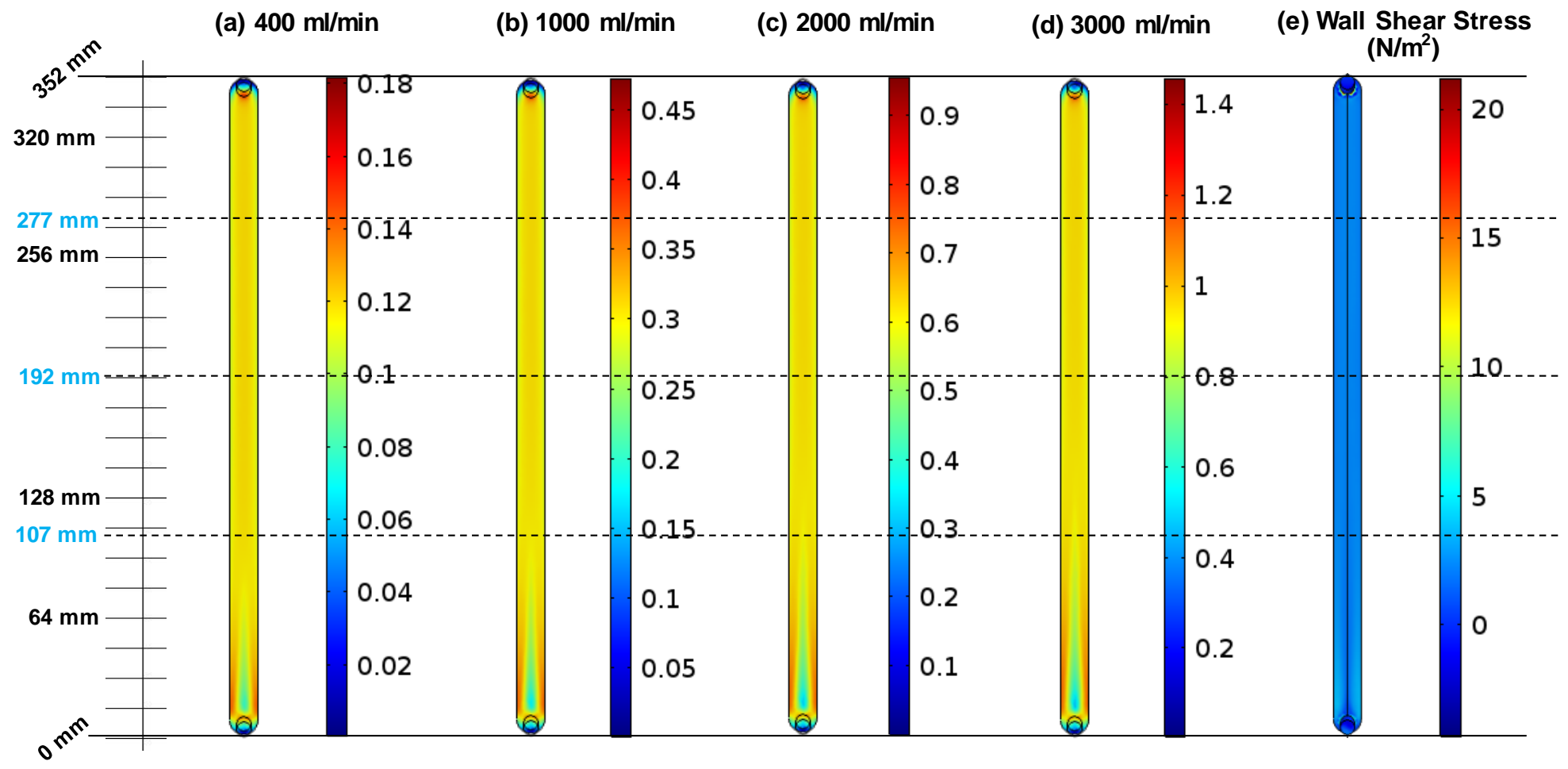


Figure 7.3 (a) – (d) Computational results showing the velocity fields in (m/s) for each indicated flow setting. Scale is used to determine and indicate, using dotted line, location of three samples. (e) Indicates wall shear stress across surface.

7.4 Experimental Methodology

Corrosion rates were measured in the thin channel flow cell (TCFC) using electrochemical methods and mass gain measurements were taken at the end of 20 hours to determine the precipitation rate similar to the weight change method discussed in Chapter 6.2. The following section covers the experimental set-up of the flow cell.

7.4.1 Solution Preparation

Initially, a solution of 1 litre of distilled water and 3.5 wt% sodium chloride (NaCl) was heated to a temperature of 80°C. CO₂ was bubbled into the solution for at least 4 hours prior to the experiment and throughout the duration of the experiment ensuring the solution was completely saturated with CO₂. The experiment was conducted at atmospheric pressure. The temperature of the solution was maintained at 80°C using a hotplate with an integrated stainless steel temperature sensor that was immersed into the 1 litre beaker. The pH of the test solution is set to a pH of 6.8 through the addition of sodium hydrogen bicarbonate (NaHCO₃) and is tested using a pH probe. Finally, the solution was continually/ evenly mixed throughout the test within the beaker using a magnetic stirrer rotating at 200 rpm controlled by the hotplate.

7.4.2 Sample Preparation

Prior to the start of the experiment, three test samples were wet ground up to 600 silicon grit paper, degreased with acetone, rinsed with distilled water and dried with compressed air. The samples were then fitted into a cable gland using epoxy resin and then screwed into the acetyl base of the flow cell shown in Figure 7.4

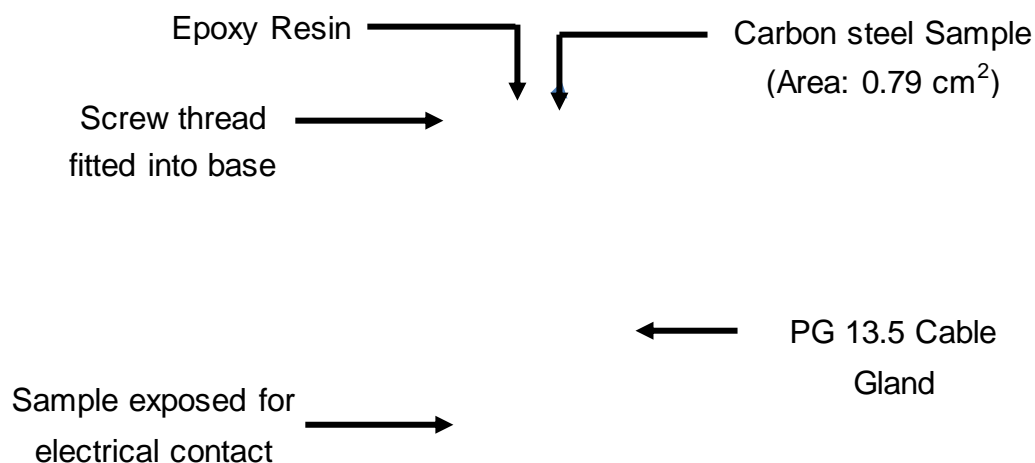




Figure 7.4 Test sample fitted into cable gland and screwed into flow cell base.

A part of the sample is left protruding uncovered with resin for electrical contact for electrochemical measurements. The cylindrical samples used within the flow cell are 1 cm in diameter with an exposed surface area of 0.79 cm^2 . The carbon steel samples are of the same chemical composition as that used in the experiments conducted in the glass cell and is shown in **Erreur ! Source du renvoi introuvable..**

7.4.3 Laboratory Flow Loop Set-Up

The full TCFC system is shown in Figure 7.5. When the solution was deemed ready, the CO_2 saturated water is pumped into the test section/ flow cell and then back into the beaker in a recirculating closed flow loop and corrosion measurements were initiated. The pump used is a centrifugal micro pump and was controlled using a magnetic drive gear micro-pump (Ismatec Series GJ-N23) capable of flow rates 250 to 3200 ml/min.

7.4.4 In-Situ Electrochemical Measurements

The electrochemical set-up used for the flow cell design is a standard three-electrode cell which is commonly used for corrosion studies. The working electrode is the X65 grade carbon steel sample and an Ag/AgCl redox electrode is used as the reference/ counter electrode which is positioned directly downstream from each sample as shown in Figure 7.5. Electrochemical measurements were carried out using an ACM potentiostat, in order to determine the corrosion rate of each X65 carbon steel working electrode. Linear polarisation resistance (LPR) measurements were performed by polarising the sample $\pm 10 \text{ mV}$ vs. OCP at a scan rate of 0.10 mV/s to obtain a polarisation resistance measurement (R_p). LPR measurements were undertaken every 10 minutes, allowing the sample to remain at OCP between each reading. Tafel polarisation measurements

were completed by performing anodic and cathodic sweeps $\pm 250\text{mV}$ vs. OCP at a scan rate of 0.20 mV/s . Anodic and cathodic Tafel constants were obtained from the Tafel plots allowing the true Stern-Geary coefficient to be calculated. Once the Stern-Geary coefficient was established, it can then be used in combination with Faraday's Law and the measured values of R_p to estimate the true general corrosion rate of the system. AC impedance measurements were performed before the test to determine the solution resistance. The data obtained was used to compensate for solution resistance in the system when determining the corrosion rates using the LPR method.

7.4.5 Post-Experimental Analysis

At the end of each experiment, the sample was cracked out of the resin and cable gland and was rinsed with ethanol, distilled water and then dried with compressed air. Mass measurements were carried out similar to that conducted in the static tests. The sample weight was measured determining the mass of the sample with the FeCO_3 film formed. The scale was removed using Clarke's solution and a final mass measurement was taken. SEM images and XRD analysis was also carried out on the surface of the samples.

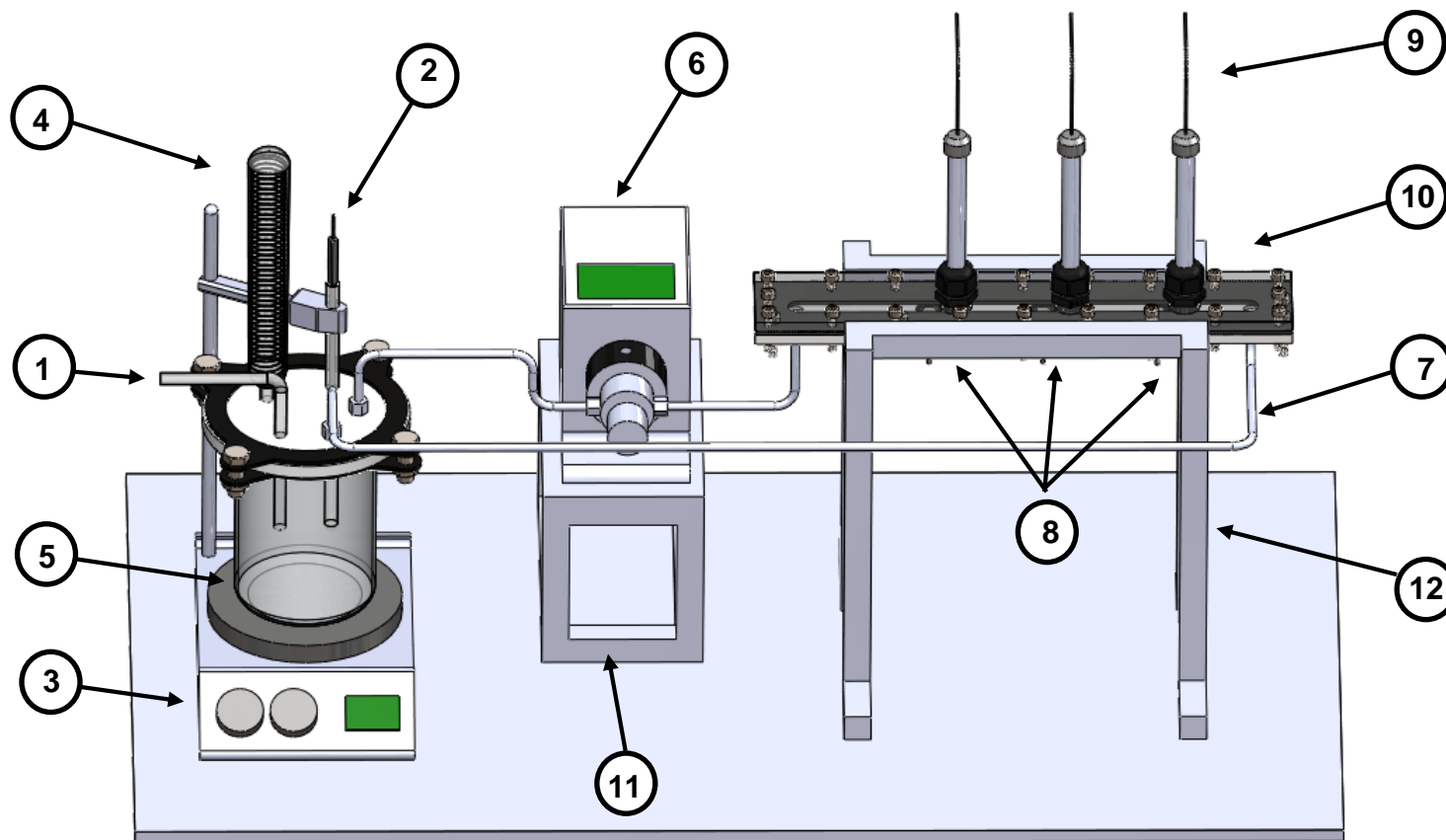


Figure 7.5 Labelled 3D CAD drawing of laboratory flow loop set-up. 1) CO₂ feed. 2) Temperature probe. 3) Hot plate. 4) Condenser. 5) Glass beaker. 6) Pump. 7) Tubing. 8) X65 Carbon Steel Samples. 9) Reference/ counter electrode. 10) Flow cell. 11) Pump stand. 12) Flow cell

Chapter 8

Static Experimental Results

The following chapter comprises the reporting of results and analysis of the results obtained from experiments conducted in a glass cell. The experimental work was divided into three different stages, shown in Figure 6.1 and will be individually presented in the following sub sections. In all cases, the experiments were repeated and error bars were included to express the sensitivity of the results. The data points plotted in the figures representing experimental data show the mean value describing the central tendency about which the data points vary. The mean is calculated using the AVERAGE function in Excel. The error bars represent the overall distribution of the data and is determined through the standard error which is the standard deviation of the mean. The standard error is determined by initially calculating the standard deviation of the data using the Excel function STDEV and dividing it by the square root of the number of measurements that make up the mean. The error bars shown represents how accurately the mean represents the true measured value.

8.1 Parametric Analysis of CO₂ Corrosion of Carbon Steel

The effect of varying parameters such as temperature, pH, surface roughness and salinity were tested on the corrosion of X65 carbon steel in a CO₂ saturated environment. Table 8.1 shows an experimental matrix of the tests performed in this stage of the experimental work.

Table 8.1 Experimental matrix

Parameters	Conditions
Material	X65 Carbon Steel
Solution	1 L Distilled water
CO ₂ Partial Pressure (bar)	0.54 bar
Temperature (°C)	40°C, 60°C, 80°C
pH	6.3, 6.8, 7.0
Salinity	1.0, 3.5, 5.0 wt% NaCL
Surface roughness	120, 600, 1200 grit

8.1.1 Effect of Temperature

Initial tests were performed to observe the effect of temperature on CO₂ corrosion. The tests were performed for a solution of 3.5 wt% NaCl dissolved in distilled water at a pH 6.8. The working sample was polished to 600 grit. Figure 8.1 shows the results of the experiments for a temperature of 40°C, 60°C and 80°C. At 40°C and 60°C, there is no significant drop in corrosion rate. It gradually decreases slightly at 60°C and the drop in the corrosion rate at the end of 20 hours is only 0.2 mm/ year. At 40°C, the corrosion rate remains at more or less the same. However, at 80°C, the curves initially shows the corrosion rate to increase. Once it has reached its peak, the corrosion rate starts to drop relatively quickly before stabilising at a significantly lower corrosion rate. The kinetics are observed to be faster for a higher temperature and the drop in corrosion rate by 1.6 mm/ year is due to iron carbonate film formation on the surface of the sample blocking the active corrosive sites. The initial increase in the corrosion rate observed at a high temperature of 80°C may be due to the increase in surface area of the exposed the Fe₃C layer. FeCO₃ crystals may have precipitated at 40°C and 60°C, however the film is not protective.

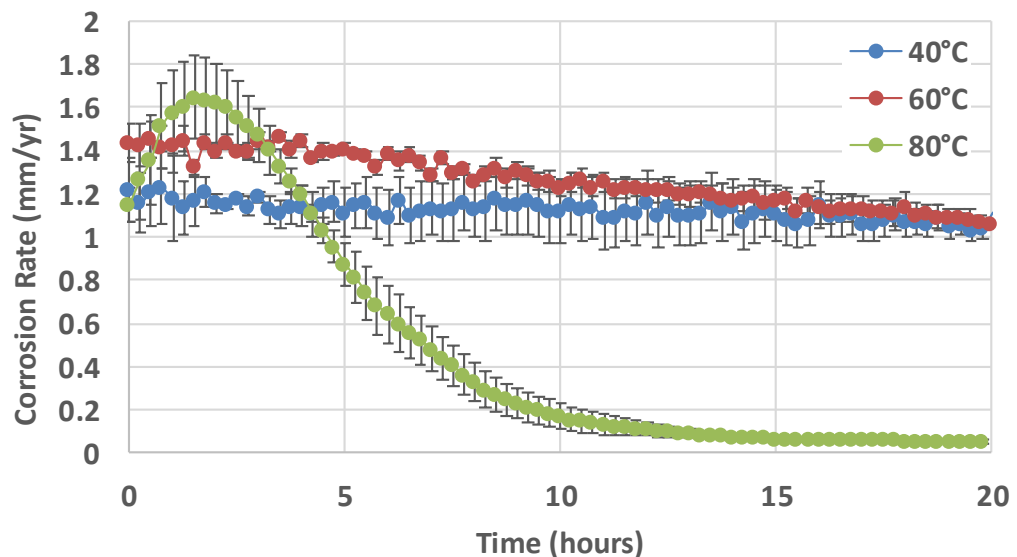


Figure 8.1 Effect of temperature on CO₂ corrosion of X65 carbon steel. (Working Conditions: 3.5 wt% NaCl, pH 6.8, 0.54 pCO₂, 600 grit).

8.1.2 Effect of Salinity

The second parameter tested is the effect of salinity on the CO₂ corrosion rate. The tests were performed for a 1 litre solution heated to 80°C and set to a pH 6.8. The working sample was similarly polished to 600 grit. Figure

8.2 shows the results of the experiments for a 1, 3.5 and 5.0 weight % of NaCl.

NaCl is added into the solution during experimental analysis as it increases the conductivity of the solution. In literature, most CO₂ research is done at lower salt concentrations typically from 1wt% to 3wt% NaCl and no significant effects of salt concentration on general CO₂ corrosion has been observed in this range [77]. Fang et al. [95] tested the effect of high salt concentrations on CO₂ corrosion with salt concentrations up to 25 wt%, close to the solubility limit. The corrosion rate of carbon steel was found to be significantly affected by the high content of salt and was observed to decrease with increasing salt concentration. This occurs as increasing the salt concentration increases the solution resistance, reducing the solubility of CO₂ and is found to retard the cathodic reaction, the anodic reaction and the limiting current [95, 96]. However, the experiments were conducted for salt concentrations greater than 15 wt%.

In the following work, as shown in Figure 8.2, the effect of salinity is shown to not have a significant effect on the corrosion rate at salt concentrations of 1.0wt% and 3.5wt % and the corrosion rate is observed to follow a similar trend over 20 hours.

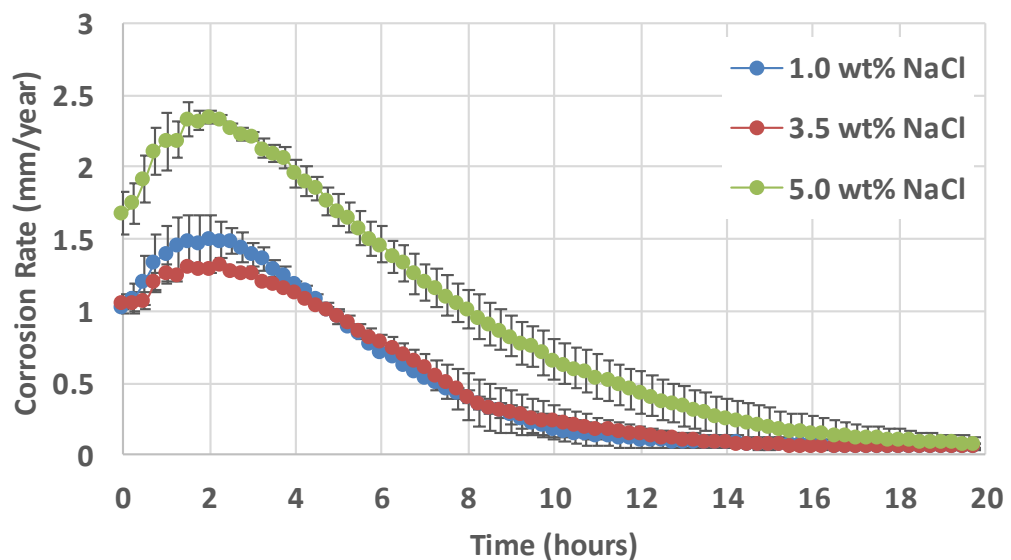


Figure 8.2 Effect of salinity on CO₂ corrosion of X65 carbon steel. (Working Conditions: 80°C, pH 6.8, 0.54 pCO₂, 600 grit)

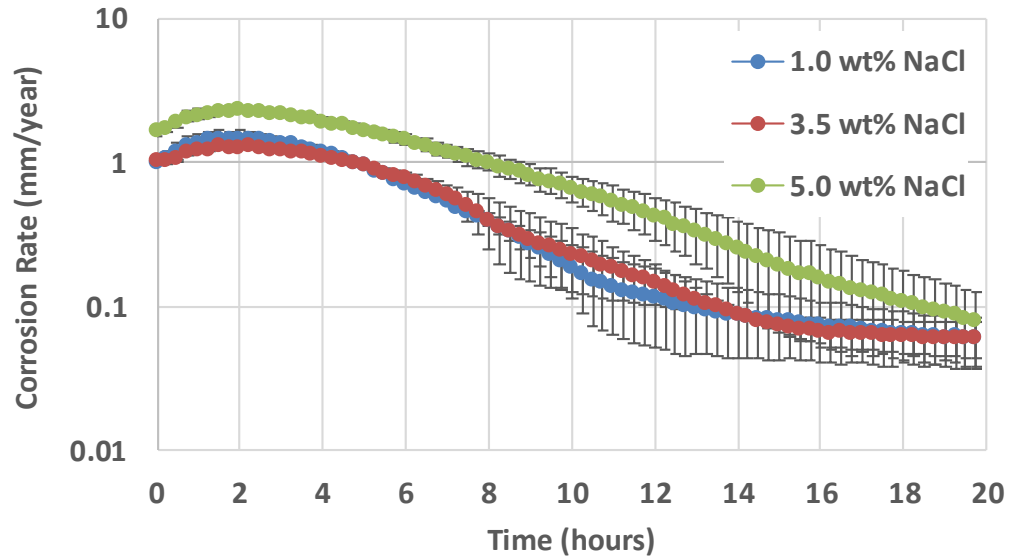


Figure 8.3 Effect of salinity on CO₂ corrosion of X65 carbon steel, logarithmic plot. (Working Conditions: 80°C, pH 6.8, 0.54 pCO₂, 600 grit)

For a higher salt concentration of 5.0 wt%, a higher initial corrosion rate is observed. However, the rate of decrease in the corrosion rate over time is observed to be similar to that of the lower salt concentrations. Figure 8.3 shows the corrosion rates on a logarithmic scale. The figure shows a more clear identification of the corrosion rate at the end of the test which indicates the level of protectiveness of the FeCO₃ film formed in each condition. The relative protectiveness of the film is similar for the different salt concentrations tested at the end of 20 hours with an average corrosion rate of approximately 0.05 mm per year.

8.1.3 Effect of Surface Roughness

There is limited literature focussing on the effect of surface roughness on CO₂ corrosion. A substantial layer of metal is removed upon polishing the test samples and manually polishing leaves room for metallic surface variations which can affect the corrosion rate measurement. Work done by Asma et al. [97] tests the effect of surface finish on corrosion of carbon steel in a CO₂ environment. Their results have shown that the corrosion rate for a rough surface is found to be higher than a smooth surface by increasing the surface area which involves the distribution of electrochemical reaction. However, this work has been done at room temperature, pH 5.5, 3.0 wt% NaCl and for carbon steel BS970. FeCO₃ film precipitation has not been found to occur in these conditions and the effect of surface roughness on film formation has not been found in literature.

In the following study, surface roughness on the CO₂ corrosion rate was tested for a 3.5 wt% NaCl, 1 litre solution heated to 80°C and set to a pH of 6.8. The working samples were polished using SiC paper to 120, 600 and 1200 grit. Figure 8.4 shows the results from the experiments carried out.

The figure shows a higher initial corrosion rate for a rougher surface, polished to 120 grit, agreeing with Asma et al. [97]. The corrosion rate then steadily decreases over time and remains somewhat constant after approximately 13 hours. The corrosion rate for a more finely polished sample at 600 grit is observed to be lower at all-time instances. The corrosion rate decreases at approximately the same rate and settles after approximately 16 hours. The lowest corrosion rate, hence the most protective film, occurs under these conditions over 20 hours. For a sample polished to 1200 grit, the corrosion rate is observed to drop at a much slower rate. The corrosion rate is similar to that of a 120 grit polished surface after 20 hours however, it has not yet steadied out and may continue to drop.

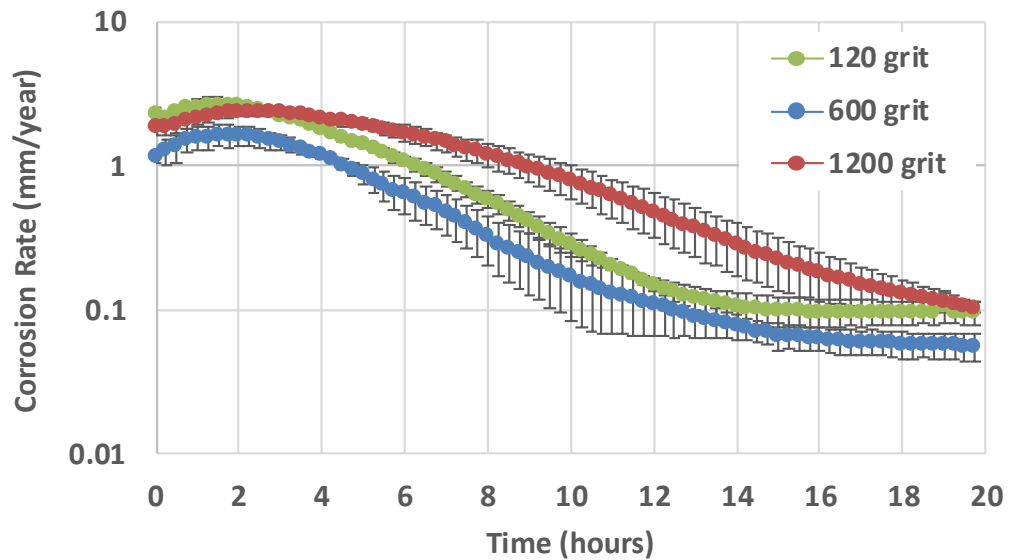


Figure 8.4 Effect of surface roughness on CO₂ corrosion of X65 carbon steel, logarithmic plot. (Working Conditions: 80°C, pH 6.8, 0.54 pCO₂, 3.5 wt% NaCl)

8.1.4 Effect of pH

The final parameter analysed is the effect of pH on the CO₂ corrosion of carbon steel. The test conditions are 3.5 wt% NaCl, 1 litre solution heated to 80°C and the working sample polished to 600 grit. The corrosion rate was observed for a pH of 6.3, 6.8 and 7.0.

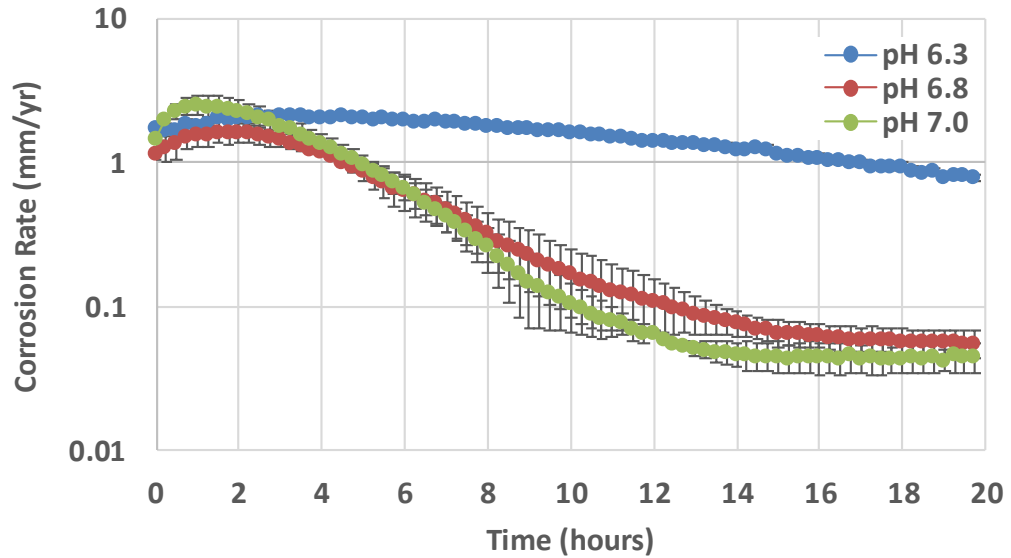


Figure 8.5 Effect of pH on CO₂ corrosion of X65 carbon steel, logarithmic plot. (Working Conditions: 80°C, 0.54 pCO₂, 3.5 wt% NaCl, 600 grit)

Figure 8.5 shows that at a pH of 6.3, there is no significant decrease in the corrosion rate over 20 hours. However, an increase in the pH for the same conditions results in a significant drop in corrosion rate and much lower corrosion rate. A similar trend is observed for both pH 6.8 and pH 7.0. The corrosion rate is observed to decrease over time due to formation of a protective FeCO₃ film. At pH 7.0, results do show faster kinetics of film formation with a slightly lower corrosion rate after 20 hours.

SEM images were taken of each sample at the end of the 20 hour period to identify the characteristics of the film formed in respect to size, surface coverage, distribution, etc. Multiple images were taken across the sample to attain an overall perspective. However, in some aspects, there are areas of the surface where a higher surface coverage, density of crystal formation is found in comparison to other areas. This non-uniformity of the film formed may be due to differences in the surface finish across the sample, different local conditions at locations of the sample due to differences in solution composition in a static cell. There may be many possible reasons for the varying conditions.

Figure 8.6 shows select images that best represent the surface of the sample at these conditions. The images are taken at $\times 1000$ magnification and represents approximately $175 \times 175 \mu\text{m}^2$ area of the sample surface. SEM surface analysis software offers the capability to annotate the image with the approximate size of the crystals. The figure shows that the crystals are much larger in size for a pH 6.3 and more discrete whereas for both pH

6.8 and pH 7, the crystal are much smaller, compact and dense which tend to favour a more protective film.

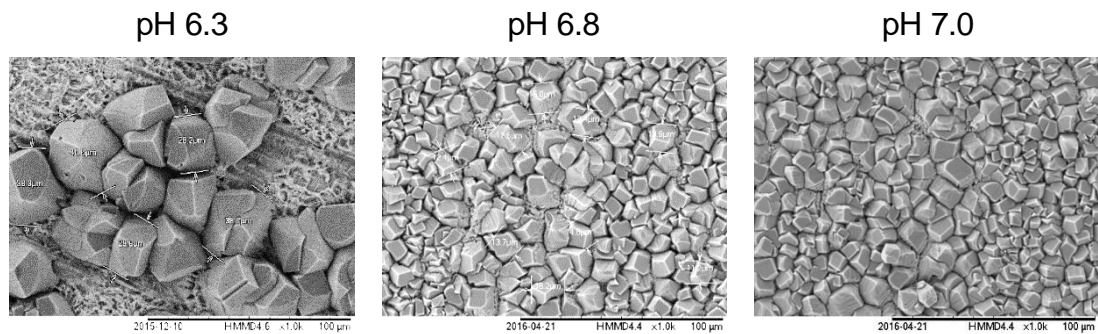


Figure 8.6 SEM Imaging of X65 carbon steel surface at varying pH. (Working Conditions: 80°C, 0.54 pCO₂, 3.5 wt% NaCl, 600 grit)

In static cell experiments, there are many variables that can affect the corrosion rate and the nature of the film formed. The effect of some of these parameters are well-known in literature whereas for others the understanding is limited. The results of this section focused on the analysis of four parameters that were believed to have an instrumental effect. The experiments were repeated and error bars were included to express the sensitivity of the results.

8.2 Nucleation and Growth of FeCO₃ over Time

In the previous section, the effect of pH on the corrosion rate and FeCO₃ film formation was analysed in a static CO₂ environment. Results showed that nucleation and growth of FeCO₃ crystals occurred at both pH 6.3 and pH 6.8 within 20 hours however the protectiveness of the film varied significantly. In the following stage, experiments are carried out to:

- Investigate the main contributing factor to the significant change in protectivity of the film for a minor change in pH through mass gain and mass loss measurements at different time intervals.
- Analytically determine the precipitation rate and corrosion rate over time from the observed mass gain and mass loss results.
- Compare the corrosion rate results from both techniques, LPR and weight change method.
- Determine a relationship between the precipitation rate and the bulk saturation ratio (SR) determined through spectroscopy.

- Correlate the results with scanned electron microscopy (SEM) images at the end of each time interval to support the observed trends.

The static cell was set-up for working conditions; 80°C, 3.5 wt% NaCl, 1 L CO₂ saturated solution of CO₂ partial pressure 0.54 bar. X65 carbon steel samples of 25 mm diameter were polished to 600 grit. Multiple experiments were carried out for variable time periods of 2, 5, 10, 15 and 20 hours for a pH of 6.3 and 6.8. The weight change of each sample was determined at the end of each time period and a sample of the solution was taken for Fe²⁺ ion measurement. The detailed experimental procedure was discussed in the chapter. The experiments were repeated to ensure reliability and the accuracy of the results. Error bars are displayed on the graphs to show the variability of data and indicate the error, or uncertainty in the measurements.

8.2.1 Quantitative Analysis of FeCO₃ Precipitation

Figure 8.7 shows the mass gain for each individual time period due to FeCO₃ precipitation at pH 6.3 and pH 6.8. Results show that the mass gain is higher for a pH of 6.8 at the earlier time periods. However for longer time periods the gap between the mass gain results decreases. The mass gain at pH 6.3 continues to increase and is observed to larger than that at pH 6.8 at the end of 20 hours.

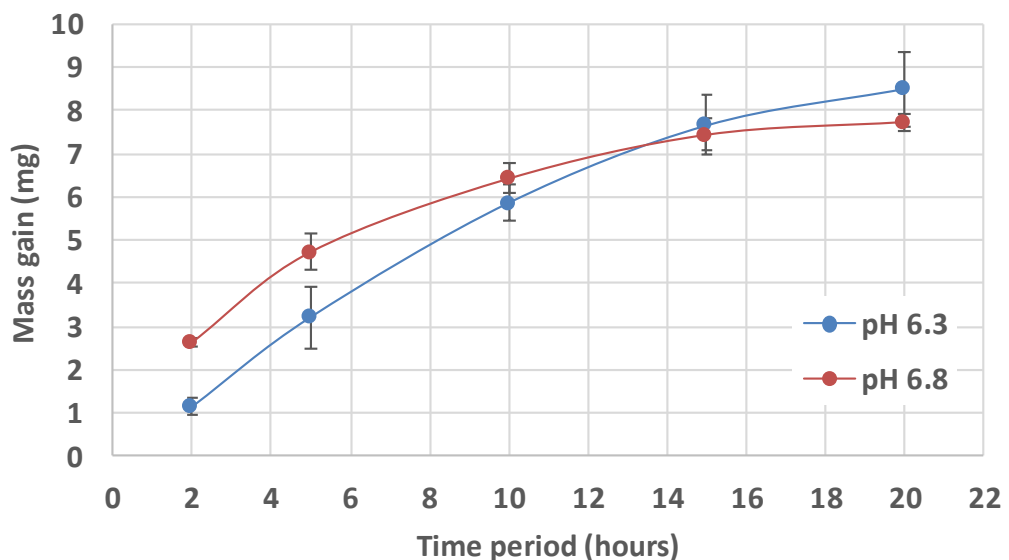


Figure 8.7 Mass gain due to FeCO₃ precipitation at pH 6.3 and pH 6.8 over variable time periods (Working Conditions: 80°C, 0.54 pCO₂, 3.5 wt% NaCl, 600 grit).

In the previous section, we were able to conclude that a significantly more protective FeCO₃ film forms at a pH 6.8 after 20 hours. Therefore, a

quantitative analysis of FeCO_3 film shows that at pH 6.3, after 20 hours, a slightly larger mass gain is observed however for a considerably less protective film.

These results are correlated with SEM images in Figure 8.9, Figure 8.12 and Figure 8.13. At the end of each time period, the nucleation and growth of crystals is more significant for a pH 6.8 with a significantly higher surface coverage being noted over the image square area. However, the average crystal size is seen to be larger at pH 6.3 especially over longer time periods. Correlating the SEM images with the mass gain results indicates that there are many smaller crystals at pH 6.8 versus fewer larger crystals at pH 6.3 providing an explanation for the converging behaviour of the mass gain results.

Figure 8.8 shows the mass loss at the end of each time period due to corrosion at pH 6.3 and pH 6.8. Results show that the mass loss is progressively greater for pH 6.3 in comparison to pH 6.8. This links to a higher degradation of the surface of the sample due to a less protective film being formed over time in comparison to that at pH 6.8.

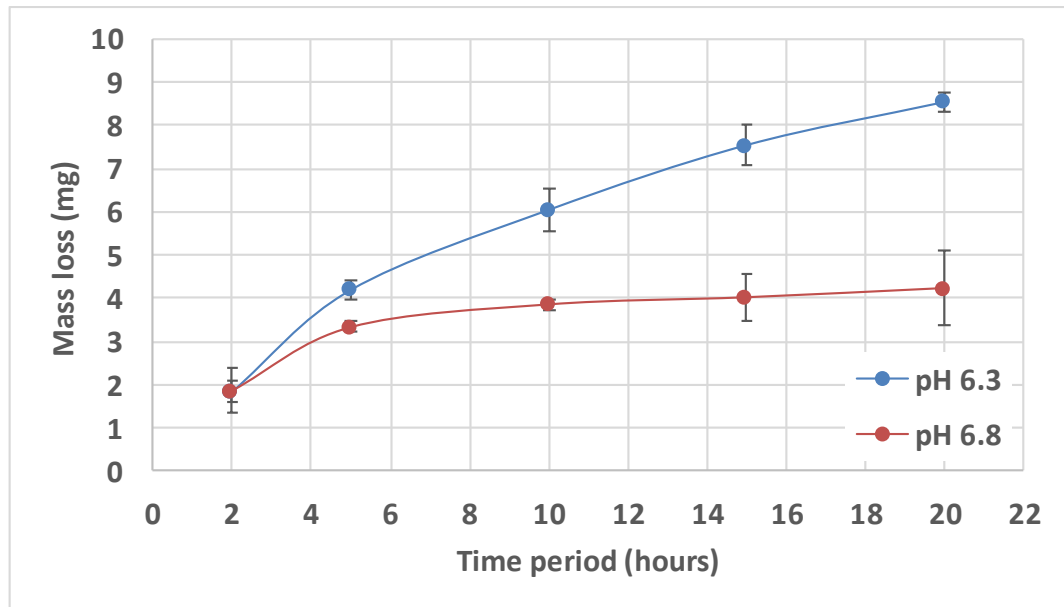
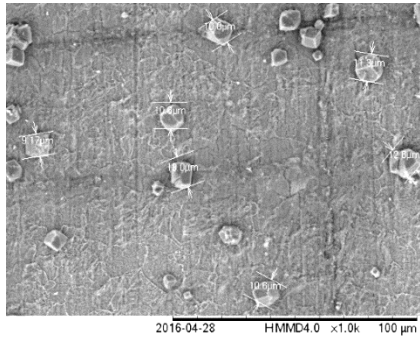


Figure 8.8 Mass loss due to FeCO_3 precipitation at pH 6.3 and pH 6.8 over variable time periods (Working Conditions: 80°C, 0.54 pCO₂, 3.5 wt% NaCl, 600 grit).

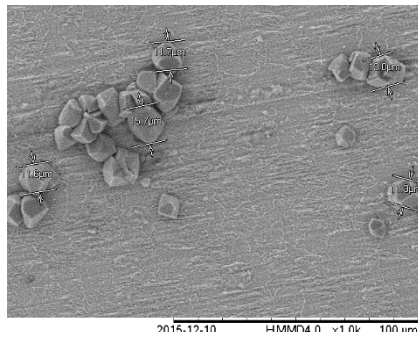
8.2.2 SEM images of Sample Surface

Scanning Electron Microscopy (SEM) was used to observe the surface of the carbon steel sample at the end of each time period and the images were carefully analysed to determine the crystal morphology, crystal size and the

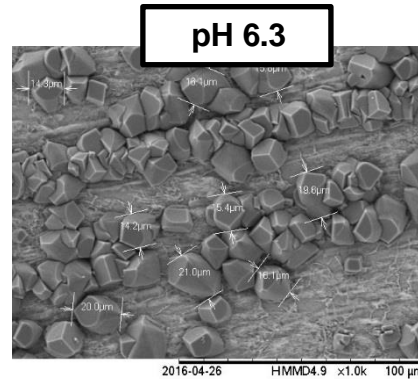
surface coverage. Multiple images were taken across the sample to attain an overall perspective. In Figure 8.9, the surface of the sample is observed for both pH 6.3 and pH 6.8. The figure is annotated to include the average crystal size, mass gain and corrosion rate at the end of each time period. The figure shows the crystals to be more discrete and larger in size at pH 6.3 with crystals as large as 40 μ m being formed after 20 hours. At pH 6.8, the maximum crystal size has been observed to be approximately half the size. The images were taken at the same magnification and the density and compactness of the film formed at pH 6.8 in comparison is clearly observed. Small crystals can be seen to form in tiny spaces and then grow into the surrounding crystals, conjointly working at blocking the surface from further corrosion. Figure 8.10 compares the average crystal size as a function of time for pH 6.3 and pH 6.8. The crystal size was determined using SEM image analysis software to approximately measure the size of each individual crystal.



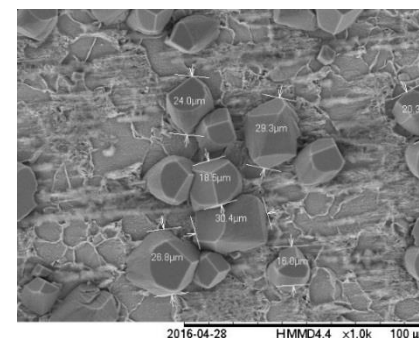
2 HOURS
 Av. Crystal Size: 11.15μm
 Av. Mass Gain: 1.15 mg
 Corrosion Rate: 2.10 mm/yr



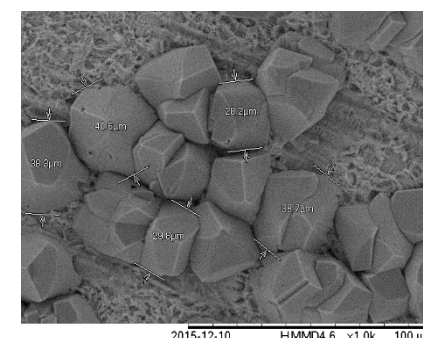
5 HOURS
 Av. Crystal Size: 12.66 μm
 Av. Mass Gain: 3.23 mg
 Corrosion Rate: 1.64 mm/yr



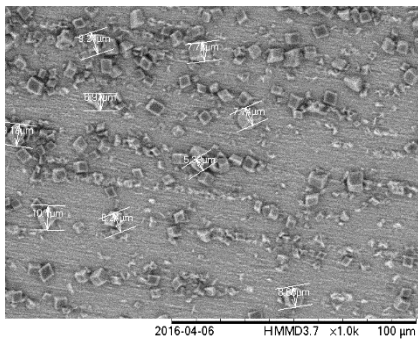
10 HOURS
 Av. Crystal Size: 16.9 μm
 Av. Mass Gain: 5.87 mg
 Corrosion Rate: 0.75 mm/yr



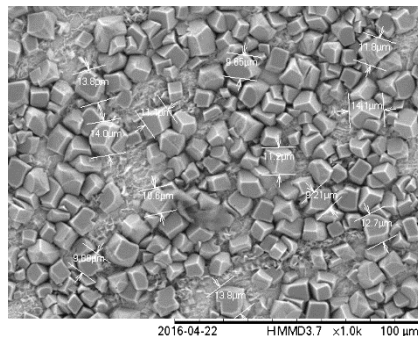
15 HOURS
 Av. Crystal Size: 23.6 μm
 Av. Mass Gain: 7.66 mg
 Corrosion Rate: 0.73 mm/yr



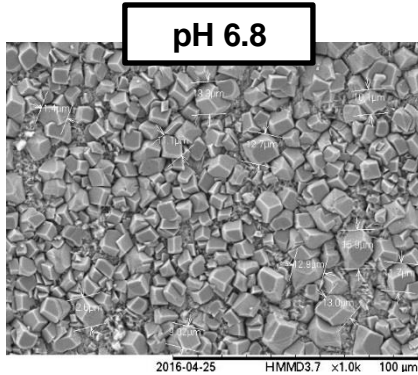
20 HOURS
 Av. Crystal Size: 35.12 μm
 Av. Mass Gain: 8.50 mg
 Corrosion Rate: 0.59 mm/yr



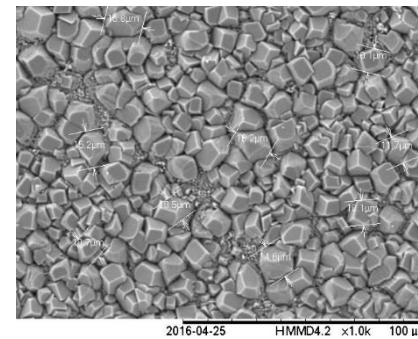
2 HOURS
 Av. Crystal Size: 7.9 μm
 Av. Mass Gain: 2.64 mg
 Corrosion Rate: 2.32 mm/vr



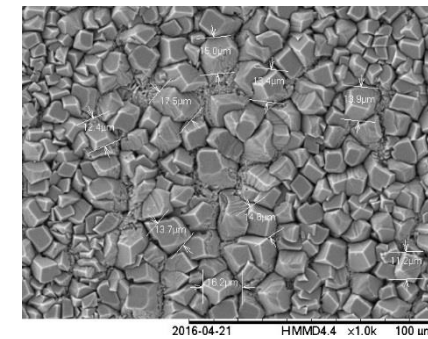
5 HOURS
 Av. Crystal Size: 11.80 μm
 Av. Mass Gain: 4.73 mg
 Corrosion Rate: 0.89 mm/yr



10 HOURS
 Av. Crystal Size: 12.16 μm
 Av. Mass Gain: 6.43 mg
 Corrosion Rate: 0.30 mm/yr



15 HOURS
 Av. Crystal Size: 12.88 μm
 Av. Mass Gain: 7.44 mg
 Corrosion Rate: 0.08 mm/vr



20 HOURS
 Av. Crystal Size: 14.2 μm
 Av. Mass Gain: 7.74 mg
 Corrosion Rate: 0.04 mm/yr

Figure 8.9 SEM images illustrating FeCO₃ crystal formation at different time periods for pH 6.3 and pH 6.8. Images are also annotated to indicate average crystal size, average mass gain and corrosion at these time steps.

An average of the crystal size was determined across the images taken at the end of each time period for a pH of 6.3 and pH 6.8. Results show that the crystal size increases exponentially at pH 6.3 whereas the growth of crystals are more limited at pH 6.8 where only a slight increase in average crystal size is observed over time.

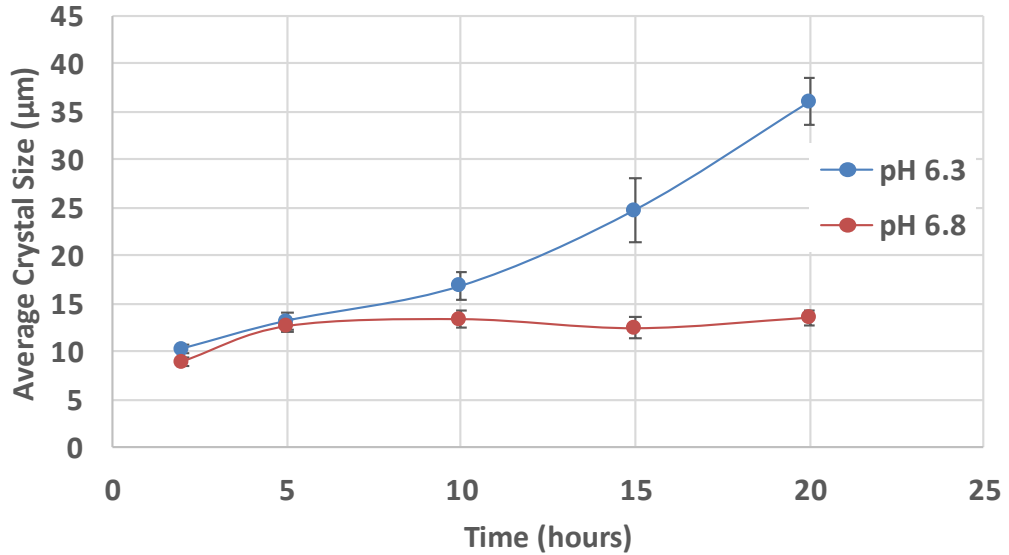


Figure 8.10 Analysis of SEM images over time to determine average crystal size for pH 6.3 and pH 6.8.

The percentage of the carbon steel surface covered with FeCO_3 crystals may provide an indication to the protectiveness of the film. It is obtained through processing multiple random images from across the sample into a MATLAB programme that utilizes the difference in contrast of the crystals formed against the bare steel surface to produce a binary output image. The programme then plots the percentage of black pixels (crystals) against the white pixels (no crystals).

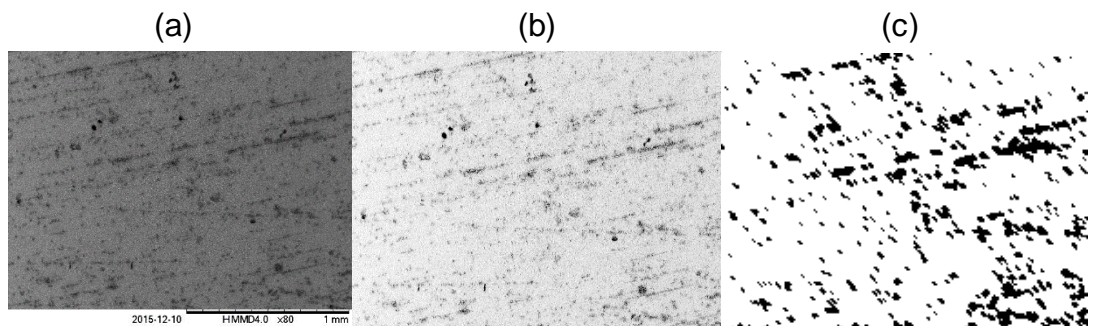


Figure 8.11 Image analysis using MATLAB to determine surface coverage. a) Image as attained from SEM for 80°C, 6.3 pH, 5 hours. b) Image corrected for contrast and brightness. c) Matlab correction into black and white pixels.

Figure 8.11 shows the MATLAB analysis of a SEM image of the surface at pH 6.3 after 5 hours. The image was set to a contrast and brightness factor of +40% and -40% respectively in order to make the crystals more detailed and the image annotation was cropped out. The MATLAB programme analyses the image and produces the binary image shown in Figure 8.11 (c). The surface coverage of the selected image was computed to be approximately 11.86%.

For a pH 6.3, images were taken at a magnification of $\times 80$ in order to obtain the largest overall perspective of the surface as shown in Figure 8.12. Images were taken across the surface, each comprising of an area of 2×2 mm. A similar analysis was performed for a pH 6.8 after each time period and is shown in Figure 8.13. The images under these conditions were taken at a magnification of $\times 100$ as the crystals were too small to be analysed for surface coverage at a lower magnification. It is noted that the crystals at pH 6.3 are observed more clearly at a lower magnification than crystals at pH 6.8 at a higher magnification. This adds to the finding that the crystals at pH 6.3 are significantly larger in size than at pH 6.8.

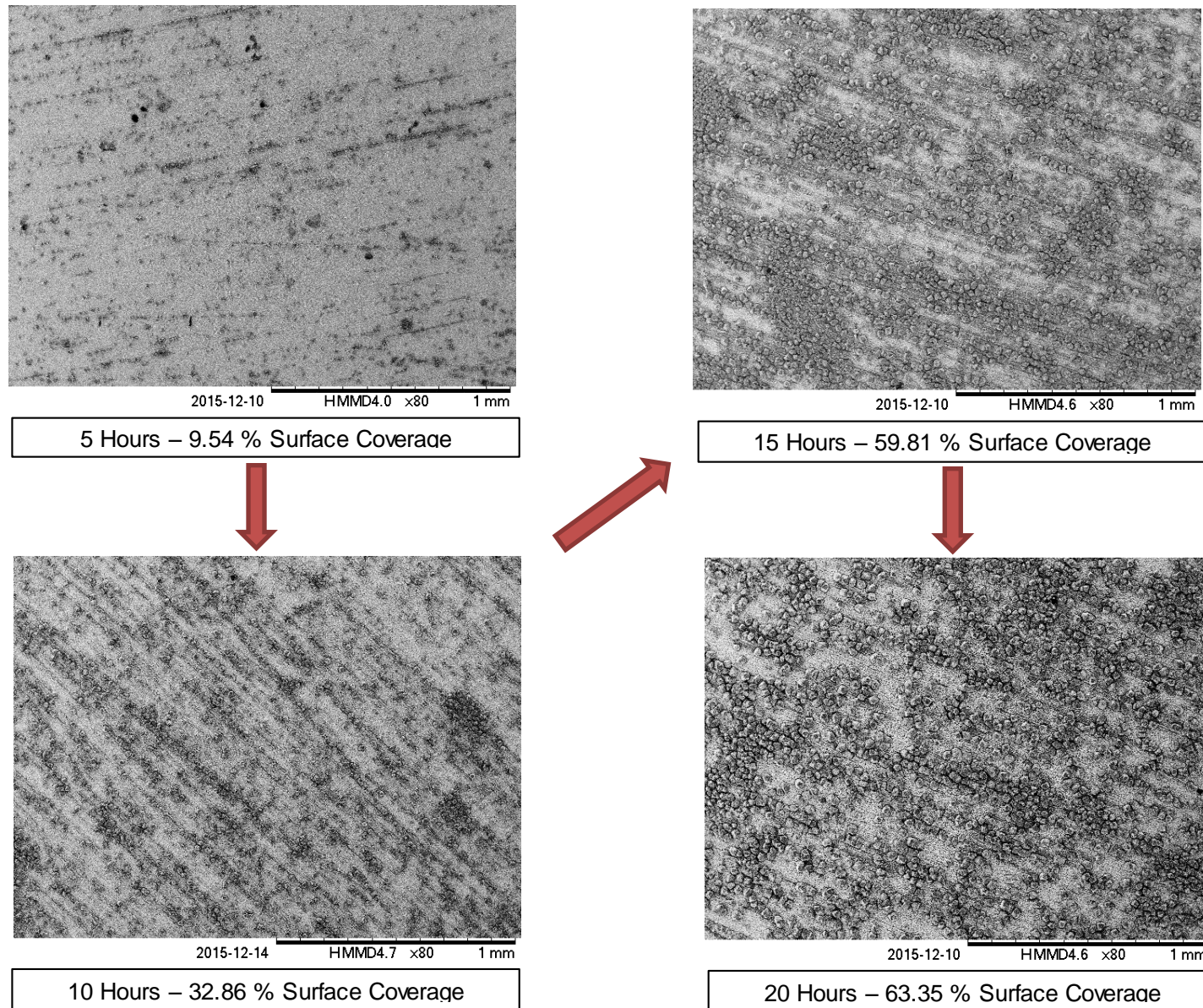


Figure 8.12 SEM images illustrating FeCO_3 crystal formation at different time periods for pH 6.3. Images are also annotated to indicate surface coverage at these time steps.

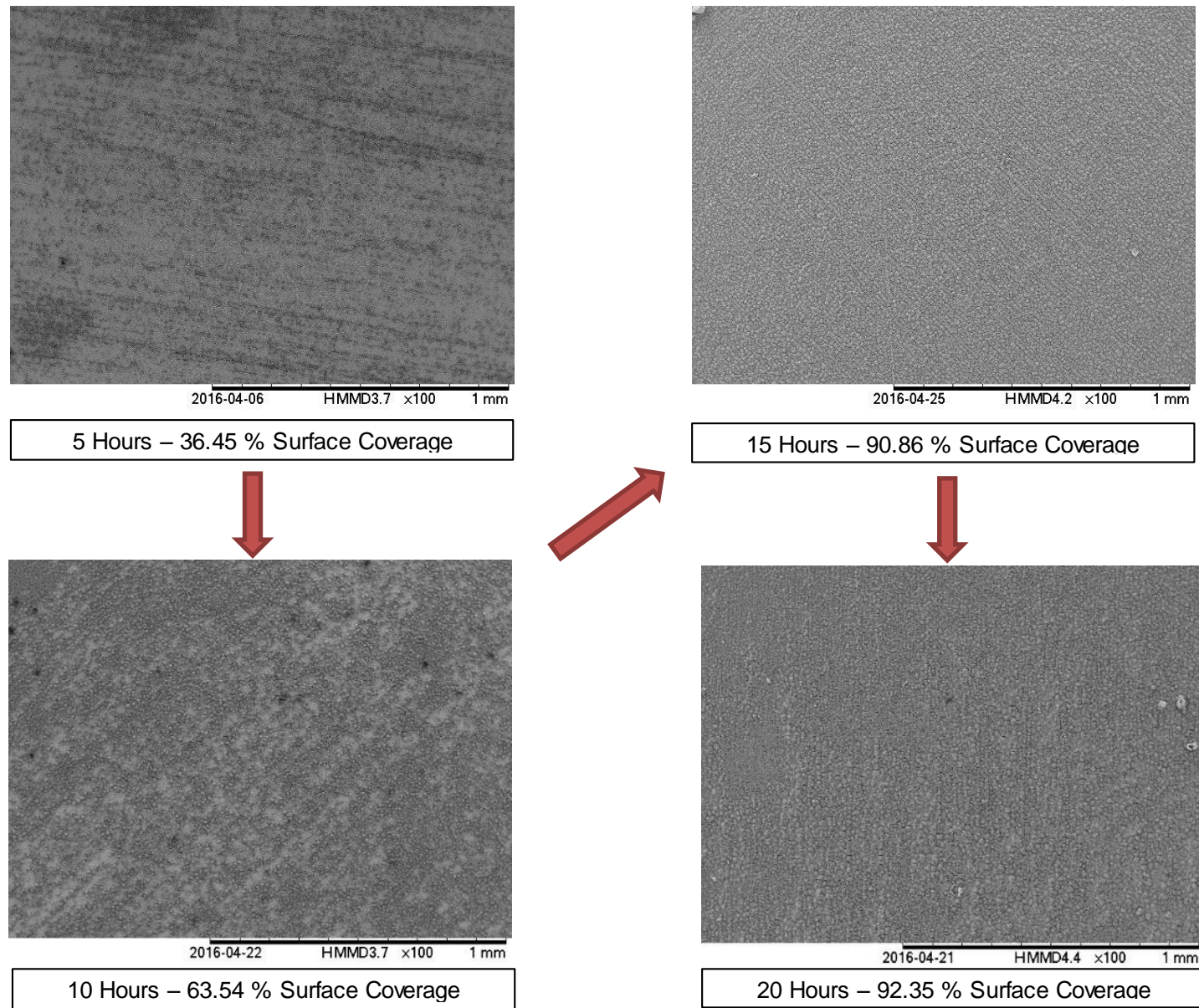


Figure 8.13 SEM images illustrating FeCO_3 crystal formation at different time periods for pH 6.8. Images are also annotated to indicate surface coverage at these time steps.

Figure 8.14 compares the percentage surface coverage over time for pH 6.3 and pH 6.8. The trend is observed to be very similar for pH 6.3 and pH 6.8 with it steadily increasing over time over 15 hours and then considerably slowing down there after. The surface coverage at pH 6.8 is found to be much higher at the end of each time period in comparison to at pH 6.3, as is expected, with a surface coverage of approximately 92% after 20 hours and approximately 63% for a pH 6.3.

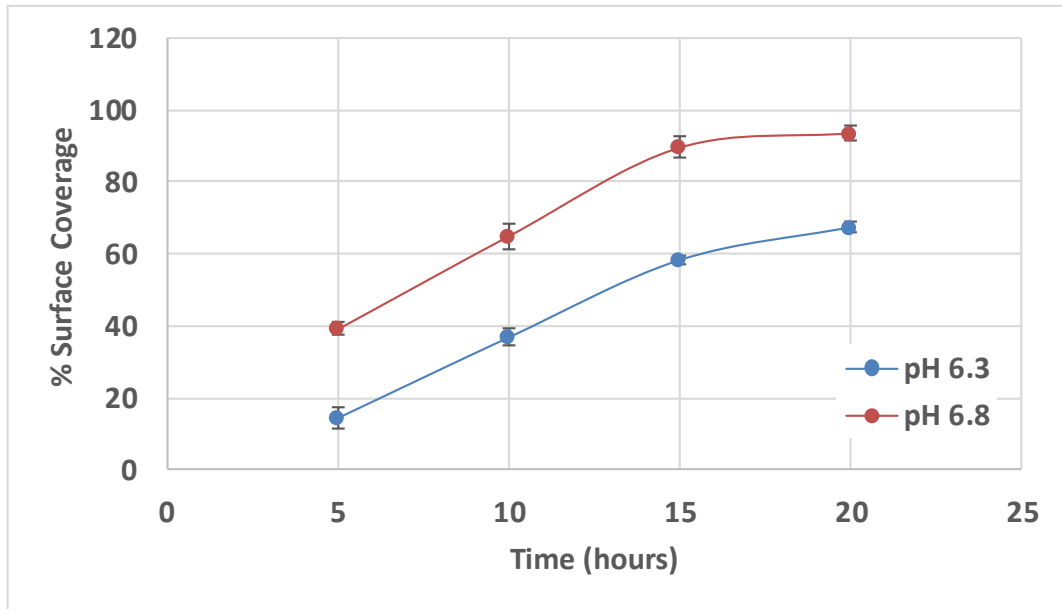


Figure 8.14 Analysis of SEM images over time to determine average surface coverage for pH 6.3 and pH 6.8.

It is noted that the developed MATLAB model is limited in determining the surface coverage at the end of time periods where there is no clear visual contrast between the FeCO_3 crystals and the remaining surface such as the SEM image after 20 hours at pH 6.8. At this stage, the image represents a close to full surface coverage. The model is more accurate in determining the surface coverage for earlier time periods.

8.2.3 Corrosion Rate Analysis

The corrosion rate over time is analytically calculated from the mass loss measurements at the end of each time period. Equation 6.8, in Chapter 6.2, provides the corrosion rate at the end of each time period assuming it is constant over the total time period. However, altering the equation for a change in mass loss over time, from one period to the next, allows for a more accurate tracking of corrosion rate over time as shown in Equation (8.1).

$$CR\left(\frac{mm}{yr}\right) = \frac{ML_{t_2}(g) - ML_{t_1}(g)}{MW_{Fe} \left(\frac{g}{mol}\right) \times t (hr) \times S (m^2)} \times \frac{365 \left(\frac{days}{yr}\right) \times 24 \left(\frac{hrs}{day}\right) \times MW_{Fe} \left(\frac{g}{mol}\right)}{\rho \left(\frac{kg}{m^3}\right)} \quad (8.1)$$

Where CR is the corrosion rate (mm/year), $ML_{t_2}-ML_{t_1}$ is the change in mass loss from one time interval to the next (g), MW_{Fe} is the molecular weight of iron (g/mol), t is the time interval in between measurements (hours), S is the exposed sample area (m^2) and ρ is the density of the sample (kg/m^3).

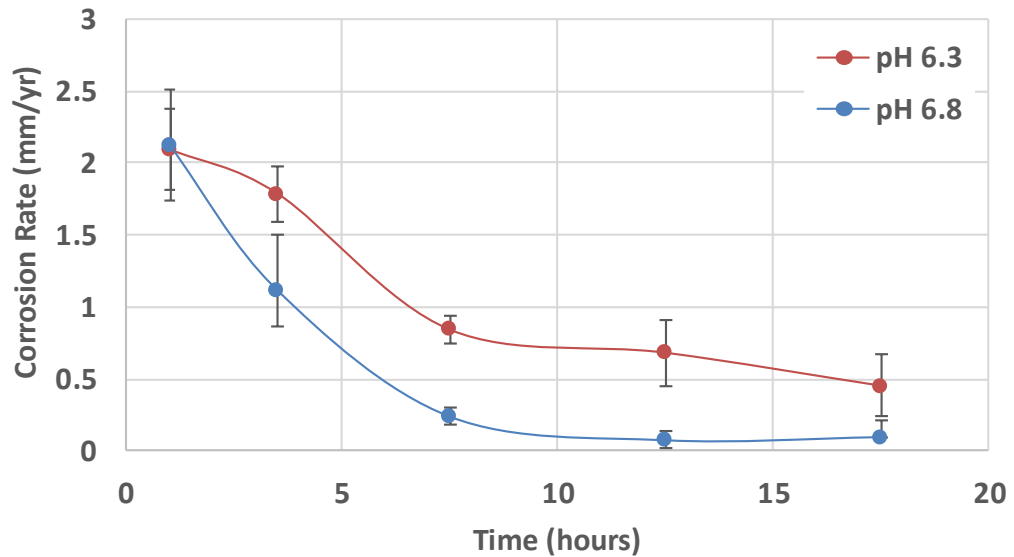


Figure 8.15 Corrosion rate (mm/year) calculated over time from mass loss measurements.

Figure 8.15 shows the corrosion rate results over time for pH 6.3 and pH 6.8. The results show that there is a more significant drop in the corrosion rate for a pH of 6.8. After a time period of approximately 10 hours, however, the rate in the drop of the corrosion rate is observed to significantly slow down and almost remains constant thereafter. For a pH 6.3, the corrosion rate is observed to steadily decrease over time with the rate slowing down after 8 hours. The observed trend may be compared with the LPR measurement results in Figure 8.5 and is found to be similar with the corrosion rate for a pH of 6.3 being higher at each time instant. The difference between the corrosion rate values may be attributed to the Stern-Geary coefficient, B . The Stern-Geary coefficient used in the LPR measurements was assumed to be 26 mV/decade. Referring back to Chapter 6.1.3, Stern et al. [81] described β_a and β_c as a function of temperature. For 80°C, β_a and β_c can be calculated to be 46.7 mV/decade and 140mV/decade respectively therefore

resulting in a Stern-Geary coefficient of 15.2 mV/decade. Correcting the LPR measurement for the new Stern-Geary coefficient provides a better comparison as shown in Figure 8.16.

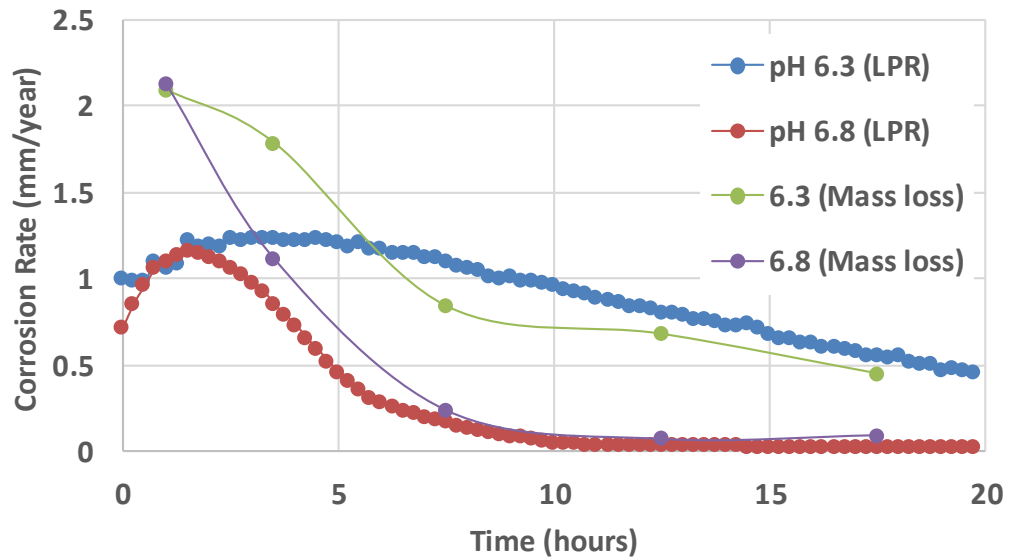


Figure 8.16. Comparison of weight loss measurements with corrected LPR measurements for pH 6.3 and pH 6.8.

However, there is a discrepancy in the data mainly at the initial time periods where the corrosion rate attained through the mass loss measurements being much higher for both pH of 6.3 and 6.8. After approximately 7.5 hours, the results are seen to match more closely.

The possible reason for the difference in the corrosion rate results from mass loss and LPR measurements is that as the sample surface corrodes, the surface area and surface roughness increases due to the surface profile of the Fe_3C layer. Mass loss is a direct measurement due to the corrosion at the surface. However, LPR measurements do not take into account the changing surface area. This may be the reason for the significantly higher corrosion rate determined from the mass loss measurements at the initial time periods. Furthermore, correcting the LPR measurements for a Stern-Geary coefficient, B based on mass loss measurements at the end of the 20 hour period or equations by Stern et al. [81] for the entire set of measurements may be considered inaccurate as the B parameter varies over time as surface conditions, microstructure change therefore as observed from the comparison in Figure 8.16, a different Stern-Geary coefficient for the initial time periods may be more viable.

8.2.4 Precipitation Rate and Bulk Saturation Ratio Analysis

The precipitation rate is calculated from the mass gain measurements according to Equation (8.2).

$$PR\left(\frac{\text{mol}}{\text{m}^2\text{s}}\right) = \frac{MG_{t_2}(g) - MG_{t_1}(g)}{MW_{\text{FeCO}_3} \left(\frac{\text{g}}{\text{mol}}\right) \times t (\text{hr}) \times S (\text{m}^2) \times 3600 \left(\frac{\text{s}}{\text{hr}}\right)} \quad (8.2)$$

Where PR is the precipitation rate ($\text{mol}/\text{m}^2\text{s}$), $MG_{t_2}-MG_{t_1}$ is the change in mass gain from one time interval to the next (g), MW_{FeCO_3} is the molecular weight of iron carbonate, t is the time interval in between measurements (hours) and S is the exposed sample area (m^2).

Figure 8.17 shows the calculated precipitation rate over time for pH 6.3 and pH 6.8. The theory behind the calculation is similar to that used to determine the corrosion rate and can be explained as follows. The mass gain was experimentally determined for a time period of 2 hours and 5 hours. Therefore the change in mass between that time period of 3 hours is the difference of the mass gain. Equation (8.2) provides an estimated precipitation rate over the time from 2 to 5 hours. The resulting numerical value is plotted for 3.5 hours and error bars are used to show the approximate time span of this precipitation rate. This method was subsequently applied for the remaining time periods.

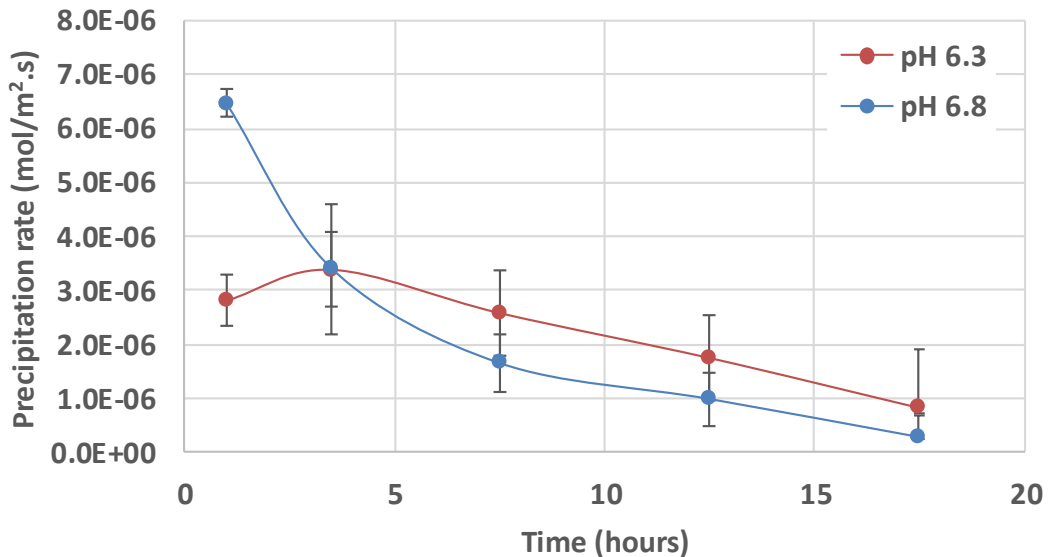


Figure 8.17 Precipitation rate ($\text{mol}/\text{m}^2\text{s}$) calculated over time from mass gain measurements.

Results show that at pH 6.8, the precipitation rate is at its highest over the initial time period and then gradually decreases. In comparison, at pH 6.3, the precipitation is significantly lower, less than half, at the initial time period.

The precipitation rate is seen to increase and overlap with the precipitation rate at pH 6.8 over the time period of 2 to 5 hours. It then steadily decreases but remains higher than that at pH 6.8. This is due to the higher change in mass gain over time observed at pH 6.3 as the crystal size progressively grows in comparison to pH 6.8. The higher change in mass gain directly corresponds to the higher precipitation rate observed over time.

In literature, precipitation rate is commonly linked with the bulk saturation ratio (SR) as shown in the precipitation models reviewed in Chapter 5. Experimentally determining surface chemistry is very difficult and a method has yet to be determined. Therefore, most of the physical phenomena observed in literature have been linked to the bulk properties and in the following work, the Fe^{2+} ion concentration and subsequently bulk saturation ratio is determined through analysing a sample of the solution using spectroscopy.

Figure 8.18 shows that for pH 6.8, the bulk SR is observed to follow the same trend as the precipitation rate at initial time periods. Results suggest that a higher bulk SR gives more precipitation. However, for a pH of 6.3, a different correlation is observed as the bulk SR increases over time. Furthermore, after 7.5 hours, the bulk SR at both pH remains approximately constant with time while the precipitation continues to drop in a linear fashion.

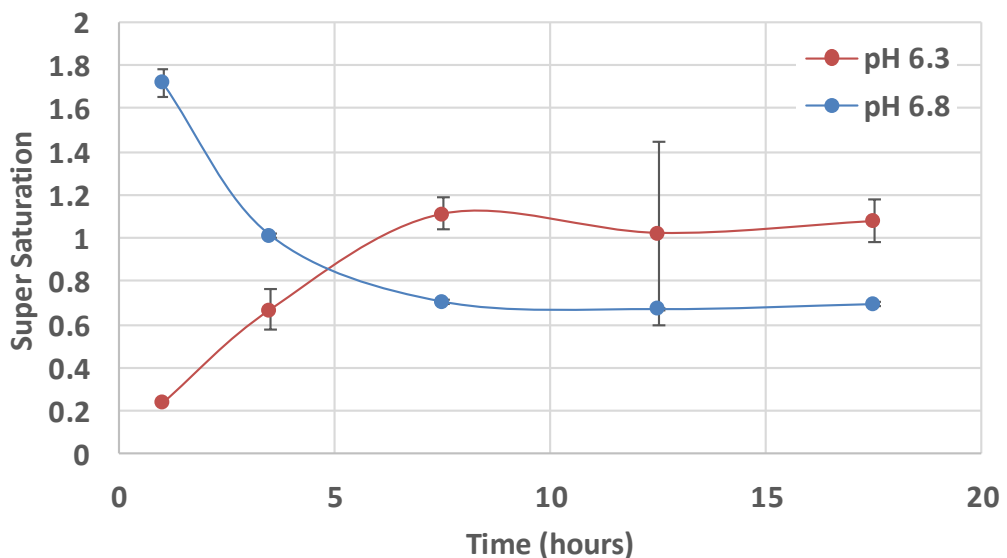


Figure 8.18 Bulk saturation ratio over time determined through spectroscopy for pH 6.3 and pH 6.8.

Reverting back to its calculation, Figure 8.19 shows that at pH 6.8, the bulk Fe^{2+} ion concentration is approximately only 0.1 ppm and a small decrease

in the concentration results in a more significant change in the calculated SR as shown in Figure 8.18. At pH 6.3, the Fe^{2+} ion concentration increases with time and then remains approximately the same after 7.5 hours. The results indicate that at pH 6.3, there is more diffusion of Fe^{2+} ions to the bulk in comparison to pH 6.8 where a much lower bulk Fe^{2+} ion concentration is observed. This observation implies that more of the Fe^{2+} ions at pH 6.8 is being consumed at the surface as FeCO_3 or remains close to the surface resulting in the much lower bulk Fe^{2+} ion concentration observed in the bulk. The observed trend after approximately 7.5 hours for bulk SR and Fe^{2+} ion concentration may be linked to the corrosion rate results in Figure 8.15. The results are somewhat stable after this time period indicating that the rate of dissolution of Fe^{2+} ions and hence the diffusion of Fe^{2+} to and away from the surface may be considered to be at equilibrium.

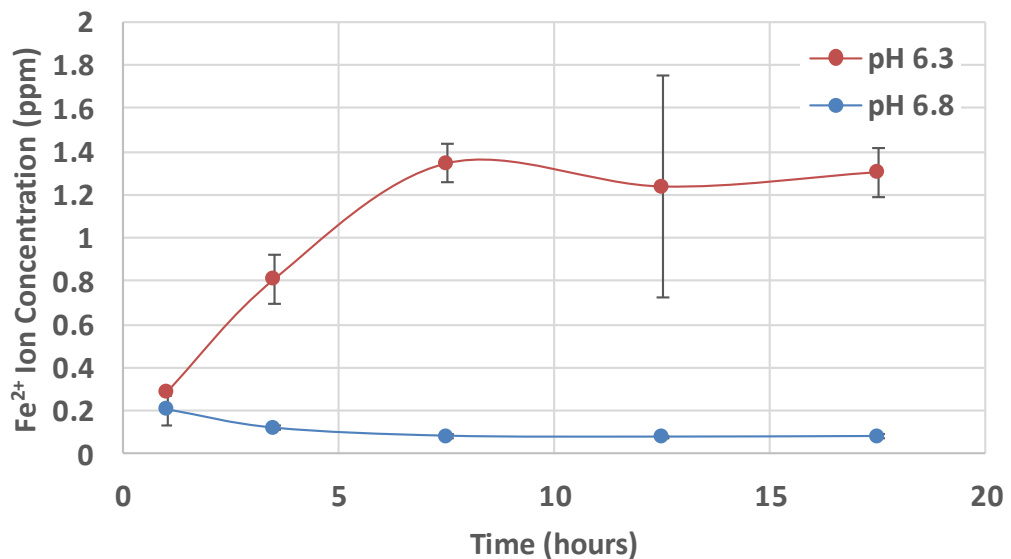


Figure 8.19 Comparison of bulk Fe^{2+} ion concentration at pH 6.3 and pH 6.8.

Therefore, the following observations show that there can be no direct correlation between the precipitation rate and the bulk saturation ratio for a freely corroding system. This indicates that the reaction is surface dominated and there may be a significant difference between bulk and surface properties.

8.2.5 Comparison of Precipitation Rate to Corrosion Rate

Figure 8.20 shows a comparison of the percentage of Fe^{2+} ions lost from the surface due to corrosion that is precipitated as FeCO_3 at the end of each time period. A significantly higher percentage of Fe^{2+} ions produced due to corrosion is observed to have precipitated as FeCO_3 at a pH 6.8 than at pH

6.3. On average, the percentage of Fe^{2+} ions consumed at the surface at all time periods is approximately 77.4% at pH 6.8 and 43% at pH 6.3. For both pH 6.3 and pH 6.8, the percentage is observed to increase for a longer time period. This is due to the protective FeCO_3 film develops over time resulting in a lower rate of dissolution of Fe^{2+} ions. Therefore, the difference in mass gain and mass loss measurements is larger and the ratio of the precipitation rate to the corrosion rate, also known as the scaling tendency, increases.

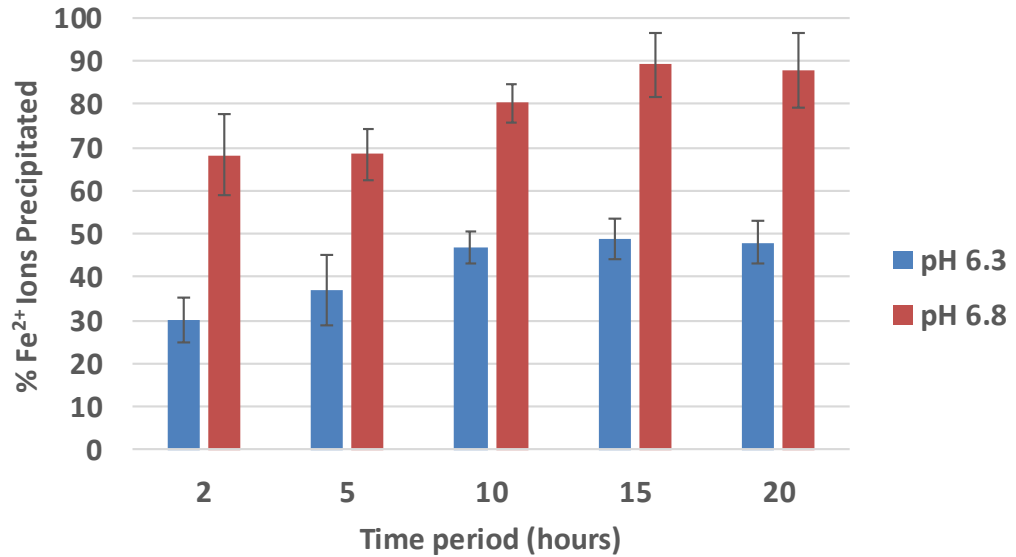


Figure 8.20 % Fe^{2+} ions lost from surface that precipitates as FeCO_3 determined from weight change results.

8.2.6 XRD Surface Analysis

The surface was analysed using X-Ray Diffraction (XRD) in order to identify the phases which constitute the film and ensure that the crystals formed over the surface is entirely FeCO_3 . Both Figure 8.21 and Figure 8.22 confirm that FeCO_3 is the only main formation on the surface at both conditions.

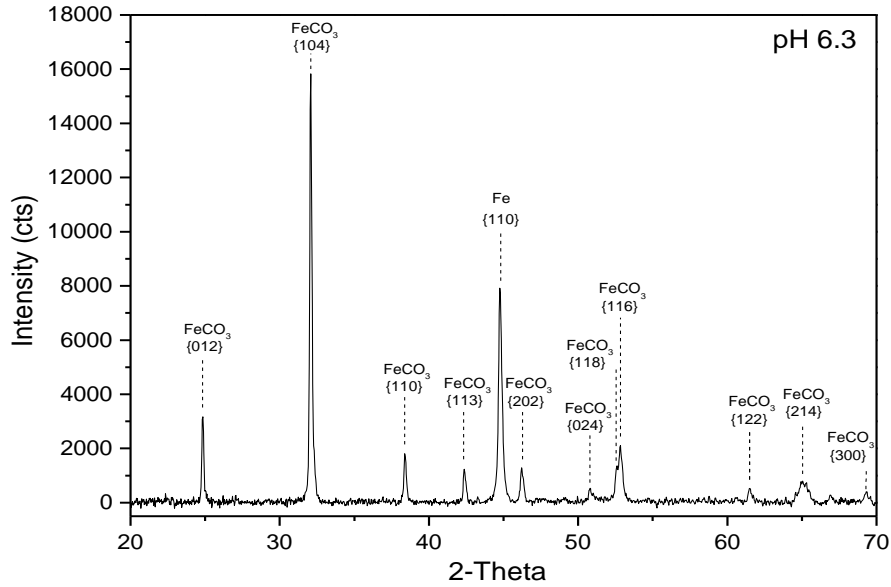


Figure 8.21 XRD patterns of X65 carbon steel exposed to a CO₂ saturated environment at 80°C, pH 6.3 and pCO₂ 0.54 bar for 20 hours.

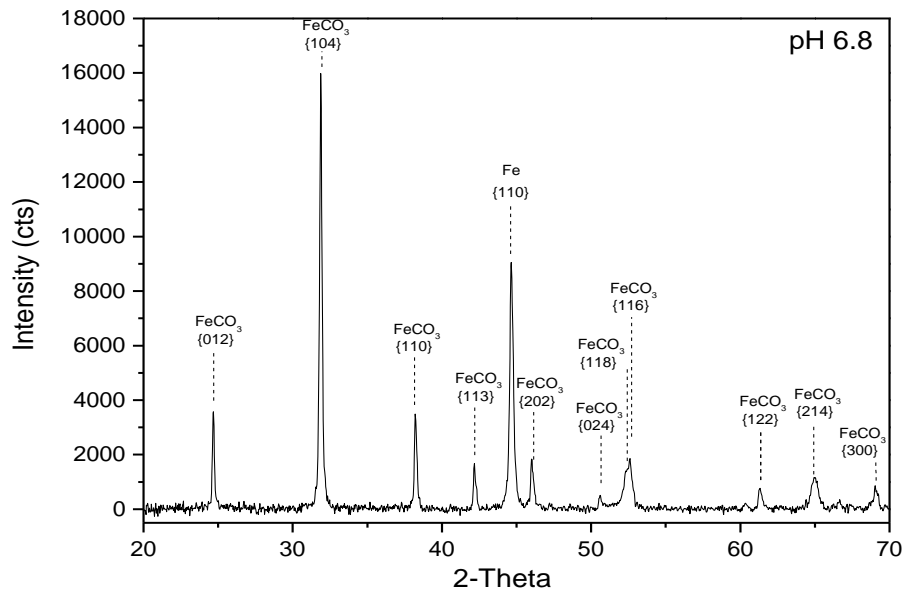


Figure 8.22 XRD patterns of X65 carbon steel exposed to a CO₂ saturated environment at 80°C, pH 6.3 and pCO₂ 0.54 bar for 20 hours.

8.3 Accelerating FeCO₃ Precipitation Kinetics

This section covers the final stage of the experimental work under static working conditions. Experiments have been carried out with the addition of hydrated FeCl₂.4H₂O where the corrosion and precipitation rate is determined from mass gain and loss measurements and the bulk super saturation through spectroscopy. Table 8.2 shows an experimental matrix of the experiments carried out.

The aim of the experimental analysis in this section is to test the effect of controlling the bulk saturation ratio on the observed kinetics of FeCO_3 film formation and compare with the observations in a freely corroding system. A large part of the work done in literature observing FeCO_3 formation kinetics has been conducted with the addition of $\text{FeCl}_2 \cdot 4\text{H}_2\text{O}$ and this section of this work contributes to critically analysing the contribution of the added Fe^{2+} ions to the corrosion rate and precipitation of FeCO_3 at the carbon steel surface.

Table 8.2 Experimental Matrix

Parameters	Conditions
Material	X65 Carbon Steel
Solution	1 L Distilled water
CO_2 Partial Pressure (bar)	0.54 bar
Temperature ($^{\circ}\text{C}$)	80°C
pH	6.8
Salinity	3.5 wt% NaCL
$\text{FeCl}_2 \cdot 4\text{H}_2\text{O}$	10, 25 and 50 ppm
Surface roughness	600 grit

8.3.1 Effect of $\text{FeCl}_2 \cdot 4\text{H}_2\text{O}$ Addition

The first set of experiments were aimed at determining the effect of adding varying amounts of $\text{FeCl}_2 \cdot 4\text{H}_2\text{O}$ on the corrosion rate and precipitation rate. A series of 2 hour experiments were run at 80°C , pH 6.8 and 3.5 wt% and were compared with that of a freely corroding system. Figure 8.23 shows the FeCO_3 precipitation rate and corrosion rate determined from mass gain and mass loss measurements as a function of the average bulk saturation ratio at the end of 2 hours. Each set of values represented by the bar graph corresponds with the amount of Fe^{2+} ions added at the start of the experiment (0, 10, 25, 50 ppm respectively).

The figure shows that the precipitation rate progressively increases with the addition of $\text{FeCl}_2 \cdot 4\text{H}_2\text{O}$. The corrosion rate, on the other hand, is significantly lower when $\text{FeCl}_2 \cdot 4\text{H}_2\text{O}$ is added in comparison to a freely corroding system. This indicates that the source of ferrous ions forming iron carbonate scale may include ferrous ions both released from the steel surface and those

provided by the bulk of the solution. Due to this additional source of Fe^{2+} ions, a higher precipitation rate is observed and less Fe^{2+} ions are dissolved from the surface. Comparing the corrosion rate for the experiments conducted with the addition of Fe^{2+} ions, results show that the corrosion rate slightly increases for a higher bulk SR however, considering the error bars, this may be due to the variability in the measurements and corrosion rate after 2 hours may be considered to be approximately similar.

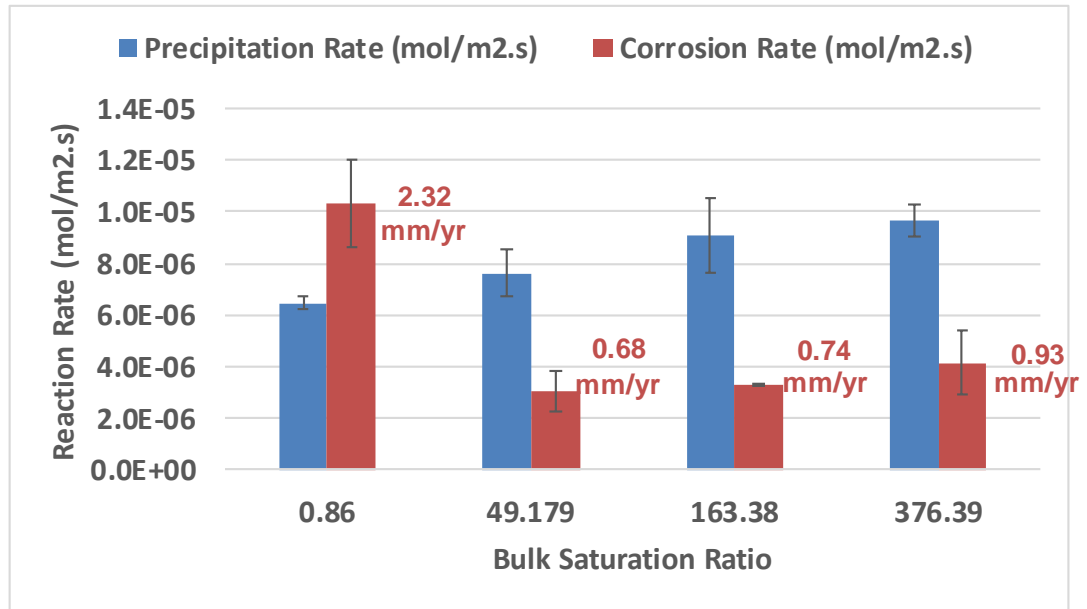


Figure 8.23 Effect of initial SR on corrosion rate and precipitation rate over 2 hour period. (Working Conditions: 80°C, pH 6.8, 0.54 pCO₂, 3.5 wt% NaCl)

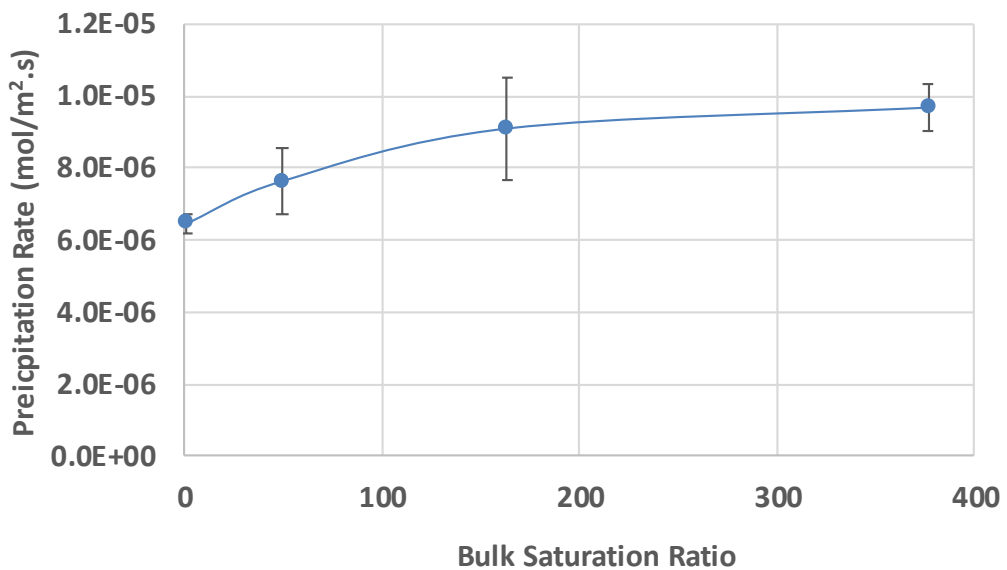


Figure 8.24 Precipitation rate vs. bulk saturation ratio for varying amounts of $\text{FeCl}_2 \cdot 4\text{H}_2\text{O}$ added over 2 hour period. (Working Conditions: 80°C, pH 6.8, 0.54 pCO₂, 3.5 wt% NaCl)

The bulk saturation ratio was determined at the end of each test. Figure 8.24 shows the precipitation rate as a function of the average bulk saturation ratio over the 2 hour period. The figure shows that adding $\text{FeCl}_2 \cdot 4\text{H}_2\text{O}$ has a significant effect on the bulk solution properties and the precipitation rate is observed to increase for a higher bulk saturation ratio. Furthermore, during the experiments, bulk precipitation is observed to occur within the glass cell and is found to be more significant and spontaneous for a higher amount of $\text{FeCl}_2 \cdot 4\text{H}_2\text{O}$ added.

8.3.2 Effect of Adding $\text{FeCl}_2 \cdot 4\text{H}_2\text{O}$ on Results over Time

Experiments were run over a time period of 2, 5, 7.5 and 10 hours to observe the effect adding an initial quantity of $\text{FeCl}_2 \cdot 4\text{H}_2\text{O}$ on the precipitation and corrosion rate over time.

In the previous section, the effect of adding variable concentrations of $\text{FeCl}_2 \cdot 4\text{H}_2\text{O}$ was observed on the precipitation and corrosion rate at an initial time period of 2 hours and it was seen to have a significant effect on the initial precipitation rate. A similar observation is seen in Figure 8.25 however, over time, the precipitation rate drops to a much lower value and continues to drop over time. The corrosion rate is observed to decrease and remains approximately the same after 5 hours with an average corrosion rate of 0.60 mm/year.

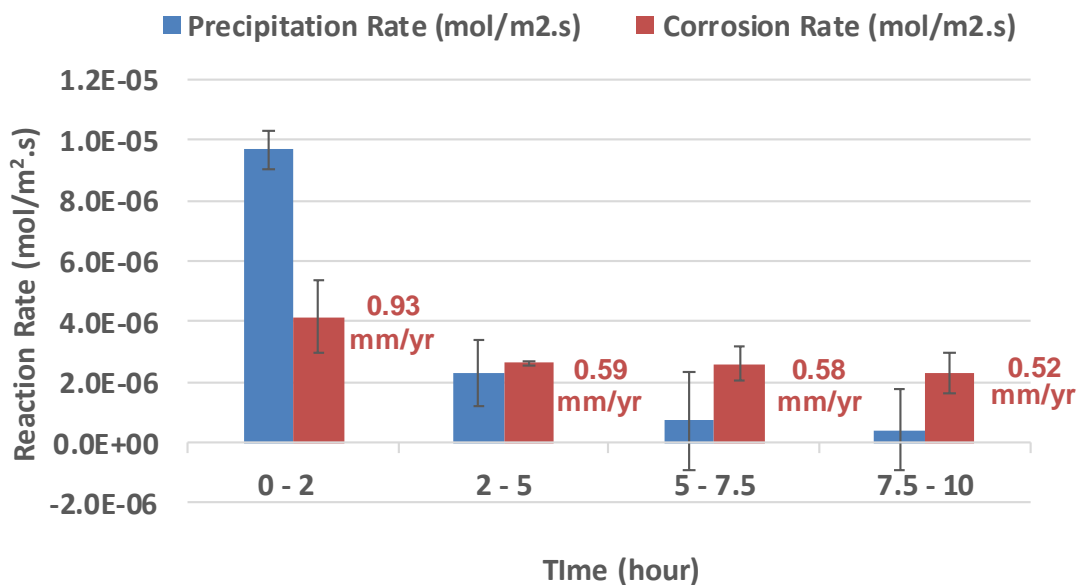


Figure 8.25 Effect of initial SR on precipitation rate and corrosion rate over time. (Working Conditions: 80°C, pH 6.8, 0.54 pCO₂, 3.5 wt% NaCl, 50 ppm $\text{FeCl}_2 \cdot 4\text{H}_2\text{O}$)

Comparing the precipitation rate with the corrosion rate in the same molar units, the precipitation rate is significantly higher than the corrosion rate at the initial time period which indicates that the bulk Fe^{2+} is a more significant source of ferrous iron forming FeCO_3 . At later time periods, the corrosion rate is higher than the precipitation rate. The results may indicate that over time, the Fe^{2+} ions contributes more to bulk precipitation that is observed elsewhere in the beaker therefore resulting in a lower contribution to FeCO_3 precipitation at the surface.

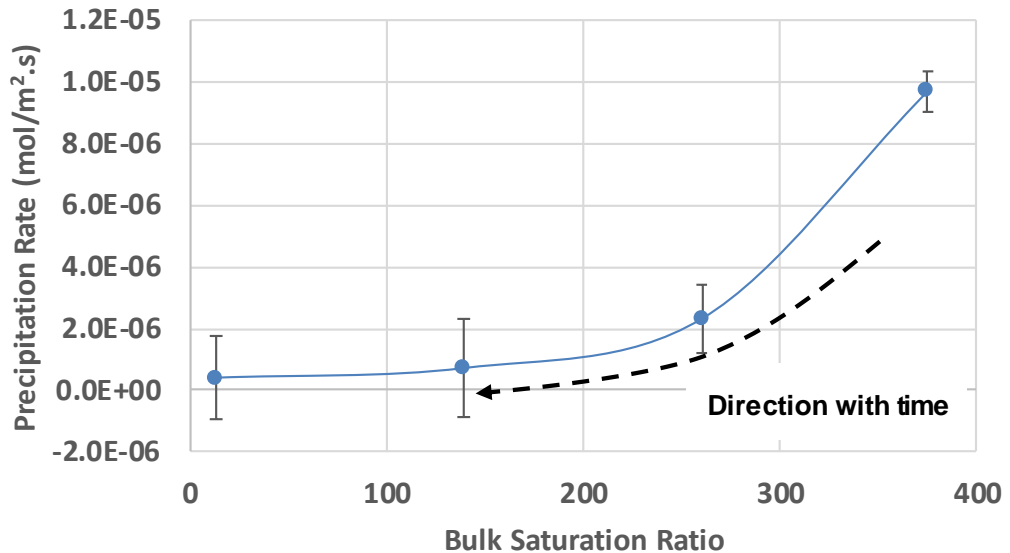


Figure 8.26 Precipitation rate as a function of the bulk saturation ratio. Arrow indicated direction with time. (Working Conditions: 80°C, pH 6.8, 0.54 pCO₂, 3.5 wt% NaCl, 50 ppm FeCl₂.4H₂O)

Figure 8.26 shows the results of the precipitation rate plotted as a function of bulk saturation ratio and the arrow indicates the direction of the trend over time. The results shows an exponential drop in precipitation rate with bulk super saturation. The drop in saturation ratio confirms the observed bulk precipitation. The results show that the bulk Fe^{2+} ions reduce significantly over time and the corresponding reduction in precipitation rate implies that the Fe^{2+} are being consumed elsewhere.

8.3.3 Later Stages of FeCO_3 Nucleation and Growth

In the following section, the properties of a fully formed protective FeCO_3 film is studied to represent the later stages of FeCO_3 nucleation and growth. Initially, a FeCO_3 film is precipitated on a carbon steel sample over 20 hours at 80°C, pH 6.8, 1 bar total pressure and 3.5 wt% NaCl. Results have shown that the film developed within this time frame under these conditions is a

compact and dense protective layer. The sample is then placed under two different conditions:

- a fresh CO₂ saturated solution at 80°C, pH 6.8, 1 bar total pressure and 3.5 wt% NaCl with the magnetic stirrer rotating at 750 rpm to introduce turbulence to the system. The following test is conducted over two hours to test the stability of the developed film.
- a fresh CO₂ saturated solution at 80°C, pH 6.8, 1 bar total pressure and 3.5 wt% NaCl with 10 ppm and 50 ppm of Fe²⁺ ions added to the bulk solution. The following test is again conducted over two hours and used to determine whether increasing the bulk super saturation has an influence on the pre-formed protective FeCO₃ film.

Mass loss and gain measurements are taken and the subsequent effect of the new conditions on the developed film is studied. Figure 8.27 shows the mass change in mg at the end of each test with the pre-formed film over 20 hours. Figure 8.28 shows the resulting change in precipitation rate and corrosion rate in mol/m².s. The bar chart is labelled according to the condition that it is introduced into as turbulence, 10 ppm FeCl₂.4H₂O and 50 ppm FeCl₂.4H₂O respectively.

In the initial case of introducing the sample with a pre-formed film into a solution with turbulent flow characteristics, results show that there is a negative change in mass gain and precipitation rate. This indicates that some of the unstable FeCO₃ crystals may have dissolved back in to the solution. However, there is no increase in corrosion rate which implies that the film is still protective. The corrosion rate is seen to be negative due to slightly smaller mass loss measurements recorded. This value is not significant and may be due to human error or slight variations in the experimental procedure. There is no true meaning that can be attained from a negative change in mass loss. In all cases, a negative change in mass loss or corrosion rate may be due to differences in cell set-up or human errors. However, an increase in mass loss would indicate that the film is no longer protective and corrosion rate has increased.

In the next sequence of experiments, the pre-formed film is placed in a solution with 10 ppm and 50 ppm of FeCl₂.4H₂O in the same conditions of temperature and pH. Contradictory results are observed where adding 10 ppm of Fe²⁺ ions resulted in a higher mass gain and an increase in precipitation rate as more FeCO₃ crystals are formed at the surface.

However, adding a significantly higher amount of Fe^{2+} ions (50 ppm) did not result in an even higher precipitation rate but the mass change remained approximately the same or even slightly lower as some FeCO_3 crystals may have dissolved into the solution. This may be because the bulk precipitation is more spontaneous and due to the limited Fe^{2+} ions at the surface, the Fe^{2+} added to the solution may contribute significantly more to the nucleation and growth of crystals in the bulk. Adding $\text{FeCl}_2 \cdot 4\text{H}_2\text{O}$ does not seem to have a significant effect on the mass loss results.

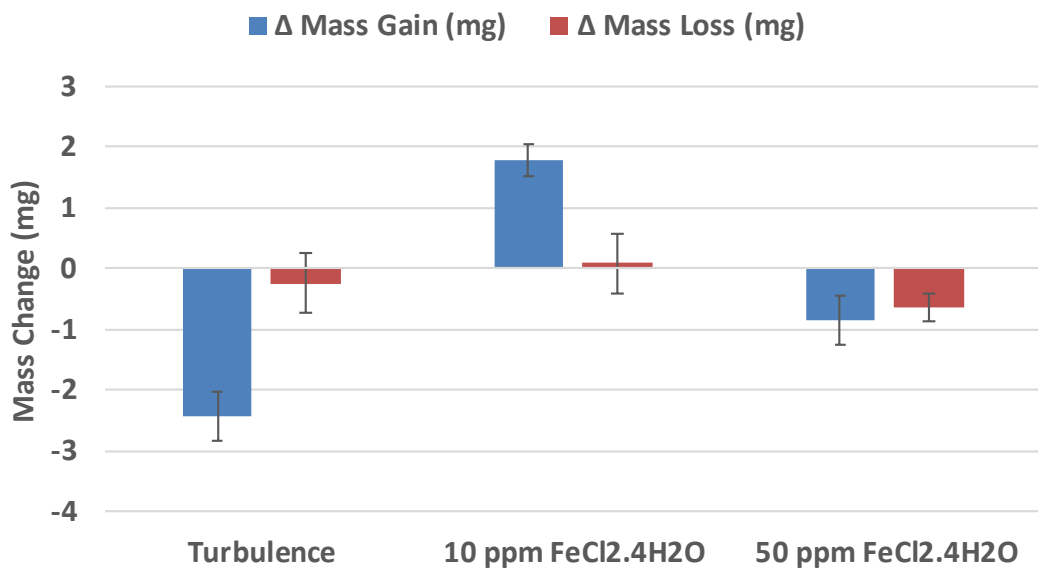


Figure 8.27 Change in mass gain and mass loss measurements testing the effect of turbulence and adding $\text{FeCl}_2 \cdot 4\text{H}_2\text{O}$ on a pre-formed protective film.

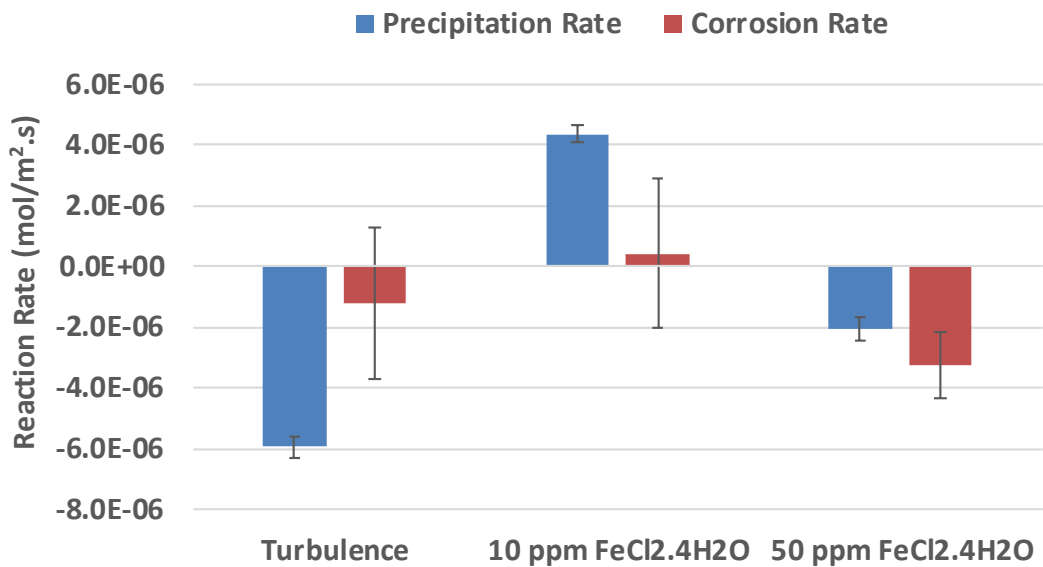


Figure 8.28 Calculated precipitation rate and corrosion rate testing the effect of turbulence and adding $\text{FeCl}_2 \cdot 4\text{H}_2\text{O}$ on a pre-formed protective film.

Chapter 9

Flow Cell Experimental Results

Experiments were carried out at 80°C, pH 6.8, 3.5 wt% NaCl and at four variable speeds (0.1, 0.3, 0.6, 1m/s) across the surface of the samples. Electrochemical measurements were taken in the form of LPR, AC impedance and Tafel polarisation measurements. The experiments were repeated to ensure consistency of data. The samples at the end of each test were also analysed for mass gain, SEM and XRD.

9.1 Comparison between Results in Same Flow Channel

In each test, results were obtained from three different samples in the same channel. Each sample was exposed to the same conditions and the same velocity as computed in Chapter 7.2. In the first stage of the analysis, the results of each of the samples was analysed to determine if there was any relative effect.

The original value of LPR corrosion rate was calculated using the measured value of polarisation resistance. However, charge transfer resistance should be used to calculate the corrosion rate to account for any solution resistance according to Equation (6.1) in Chapter 6.1.3. Figure 9.1 shows the Nyquist plot of sample 2 (middle sample) for working conditions of 80°C, pH 6.8, 3.5 wt% NaCl and velocity of 1 m/s.

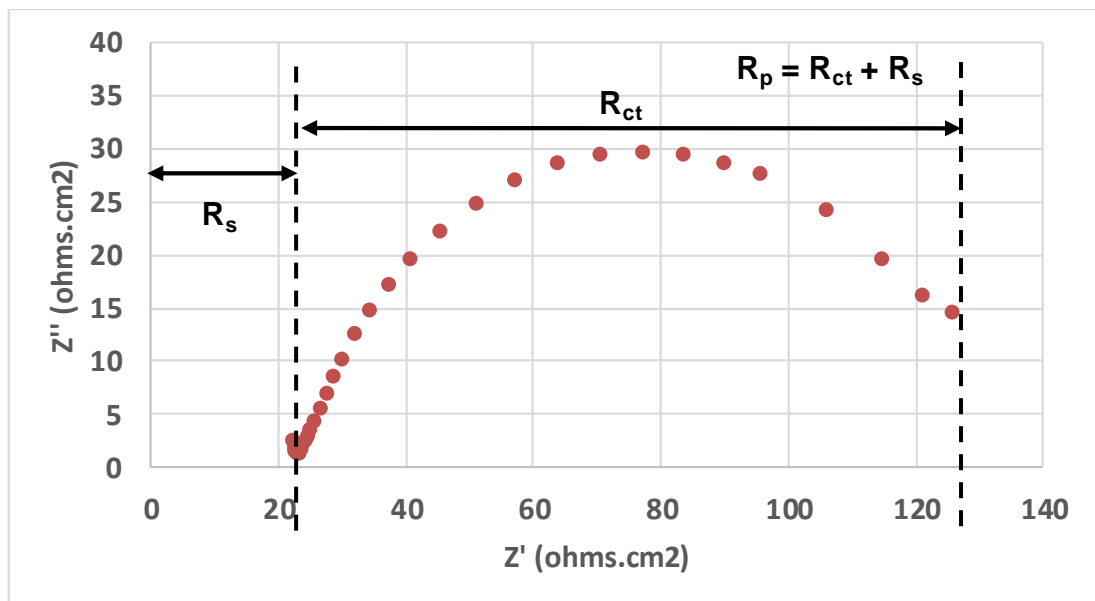


Figure 9.1 Nyquist plot indicating solution resistance and charge transfer resistance. Working conditions (80°C, pH 6.8, 3.5 wt% NaCl and velocity of 1 m/s)

The solution resistance (R_s) was taken from the Nyquist plot by determining the first value of Z' when $Z'' = 0$. The polarisation resistance measurements were then corrected for by account for the solution resistance ($R_{ct} = R_p - R_s$).

Another essential parameter is the Stern-Geary coefficient that was previously discussed in Chapter 6.1.3. The coefficient value used to calculate the corrosion rate initially was 26, as it was assumed the Tafel constants were equal to 120 mV/decade. To correct the Stern-Geary coefficient, the gradient of the anodic and cathodic branches were calculated at the end of each test.

The Tafel plot for sample 2 for working conditions of 80°C, pH 6.8, 3.5 wt% NaCl and velocity of 1 m/s is shown in Figure 9.2. The gradient of the anodic branch, β_a can be seen to be approximately 50 mV/decade and the gradient of the cathodic branch, β_c is approximately 140 mV/decade. This results in a Stern-Geary coefficient, B of 16.0 mV/decade.

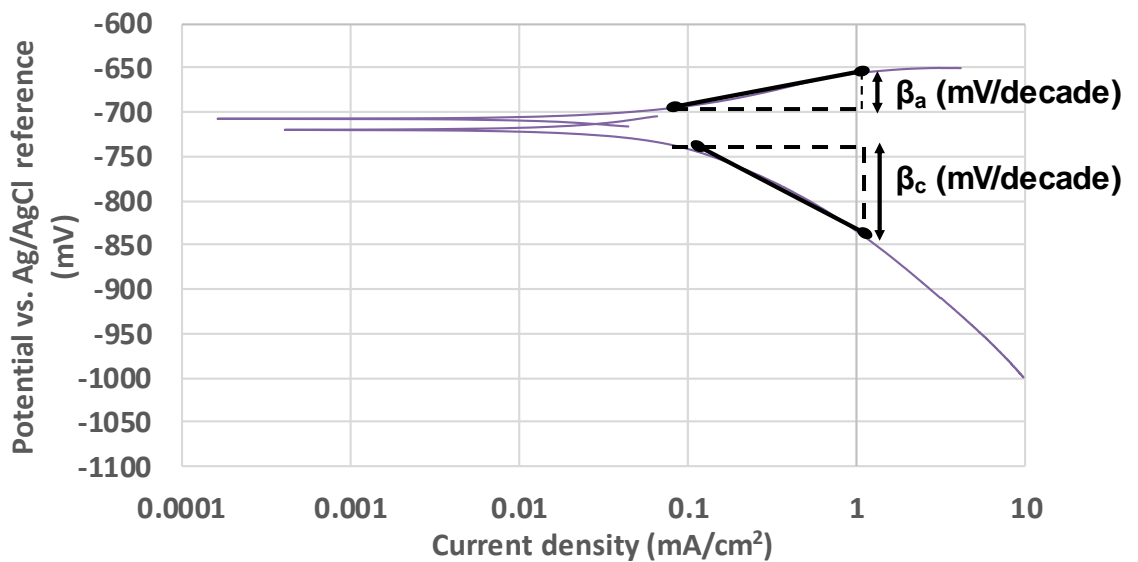


Figure 9.2 Tafel plot for 80°C, pH 6.8, 3.5 wt% NaCl and velocity of 1 m/s across sample surface.

The flow cell was initially run for a velocity of 1 m/s across the surface of the samples (pump setting 3000 ml/min) at 80°C and pH 6.8 for a period of 20 hours and electrochemical measurements were carried out. Figure 9.3 illustrates a complete analysis from the electrochemical results for each sample in the configuration. Figure 9.3 (a) shows a 3D solid works drawing identifying the three different samples in sequence within the flow cell and their respective electrodes from inlet to outlet. Figure 9.3 (b) shows the AC

impedance measurements carried out at the beginning of each test for each sample.

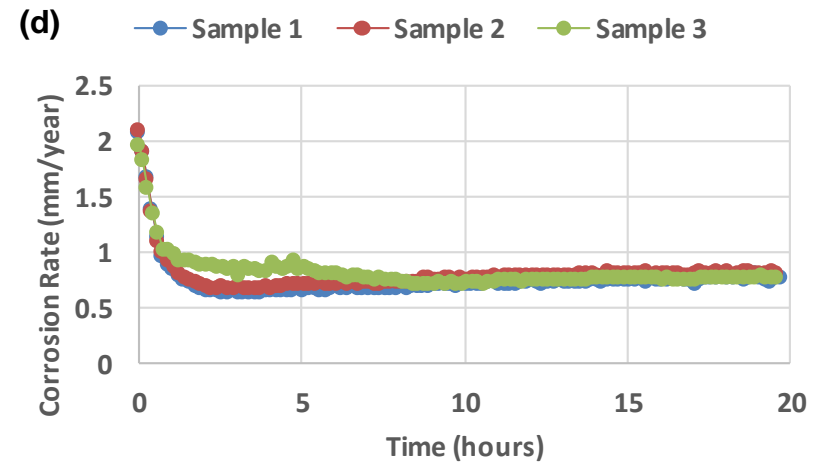
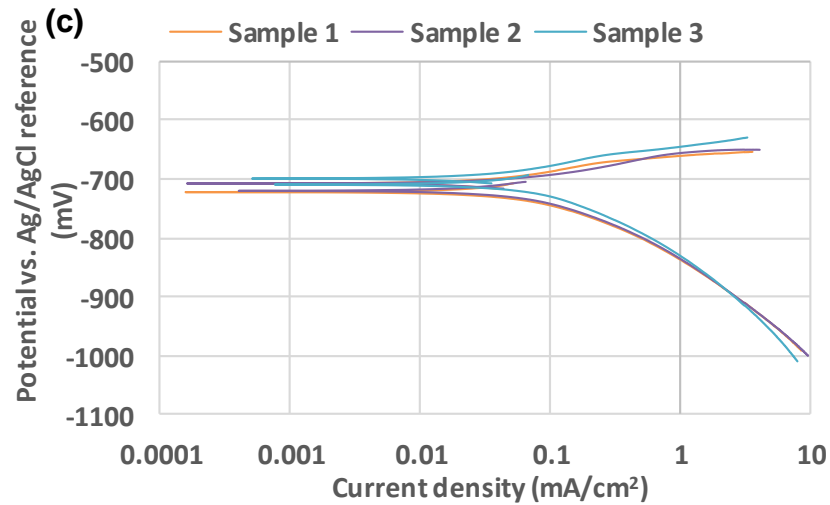
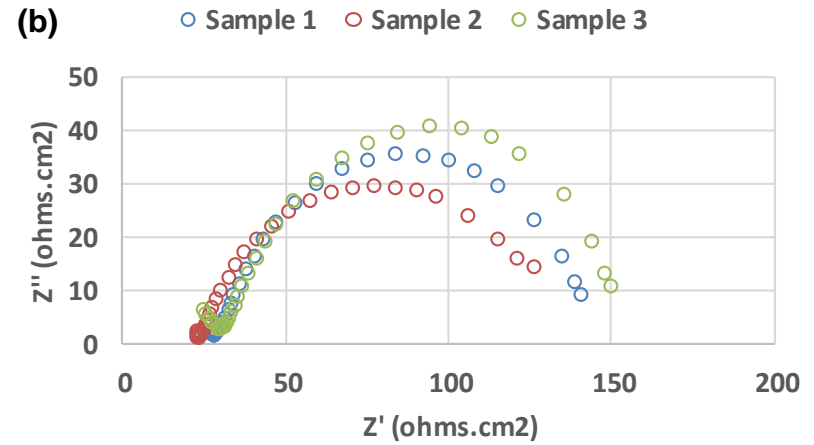
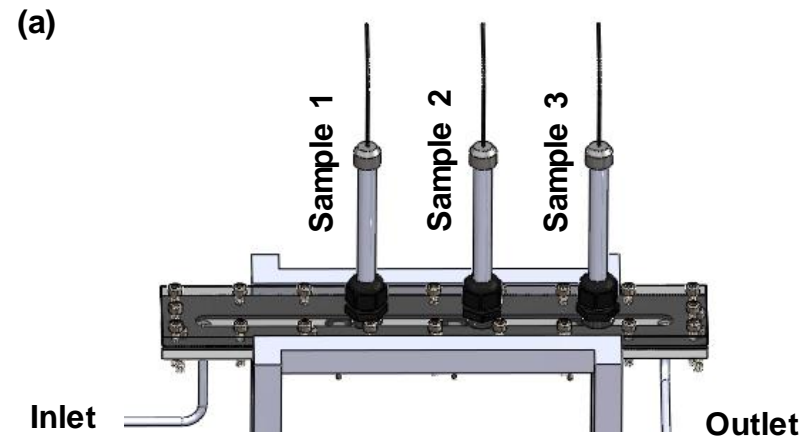


Figure 9.3 Overall analysis of electrochemical measurements of X65 carbon steel at 80°C, pH 6.8, 3,5 wt % NaCl and a flow velocity of 1 m/s. (a) 3D representation of flow cell identifying samples and their corresponding redox electrode. (b) Nyquist plot. (c) Tafel plot. (d) Corrected corrosion rate over time for each sample.

Results show that the solution resistance is approximately the same for each sample with values of 26.49, 22.40, and 24.33 Ω/cm^2 respectively. Figure 9.3 (c) shows the results of the Tafel anodic and cathodic polarisation at the end of the test. The β_a and β_c slopes are seen to approximately overlap and therefore, as in Figure 9.2, the Stern-Geary coefficient for the specified working conditions for each sample is 16.0 mV/decade. Upon correcting the corrosion rates, Figure 9.3 (d) shows the resulting values for each sample over the 20 hour period. The results for each sample are seen to be very similar in trend and it can be inferred from results that there is no relative effect on the samples and they may be considered a repeat measurement. A similar observation is found for all tests carried out in the flow cell supporting the analysis.

9.2 Effect of Flow Velocity

The next sequence of results analysed is the effect of flow on the solution resistance, Tafel plots and finally the corrected corrosion rate.

9.2.1 Effect of Flow on Solution Resistance for TCFC

Figure 9.4 shows the Nyquist plot as a result of AC impedance measurements carried out at the start of each test. The results show that the solution resistance is approximately similar for each velocity with a solution resistance for each sample of approximately 25 Ω/cm^2 . Main parameters that effect solution resistance is temperature and ionic strength which are maintained in the following experiments and therefore the results are as expected.

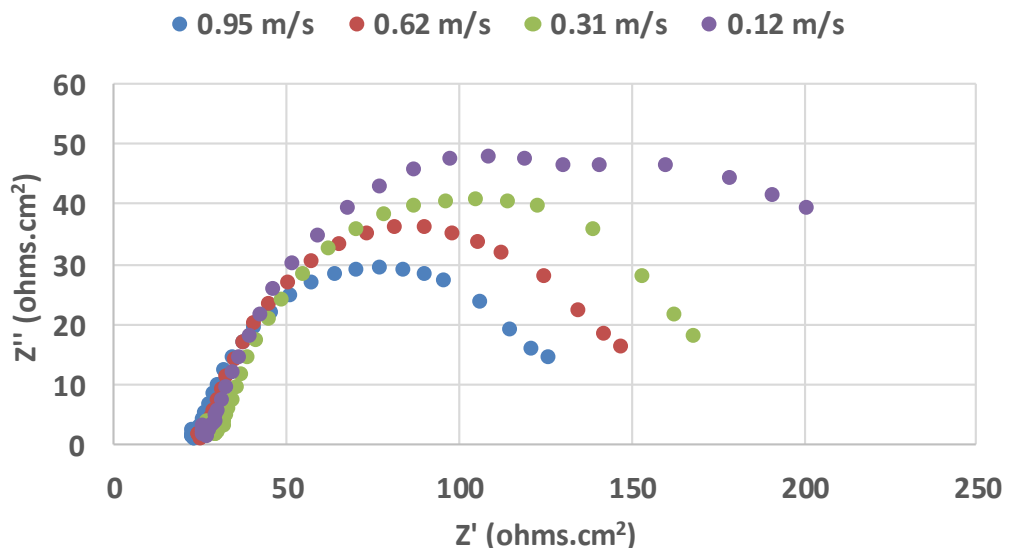


Figure 9.4 Nyquist plot showing solution resistance for variable flow velocities at 80°C, pH 6.8, pCO₂ 0.54 bar and 3.5 wt % NaCl.

9.2.2 Effect of Flow on Tafel Plot for TCFC

Figure 9.5 shows Tafel plot results for anodic and cathodic polarisation measurements carried out at the end of the test at variable flow velocities in the thin channel flow cell. The figure shows that there appears to be a shift in the cathodic Tafel as an increase in velocity results in an increase in potential and the rate of cathodic reaction. The slopes, β_a and β_c appear to have a similar value for all flow velocities across the surface of the sample. Reading the plot allows us to discern the β_a and β_c to be 50 and 140 mV/decade approximately. This corresponds well with the equations for Tafel constants by Stern et al. (Section 6.1.3).

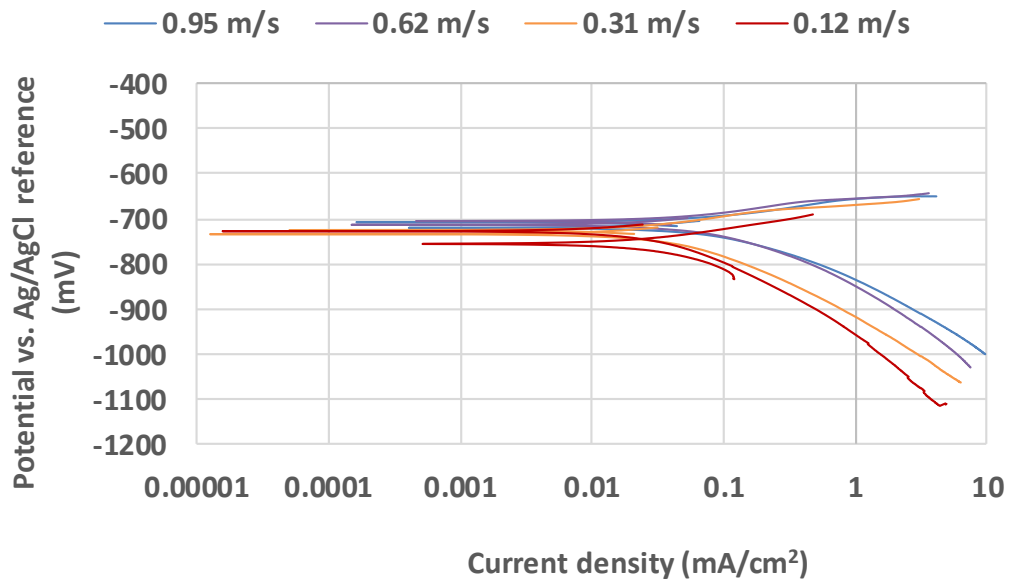


Figure 9.5 Tafel plot, effect of velocity at 80°C, pH 6.8, pCO₂ 0.54 bar and 3.5 wt % NaCl.

9.2.3 Effect of Flow on Corrosion Rate for TCFC

After correcting each of the results, Figure 9.6 shows the corrosion rate as a function time for the different velocities across the sample. A velocity of 0.95, 0.62 and 0.31 m/s correspond to turbulent flow across the surface of the sample whereas a velocity of 0.12 m/s correspond to laminar flow. The figure shows a higher initial corrosion rate is observed for a higher velocity. This is as expected as a higher flow across the surface of the sample results in higher mass transport of species away from the surface, a lower surface saturation ratio and hence a higher corrosion rate. However, a faster drop in corrosion rate is observed for a faster velocities which may imply a faster rate of FeCO₃ film formation. This observation may be an aspect of a

recirculating flow loop. It may be argued that for a faster velocity the concentration of Fe^{2+} ions that would pass across the surface for a specific time instant would be higher. And the combined Fe^{2+} ions from the three samples would cause a higher surface SR and a higher FeCO_3 precipitation rate resulting in the more significant drop in corrosion rate observed for a higher velocity.

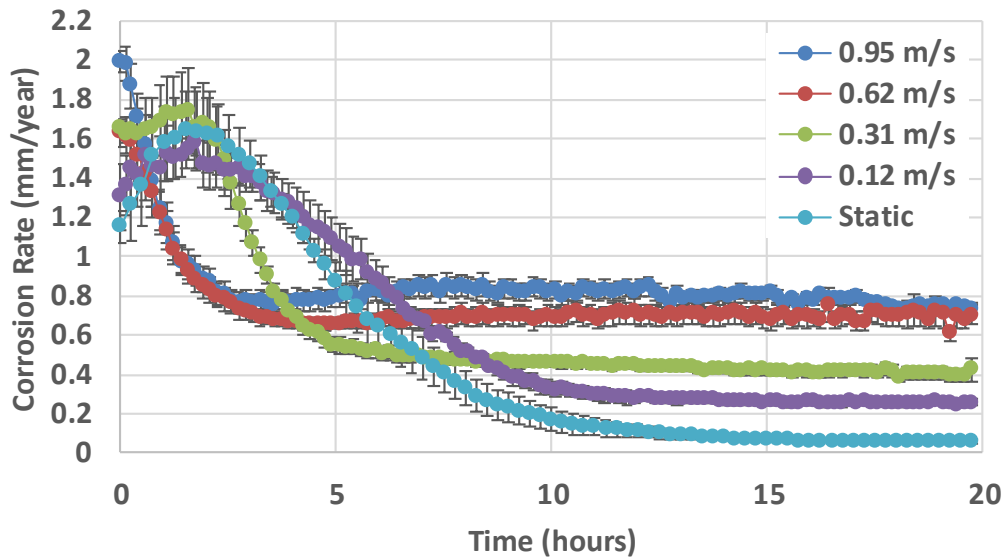


Figure 9.6 Effect of velocity on corrosion rate for working conditions 80°C, pH 6.8, pCO_2 0.54 bar and 3.5 wt % NaCl.

At the end of 20 hours, the corrosion rate is observed to be lower for a lower velocity and the most protective film is formed for a static system. A faster flow rate may imply a lower adherence to the surface therefore resulting in a less protective film for a higher velocity after 20 hours.

A similar observation is reported in experiments conducted using a rotating cylinder electrode (RCE) in a study by Nescic et al. [53]. The results showed that the corrosion rate dropped at a faster rate for higher rotational velocity of the RCE but the corrosion rate at the end of the test was observed to be lower for a lower rotational velocity. It was concluded that the FeCO_3 precipitated on the surface dissolved back or were chemically damaged resulting in the higher corrosion rate at a higher flow rate supporting the observations within the flow cell.

Mass gain measurements were taken at the end of each test and Figure 9.7 shows the precipitation rate at the end of 20 hours. The figure shows that the precipitation rate reduces for a higher velocity which agrees with the LPR measurements. The results are correlated with SEM images taken at the end of each test. The images shown in Figure 9.8 are the best

representation of the overall surface. At a velocity of 0.95 m/s and 0.62 m/s, the crystals formed on the surface after 20 hours is observed to be similar in microstructure. The average crystal size is approximately 12 μm and a similar surface coverage is observed. This corresponds with Figure 9.6 and Figure 9.7 where the precipitation rate and corrosion rate are approximately the same for both velocities. At a velocity of 0.13 m/s, the crystal size is observed to be larger with an average size of 30 μm . However, the surface coverage is observed to be higher which relates to the lower corrosion rate and significantly higher precipitation rate observed. At 0.12 m/s across the surface of the sample, the flow is laminar. A significantly higher surface coverage and smaller crystal size is observed with an average crystal size of 5 μm .

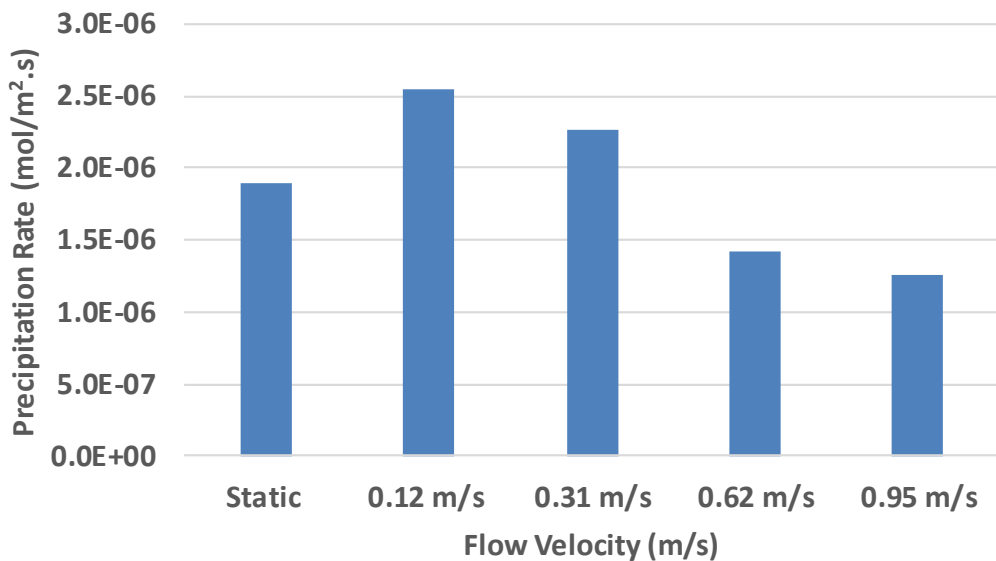


Figure 9.7 Precipitation rate determined from mass gain measurements at the end of 20 hours for variable flow velocity and working conditions 80°C, pH 6.8, pCO₂ 0.54 bar and 3.5 wt % NaCl.

The corrosion rate results in Figure 9.6 show the corrosion rate to be lowest at the end of 20 hours and hence the more protective film is formed at this flow condition. Comparing laminar flow (0.12 m/s) with results from the static system, Figure 9.6 shows a more protective film is formed under static conditions. However, Figure 9.7 shows a higher precipitation rate for a flow velocity of 0.12 m/s and SEM images show that the crystals are much smaller in size. There is a significant difference in exposed surface area of the samples used in the static glass cell experiments and flow cell experiments. Despite the surface area being taken into account in the electrochemical measurements and the precipitation rate calculations, the characteristics of the film formed may attribute to the difference.

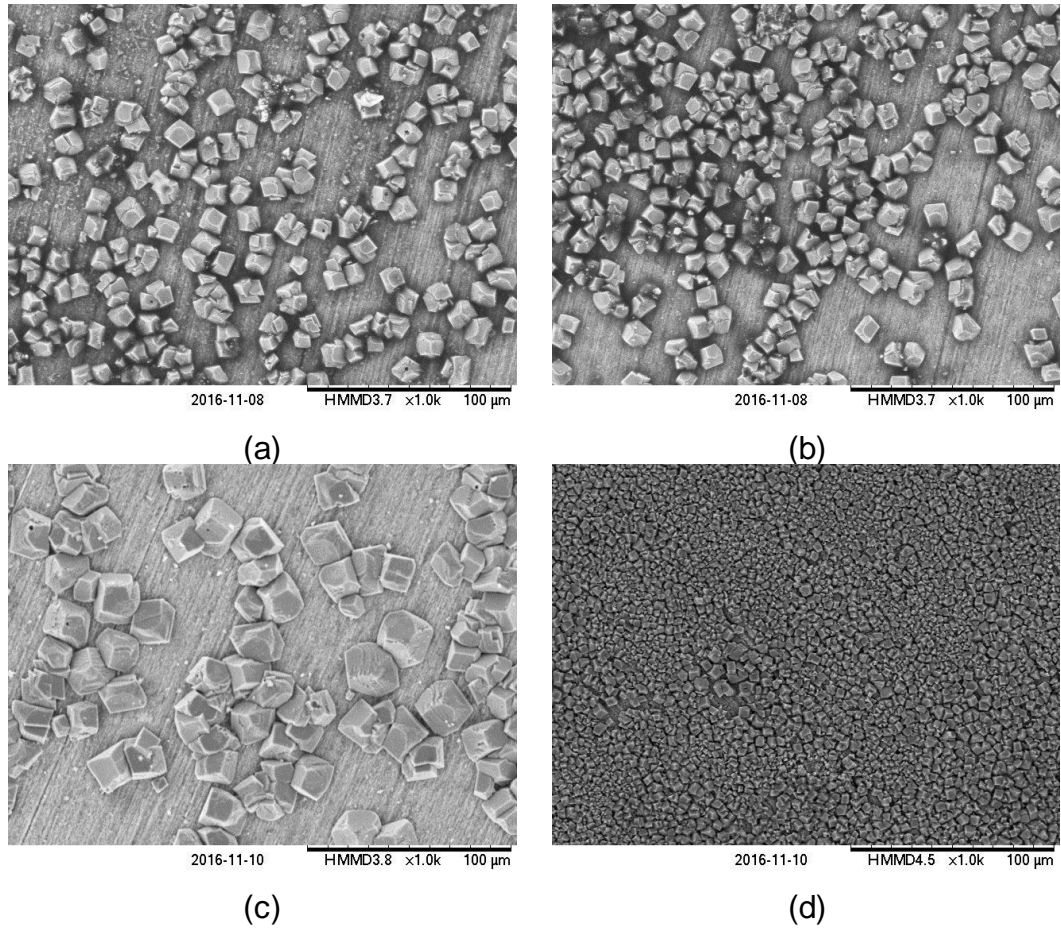


Figure 9.8 SEM images of the surface of the sample at variable flow velocities (a) 0.95 m/s (b) 0.63 m/s (c) 0.31 m/s (d) 0.12 m/s.

9.2.4 XRD Surface Analysis

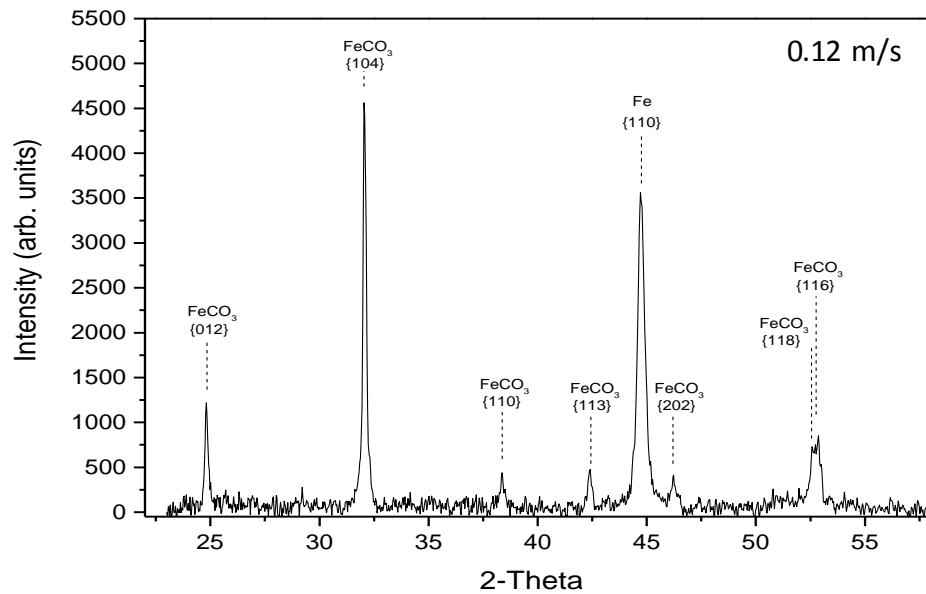


Figure 9.9 XRD patterns of X65 carbon steel exposed to a CO_2 saturated environment at 80°C, pH 6.8, pCO_2 0.54 bar and flow velocity 0.12 m/s for 20 hours.

XRD analysis was performed at the end of the each test to ensure that the film formed is FeCO_3 and to ensure there is no oxygen contamination within the cell resulting in a by-product such as magnetite, Fe_3O_4 . Figure 9.9 and Figure 9.10 shows the results for a velocity of 0.12 m/s and 0.95 m/s respectively. The observed difference in peak intensities may be due to the substantial difference in the amount of crystals observed on the surface.

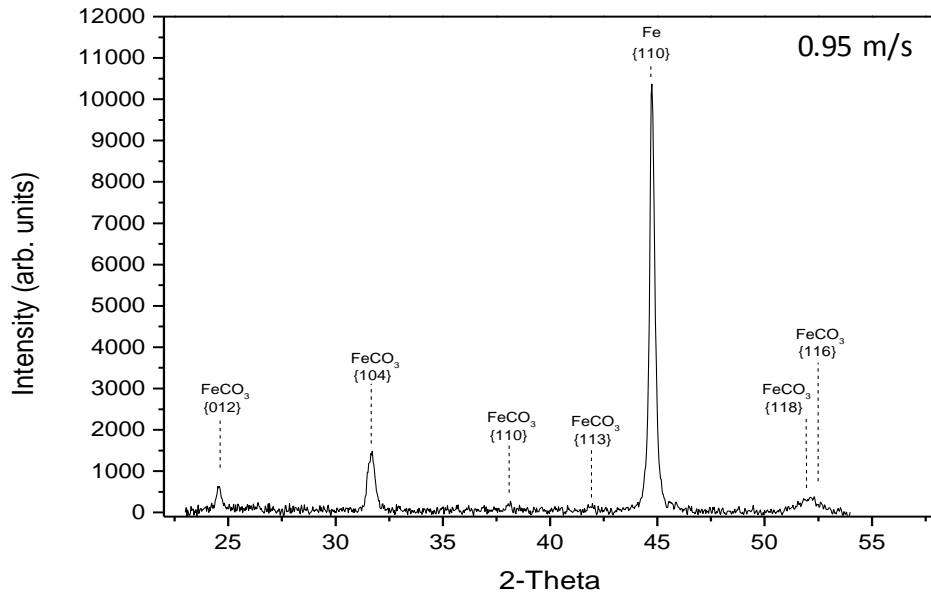


Figure 9.10 XRD patterns of X65 carbon steel exposed to a CO_2 saturated environment at 80°C , pH 6.8, pCO_2 0.54 bar and flow velocity 0.95 m/s for 20 hours.

9.3 Summary of Experimental Results

The results presented in Chapter 8 and Chapter 9 demonstrate that

1. High bulk pH and high temperature contribute to a faster reduction in corrosion rate and a more protective FeCO_3 film after 20 hours.
2. The corrosion rate is observed to follow a similar trend for low salt concentrations (1.0 and 3.5 wt% NaCl). Increasing the salt concentration (5.0wt %) results in a higher corrosion rate over time.
3. Sample polished to 600 grit is observed to have the lowest corrosion rate after 20 hours and hence the more protective FeCO_3 film. A rougher surface results in a less protective film and a smoother surface results in a slower reduction in corrosion rate.

4. Surface analysis (SEM) shows that nucleation and growth is a simultaneous process. For a more protective film formation, the crystals are observed to be more compact, dense with a smaller crystal size. A less protective film is observed to have larger, more discrete crystals.
5. Crystal size is higher for a less protective film whereas surface coverage is higher for a more protective film.
6. Mass gain does not directly relate to the protectiveness of the film. Over a period of 20 hours, the corrosion rate is observed to be lower for a higher mass gain. A fewer, larger crystals may have a similar mass gain to many, smaller crystals.
7. There is no clear correlation between bulk saturation ratio and precipitation rate for a freely corroding system.
8. A more significant percentage of the Fe^{2+} ions dissolved from the surface is precipitated as FeCO_3 for a higher pH and more protective film.
9. The source of ferrous ions forming iron carbonate scale includes ferrous ions both released from the steel surface and those provided by the bulk of the solution when $\text{FeCl}_2 \cdot 4\text{H}_2\text{O}$ is added to the solution. Addition of $\text{FeCl}_2 \cdot 4\text{H}_2\text{O}$ is observed to accelerate the kinetics of FeCO_3 film formation over initial time periods.
10. The precipitation rate of iron carbonate scale is more strongly affected by the corrosion rate of the steel at low bulk supersaturation. At high bulk supersaturation, the corrosion rate has little effect on the precipitation rate. This is observed as the precipitation rate is higher than the corrosion rate upon comparison.
11. At high bulk super saturation, bulk precipitation is observed and is observed to dominate the precipitation reaction over time.
12. At later stages of FeCO_3 nucleation and growth, turbulence is observed to result in FeCO_3 being removed from the surface; however, the film remains protective as the corrosion rate does not increase.

13. FeCO_3 may be enticed to precipitate on to a pre-formed protective film through addition of $\text{FeCl}_2 \cdot 4\text{H}_2\text{O}$. However, increasing the bulk Fe^{2+} does not progressively increase the precipitation on to the film as bulk precipitation dominates.
14. For a flowing system, a more protective film is observed to form for a lower velocity at the end of 20 hours. However, a faster drop in corrosion rate is observed at a faster velocity.
15. In turbulent flow across the surface of a sample, SEM images show the precipitated FeCO_3 crystals to be scattered and discrete. The film formed is less protective than for laminar flow and static conditions.
16. In laminar flow conditions, a compact and dense FeCO_3 film is formed across the surface. However, corrosion rate calculations from LPR measurements observe a more protective film formed for static conditions.
17. XRD analysis confirms that the film formed is FeCO_3 and there is no contamination within the flow cell.

Chapter 10

Development of Corrosion Rate Model

In literature, CO₂ corrosion models have been developed [49, 69, 70] that predict the corrosion rate over time accounting for FeCO₃ film development. However, the models have been developed for turbulent pipe flow and the FeCO₃ precipitation rate model used is based on experiments conducted under static conditions. Experimental results, in this work, have shown that the kinetics of film development and the characteristics of the film are very different under flowing conditions and the limitations of the developed precipitation models have been identified. Therefore, the theory used in the development of these corrosion models in conditions of where a FeCO₃ film is considered is found to be unrealistic.

The following chapter focuses on the development of a steady state corrosion rate model. In the previous chapter, the effect of flow was observed on the corrosion rate in a thin channel flow cell. This work carries forward and utilises existing theoretical knowledge on CO₂ corrosion to predict the steady state corrosion rate, the maximum corrosion rate, under varying environmental conditions. The model does not account for film development as a complete understanding of the film under varying conditions is required to be accounted within a model and to predict the resulting corrosion rate over time. The results from the developed model is intended to complement the experimental work carried out and to provide an understanding of surface characteristics where an experimental investigation is limited. The model is run for conditions where a film is expected to form and provides an understanding of conditions at the initial stages that may drive the precipitation of the film.

Figure 10.1 represents a flow chart outlining the stages of the corrosion model and the subsequent sections that shall cover each concept in the following chapter.

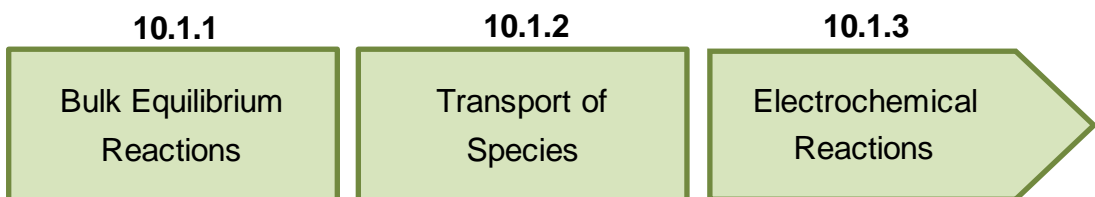


Figure 10.1 Stages of corrosion model.

10.1 Modelling Framework

The model accounts for the key processes underlying the CO₂ corrosion of carbon steel; chemical reactions in the bulk solution, mass transport of aqueous species through the liquid boundary layer and electrochemical reactions at the steel surface. The model based on these key physiochemical processes is mechanistic and has been developed using MATLAB software package which is a well-known and widely used numerical computing program. It is able to predict the steady state corrosion rate for varying input parameters of velocity, temperature, pH, pCO₂, ionic strength and total pressure.

The concentration of the species can be very different in the bulk solution and at the corroding steel surface due to corrosion, mass transfer effects and chemical reactions. This was observed experimentally in experiments conducted in a glass cell in Chapter 8. The model presented in this chapter is based on theory behind a predictive corrosion model by Netic et al. [35, 69, 71, 98] in CO₂ and H₂S containing environments; however is only considered for CO₂ conditions in the following work. Two calculation nodes were used in the computational domain. One for the species concentration in the bulk solution and the other for the species concentrations in the thin water layer adjacent to the corroding steel surface. Figure 10.2 depicts a sketch of the corrosion process and the three related physiochemical processes.

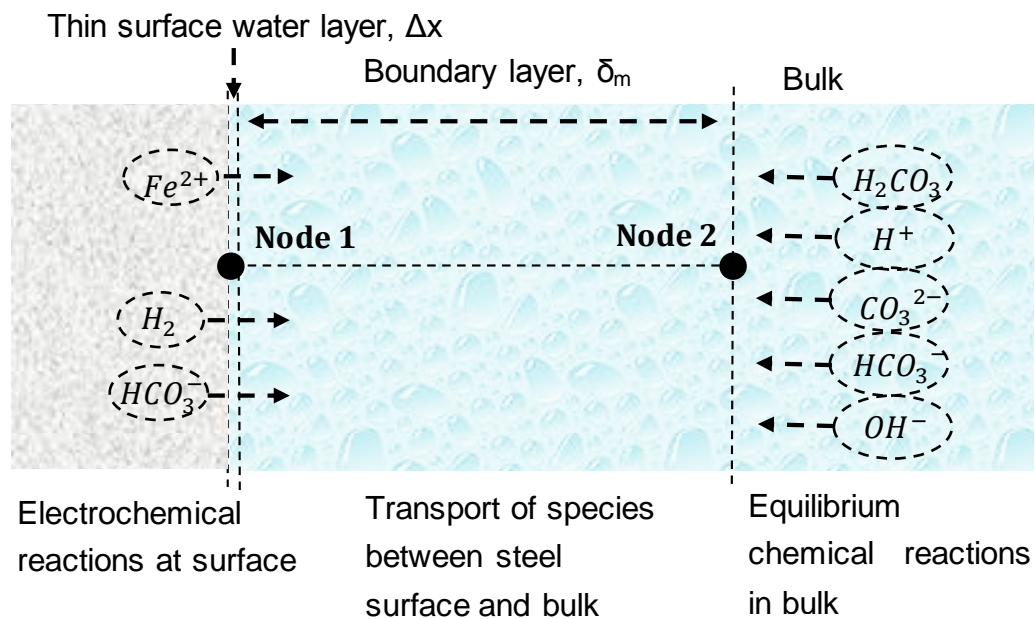


Figure 10.2 Illustration of computation domain for CO₂ corrosion rate model.

The three processes are interconnected and can be expressed by writing a mass balance or species conservation equation for a thin surface water layer [71].

$$\frac{\partial c_{surface,j}}{\partial t} = \frac{N_{e,j} - N_{w,j}}{\Delta x} + R_j \quad (10.1)$$

Where $c_{surface,j}$ is the concentration of species j , $N_{e,j}$ is the flux of species j on the boundary due to mass transfer from the bulk solution to the surface, $N_{w,j}$ is the flux of species j on the boundary due to electrochemical reactions at the steel surface, and R_j is the source/sink term due to homogenous chemical reactions involving species j . Each process shall be discussed in detail in the following sections.

10.1.1 Equilibrium Chemical Reactions in Bulk

Chemical reactions are the local sources or sinks of species in the solution (term R_j in the mass balance Equation (10.1)). They are often very rapid when compared to other processes involved in corrosion, such as species transport and electrochemical reactions, thus preserving chemical equilibria throughout the solution. On the other hand, in the case of slow chemical reactions such as the CO₂ hydration reaction, other faster processes can lead to local non-equilibrium conditions at the corroding steel surface. Therefore, chemical reactions can significantly affect the rates of electrochemical processes at the steel surface and ultimately the corrosion rate [69].

Table 10.1 Chemical reactions accounted for in the model and their equilibrium constants.

Description	Reaction	Equilibrium Constant
Dissolution of carbon dioxide	$CO_2(g) \leftrightarrow CO_2(aq)$	$K_{sol} = [CO_2]/p_{CO_2}$
Water dissociation	$H_2O \rightarrow H^+ + OH^-$	$K_{wa} = [H^+][OH^-]$
Carbon dioxide hydration	$CO_2 + H_2O \leftrightarrow H_2CO_3$	$K_{hy} = [H_2CO_3]/[CO_2]$
Carbonic acid dissociation	$H_2CO_3 \leftrightarrow H^+ + HCO_3^-$	$K_{ca} = [H^+][HCO_3^-]/[H_2CO_3]$

Bicarbonate anion dissociation	$HCO_3^- \leftrightarrow H^+ + CO_3^{2-}$	$K_{bi} = [H^+][CO_3^{2-}]/[HCO_3^-]$
--------------------------------	---	---------------------------------------

The relevant chemical reactions and their equilibrium constants are tabulated in Table 10.1 with the equilibrium, forward and backward reaction rate values for reactions included in the model listed in Table 10.2.

Table 10.2 Equilibrium (K), forward (k_f) and backward (k_b) reaction rate coefficients (K=k_f/k_b) where T_f is temperature in degrees Fahrenheit, T_K is absolute temperature in Kelvin, T_c is temperature in degrees Celsius, I is ionic strength in molar and p is the total pressure in psi [69].

Chemical Reaction Constants	Source
$K_{sol} = \frac{14.5}{1.00258} \times 10^{[-(2.27+5.65 \times 10^{-3}T_f-8.06 \times 10^{-6}T_f^2+0.075I)]}$ molar/ bar	Oddo and Tomson [84]
$K_{wa} = 10^{[-(29.3868-0.0737549T_K-7.47881 \times 10^{-5}T_K^2)]}$ molar ²	Kharaka et all [99]
$K_{hy} = 2.58 \times 10^{-3}$	Palmer and van Eldik [85]
$k_{f,hy} = 10^{[329.85-110.541 \times \log T_K - \frac{17265.4}{T_K}]}$ s ⁻¹	Palmer and van Eldik [85]
$K_{ca} = 387.6 \times 10^{[-(6.41-1.59 \times 10^{-3}T_f+8.52 \times 10^{-6}T_f^2-3.07 \times 10^{-5}p-0.4772I^{1/2}+0.1180I)]}$ mol	Oddo and Tomson [84]
$K_{bi} = 10^{[-(10.61-4.97 \times 10^{-3}T_f+1.331 \times 10^{-5}T_f^2-2.624 \times 10^{-5}p-1.166I^{1/2}+0.3466I)]}$ m	Oddo and Tomson [84]

The reaction rate (net rate of change) of a species is determined as a function of the species concentration, forward and backward reaction rate constants. Equations (10.2 - 10.4) describe the method of determining the rate of a chemical reaction for species a and b,



$$R_a = -k_f[a] + k_b[b] \quad (10.3)$$

$$R_b = k_f[a] - k_b[b] \quad (10.4)$$

In the case that the reaction is at equilibrium, the net rate R_i is equal to zero. If the chemical reaction rates k_f and/ or k_b for a particular reaction is very large, the net reaction term R_i will be much larger than the other terms in mass balance Equation (10.1) giving $R_i = 0$. This means that the concentrations of the species involved will be at equilibrium irrespective of other processes such as diffusion or migration.

In the case of slow reactions, the concentrations of species are determined by other terms in mass balance Equation (10.1) resulting in a non-equilibrium concentration field. This is the case for carbon dioxide hydration reaction and the reaction rate of species are calculated as shown in Equations (10.6) and (10.7) below.



$$R_{CO_2} = -k_{f,hy}[C_{CO_2}] + k_{b,hy}[C_{H_2CO_3}] \quad (10.6)$$

$$R_{H_2CO_3} = k_{f,hy}[C_{CO_2}] - k_{b,hy}[C_{H_2CO_3}] \quad (10.7)$$

Solving the concentration of the species in the bulk for a known bulk pH and assuming equilibrium, Figure 10.3 depicts the concentrations for variable pH at a temperature of 80°C and $pCO_2 = 0.54$ bar.

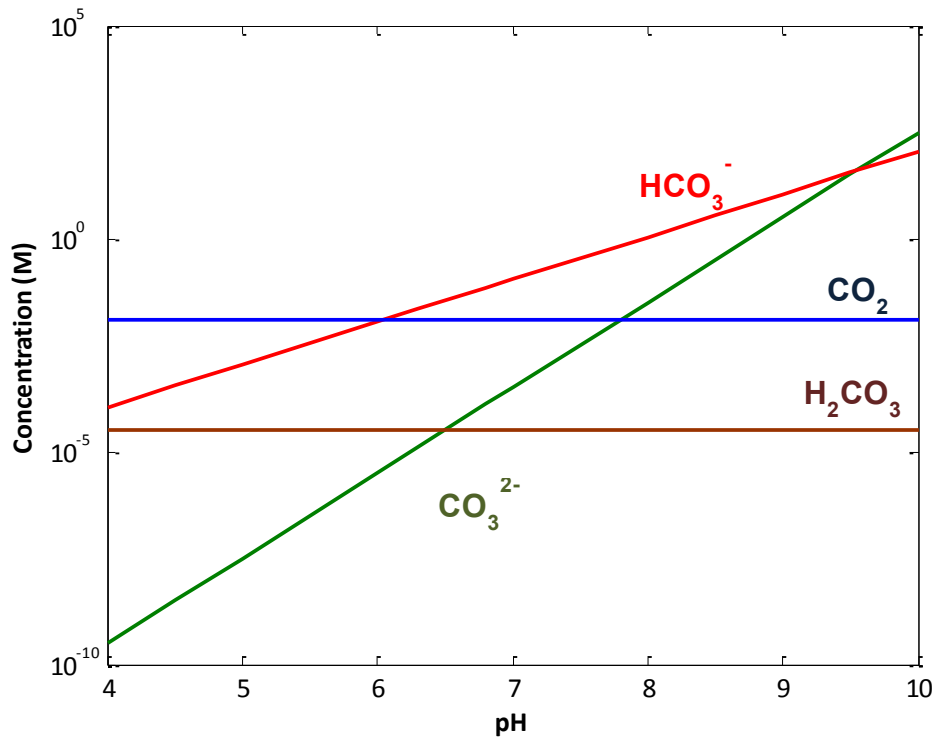


Figure 10.3 Equilibrium distribution of species concentration in bulk solution as a function of pH at T=80°C, pCO₂ = 0.54 bar

10.1.2 Transport of Species between Steel Surface and Bulk

The mass transfer flux between the bulk solution and steel surface is computed for seven different species (CO₂, H₂CO₃, HCO₃⁻, CO₃²⁻, OH⁻, H⁺ and Fe²⁺). The species concentration of Na⁺ and Cl⁻ exceeds the concentration of other species by orders of magnitude. However, the flux of these species are discounted in the following model as they do not directly affect the chemistry of CO₂ corrosion. In the following model, two calculation nodes are used, one in the bulk and the other at the steel surface, so the mass transfer flux between the bulk solution to the steel surface can be calculated for each of the species using a mass transfer coefficient, $k_{m,j}$ approach [71].

$$N_{e,j} = k_{m,j}(C_{bulk,j} - C_{surface,j}) + k_{m,j} \frac{z_j F}{RT} c_{bulk,j} \Delta\phi \quad (10.8)$$

Here $C_{bulk,j}$ is the concentration of the species j in the bulk solution, $C_{surface,j}$ is the concentration of the species j at the steel surface, z_j is the electric charge of species j . The last term, $\Delta\phi$ in the transport equation represents electro-migration due to a small electrical potential difference between the bulk solution and the surface water layer. This term is significant only for the transport of species (Na⁺ and Cl⁻) and therefore can

be assumed to be zero in the mass transfer flux calculations for the above species. Therefore equation (10.8) can be simplified to give [71]:

$$N_{e,j} = k_{m,j}(C_{bulk,j} - C_{surface,j}) \quad (10.9)$$

The mass transfer coefficient, k_m is calculated from correlations for a thin channel flow cell (TCFC), proposed by Sleicher and Rouse [100].

$$k_m = \frac{Sh_T D}{h} \quad (10.10)$$

$$Sh_T = 5 + 0.015(Re_T^a)(Sc^b) \quad (10.11)$$

$$Re_T = \frac{V_T h}{\nu} \quad (10.12)$$

Where Sh_T is Sherwood's number for a TCFC, h is the height of the TCFC, Re_T is the Reynolds number for the TCFC, V_T is the linear velocity of the liquid in the TCFC in (m/s), a, b are empirical constants defined by:

$$a = 0.88 - \frac{0.24}{(4 + Sc)} \quad (10.13)$$

$$b = \frac{1}{3} + 0.5e^{(-0.65c)} \quad (10.14)$$

D is the molecular diffusion coefficient of species in (m^2/s) and is determined from the Equation (10.15). The reference diffusion coefficient [69] for the relevant species is available in literature and tabulated below in Table 10.3.

$$D = D_{ref} \times \frac{T}{T_{ref}} \times \frac{\mu_{ref}}{\mu} \quad (10.15)$$

The dynamic viscosity, μ in kg/m.s and is determined by Equation (10.16) and density, ρ in kg/m^3 by Equation (10.17).

$$\mu = 0.001002 \times 10^{\frac{1.3277 \times (293.15 - T) - 0.01053 \times (298.15 - T)^2}{T - 168.15}} \quad (10.16)$$

$$\rho = (753.596 + 1.87748 \times T - 0.003564 \times T^2) \quad (10.17)$$

μ_{ref} is determined for a reference temperature, T_{ref} of 20°C.

Table 10.3 Reference molecular diffusion coefficient, D_{ref} [69].

Species	Diffusion Coefficient (m^2/s)	Source
CO ₂	1.96×10 ⁻⁹	Perry [101]
H ₂ CO ₃	2.00×10 ⁻⁹	Kvarekva [102]
HCO ₃ ⁻	1.105×10 ⁻⁹	Newman [103]
CO ₃ ²⁻	0.92×10 ⁻⁹	Kvarekva [102]

H ⁺	9.312×10 ⁻⁹	Newman [103]
OH ⁻	5.26×10 ⁻⁹	Newman [103]
Fe ²⁺	0.72×10 ⁻⁹	Kvarekva [102]

10.1.3 Electrochemical Reactions at Surface

The electrochemical reactions at the steel surface considered in the following model are listed in Table 10.4

Table 10.4 Electrochemical reactions at steel surface

Process Description	Reaction
Electrochemical dissolution of iron	$Fe \rightarrow Fe^{2+} + 2e^{-}$
Hydrogen evolution	$2H^{+} + 2e^{-} \rightarrow H_2$
Direct reduction of carbonic acid	$2H_2CO_3 + 2e^{-} \rightarrow H_2 + 2HCO_3^{-}$

The species flux due to the electrochemical reactions at the steel surface can be determined from:

$$N_{w,j} = \pm \frac{i_j}{n_j F} \quad (10.18)$$

Where i_j is the total current density (A/m²), n_j is the number of moles of electrons exchanged per mole of species j participating in a particular electrochemical reaction. The positive sign is applied for species consumed and the negative sign for species produced by electrochemical reactions at the steel surface. For those species that are not involved in the electrochemical reactions, $i_j = 0$.

The current density for reduction of H⁺ consists of two components [104]: charge transfer current and mass transfer limiting current. Total current density is calculated as follows:

$$i_{H^+} = (i_{\alpha,H^+} \times i_{lim,H^+}^d) / (i_{\alpha,H^+} + i_{lim,H^+}^d) \quad (10.19)$$

Where i_{H^+} is total current density of H⁺ reduction (A/m²), i_{α,H^+} is the charge transfer current density (A/m²), i_{lim,H^+}^d is the diffusion limiting current density calculated by the equation (10.20).

$$i_{lim,H^+}^d = k_{m,H^+} F C_{H^+} \quad (10.20)$$

Where k_{m,H^+} is the H^+ mass transfer coefficient (m/s) and C_{H^+} is the bulk concentration of H^+ (mol/m³).

Similarly, the total current density of H_2CO_3 reduction [105] is given by:

$$i_{H_2CO_3} = (i_{\infty,H_2CO_3} \times i_{lim,H_2CO_3}^r) / (i_{\infty,H_2CO_3} + i_{lim,H_2CO_3}^r) \quad (10.21)$$

Where $i_{H_2CO_3}$, i_{∞,H_2CO_3} , $i_{lim,H_2CO_3}^r$ are the total current density, the charge transfer current density, and the mass transfer limiting current density of the reaction in A/m² respectively.

The CO_2 hydration reaction limiting current density is calculated by:

$$i_{lim,H_2CO_3}^r = F \times C_{CO_2} \times (D_{H_2CO_3} K_{hy} K_{f,hy})^{0.5} \quad (10.22)$$

Where F is Faraday's constant, C_{CO_2} is the bulk concentration of dissolved carbon dioxide, $D_{H_2CO_3}$ is the diffusion coefficient of H_2CO_3 , K_{hy} is the equilibrium constant of the CO_2 hydration reaction and $K_{f,hy}$ is the forward hydration reaction constant.

The charge transfer current density for each species is calculated using the tafel equation [71].

$$i = i_0 \times 10^{\pm \frac{E-E_0}{b}} \quad (10.23)$$

Where i represents the reaction current density in A/m², i_0 represents a reference current density in A/m², E represent the corrosion potential of the steel in V, E_0 represent a reference potential in V and b represent the tafel slope in V/decade. In the model, the current density for each electrochemical reaction depends on the surface concentration of species, which is not explicitly known and needs to be calculated. For a spontaneous corrosion process, the unknown corrosion potential of the steel, E can be calculated from the charge balance equation at the steel surface [71]:

$$\sum_{cathodic} i = \sum_{anodic} i \quad (10.24)$$

The exchange current density, i_0 for each electrochemical reaction is calculated by the following equation [69] with the constant defined in Table 10.5:

$$i_0 = \left(\frac{C_{H^+}}{C_{H^+ref}} \right)^{a_1} \left(\frac{C_{CO_2}}{C_{CO_2ref}} \right)^{a_2} \left(\frac{C_{H_2CO_3}}{C_{H_2CO_3ref}} \right)^{a_3} \times e^{-\frac{\Delta H}{R} \left(\frac{1}{T} - \frac{1}{T_{ref}} \right)} \quad (10.25)$$

Substitution of flux density due to electrochemical reactions expressed by Equation (10.18) and mass transfer processes (10.9) into mass balance Equation (10.1) yields the final transport equation which is written for each species.

$$\Delta x \frac{\partial c_{surface,j}}{\partial t} = - \left(\pm \frac{i_j}{n_j F} \right) + k_{m,j} (C_{bulk,j} - C_{surface,j}) + \Delta x \times R_j \quad (10.26)$$

Table 10.5 Electrochemical parameters for the reactions included in the model which fit the general rate Equation (10.23) and exchange current density Equation (10.25) [69].

Reaction	i_{0ref} $\left(\frac{A}{m^2}\right)$	a_1	c_{H^+ref} (M)	a_2	c_{CO_2ref} (M)	a_3	$c_{H_2CO_3ref}$ (M)	ΔH $\left(\frac{kJ}{mol}\right)$	T_{ref} (°C)	E_{rev} (V)	b (V)
$2H^+ + 2e^- \rightarrow H_2$	0.05	0.5	10^{-4}	0	N/A	0	N/A	30	25	$-\frac{2.3RT}{F}pH$	$\frac{2.3RT}{2F}$
$2H_2CO_3 + 2e^- \rightarrow H_2 + 2HCO_3^-$	0.06	-0.5	10^{-5}	0	N/A	1	10^{-4}	50	20	$-\frac{2RT}{F}pH$	$\frac{2.3RT}{2F}$
$Fe \rightarrow Fe^{2+} + 2e^-$	1	$p_{CO_2} < 1 \text{ bar} - 1$ $p_{CO_2} = 1 \text{ bar} - 0$	10^{-4}	pH < 4 - 2 4 < pH < 5 - 1 pH > 5 - 0	0.0366	0	N/A	37.5	25	-0.488	pH < 4 - 0.03 4 < pH < 5 - 0.08 pH > 5 - 0.12

10.2 Step-wise Implementation of MATLAB Model

The above theory is implemented into MATLAB numerical programming to predict the steady state corrosion rate of X65 carbon steel in a CO₂ containing environment. The model shall be validated experimentally through comparison with results from the thin channel flow cell discussed in Chapter 8. The model initially provides a user interface to define input parameters in the form of temperature, partial pressure CO₂, flow velocity, height of thin channel, ionic strength, total pressure and bulk pH. These parameters are then fed into a sequence of equations to solve for the three physiochemical processes. The model is solved for steady state conditions and therefore the surface concentration as a function of time, $\frac{\partial C_{surface,j}}{\partial t}$ is equal to 0. The bulk concentrations of all related species are determined; assuming chemical reactions in Table 10.1 are in equilibrium. Equilibrium reaction rate coefficients are listed in Table 10.2. This solves for the $C_{bulk,j}$ term in the final transport Equation (10.26) for all species.

$$0 = -\left(\pm \frac{i_j}{n_j F}\right) + k_{m,j} (C_{bulk,j} - C_{surface,j}) + \Delta x \times R_j \quad (10.27)$$

The mass transfer coefficient for each species is dependent on input parameters and are calculated for either turbulent pipe flow or thin channel flow depending on the system under consideration. Therefore solving a second term of the final transport equation.

$$0 = -\left(\pm \frac{i_j}{n_j F}\right) + k_{m,j} (C_{bulk,j} - C_{surface,j}) + \Delta x \times R_j \quad (10.28)$$

The surface concentration of species are unknown and an initial assumption of the surface concentration of H⁺ (C_{s,H}) is initially predicted by MATLAB. As discussed in Section 8.1, the chemical reaction rates k_f and k_b for water, carbonic anion and bicarbonate anion dissociation are very large, therefore the rate of reaction R_i ≈ 0 and concentrations of the species involved are assumed to be in equilibrium. Hence the surface concentration of OH⁻ is determined from the equilibrium equation.

$$C_{s,OH^-} = K_{wa}/C_{s,H^+} \quad (10.29)$$

The final transport Equation (10.26) is then listed for the remaining species. The reaction rate of species in carbon dioxide hydration reaction are implemented from Equation (10.6, 10.7).

$$0 = -\frac{i_{H_2CO_3}}{F} + k_{m,H_2CO_3}(C_{b,H_2CO_3} - C_{s,H_2CO_3}) + (k_{f,hy}[C_{s,CO_2}] - k_{b,hy}[C_{s,H_2CO_3}]) \quad (10.30)$$

$$0 = \frac{i_{HCO_3}}{F} + k_{m,HCO_3}(C_{b,HCO_3} - C_{s,HCO_3}) \quad (10.31)$$

$$0 = k_{m,CO_3}(C_{b,CO_3} - C_{s,CO_3}) \quad (10.32)$$

$$0 = k_{m,CO_2}(C_{b,CO_2} - C_{s,CO_2}) + (k_{b,hy}[C_{s,H_2CO_3}] - k_{f,hy}[C_{s,CO_2}]) \quad (10.33)$$

The four transport Equations (10.30– 10.33) are rearranged and substituted and the surface concentrations are then solved for using MATLAB solver.

The next stage of the program is determining the surface potential, E. With the initial assumption of the surface concentrations, the unknown corrosion potential of the steel, E is calculated from the charge balance equation (10.24) at the steel surface.

The total cathodic current density can be calculated from the calculated potential, E and initial guess for surface concentrations.

$$i_{cathodic} = i_{H^+} + i_{H_2CO_3} \quad (10.34)$$

The final stage of the MATLAB program is to verify if the initial assumption of C_{H^+} satisfies the steady state condition in Equation (10.27). Failing which, a new initial surface concentration, C_{H^+} is determined by bi-section method. This method is a root finding method that repeatedly bisects an interval and then selects a subinterval in which a root must lie for further processing. The process is continued until the steady state condition is met.

10.3 Steady State Corrosion Rate Model Results

10.3.1 Model Validation with Literature

The MATLAB model was implemented and run for varying pH, temperature and velocity values. At the initial stage, the model was compared against results from Nestic et al. [71] published working model in order to validate against literature. Figure 10.4 and Figure 10.5 show the results of the comparison for the steady state corrosion rate against varying velocity for a pH of 4 and 6 respectively. The working conditions were for a turbulent pipe flow of diameter of 0.01 m and fluid parameters of 20°C, 1 bar pCO₂ and 1 wt% NaCl.

The comparison shows a close correlation between the two models however there are observed differences. At a lower pH of 4, the pattern of corrosion rate against velocity is seen to follow the same trend for both models with

the predicted values being more similar for lower velocities. At a pH of 6, the Nescic model corrosion rate is seen to vary a little more with velocity than the developed model. However they both do not vary significantly.

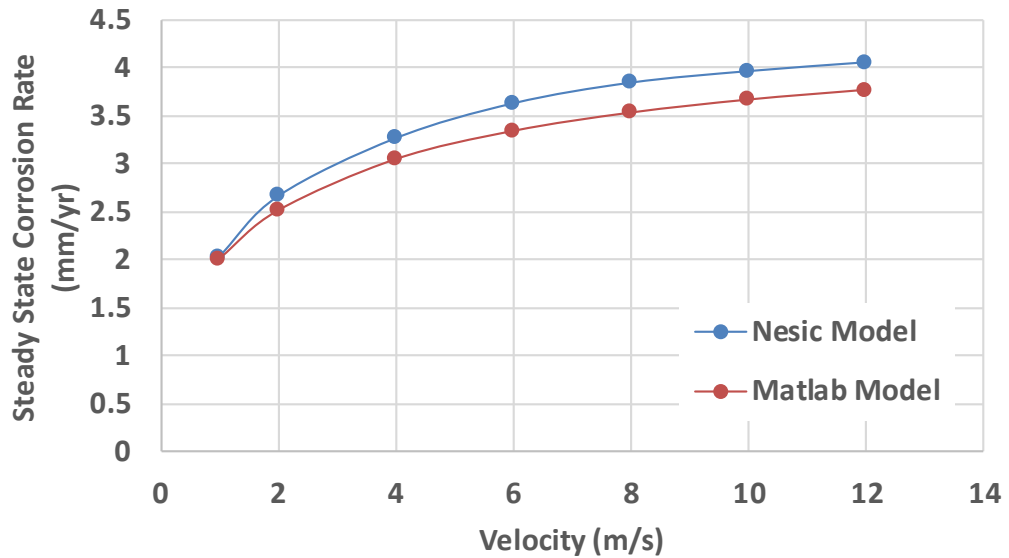


Figure 10.4 Comparisons between model predictions results at 1 bar CO₂, 20°C, pH 4 and 1wt% NaCl.

In Figure 10.5, at pH 6, the H⁺ ion concentration in the bulk is significantly small therefore the surface concentration due to mass transfer would be even lower. Despite there being a slightly higher H⁺ ion concentration at the surface at a higher velocity due a higher mass transfer coefficient, the resulting change in corrosion rate would be predicted to be very minor. In comparison, at pH 4, there is a much larger bulk H⁺ ion concentration resulting in a more significant difference in surface H⁺ ion concentration due to mass transport and the more variable corrosion rate as a function of velocity observed in Figure 10.4.

The slight differences between the models may be due to many possible reasons. In Nescic et al. publications [35, 36, 71, 98, 104, 105], as discussed, there is a theoretical foundation to the models however there are gaps in each individual research which were developed based on a more combined understanding from various sources leading to possible differences in the development of the model. Furthermore, the values of corrosion rate against velocity for the two pH values were obtained from published figures [71] through a web plot digitiser with a sensitive marker which may attribute to slight differences in accurately reading the graph.

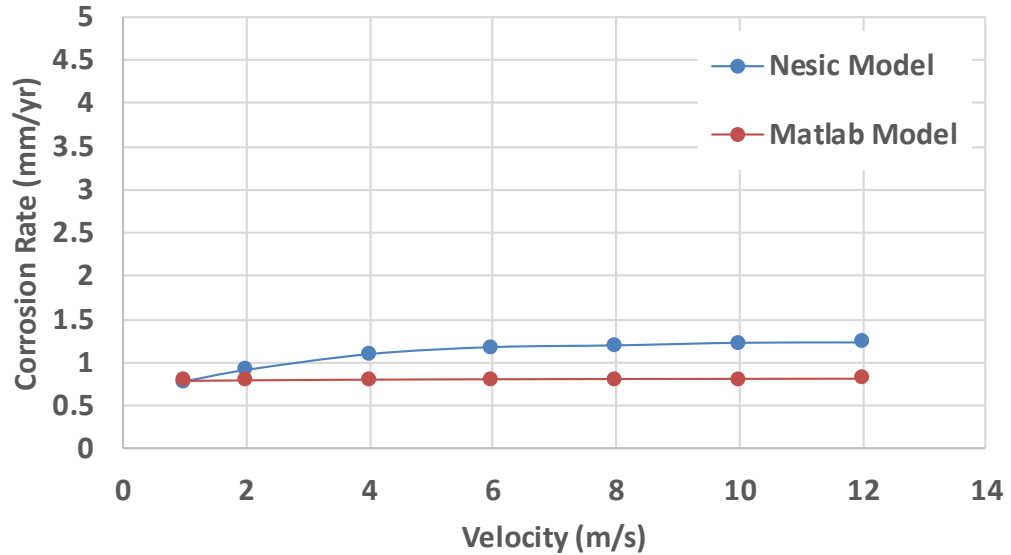


Figure 10.5 Comparisons between model predictions results at 1 bar CO₂, 20°C, pH 6 and 1wt% NaCl.

Overall, however, it may be reasoned that the two models have a similar trend and both effectively predict the steady state corrosion rate to a certain degree of error.

10.3.2 Model Sensitivity Analysis

In the next stage, a sensitivity analysis of the effect of pH and temperature on the predicted steady state corrosion rate was determined.

Figure 10.6 shows the effect of pH where the pH was varied from 4 to 7 for fluid parameters of 80°C, 0.54 bar pCO₂, 3.5 wt % NaCl and a flow velocity of 1 m/s. The figure shows a higher corrosion rate for a lower pH. The corrosion rate decreases significantly from a pH of 4 to 5. Further increasing the pH reduces the corrosion rate however the trend is observed to be less dependent on the pH. The observed trend is as would be expected in an experimental system. A higher bulk pH corresponds to a lower bulk concentration of H⁺ ions. Therefore a lower flux of H⁺ ions towards the surface that principally determines the rate of the electrochemical reaction resulting in a lower corrosion rate.

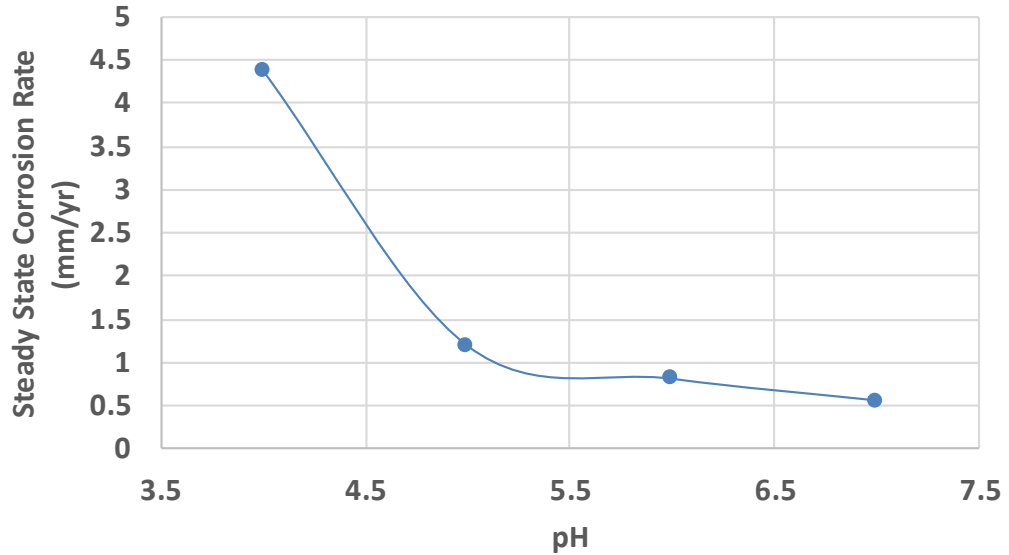


Figure 10.6 Effect of pH on predicted steady state corrosion rate using developed model.

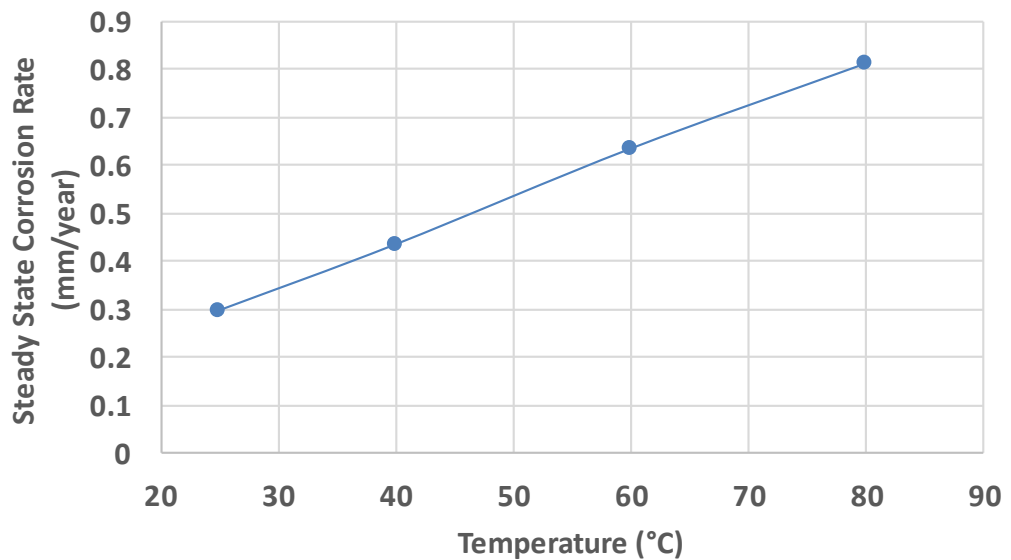


Figure 10.7 Effect of temperature on predicted steady state corrosion rate using developed model.

Figure 10.7 shows the effect of temperature which was varied from 25°C to 80°C for fluid parameters of pH 6, 0.54 bar pCO₂, 3.5 wt % NaCl and a flow velocity of 1 m/s. A linear trend is observed with an increasing temperature due to an increase in the rate of kinetics that makes the bare steel corrosion rate higher especially when there is no corrosion product layer formed/ in the beginning of experiments. The formation of protective iron carbonate layer is also promoted at high temperatures and therefore the corrosion rate decreases more rapidly with temperature increase if corrosion product and time dependency was taken into consideration.

10.3.3 Model Validation with Experimental Results

The final stage of the development of the steady state corrosion model is its validation with experimental data. In the previous chapter, the corrosion rate was observed in a thin channel flow cell for working condition of 80°C, pH 6.8, 3.5 wt% NaCl, pCO₂ 0.54 bar and varying velocity. The model was modified to theoretically predict the mass transfer in a thin channel flow cell and was applied for the same parameters. Figure 10.8 shows the comparison between the experimental corrosion rate and the predicted corrosion rate for the defined conditions.

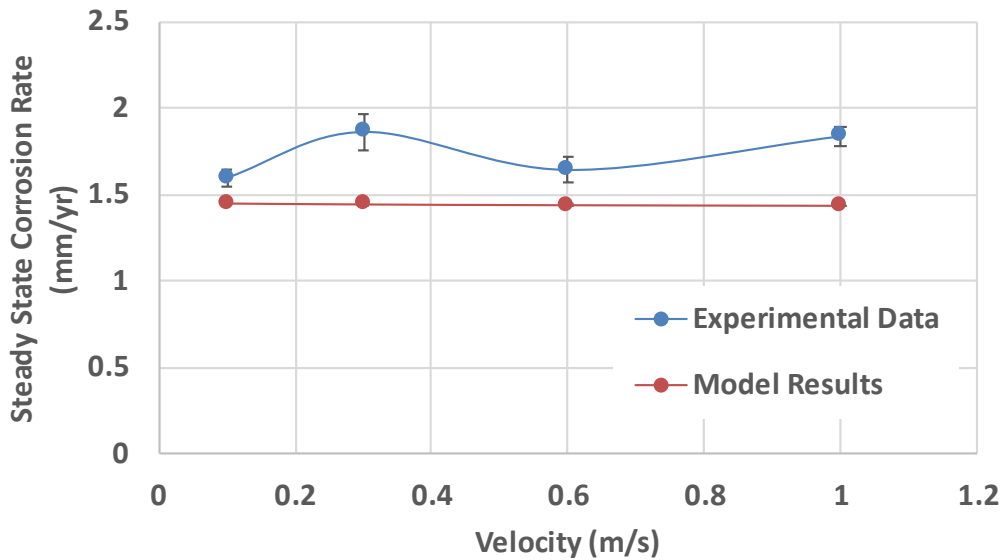


Figure 10.8 Comparison of experimental results with model output for variable velocity at 80°C, pH 6.8, pCO₂ 0.54 bar and 3.5 wt% NaCl.

The steady state corrosion rate from the experimental results in the thin channel flow cell (Figure 9.6) was inferred to be the maximum corrosion rate in each test as it does not involve significant formation of any film. There is a good correlation between the experimental results and the output from the steady state corrosion model supporting the validity of the model.

Chapter 11

Modelling Near Surface Region for CO₂ Corrosion

The developed mechanistic model in the following PhD consists of two parts: a MATLAB steady state corrosion model and a COMSOL model. The MATLAB model was described in detail in the previous chapter and is limited to a bimodal computational domain. It provides the steady state corrosion rate at the surface which determines the resulting flux of species at the surface. The MATLAB model can be applied to pipe flow, RCE flow or thin channel flow depending on input parameters. The COMSOL model which shall be described in the following chapter extends this analysis to a two-dimensional domain consisting of multiple nodes providing information on the nature of the near surface region for a thin channel flow cell. The model geometry was developed based on the design of the flow cell discussed in Chapter 7 and is intended to predict the surface characteristics to complement the experimental work carried out. Simulating the model for the same working conditions carried out within the flow cell shall provide an understanding of the surface conditions at the initial stage, prior to any substantial film development that may drive the precipitation of the film that is observed experimentally.

11.1 COMSOL Model Development

COMSOL Multiphysics is a finite element analysis, solver and simulation software package for various physics and engineering applications. It provides the ability to couple different physics and in the following model, fluid flow and distribution of diluted species are combined to analyse a carbon steel surface under CO₂ corrosion.

The model geometry, as shown in Figure 11.1 is a two dimensional flow channel with an outflux of Fe²⁺ ions and influx of H⁺ across a length of 10 mm which is the size of the X65 carbon steel sample used in the experimental analysis.

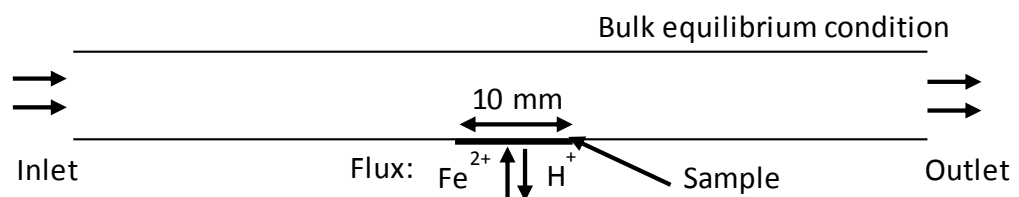


Figure 11.1 Schematic diagram describing COMSOL analysis

The COMSOL model is developed through five different stages:

- **Geometry:** This is where the two dimensional space in Figure 11.1 is defined. The geometry is drawn to best fit a simplification of the problem in question. The sample is 10 mm in length to represent sample size in the lab for future experimental correlation.
- **Materials:** The area passing over the sample/ flowing through the system is defined as water with all its relative properties such as viscosity and density at the indicated fluid temperature.
- **Physics:** In this stage, two different physics are defined. Fluid flow which can be laminar or turbulent depending on the flow rate/ Reynold's number at the inlet. This is coupled with distribution of diluted species which facilitates the definition of flux at the sample surface as a result of corrosion, bulk equilibrium species concentration, reaction rates of species, etc. Defining the flow across the sample is essential to determine the resulting transport of species.
- **Mesh:** The most appropriate mesh is defined for accurate, efficient Multiphysics solutions. A mesh sensitivity analysis is performed in order to determine the optimum mesh density.
- **Study:** A stationary solver is used in the model as the field variables do not change with time and the model is solved for steady state conditions.

The chemistry behind the COMSOL model is identical to the MATLAB model in terms of bulk equilibrium and reaction rates. The boundary conditions are determined for bulk equilibrium where the species concentrations are determined from their equilibrium constants. As in the MATLAB model, the forward and backward dissociation reaction rates are significantly large and the reaction is assumed to be at equilibrium. The reaction rates taken into account in the model are that of the slow hydration reaction where R_{CO_2} and $R_{H_2CO_3}$ are determined as expressed in Equation (10.6) and (10.7). The steady state corrosion rate determined from the MATLAB model is used to determine the surface flux of Fe^{2+} and H^+ ions at a certain set of conditions (pH, temperature, total pressure, etc.). The flux is determined from Faraday's Law as shown in equation (11.1 – 11.3).

$$CR = \frac{M}{nF\rho} i_{corr} \quad (11.1)$$

$$N_{Fe} = + \frac{i_{corr}}{2 \times F} \quad (11.2)$$

$$N_H = - \frac{i_{corr}}{F} \quad (11.3)$$

Where M is the atomic weight in (g/mole), ρ is the density in (g/m³), n is the charge number which indicates the number of electrons exchanged in the dissolution reaction, F is the Faraday constant (96486 C/mol), i_{corr} is the corrosion current (A/cm²) and CR is the corrosion rate in (mm/yr).

The transport of the diluted species module calculates the concentration field of the relevant species with the defined mesh that provides the nodes for the computational domain. The driving forces for transport are diffusion by Fick's law and convection that is coupled to the defined flow field. Migration is not taken into account in the following model as it assumed to be negligible due to the significantly small magnitude of the concentration of the ionic species. Whenever mass transport of a dissolved species is considered, concentration gradients will cause diffusion. If there is bulk fluid motion, convection will also contribute to the flux of chemical species. Therefore, the following model is solved for the combined effect of both convection and diffusion.

A simplification of the computational grid for the solution to the COMSOL model is shown in Figure 11.2.

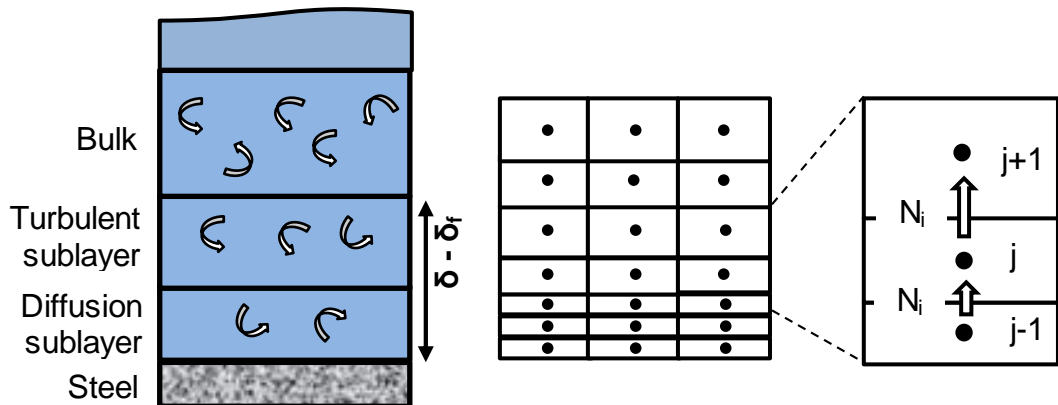


Figure 11.2 Simplified sketch of computational grid and control volumes used for discretisation of the computational domain in COMSOL. δ - δ represents the liquid boundary layer thickness.

Figure 11.2 represents a sketch of the computational grid solved using COMSOL. The number and size of the domain elements are dependent on the mesh density and are analysed in the following section.

The transport of diluted species interface models chemical species transport through diffusion and convection and solves the mass conservation equation for the relevant chemical species i :

$$\frac{\partial c_i}{\partial t} + \nabla \cdot N_i = R_i \quad (11.4)$$

$$N_i = -D_i \nabla c_i + c_i u \quad (11.5)$$

Where c_i is the concentration of species (mol/m^3), D_i denotes the diffusion coefficient (m^2/s), R_i is a reaction rate expression for the species ($\text{mol/m}^3 \cdot \text{s}$) and u is the velocity vector (m/s). The flux vector N is associated with the mass balance equation and used in boundary conditions and flux computations. The first term of Equation (11.4), $\frac{\partial c_i}{\partial t}$ corresponds to the accumulation (or consumption) of the species. It is considered to be equal to zero in the following model as it is being solved for steady state and computed using a stationary solver. $\nabla \cdot N_i$ in Equation (11.4) accounts for the transport mechanisms where the second term, $\nabla \cdot N_i$ accounts for diffusive transport, accounting for the interaction between the dilute species and the solvent. An input field for the diffusion coefficient is available and the values are input from Equation (10.15) as computed in the MATLAB model. The third term on the right side of Equation (11.5), $c_i u$ describes the convective transport due to a velocity field u . This field can be expressed analytically or obtained from coupling this physics interface to one that computes fluid flow. On the right hand side of the mass balance equation, R_i represent as source or sink term, typically due to a chemical reaction. To specify R_i , another component is added to the transport of diluted species interface, the reaction node, which has a field for specifying a reaction equation using the variable names of all participating species discussed previously.

Equation (11.5) is for the case where the diffusion and convection are the only transport mechanisms considered. If migration in electric fields is activated, the flux vector is amended with the migration term as shown in equation (11.6).

$$N_i = -D_i \nabla c_i + c_i u - z_i u_i F c_i \frac{\partial \phi}{\partial x} \quad (11.6)$$

Where z_i is the electrical charge of species i , u_i is the mobility of species, F is the Faraday's constant and ϕ is the electrical potential. However, it is noted in Nesic et al. [35, 69] that the proportionality constant $\frac{\varepsilon F}{k \xi}$ in equation (11.6) is so large that even a tiny separation of charge results in an appreciable potential gradient which in practise prevents any significant separation in charge. Instead of equation (11.7), the simple electro-neutrality equation (11.8) is implemented:

$$\frac{\partial}{\partial x} \left(\kappa \xi \frac{\partial \phi}{\partial x} \right) = -\varepsilon F \sum_i z_i c_i \quad (11.7)$$

$$\sum_i z_i c_i = 0 \quad (11.8)$$

This electro-neutrality equation is based on an assumption that any, however small, amount of solution is always electroneutral therefore there is a perfect balance between the positively and negatively charged species everywhere in the solution. In other words, there is no charge separation that occurs.

Finally, the model is developed from the above discussed input parameters and combined physics producing an output in the form of the species concentration at the very near surface of a carbon steel sample. It provides insight into the flux of the different relevant species at the very early stages of CO₂ corrosion. It also allows us to determine, for a specific set of conditions, the liquid boundary layer thickness, the pH and saturation profile as a function of distance from the surface.

11.2 Mesh Sensitivity Analysis

The created mesh is an integral part of the COMSOL model development. The accuracy of the model output is directly dependant on the mesh density, element type and shape. A high density mesh will produce results with high accuracy. However, if a mesh is too dense, it will require a large amount of memory and computational time.

In the following study, the quality of the mesh is evaluated through mesh refinement and interpretations of result discontinuities. The mesh is refined until the critical result at a specific location converges. The output under study is the super saturation ratio as it is a key aspect in the following study. Recalling from literature, the saturation ratio is calculated from the concentration of the Fe²⁺ and CO₃²⁻ ions at each node and divided by the solubility constant at the given conditions. The model is run for input conditions of 80°C, pH 6.8, CO₂ partial pressure of 0.54 bar, 3.5 wt% NaCl and 1 m/s inlet velocity. The steady state corrosion rate is determined through the MATLAB model and fed into COMSOL.

The main shift in super saturation takes place at the very near surface region approximately within 120 µm from the defined sample surface. Therefore a well-defined boundary layer mesh is applied and the number of boundary layers is increased until there is no significant change in results for a change in number of elements. Figure 11.3 shows that there is a significant change in the SS trend as a function of the distance of the metal surface for different

number of elements and the curve is observed to be smoother for a higher mesh density as there are more nodal points. Above 47518 total elements (boundary and domain), the SS curve tends to overlap. Therefore the results are consistent and a suitable mesh has been determined. The defined mesh consists of 120 boundary layers with a nodal distance of 10^{-8} m.

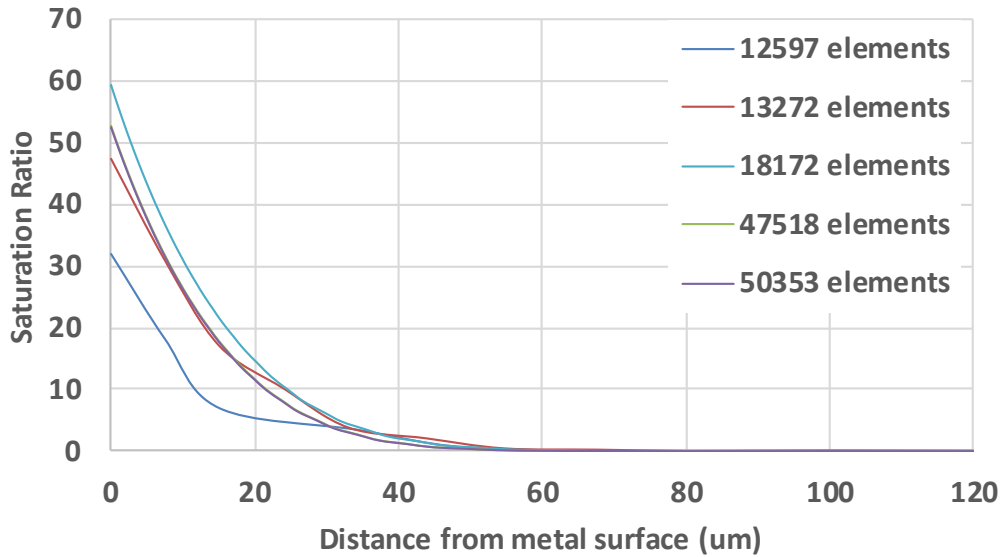


Figure 11.3 Saturation ratio trend for varying number of mesh elements.

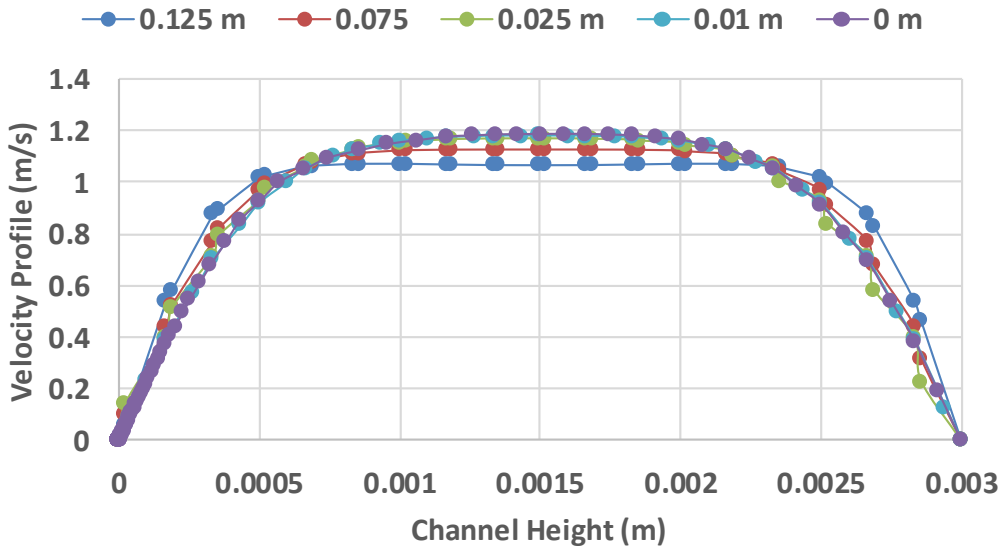


Figure 11.4 Flow velocity profile across channel height at different sections of the flow channel.

Another key parameter to the COMSOL model is the flow velocity profile. The flow is considered to be fully developed when the velocity profile remains unchanged. Therefore, the velocity profile is determined at different sections of the flow channel, for 1 m/s, to ensure the flow across the surface

of the sample is fully developed at the fastest velocity run through the flow cell. Figure 11.4 shows the results of the velocity profile for a varying distance from the sample where 0.165 m is at the start of the defined channel and 0 m is the location of the sample as indicated in the legend. The results show that as the flow moves along the channel, the velocity profile becomes more parabolic and at a distance of 0.025 m from the sample, the flow enters the fully developed stage where it remains unchanged thereafter.

Furthermore, the velocity profile is predicted for a mesh of 47518 and 50353 total elements in order to ensure that there is no change in predicted values for the selected mesh density. Increasing the number of elements produces no observable change in velocity profile and the results to overlap as shown in Figure 11.5. Therefore, the defined mesh consisting of 47,518 elements may be considered to accurately simulate the model output. The computational time for the model is 152s and is used throughout future model computations.

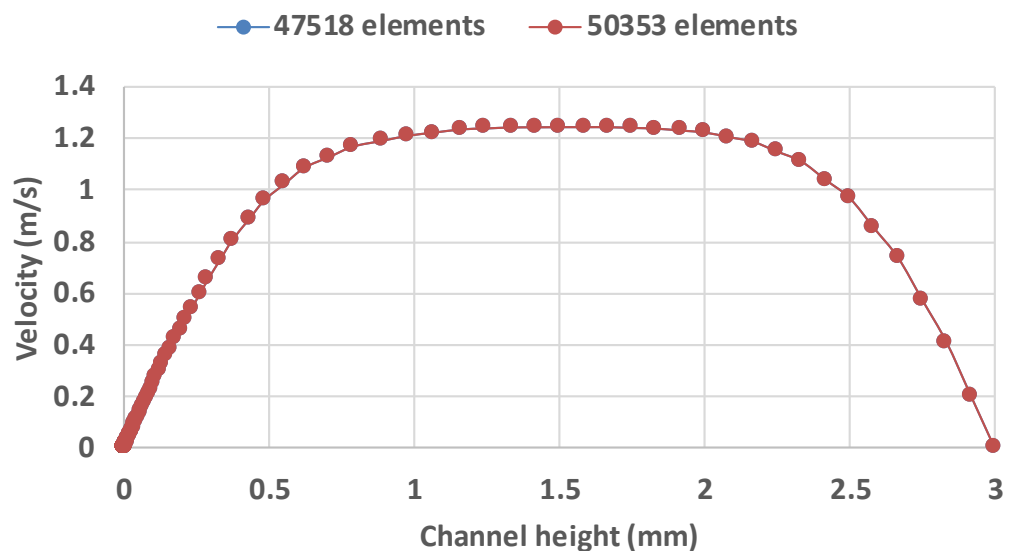


Figure 11.5 Flow velocity across height of channel at centre of geometry.

11.3 Model Validation with Literature

The next stage of the development of the model is its validation in order to ensure that the attained results are sensible and effectively represent what occurs in a CO₂ corrosive environment. In this stage, the only available method is comparison with existing published model results. Figure 11.6 shows the published figure by Nestic et al. [35] for the concentration deviation from bulk as a function of distance from the metal surface. In this work, Nestic's model was computed for conditions of no film at 20°C, pH 6,

partial pressure of CO₂ of 1 bar, 1 m/s inlet velocity and pipe diameter of 0.1m diameter.

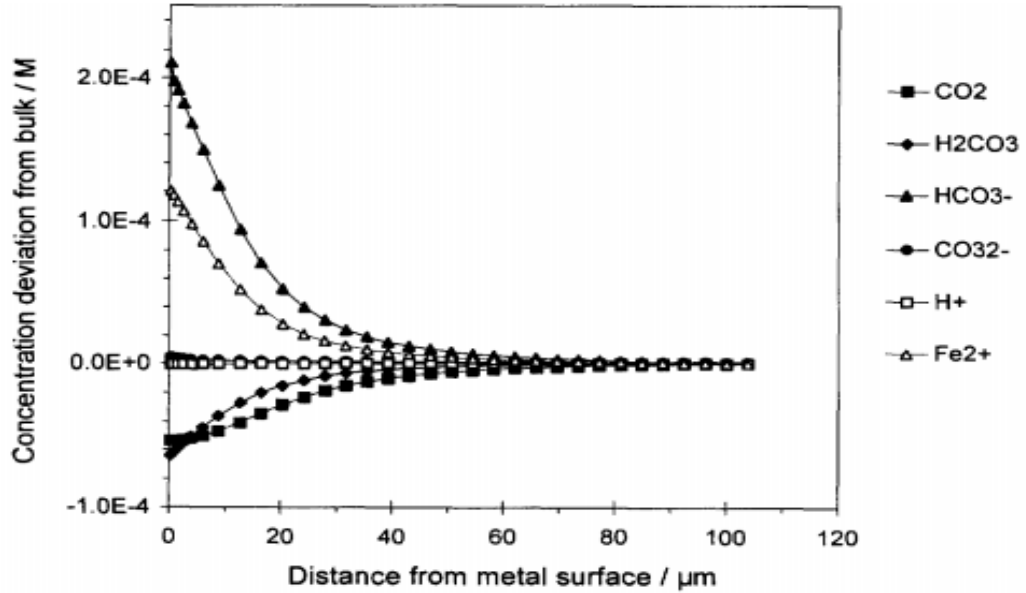


Figure 11.6 Deviation of dissolved species concentration from the bulk values as a function of distance from the steel surface; 20°C, pipe diameter 0.1 m, flow velocity 1 m/s and pH 6, pCO₂ = 1 bar.

The model by Nestic et al. [35] is for turbulent pipe flow where as the model developed in COMSOL is for thin channel flow. Therefore there is a main difference in the transport mechanisms used in the two models.

According to work done by Nor et al. [100], the equivalent flow velocity of two different flow geometries can be calculated by equating the mass transfer coefficients. The same mass transfer coefficients imply a similar corrosion rate for the same operational parameters and water chemistry.

The mass transfer coefficient, k_m for a thin channel flow cell (TCFC) is calculated according to Equations (11.9 – 11.12) and was proposed by Sleicher and Rouse [106].

$$k_{m,T} = \frac{Sh_T D}{h} \quad (11.9)$$

$$Sh_T = 5 + 0.015(Re_T^a)(Sc^b) \quad (11.10)$$

$$Sc = \frac{\nu}{D} \quad (11.11)$$

$$Re_T = \frac{V_T h}{\nu} \quad (11.12)$$

where $k_{m,T}$ is the mass transfer for the TCFC, Sh_T is Sherwood's number for a TCFC, Sc is Schmidt number, h is the height of the TCFC in m, Re_T is the Reynolds number for the TCFC, D is the diffusion coefficient in m²/s, ν is the

kinematic viscosity of water in m²/s, V_T is the linear velocity of the liquid in the TCFC in (m/s), a, b are empirical constants defined by:

$$a = 0.88 - \frac{0.24}{(4 + Sc)} \quad (11.13)$$

$$b = \frac{1}{3} + 0.5e^{(-0.6Sc)} \quad (11.14)$$

The mass transfer coefficient, k_m for pipe flow [107] is calculated according to Equations (11.9 – 11.12).

$$k_{m,Pipe} = \frac{Sh_p D}{Dia} \quad (11.15)$$

$$Sh_p = 0.0165 * (Re_p^{0.86})(Sc^{0.33}) \quad (11.16)$$

$$Sc = \frac{v}{D} \quad (11.17)$$

$$Re_p = \frac{V_p Dia}{v} \quad (11.18)$$

where $k_{m,Pipe}$ is the mass transfer coefficient for the pipe, Sh_p is Sherwood's number for pipe flow, Dia is the diameter of the pipe, Re_p is the Reynolds number for the pipe, D is the diffusion coefficient in m²/s, V_p is the linear velocity of the liquid in (m/s).

The diffusion coefficient, D is a main factor in the calculation of the mass transfer coefficient and is a function of temperature and dynamic viscosity according to Equation (11.19) [108].

$$D = D_{ref} \times \frac{T}{T_{ref}} \times \frac{\mu_{ref}}{\mu} \quad (11.19)$$

The equations were implemented into a MATLAB program and was computationally solved for a pipe diameter (Dia) of 0.1m and flow channel height (h) of 0.003m. Therefore, for a flow velocity of 1m/s through at 0.1m diameter pipe at 20°C, pH 6 and pCO₂ of 1 bar, the corresponding flow velocity in a thin channel is approximately 0.47 m/s.

The conditions are input and modelled through a combination of the developed MATLAB and COMSOL models. The results are shown in Figure 11.7. There are slight variations in the concentrations however they fall within the same order of magnitude and follow the same trend with the species concentration deviation merging after approximately 100 μm. This corresponds to the liquid boundary layer thickness. The combined MATLAB and COMSOL model have been developed on a similar literature background to that performed by Nestic et al. Due to certain limitations in the information available, a more accurate correlation is deemed unachievable

however, the low margin of difference in the comparison proves that the model is successful in its computation.

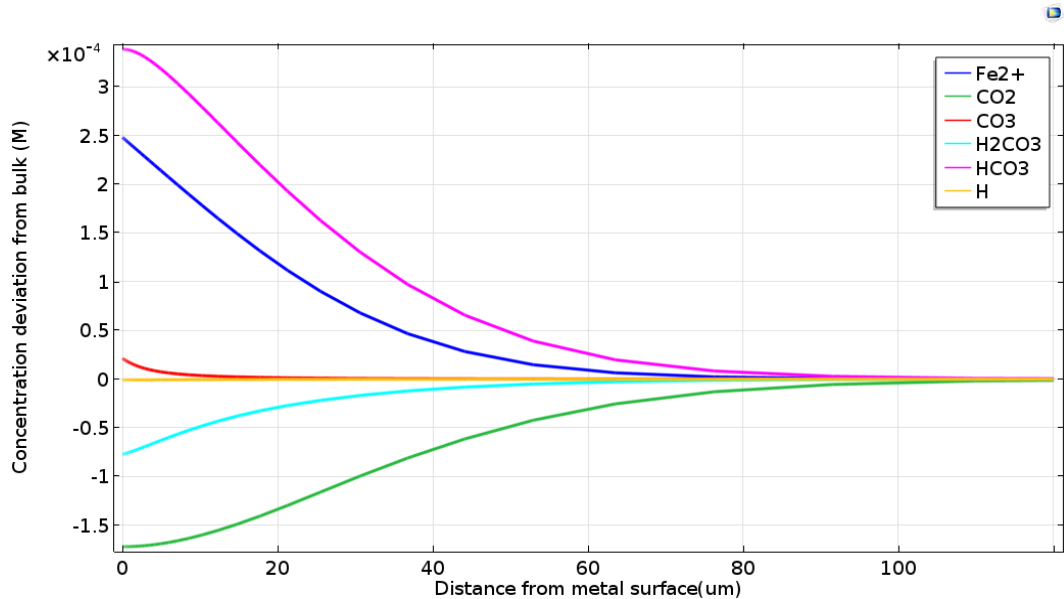


Figure 11.7 COMSOL model output for deviation of dissolved species concentration from the bulk values as a function of distance from the steel surface; 20°C, 3mm channel height, flow velocity 0.47 m/s and pH 6, $p\text{CO}_2 = 1$ bar.

Figure 11.7 shows that the concentration deviation from the bulk is negative for some species (bulk concentration greater than the surface) and positive for others (surface concentration greater than the bulk). At pH 6, there is very little H^+ available in the bulk and the relative concentration deviation is close to 0 as the mass transport of CO_2 and H_2CO_3 towards the surface are much larger than that of H^+ . These are shown as negative as these species move in the negative x direction and the bulk species concentration is always greater than the surface. In the vicinity of the surface, CO_2 is hydrated to H_2CO_3 which is then consumed at the metal surface by dissociation to H^+ which is then reduced. The corrosion products HCO_3^- and Fe^{2+} are transported away from the metal surface and is shown as positive as the surface concentration is relatively greater.

The developed model is further supported in the comparison between Figure 11.8 and Figure 11.9. In another publication by Netic et al. [35], the model was run for similar conditions however an initial bulk Fe^{2+} concentration of 1 ppm and pH is varied. Output is delivered in the form of supersaturation as a function of the distance from the metal surface. The results from the COMSOL model for the above conditions is shown in Figure 11.9.

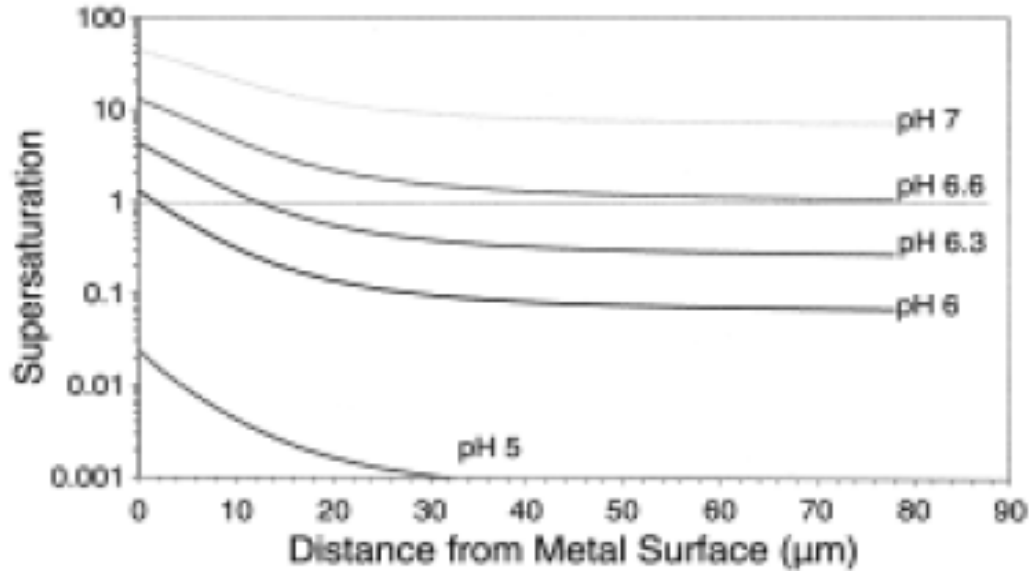


Figure 11.8 Supersaturation as a function of distance from the steel surface at conditions: 20°C, pipe diameter 0.1 m, flow velocity 1 m/s, varying pH, $p\text{CO}_2 = 1$ bar and $[\text{Fe}^{2+}] = 1\text{ppm}$ [35].

In this case, the produced results match very accurately with that published by Nestic et al. [35] despite the differences in geometry (pipe flow and thin channel flow). This close comparison provides a good validation to the developed model and can be explained that since the values, as seen before, are of the same order of magnitude, slight differences will not be observed as the saturation ratio values are plotted in logarithmic.

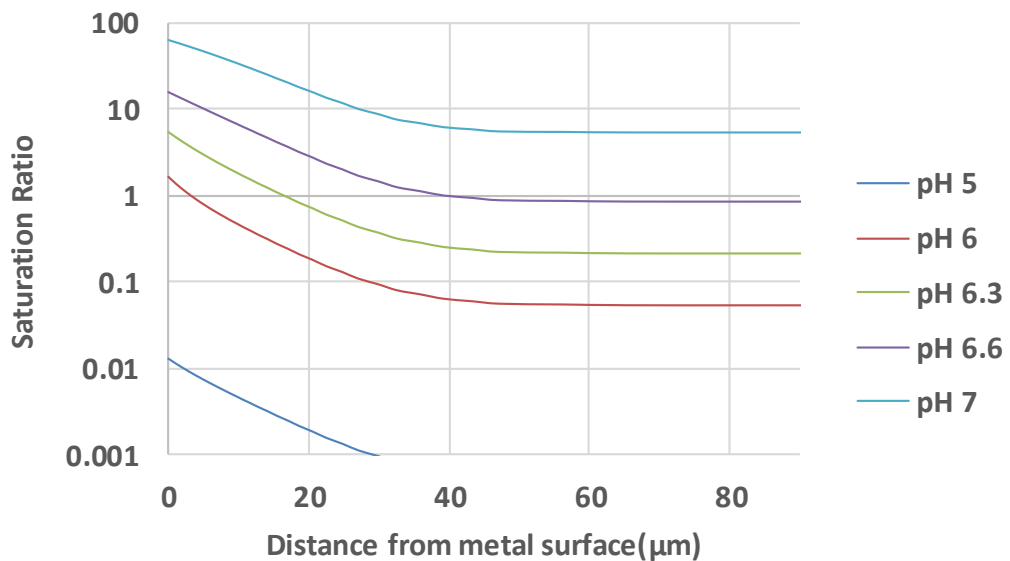


Figure 11.9 COMSOL model output for saturation ratio as a function of distance from the steel surface at conditions: 20°C, 3mm channel height, flow velocity 1 m/s, varying pH, $p\text{CO}_2 = 1$ bar and $[\text{Fe}^{2+}] = 1\text{ppm}$.

11.4 Comparison of Model with Experimental Observations

The developed COMSOL model is mechanistic and capable of predicting the species concentration profiles at the very near surface region for varying conditions. As discussed, the model was based on the design of the thin channel flow cell and is used to identify the effect of flow on the surface characteristics and its comparison with bulk properties for the initial stages prior to any substantial film development. In this section, the model is simulated for conditions carried out within the thin channel flow cell.

Figure 11.10 shows the predicted saturation ratio profile as a function of distance from the metal surface for 80°C, pH 6.8, pCO₂ 0.54 bar and varying flow velocity.

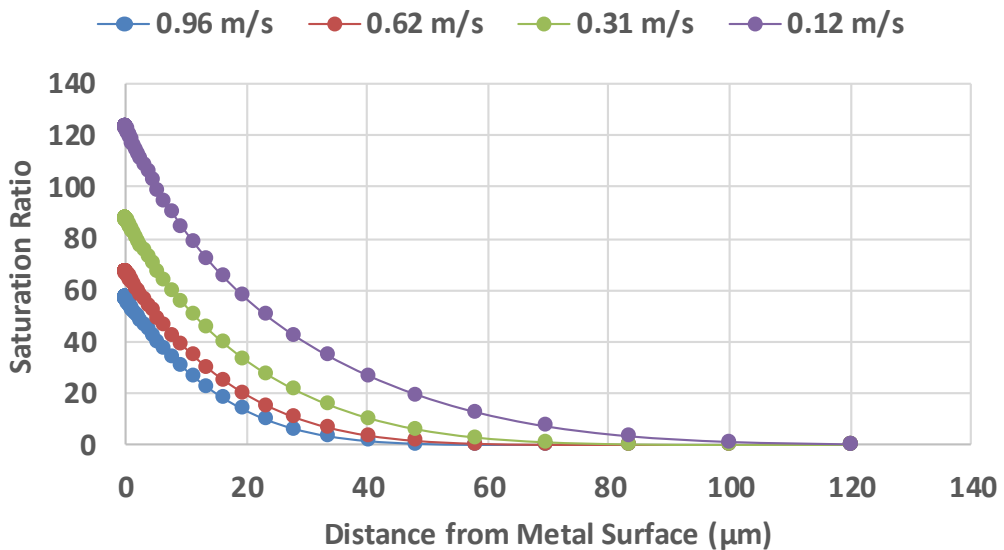


Figure 11.10 Saturation ratio as a function of distance from the surface for variable flow velocities operated within thin channel flow cell at 80°C, pH 6.8 and pCO₂ 0.54 bar.

The figure shows that the surface saturation ratio is predicted to be higher for a lower flow velocity. This agrees with literature as a faster velocity increases the rate of mass transfer of Fe²⁺ ions away from the surface resulting in a lower saturation ratio. The predicted corrosion rate at the given conditions is observed to not change significantly at varying flow velocity at these conditions due to the high pH and low H⁺ ion concentration at the surface, as discussed previously and shown in Figure 11.12. The model output shows that at a lower flow velocity, the saturation ratio is higher, therefore a higher initial precipitation rate of FeCO₃ is expected and a more protective film is favoured under these conditions over time. This statement

is supported by the experimental observations from the thin channel flow cell in Figure 9.6. Therefore, it may be inferred that the predicted surface saturation at the initial stages from the combined MATLAB and COMSOL model may indicate the protectiveness of the film developed over time under varying conditions.

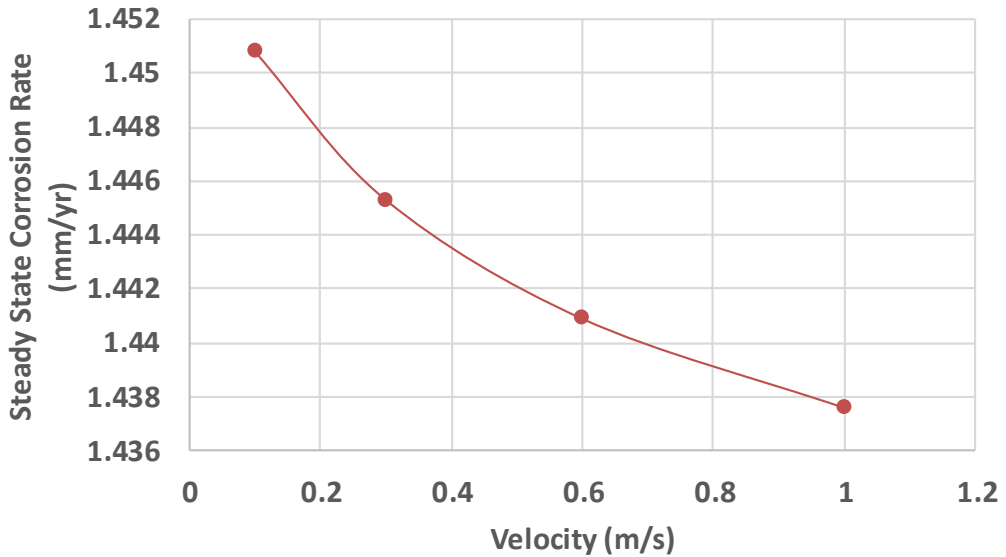


Figure 11.11 Steady state corrosion rate model output for variable velocity at 80°C, pH 6.8, pCO₂ 0.54 bar and 3.5 wt% NaCl.

Figure 11.12 shows the pH profile respectively as a function of distance from the metal surface for the working conditions applied within the flow cell. The pH at the surface is higher than the bulk however does not change significantly with velocity.

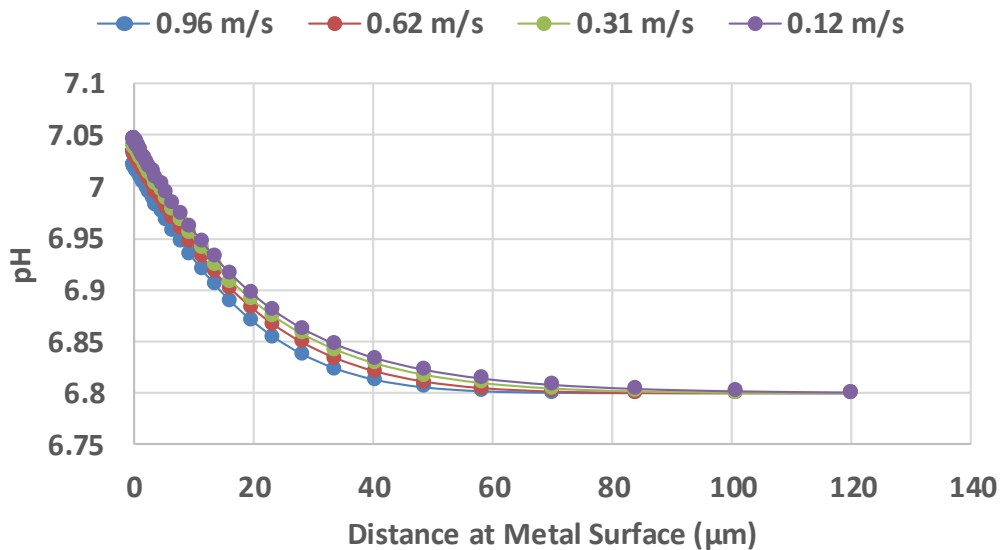


Figure 11.12 pH as a function of distance from the surface for variable flow velocities operated within thin channel flow cell at 80°C, pH 6.8 and $p\text{CO}_2$ 0.54 bar.

At a pH 6.8, the bulk concentration of H^+ ions is really small. H^+ ions are transported towards the surface where they are consumed as per the electrochemical reaction and therefore resulting in a lower concentration and a higher pH. The rate of H_2 evolution is limited by the H^+ ions available at the surface. At conditions of a higher velocity, the corrosion rate is higher therefore the combined rate of mass transport to the surface and consumption due to corrosion results in a smaller change in H^+ ions.

11.5 Summary of Modelling Analysis

The modelling work carried out within this PhD has been developed to complement the experimental work to provide an understanding of the surface conditions at the initial stage prior to any substantial film development that may drive the precipitation of the film that is observed experimentally. The combined model is based on a bi-nodal MATLAB model that predicts the corrosion rate that is fed into a COMSOL model developed based on the designed thin channel flow cell in which an experimental analysis is carried out.

The experimental analysis conducted in this study shows the complexity of the formation of FeCO_3 . The existing developed models do not accurately account for the properties of the developing FeCO_3 film and is limited to a one-dimensional control volume. The novelty of the developed model is that it extends the mechanistic understanding to a coupled analysis directly representing the flow environment and provides a link between the surface saturation ratio and the experimentally observed precipitation rate due to FeCO_3 . The model does not account for film development as a complete understanding of the film under varying conditions and its relationship to the “surface” saturation ratio is required and a comprehensive future analysis could produce a more robust mechanistic model with a more complete underlying theory.

Chapter 12

Discussion of Experimental and Modelling Results

FeCO_3 is a naturally-occurring film that precipitates on the surface of X65 carbon steel. For corrosion protection in a CO_2 environment, relevant to oil and gas production, the film is extremely important. Its formation is promoted at high temperature and pH. The film can be protective in its nature and can form a barrier to reduce the corrosion rate by blocking active corrosive sites. From the results presented in Chapter 8 and Chapter 9, the effect of varying parameters on the corrosion rate in a pure CO_2 environment and the protectiveness of the FeCO_3 film formed have been studied. In Chapter 10 and Chapter 11, the corrosion rate and species concentration at the near surface region are predicted for the initial stages under varying conditions that may drive the rate of FeCO_3 precipitation. Understanding the true nature of nucleation and growth of FeCO_3 crystals, the factors that govern the rate of precipitation, and the characteristics of the developed film is essential in assessing the practical use of FeCO_3 in the protection of pipelines. In the following chapter, the combined experimental and modelling results observed throughout this project are critically analysed and discussed highlighting the main findings and furthering the literature understanding of FeCO_3 film formation.

The discussion is divided into four parts.

1. The characteristics of the FeCO_3 film that contribute to its protectiveness are discussed. A critical analysis of experiments conducted in a glass cell and tracking the nature of the growth of the film is presented.
2. The effect of accelerating the kinetics of FeCO_3 film formation through providing an additional source of Fe^{2+} ions is discussed.
3. The stability and precipitation onto a protective FeCO_3 film are analysed.
4. The effect of laminar and turbulent flow characteristics on FeCO_3 precipitation and the nature of the film formed are discussed.

12.1 Nucleation and Growth of FeCO_3 Film Formation

FeCO_3 crystals are observed to nucleate and grow at varying conditions. However the protectiveness of the film has been observed to vary significantly. Corrosion rate measurement results showed that FeCO_3 precipitates at pH 6.3 and pH 6.8 however the film formed at pH 6.8 is

significantly more protective with the corrosion rate after 20 hours observed to be 0.09 mm/ year in comparison to 0.45 mm/ year for pH 6.3. These two conditions were critically analysed tracking the characteristics of film development over time.

Nucleation and growth of FeCO_3 are observed to be a *simultaneous* processes. Results show that at pH 6.3, fewer crystals were observed on the surface, but they were much larger in size at each time instant. At pH 6.8, the crystals were smaller in size but a larger quantity of crystals was observed on the surface. The reason behind the observed differences in the morphology of the scale is due to the competition between the nucleation and growth process.

According to crystallisation theory, crystal nucleation poses a large energy barrier which is easier to overcome at a higher levels of supersaturation and growth is limited by diffusion and existing stable nuclei. Corrosion product films are less porous and compact if the nucleation rate is higher than the growth rate.

The following analysis and discussion is a breakdown of what is believed to occur based on experimental observations. Figure 12.1 shows a representation of a typical corrosion rate graph observed under these two conditions with the trend broken into three time stages. Figure 12.2 shows a summarised pictorial representation of the development of the film observed over time for the two conditions of pH. The cubic structure of FeCO_3 is represented by blocks.

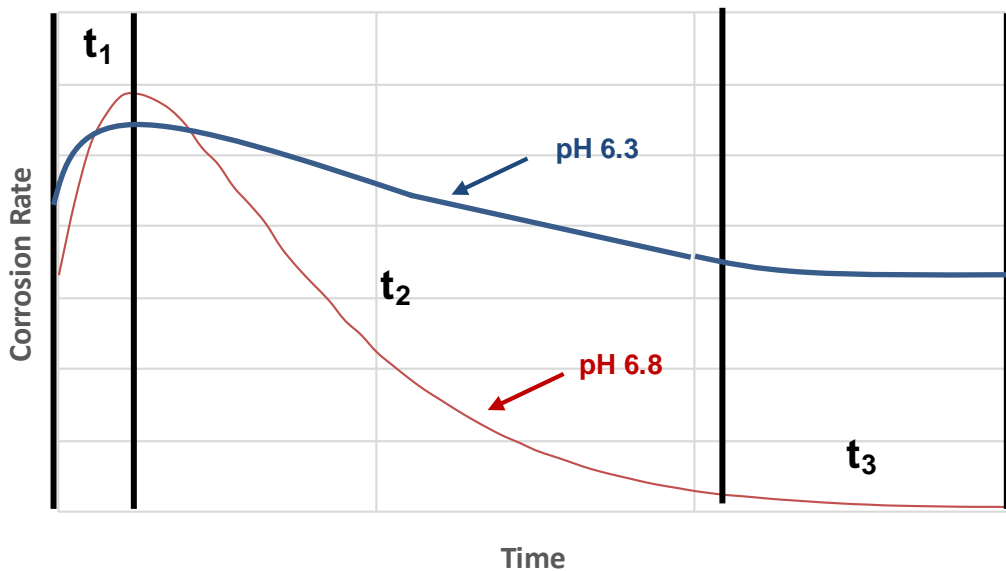


Figure 12.1 Representation of typical corrosion rate graph based on experimental observations for a pH 6.3 and pH 6.8.

The surface is initially 'clean' and there are no crystals present. Time step, t_1 represents the initial stages of nucleation and growth. The corrosion rate is believed to increase because as the sample surface corrodes, the surface area and surface roughness increases due to the surface profile of the Fe_3C layer. This time step is captured by LPR measurements to occur within the first hour. No noteworthy FeCO_3 crystals are expected to be present. After 5 hours, at pH 6.3, an average surface coverage of 9.5% is observed through experimental analysis as shown in Figure 8.12 and from the observed respective drop in corrosion rate showed in Figure 8.15, it may be inferred that zero or a very low surface coverage of FeCO_3 crystals is formed on the carbon steel surface at time step, t_1 .

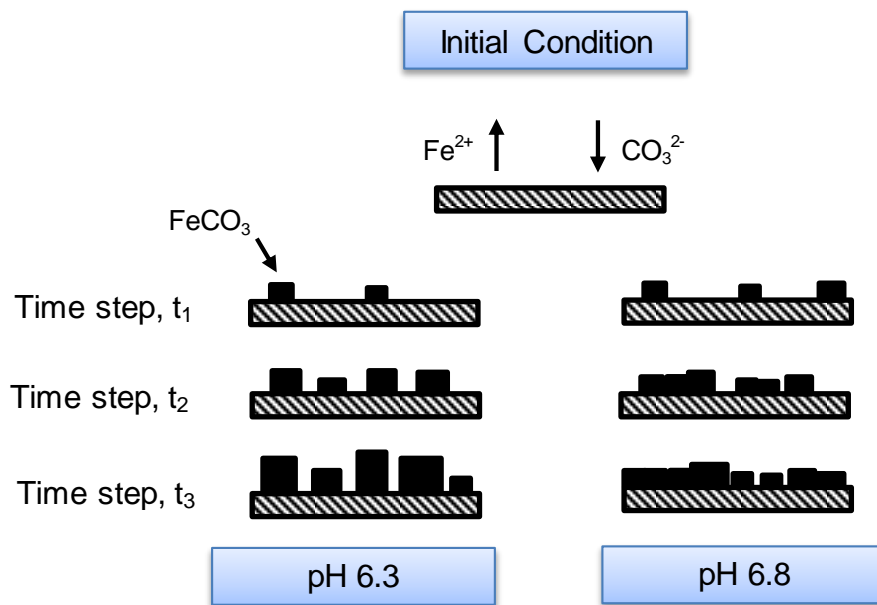


Figure 12.2 Pictorial representation of development of FeCO_3 film over time for pH 6.3 and pH 6.8.

The developed model predicts the maximum corrosion rate and corresponding surface species concentration for a specified working conditions. The surface saturation ratio is expected to increase with the corrosion rate at this region and Figure 12.3 shows the saturation ratio at the highest corrosion rate corresponding to the end of time step, t_1 for flowing conditions. The saturation ratio is observed to be significantly higher for pH 6.8.

The figure is determined from the COMSOL model for 80°C , $p\text{CO}_2$ 0.54 bar, 3.5 wt % and a velocity of 0.1 m/s. The analysis is for a flowing system however the surface saturation ratio is believed to be higher for a pH of 6.8 in comparison to pH 6.3 independent of flow conditions. Therefore Figure

12.3 is used to indicate the significant difference in saturation ratio for the two different pH values under the same conditions.

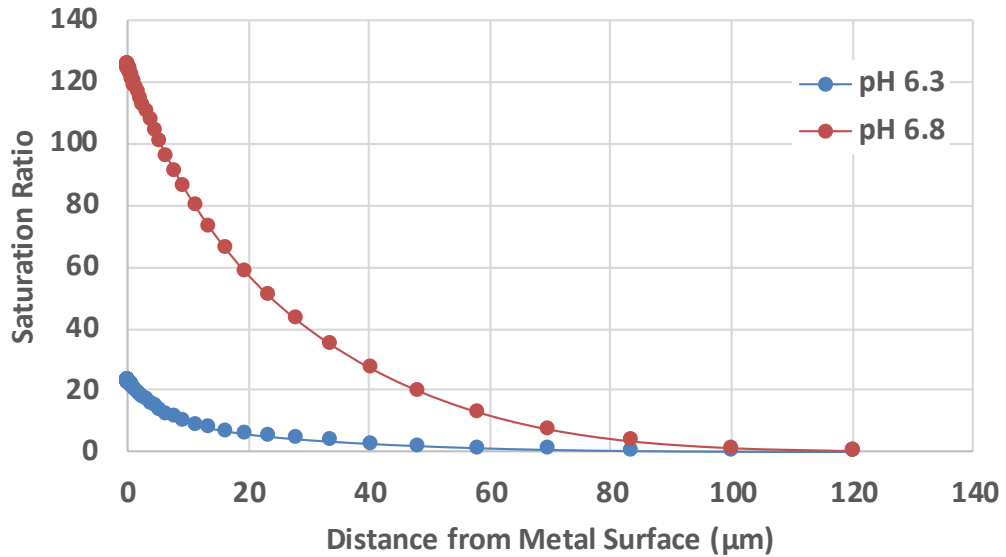


Figure 12.3 Effect of pH on saturation ratio as a function of distance from the metal surface for parameters of 80°C, pCO₂ 0.54 bar, 3.5 wt % and a velocity of 0.1 m/s.

A higher supersaturation results in a higher nucleation rate which is the number of nuclei formed per unit area and time. The literature behind crystal nucleation is discussed in Chapter 3.2 and according to Arumugam et al. [44], the nucleation rate R_{Nuc} relies on the interfacial tension, γ of the nucleated phase-solution boundary, the solution temperature, T and the saturation ratio, SR and is reiterated in Equation (12.1).

$$R_{Nuc} = P[A] \exp \left[-\frac{16\pi\gamma^3 v^2}{3(kT)^3 \ln(SR)^2} \right] \quad (12.1)$$

P is the probability that $[A]$ number of crystallising solute nuclei will grow into crystals. The nucleation rate is inversely proportional to the square of saturation ratio. Therefore, more crystals are expected to form at pH 6.8 due to the higher nucleation rate and surface saturation ratio.

FeCO₃ crystals precipitate on the corroding surface, the surface coverage progressive increases blocking the active corrosive sites. At a certain time instant, the percentage of the surface covered results in the rate of production of Fe²⁺ ions to decrease and the corrosion rate starts to drop. This represents time step, t_2 . The actual threshold value of surface coverage is unknown however is expected to be quite low.

At this time step, already present scale crystals continue to grow while new crystals are formed. The corrosion rate is observed to drop more significantly

at pH 6.8 at this stage as shown in Figure 12.1. The crystals at pH 6.3 are observed to grow more progressively whereas at pH 6.8, more crystals are formed limiting the growth of crystals. This may imply that the lower surface saturation ratio at pH 6.3 results in fewer nuclei overcoming the free energy barrier. Therefore, the surface concentration of Fe^{2+} contributes more to the growth of FeCO_3 . This process of nucleation and growth continues into time step, t_3 which corresponds to a relatively low level of super saturation. At this stage, the corrosion rate is observed to remain somewhat constant and the solution is considered in the metastable region where the precipitation of FeCO_3 may only occur on already present seed crystals. It is believed, from this work, that this metastable region corresponds to the later stages of film development where the corrosion rate is stable over time. At this condition, the rate of precipitation of FeCO_3 is considered equal to the rate of dissolution of the unstable crystals and the protective film is maintained. In order to support this hypothesis, the corrosion rate at the end of the 20 hour time period determined experimentally is entered into the COMSOL model for pH 6.3 and pH 6.8. The model is run for a low velocity of 0.1 m/s and is again limited to a flowing system however is used for a comparative basis. Furthermore, the model does not take into account the properties of the surface film and therefore is purely based on the obtained experimental corrosion rate and mass transport from the surface.

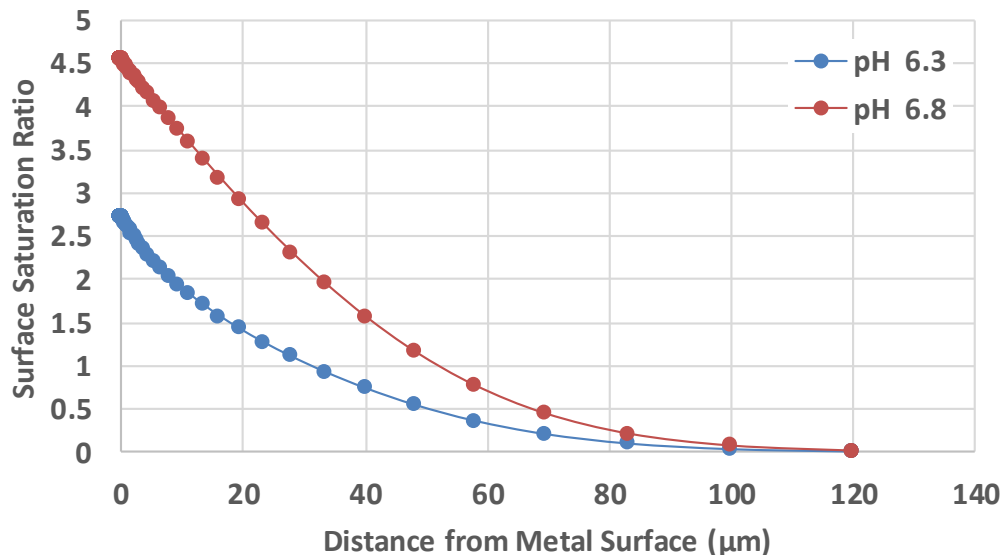


Figure 12.4 Effect of pH on saturation ratio as a function of distance from the metal surface for parameters of 80°C, $p\text{CO}_2$ 0.54 bar, 3.5 wt %, 0.1 m/s and corrosion rate of 0.45 and 0.09 for pH 6.3 and pH 6.8 respectively.

Figure 12.4 shows that surface SR at the end of the 20 hour time period for pH 6.3 and pH 6.8, based on the corrosion rate from mass loss measurements, are significantly lower than the initial saturation ratio predicted in Figure 12.3. However, the surface saturation ratio is greater than 1 which indicates that the FeCO_3 crystals are not dissolving back into the solution and the similar mass gain measurements at these time period indicate that there is no significant increase in FeCO_3 crystals forming on the surface. Therefore, the combined experimental and modelling analysis supports that at this time stage, a metastable region is observed and the corrosion rate is believed to remain constant into longer time periods. It is also noted that despite a corrosion rate at pH 6.8 being $1/5^{\text{th}}$ of the corrosion rate of pH 6.3 at the end of the 20 hour period, the predicted surface saturation ratio is higher for pH 6.8.

From the above analysis, it is observed that FeCO_3 precipitation over time is a complex process and is dependent on many surface factors. It is evident that saturation ratio is an important aspect however it is a driving force and not a kinetic parameter. Figure 12.5 shows the different parameters that were considered and studied in this work. Each parameter is dependent on each other and the observed correlations shall be discussed in the following sub sections.

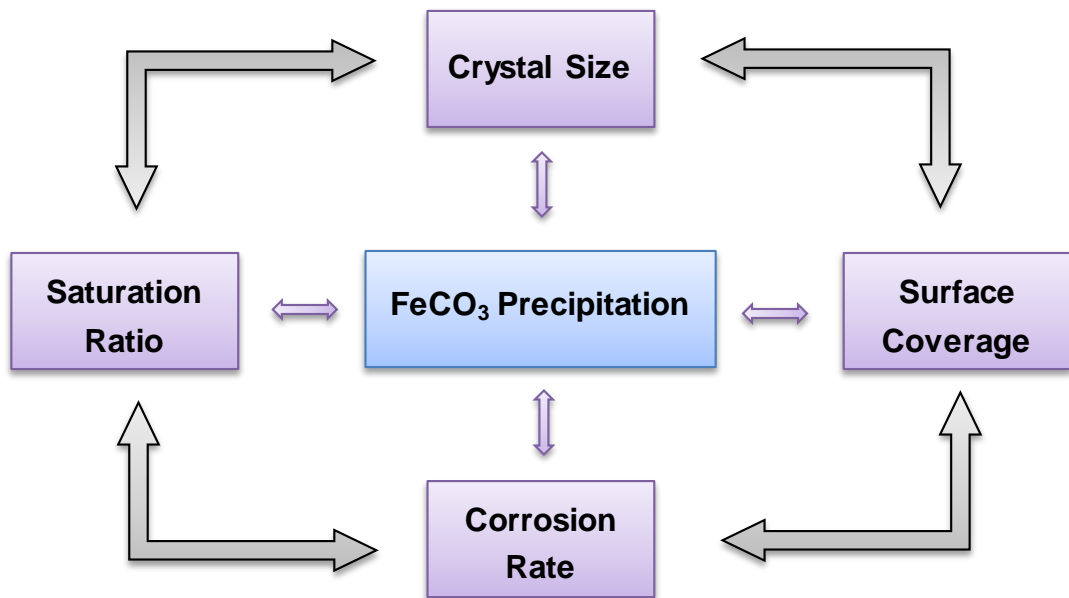


Figure 12.5 Parameters investigated and observed to have an effect on FeCO_3 precipitation rate.

12.1.1 Precipitation Rate and Film Protectiveness

A quantitative analysis was carried out through mass gain measurements at different time periods from which the precipitation rate of FeCO_3 was directly

determined. Results showed that the mass gain was higher for a pH of 6.8 at the earlier time periods however for longer time periods, the gap between the mass gain results reduce and a higher mass gain was attained for a pH of 6.3 after 20 hours.

Nucleation of crystalline films is a very difficult process to model mathematically as it is deemed to be nano-crystalline. Therefore, the rate of precipitation is believed to be controlled by the crystal growth rate. The precipitation rate at pH 6.3 was observed to be higher than that at pH 6.8 over time, as shown in Figure 8.17, after the initial time period as the change in mass is higher due to the more dominant growth of crystals observed for a lower pH. Therefore, a quantitative analysis of FeCO_3 and hence the analytically determined precipitation rate cannot be directly related to the protectiveness of the film.

At the end of each time period, the average surface coverage and crystal size was determined through analysis of SEM images taken at different areas of the sample. Surface coverage may be considered a direct representative of the protectiveness of the film as it indicates what portion of the surface is covered by the developed film. Figure 12.6 shows the average corrosion rate observed at the end of each time period as a function of the average surface coverage.

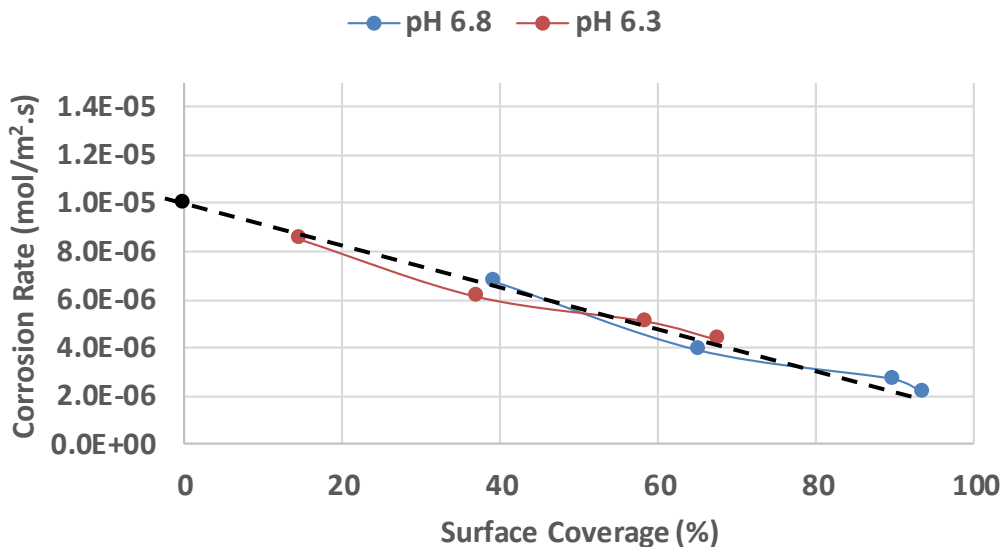


Figure 12.6 Corrosion rate as a function of surface coverage for pH 6.3 and pH 6.8 at 80°C, 3.5 wt% NaCl, $p\text{CO}_2$ 0.54 bar.

It may be observed from the figure that the surface coverage is inversely proportional with the corrosion rate. The corrosion rate values at pH 6.3 and pH 6.8 between 40 to 60% surface coverage is observed to overlap however

the values are observed to be approximately similar. Therefore, the change in corrosion rate and surface coverage may be considered parameters that directly infer the protectiveness of the film and are directly related to the precipitation rate. At pH 6.8, higher percentage of surface coverage values are observed that correspond to a lower corrosion rate. Future work under varying conditions may establish a robust linear relationship between corrosion rate and surface coverage.

Reverting back to the threshold value of surface coverage for a drop in corrosion rate. A line of best fit is applied to the trend observed in Figure 12.6 and is interpolated to approximately determine the maximum corrosion rate for a 0% surface coverage. The corrosion rate is 1×10^{-5} mol/m².s that corresponds to a value of 2.24 mm/ year. At the end of a time period of 2 hours, the corrosion rate for pH 6.8 and pH 6.3 is experimentally determined to be 2.12 and 2.09 mm/ year respectively. Therefore, from the above analysis, it may be concluded that at the initial time step t_1 , the surface coverage is 0% and no protective FeCO₃ crystals have formed on the surface. As the surface coverage increases, the corrosion rate starts to drop as the portion of the surface is covered.

12.1.2 Scaling Tendency

In a freely corroding system, the corrosion rate at a given set of conditions defines the production of Fe²⁺ ions which therefore describes the saturation ratio and resulting surface coverage, crystal size and precipitation rate. The precipitation rate provides a quantitative measure of the FeCO₃ that forms on the surface but needs to be coupled with a parameter which infers the protectiveness of the film in order to form a true representative of the film properties. Figure 12.7 shows the relationship between the precipitation rate and the corrosion rate observed at the end of each time period for pH 6.8 and pH 6.3. The precipitation rate is observed to be higher for the same corrosion rate at pH 6.8. Therefore it may directly inferred that the film is more protective at pH 6.8. Observing the precipitation rate as a function of time, Figure 8.17, the precipitation rate is observed to be higher at the later time periods at pH 6.3. Therefore, the protectiveness of the film cannot be directly determined from the precipitation rate alone.

In the experimental analysis, the percentage of Fe²⁺ ions dissolved from the surface that are precipitated as FeCO₃ is determined and is found to be significantly higher for a pH 6.8 at the end of each time period as shown in Figure 8.20. This ratio, also known as the scaling tendency (ST), is considered in literature to be a valid indicator of protective film formation. In

Nesic et al. [70], it is stated that for a ST less than one, porous and un-protective films are likely to form. Conversely when ST is greater than or equal to one, conditions become favourable for formation of dense, protective iron carbonate films. This hypothesis is proven false in the following work.

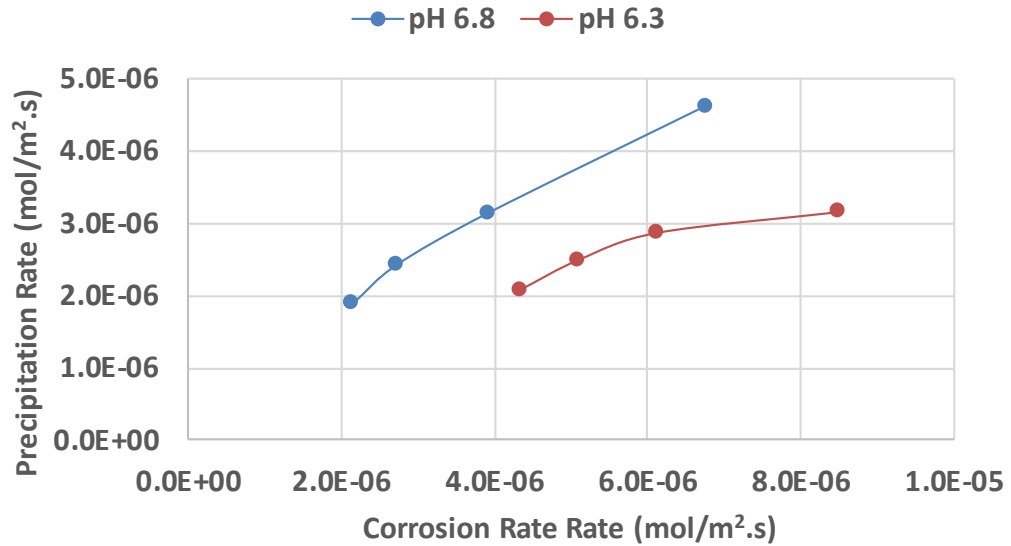


Figure 12.7 Precipitation as a function of corrosion rate for pH 6.3 and pH 6.8 at 80°C, 3.5 wt% NaCl, pCO₂ 0.54 bar.

In much of the work done by Nesic et al. [49, 62, 70], the kinetics of FeCO₃ formation is accelerated through an additional source of Fe²⁺ ions. This is representative of downstream in the pipeline. Therefore a scaling tendency of greater than one is possible. However, for a freely corroding surface without an additional bulk Fe²⁺ ion concentration, the precipitation rate cannot possibly be observed to be greater than the corrosion rate. Results have shown that a relatively dense and protective FeCO₃ film is formed at pH 6.8 in a freely corroding system. Therefore, from this work, it is agreed that scaling tendency is a valid indicator of the protectiveness of the film formed in a comparative analysis; however, there is no specific range in which the film formed on the surface offers no protection. The effect of adding FeCl₂.4H₂O shall be discussed further in a later section.

12.1.3 Surface Coverage and Crystal Size

An accurate calculation of surface coverage and crystal size theoretically should be able to determine the quantity of FeCO₃ crystals at the surface. Therefore, the precipitation may be determined from mass gain measurements, as previously carried out, and from combined surface coverage and crystal size analysis of the surface. Figure 12.8 shows the

sequence of calculations carried out. It is noted that the crystals sizes and surface coverage were observed to vary at different areas of the surface. However, an average was obtained from multiple images across the surface and in the following calculations, the crystal size and surface coverage was assumed to be uniform throughout. The density of FeCO_3 is 3960 kg/m^3 and a thickness and porosity of the film of $8 \text{ }\mu\text{m}$ and 0.8 respectively was used based on a table of calculations by Nestic et al. [10] under varying conditions.

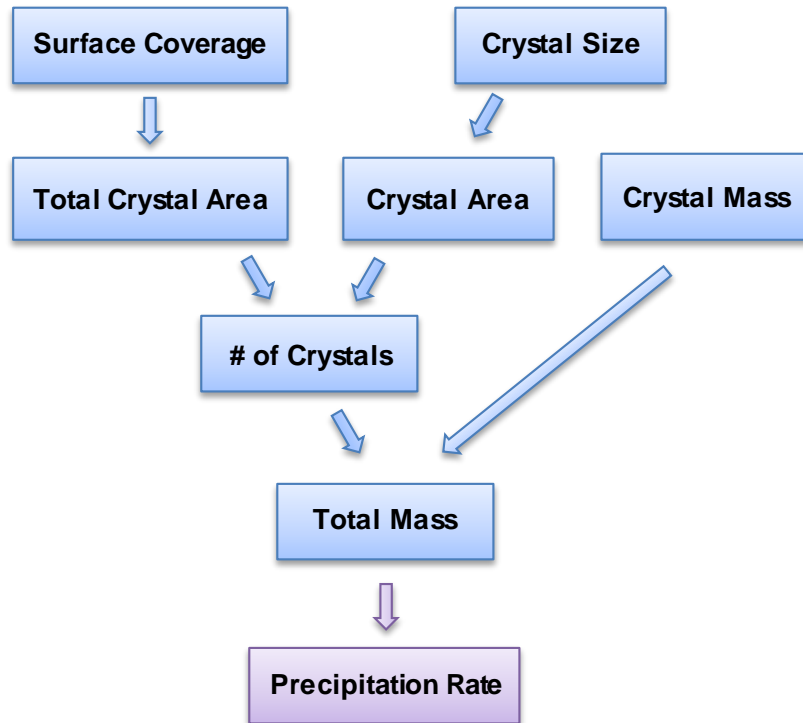


Figure 12.8 Sequence carried out to determine precipitation rate from surface coverage and crystal size.

Figure 12.9 and Figure 12.10 show the results from the comparison of the precipitation rate determined from mass gain measurements and a combined analysis of surface coverage and crystal size at the end of each time period for pH 6.3 and pH 6.8 respectively. The figures show a close comparison between the precipitation rates obtained through both methods at both pH.

Figure 12.9 shows that the comparison is closer at the later time periods. This may be because the observed crystals are more discrete and varied over the surface over the sample at the observed SEM images at the early time stages. Therefore the overall average surface coverage may be more difficult to attain. The opposite trend is observed in Figure 12.10 where the comparison is closer at the earlier time periods and is more different for the later time periods. This may be due to it being more difficult to identify an

accurate surface coverage at “close to full” surface coverage. It is approximated to be approximately 95% by the developed MATLAB programme however it is difficult for the program to identify the contrast between the corroding surface and crystals as shown in Figure 8.13. It is also noted that in determining the mass of the overall crystals formed from a combined surface coverage and crystal size analysis, it is assumed that the thickness and porosity is constant at both conditions and the values are determined from literature. Therefore, a certain percentage of error may be expected due to the assumption.

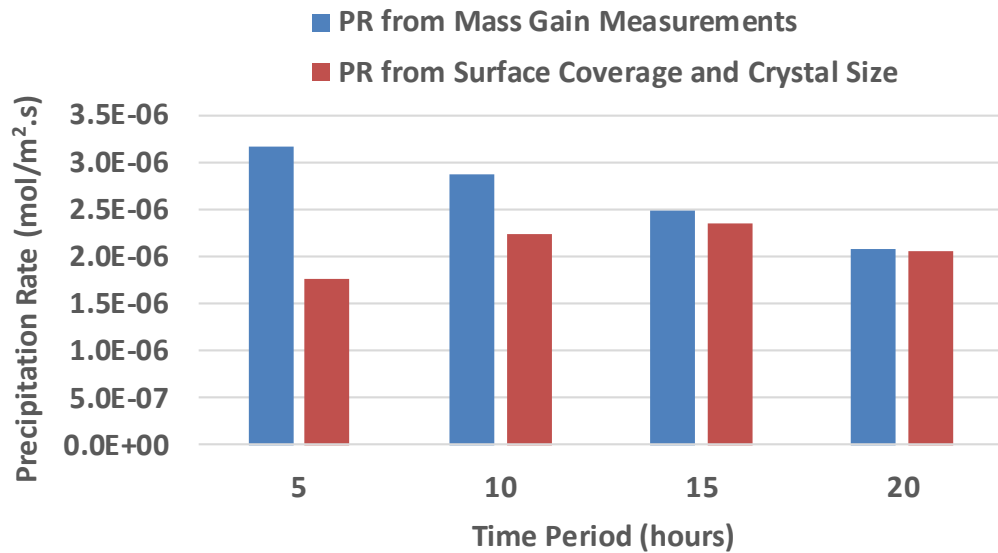


Figure 12.9 Comparison of the precipitation rate determined from mass gain measurements and a combined analysis of surface coverage and crystal size at 80°C, pH 6.3, 3.5 wt% NaCl, pCO₂ 0.54 bar.

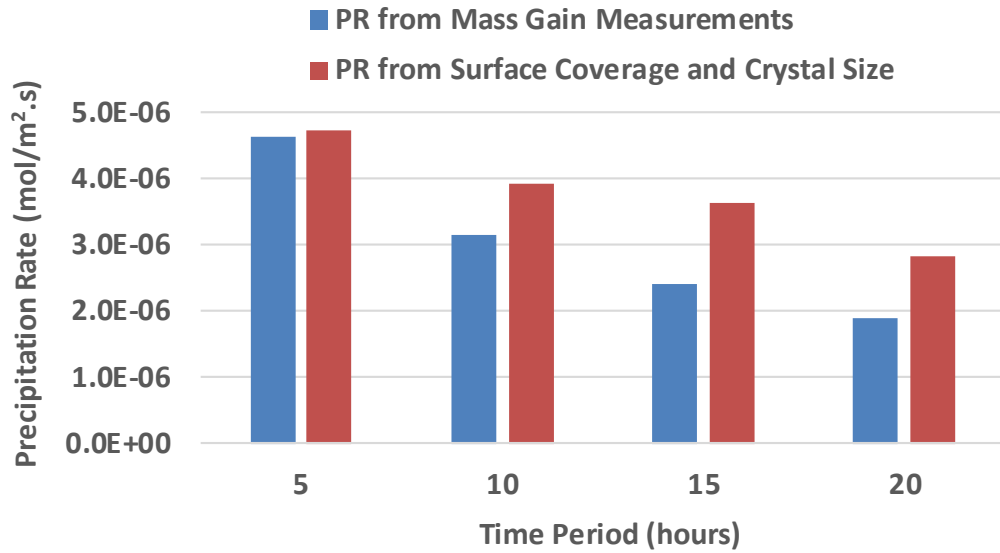


Figure 12.10 Comparison of the precipitation rate determined from mass gain measurements and a combined analysis of surface coverage and crystal size at 80°C, pH 6.8, 3.5 wt% NaCl, pCO₂ 0.54 bar.

From the following analysis, it may be reasoned that the precipitation rate may be determined from the characteristics of the crystal formed on the surface. Furthermore, it also confirms the methodology and the MATLAB program created to analyse the surface coverage and the determined average crystal size.

12.1.4 Quantifying Saturation Ratio

Saturation ratio is defined by the ratio of the product of the species concentration to the solubility limit. It is calculated by Equation (4.15) (page 43) and is quantified by the effusion of iron ions from the metal surface and infusion of carbonate ions from the bulk solution.

The solubility limit of FeCO₃ is a function of temperature and ionic strength. Since the experiments were conducted at 80°C and 3.5 wt% NaCl, the K_{sp} for both pH 6.3 and pH 6.8 is the same at 1.62×10^{-10} mol/l determined using the Sun and Nescic's model for K_{sp} . According to the bulk equilibrium calculations in Chapter 6.4, the CO₃²⁻ ion concentration can be analytically calculated and is found to be 7.50×10^{-5} mol/l for pH 6.8 and 7.50×10^{-6} mol/l for pH 6.3. The CO₃²⁻ ion concentration in the bulk is different by a factor of 10 between pH 6.3 and pH 6.8. Therefore, the Fe²⁺ ion concentration at pH 6.3 has to be higher than pH 6.8 approximately by an order of 10 in order to achieve the same SR. From this, we can infer that the saturation ratio and hence the nucleation and growth rate of FeCO₃ at a pH

of 6.3 and pH 6.8 is controlled predominantly by the CO_3^{2-} ion concentration under these conditions.

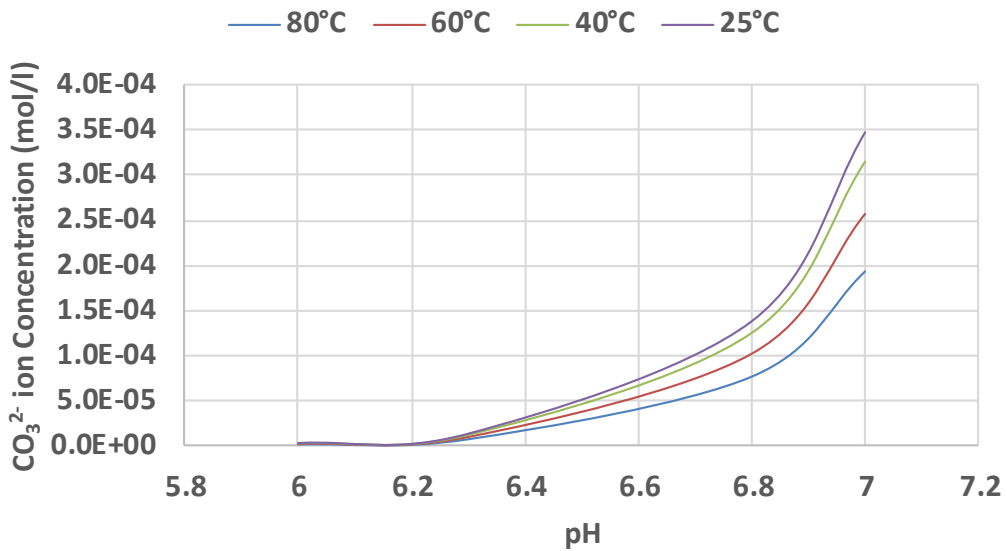


Figure 12.11 Effect of pH and temperature on CO_3^{2-} ion concentration.

Therefore the next step is defining what parameters affect the CO_3^{2-} ion concentration. A modelling analysis shows that the CO_3^{2-} ion concentration is a function of temperature, pH, ionic strength and the total pressure of the system. Furthermore, analysis from species concentration from the surface to the bulk shows that surface and bulk concentrations of CO_3^{2-} are approximately similar.

Figure 12.11 shows the varying CO_3^{2-} ion concentration as a function of the pH and temperature, the two main parameters considered in this study. The figure shows that pH has a significant effect on the concentration. At a pH of lower than 6.2 at all temperatures, the CO_3^{2-} concentrations are very low and therefore FeCO_3 precipitation would be unfavourable. However, the concentration increases exponentially at a higher pH which shall therefore result in a higher initial saturation ratio.

On the other hand, the CO_3^{2-} concentration increases for a lower temperature however, the solubility of FeCO_3 , K_{sp} increases as well. Therefore a higher initial saturation ratio is attained for a higher pH and temperature and results have shown that a lower temperature, pH favour the formation of large crystals and hence increased porosity of the scale layer.

At a specific time instant, the CO_3^{2-} concentration and K_{sp} can be analytically calculated given the working conditions. The Fe^{2+} ion concentration however poses a larger challenge. In much of the work in literature, the bulk Fe^{2+} ions

is determined through spectroscopy and surface phenomena is correlated with bulk solution properties. A similar experimental procedure was carried out and the results showed that the bulk saturation ratio is significantly lower than what would be expected at the surface for the observed nucleation and growth of FeCO_3 crystals at pH 6.3 and pH 6.8 as shown in Figure 8.18. Therefore, it is understood that the precipitation rate has no direct correlation with the bulk SR as the reaction is surface dominated.

Analysis of the bulk Fe^{2+} ion concentration at the end of each time period, as shown in Figure 8.19, results show that at a pH 6.8, a large concentration of Fe^{2+} ions is retained at the surface and reacts with CO_3^{2-} ions to form iron carbonate. On the other hand, at pH 6.3, due to limited surface concentration of CO_3^{2-} ions, a larger portion of the Fe^{2+} ions remain unreacted and diffuse to the bulk and hence a larger bulk Fe^{2+} ion concentration.

12.1.5 Limitation of Modelling Static System

In Chapter 10, the COMSOL model was developed to predict the initial surface saturation ratio however the model was unable to be refined for a static system. In a static environment, mass transport is solely due to diffusion of species. Figure 12.12 shows the surface saturation ratio and corrosion rate as the velocity was reduced in the model for a thin channel flow cell.

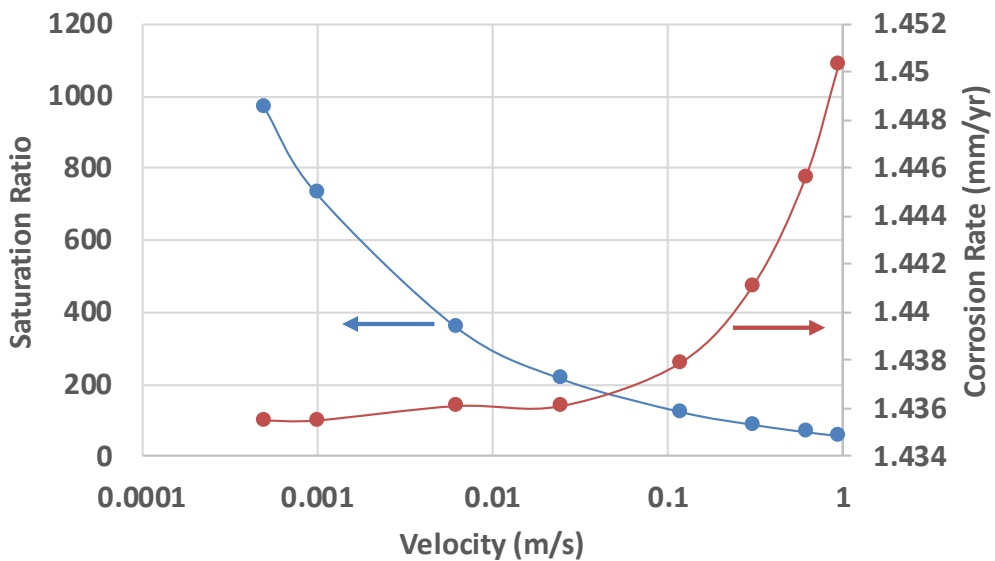


Figure 12.12 Saturation ratio and corrosion rate as a function of velocity from developed model for thin channel flow cell. Working Conditions (80°C, pH 6.8 and pCO_2 0.54 bar).

As the velocity decreases, the corrosion rate converges to a steady state corrosion rate value of 1.435 mm/ year as it is mass transfer limited by the diffusion of H^+ ions. However, the saturation ratio exponentially increases. This is due to the flux of Fe^{2+} ions due to corrosion being significantly higher than the diffusion rate of Fe^{2+} ions away from the surface and therefore resulting in a build-up of Fe^{2+} ions at the surface. The value does not converge and therefore is unable to be computed for purely static conditions.

In order to model a static system, the model will have to be adapted to a time dependant solver that takes into account and predicts the varying precipitation rate over time resulting in a negative flux of Fe^{2+} ions at the surface. This is a complex analysis and is difficult to model given the current literature.

12.2 Accelerating Kinetics of $FeCO_3$ Film Formation

Adding $FeCl_2 \cdot 4H_2O$ to the solution provides an additional source of Fe^{2+} ions and the ferrous ions forming iron carbonate scale includes ferrous ions both released from the steel surface and provided by the bulk of the solution. This is evident as the precipitation rate is observed to be higher than the corrosion rate, as shown in Figure 8.23, hence a scaling tendency of greater than one. Over the same initial time period of 2 hours, a higher amount of $FeCl_2 \cdot 4H_2O$ added resulted in a higher precipitation rate; therefore accelerating the kinetics of $FeCO_3$ film formation. A combined analysis of the observed significant difference in the corrosion rate and significantly higher bulk saturation ratio to a freely corroding system, indicates that the added $FeCl_2 \cdot 4H_2O$ increases the surface SR resulting in the a shorter induction time for the formation of $FeCO_3$ and therefore less Fe^{2+} ions being produced from the surface due to corrosion. Figure 12.13 shows the resulting initial surface saturation ratio as a result of the added Fe^{2+} ion concentration.

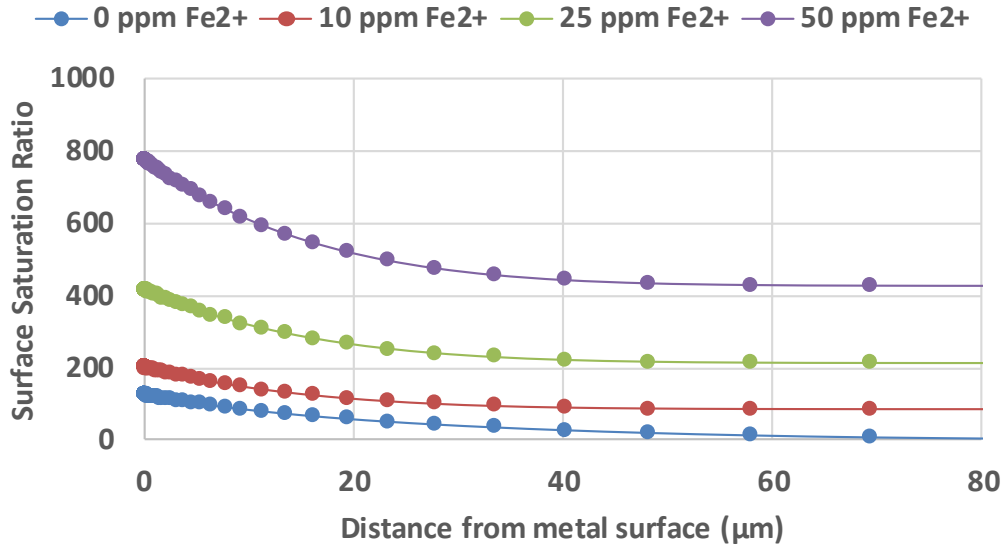


Figure 12.13 Surface saturation ratio as a function of distance from metal surface for varying concentration of Fe²⁺ added at 80°C, pH 6.8, 0.54 bar, 3.5 wt% NaCl and 0.1 m/s.

The surface saturation ratio is for a velocity of 0.1 m/s determined from the COMSOL model however is used to highlight the effect of bulk supersaturation on surface properties. The values obtained are not representative of a static system however, the behaviour from the surface to bulk may be considered similar.

The figure shows that for 10 ppm of Fe²⁺ ions added to the bulk solution, the change in the saturation ratio from the surface to the bulk is similar to that for a freely corroding system. As the amount of Fe²⁺ ions is increased, the change in the saturation ratio from bulk to surface increases. Therefore, it may be inferred that at low bulk supersaturation, the surface saturation ratio and hence the precipitation rate of iron carbonate is surface dominated and strongly affected by the corrosion rate of the steel. At high bulk supersaturation, the corrosion rate has little effect on the scale as more Fe²⁺ are contributed from the bulk solution.

However, the high bulk saturation ratio also results in bulk precipitation elsewhere in the glass cell. Experiments conducted over time, as shown in Figure 8.25, showed that adding FeCl₂·4H₂O influences the surface characteristics resulting in accelerated kinetics of FeCO₃ film formation and a lower corrosion rate at the initial time period. However, over time, the Fe²⁺ ions contribute more to bulk precipitation resulting in a lower contribution to FeCO₃ precipitation at the surface and the corrosion rate stabilising at higher corrosion rate than for a freely corroding system.

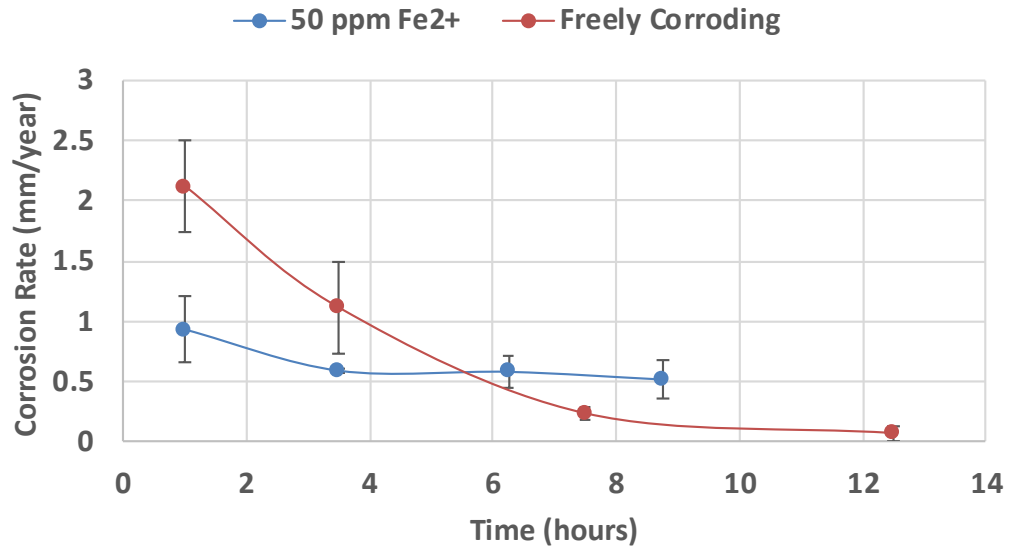


Figure 12.14 Corrosion rate vs. time compared for a freely corroding system and 50 ppm Fe²⁺ ions added for experiments conducted at 80°C, pH 6.8, 0.54 bar and 3.5 wt% NaCl.

This is shown in Figure 12.14 where the corrosion rate in mm per year is plotted as a function time for a freely corroding system and when 50 ppm of Fe²⁺ ions is added at the start of the experiment. Therefore, externally influencing the kinetics of FeCO₃ film formation, despite increasing the nucleation and growth of FeCO₃ crystals at the early stages, does not contribute to producing a protective film over time due to bulk precipitation.

Much of the work by Nestic et al. [49, 62, 70], was carried out with addition of FeCl₂·4H₂O. The development of the S&N precipitation model, described in detail in Chapter 5.2, was based on experiments carried out in static conditions with initial Fe²⁺ of 50 ppm, pH of 6.6 and range of temperatures from 60°C to 90°C. The precipitation rate was determined through mass gain measurements and correlated with the bulk super saturation over time.

Figure 12.15 shows the comparison between the experimental data and the existing precipitation rate models by Greenberg and Tomson (G&T) [4, 5], Johnson and Tomson (J&T) [6, 7], van Hunnik et al. (vP&H) [8] and Sun and Nestic (S&N) [9, 10]. The precipitation rate is plotted against the bulk saturation ratio determined through spectroscopy for the experiments carried out over the initial time period of two hours.

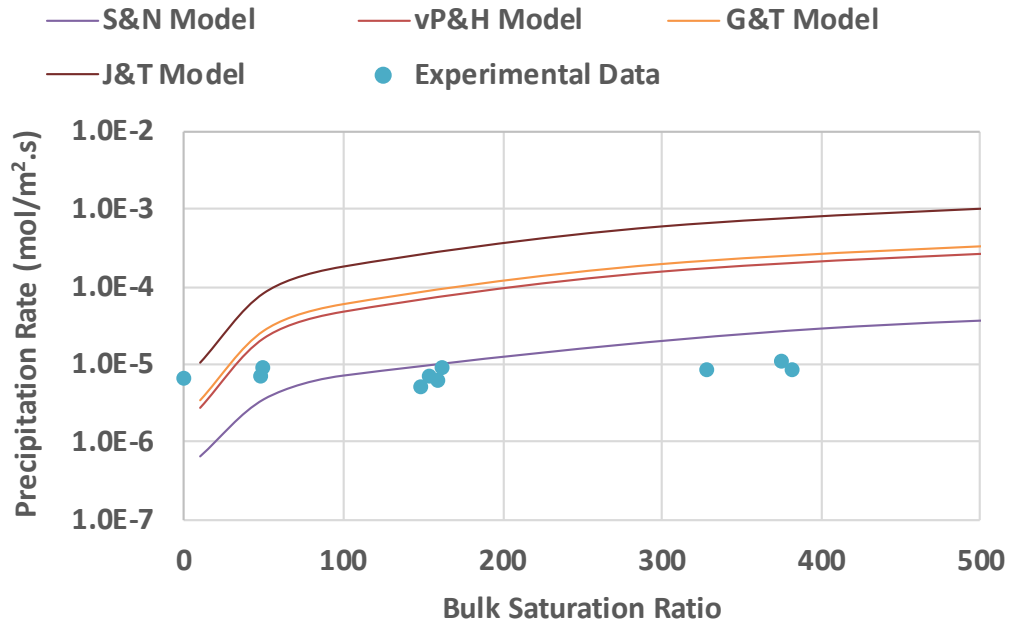


Figure 12.15 Comparison of experimental data with precipitation models for a series of test done over initial time period of 2 hours and varying initial $\text{FeCl}_2 \cdot 4\text{H}_2\text{O}$. (Working Conditions: 80°C , pH 6.8, 0.54 pCO_2 , 3.5 wt% NaCl).

The figure shows a good correlation with the S&N model for high values of bulk SR, which corresponds to experiments conducted with 25, 40 and 50 ppm of Fe^{2+} ions added to the solution, whereas the other models are observed to overestimate the precipitation rate. The models by G&T, J&T and vP&H are based on experiments where the precipitation rate is determined by the change in bulk Fe^{2+} ion concentration. However, from the observations of this work, added $\text{FeCl}_2 \cdot 4\text{H}_2\text{O}$ results in bulk precipitation therefore the assumption that the reduction in bulk supersaturation is due to precipitation only at the surface of the metal is found to be incorrect. This conclusion is supported in the work done by Nescic et al. [9, 10]. At high bulk supersaturation, the corrosion rate is observed to have little effect on the precipitation rate. The bulk Fe^{2+} ions contribute more to the formation of FeCO_3 crystals and the surface saturation ratio may be assumed similar to that in the bulk. The S&N model is observed to be efficient in predicting the precipitation rate for high bulk SR over initial time periods.

For lower values of bulk SR, the precipitation results are observed to be higher than the predicted values by the Nescic et al. model and are therefore under-predicted. These results correlate to the precipitation rate over the initial time period of 2 hours for a freely corroding system and 10 ppm of Fe^{2+} ions added to the solution.

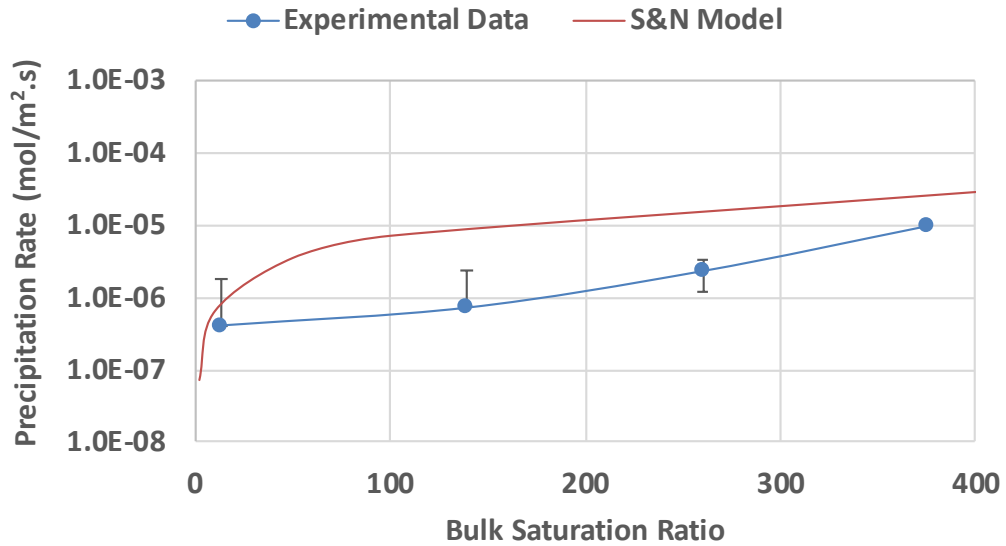


Figure 12.16 Precipitation rate as a function of supersaturation in comparison to S&N model. (Working Conditions: 80°C, pH 6.8, 0.54 pCO₂, 3.5 wt% NaCl, 50 ppm FeCl₂.4H₂O).

The precipitation model by S&N was determined based on the experimental observations where 50 ppm of Fe²⁺ ions was added and the precipitation rate and corresponding bulk SR were determined over time. Figure 12.16 shows a comparison between the S&N precipitation model and the precipitation rate determined experimentally over time for 50 ppm of Fe²⁺ added to the solution and an experiment conducted in a glass cell at 80°C, pH 6.8, 0.54 pCO₂, 3.5 wt% NaCl.

The result shows that the observed trend in S&N developed model for a low bulk saturation ratio of 0 to 50 is due to the low precipitation rate observed at later time intervals. It is believed that further experiments carried out at similar conditions would confirm a similar trend. Therefore, it may be inferred that the S&N precipitation model is limited to a system where the kinetics of FeCO₃ film formation is initially accelerated through addition of FeCl₂.4H₂O.

12.3 Later Stages of FeCO₃ Film Development

In the discussion so far, the precipitation of FeCO₃ over time on a clean X65 carbon steel surface was analysed for a freely corroding system and for varying concentrations of Fe²⁺ ions added externally influencing the precipitation of the FeCO₃ film. In the following stage, the behaviour of the later stages of film development is analysed. Results have shown that as the FeCO₃ film nucleates and grows on the surface of the carbon steel surface, the corrosion rate decreases as the surface coverage of the developing film

increases. However, at a certain time instant, the rate of reduction of the corrosion rate decreases and corrosion rate is observed to be stable. From an earlier point in the discussion, it was hypothesised that this stage refers to the metastable region where the surface SR is low. At conditions of 80°C, pH 6.8 and $p\text{CO}_2$ of 0.56 bar, the precipitated FeCO_3 film is relatively protective with a corrosion rate of 0.05 mm/year measured after 20 hours.

The protective film is placed in a fresh solution at the same conditions for three different scenarios: turbulent flow, 10 ppm of Fe^{2+} ions and 50 ppm of Fe^{2+} ions to observe the stability of the protective film and if the addition of $\text{FeCl}_2 \cdot 4\text{H}_2\text{O}$ may result in further precipitation of FeCO_3 at the surface. The experiments were conducted over 2 hours and repeated observations showed that:

1. Mass loss was observed due to the turbulent flow across the surface of the sample. Therefore, some of the FeCO_3 film dissolved into the solution however, the corrosion rate did not increase. Previously, it was discussed that a higher nucleation rate leads to a more protective film and that the precipitation rate is mostly governed by crystal growth. Therefore it may be inferred that the protectiveness of the film may not be directly compromised by a reduction in the mass or a negative precipitation rate. Unstable crystals may have dissolved into the solution causing the observed reduction in mass however, the film remained protective after a 2 hour period.
2. Adding 10 ppm of Fe^{2+} ions resulted in a mass gain due to FeCO_3 precipitation on the already protective film. For a corroding surface, the surface reaction will dominate the FeCO_3 precipitation process where the process is limited by the rate of nucleation and growth. As the layer is developed, the system moves to mass transfer control and is limited by the mass transfer of the species required to result in further FeCO_3 crystal growth. For a fully formed protective film, the surface concentration of Fe^{2+} ions is limited due to the low corrosion rate. Adding Fe^{2+} ions to the solution results in mass transport of Fe^{2+} ions to the surface and hence a higher mass gain. However, bulk precipitation is also observed.
3. Adding 50 ppm of Fe^{2+} ions does not result in a higher mass transport of Fe^{2+} ions to the surface resulting in a higher measured precipitation rate at the surface. For a high bulk saturation ratio, bulk precipitation is more spontaneous. The Fe^{2+} ions contribute more to the growth of

nuclei in the bulk of the solution and a higher precipitation rate is not observed.

12.4 Effect of Flow on FeCO₃ Film Development

The final stage of the discussion comprises of the developed flow cell and the resulting CO₂ corrosion rate and FeCO₃ precipitation for varying flow velocities. Both laminar and turbulent flow was analysed and the results showed that a more protective film and a higher precipitation rate at the end of 20 hours was observed for a lower velocity.

SEM images, Figure 9.8, showed that for turbulent flow characteristics, the FeCO₃ crystals appeared scattered with no significant surface coverage. However, the corrosion rate was observed to drop faster for a higher flow velocity. This contradictory effect may be an aspect of a recirculating flow loop as the amount of Fe²⁺ ions flowing across the surface of the sample for a given time instant would be higher for a faster velocity therefore resulting in the observed faster drop in corrosion rate. An amorphous protective layer may form under these flow characteristics resulting in the observed drop in the corrosion rate however the precipitated FeCO₃ crystals may remain unstable and be physically removed due to the turbulence across the surface resulting in the observed SEM images of the surface after 20 hours.

In a more laminar flow regime, a more compact and dense film is observed on the surface of the carbon steel sample resulting a more protective film formed after 20 hours. The crystals are observed to be much smaller in size with a significantly higher surface coverage. However, LPR measurement show that a more protective film with a lower corrosion rate is attained under static conditions.

The precipitation rate of iron carbonate is directly related to corrosion and the conditions at the steel surface. The reaction is surface dominated as discussed and determining the surface saturation ratio is essential in order to accurately predict the precipitation rate. However; experimentally determining the surface properties is difficult and a method has yet to be determined. The modelling work done in this thesis allows for a theoretical prediction of surface properties for a flowing system. The model was adapted for a thin channel flow cell in order to correlate experimental observations with the predicted surface saturation ratio. However, the model is limited for a steady state system therefore only being able to predict the initial surface saturation ratio for a flow through the flow cell. The model does

not account for film development as a complete understanding of the film under varying conditions is required to be accounted within a model and to predict the resulting corrosion rate over time.

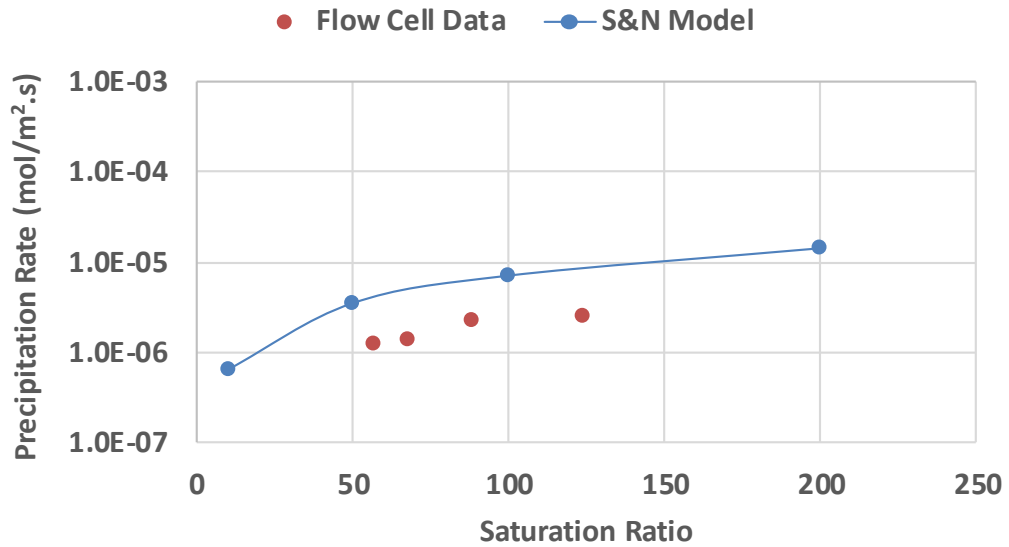


Figure 12.17 Precipitation rate as a function of surface saturation ratio for a thin channel flow cell at variable flow velocities in comparison to S&N precipitation model. (Working Conditions: 80°C, pH 6.8, 0.54 pCO₂, 3.5 wt% NaCl).

Figure 12.17 shows the correlation of the precipitation rate in mol/m².s at the end of 20 hours with the initial saturation ratio for working conditions of 80°C, pH 6.8, pCO₂ 0.54 bar and the respective flow velocities. The observed results is compared with the S&N precipitation model. It may be argued that the initial saturation ratio results in a significant percentage in the overall nucleation and growth of FeCO₃ and therefore may prove somewhat accurate in being linked with the precipitation rate over 20 hours. The surface saturation ratio drives the nucleation of FeCO₃ crystals and it was inferred from the analysis in Chapter 10.4 that a predicted initial surface saturation ratio may imply the nature of the film formed over time. The figure shows that a higher precipitation rate is observed for a higher initial surface saturation ratio and the results compare well with the S&N model considering the differences in the mechanism used in each case. The observed trend agrees with literature and further work in the area may prove valuable in testing the sensitivity of the model predicting the initial surface saturation ratio and linking the values with experimental precipitation rates.

An accurate determination of the surface saturation ratio over time would require a time dependant system and intensive knowledge on the kinetics of FeCO₃ precipitation over time at variable flow velocities in terms of

precipitation rate, porosity of the film, etc. Developing such a database is high in complexity, time intensive and currently limited by the literature in the area.

Chapter 13

Final Conclusion and Future Consideration

The work carried out in this PhD is a combined experimental and modelling approach to furthering the literature understanding of FeCO_3 precipitation and the protectiveness of the developed film. The experimental analysis is conducted in static and flowing conditions. A thin channel flow cell was designed to study the effect of laminar and turbulent flow on FeCO_3 precipitation. The modelling work is intended to complement the experimental work carried out and provide a mechanistic understanding of surface characteristics where an experimental investigation is limited.

In this final concluding chapter, the questions raised in the aims and objectives have been addressed and the following conclusions have been made.

- FeCO_3 precipitation is a complex simultaneous nucleation and growth process and the characteristics of the surface film significantly changes under varying parameters. A more protective film is formed for conditions of high temperature and pH.
- For a more protective film formation, the crystals are more compact and dense offering a higher surface coverage. A less protective film consists of larger, more discrete crystals not effectively blocking active corrosive sites. The difference in characteristics of the film results in the precipitation rate to not directly relate to the protectiveness of the developed film. Precipitation rate is based on a quantitative measure of the FeCO_3 film formed on the surface. The precipitation rate at a specific time instant can be higher due to a larger mass gain as a result of larger crystals formed on the surface.
- Scaling tendency is a valid indicator of the protectiveness of the film. It is the ratio of the precipitation rate to the corrosion rate and is higher for a more protective film. The ratio is greater than 1 for conditions where the precipitation rate is larger than the corrosion as a result of an additional contribution of Fe^{2+} ions.
- The corrosion rate is inversely proportional to the surface coverage. An accurately calculated surface coverage directly reflects to the portion of the surface covered due to the FeCO_3 film.
- The kinetics of FeCO_3 precipitation may be accelerated through addition of Fe^{2+} ions. This situation occurs downstream in a pipeline. The source of ferrous ions forming iron carbonate scale includes

ferrous ions both released from the steel surface and those provided by the bulk of the solution.

- At low bulk supersaturation, the precipitation rate of iron carbonate scale is strongly affected by the corrosion rate of the steel. At high bulk supersaturation, the corrosion rate has little effect on the precipitation rate of iron carbonate.
- Bulk precipitation takes place at high bulk supersaturation. FeCO_3 precipitation is favoured more in the bulk than on the surface over time.
- The precipitation rate of iron carbonate is directly related to corrosion and the conditions at the steel surface. It is a surface dominated reaction and bulk solution properties vary significantly from the surface.
- Saturation ratio is a main parameter in the development of FeCO_3 precipitation rate models. It is considered a driving force and a higher saturation ratio defines a higher scaling tendency.
- Precipitation models by Greenberg and Tomson (G&T), Johnson and Tomson (J&T) and van Hunnik et al. (vP&H), based on measuring the dissolved ferrous ions in the bulk solution, overestimate the precipitation of iron carbonate on the steel surface by a large margin.
- Sun and Netic (S&N) precipitation model is limited to the experimental conditions it is conducted in and underestimates the precipitation rate at low bulk supersaturation where surface conditions dominate the precipitation process. The model also does not take into account varying pH which is a main parameter in defining the characteristics of the film developed. A slight variation in pH results in an exponential increase in the CO_3^{2-} ion concentration which directly effects the saturation ratio and the precipitation rate.
- A mechanistic model is developed in this study to predict nature of near surface region at initial stages prior to any substantial film development under varying conditions. A high initial surface saturation ratio is an indication to a protective film formation.
- Thin channel flow cell is designed to study effect of laminar and turbulent flow on FeCO_3 film characteristics. A more protective film forms at lower flow velocities. FeCO_3 crystals dissolved back or were chemically damaged and has a higher corrosion rate at higher turbulent flow rates.

13.1 Limitation of this Study and Future Work

Although this study has highlighted some important findings with respect to understanding the nucleation and growth of FeCO_3 crystals, there is a multitude of avenues that the work can be carried forward.

In the development of the precipitation model by Sun and Nestic, a temperature ramp method was used in determining the precipitation rate equation to fit their data while the pH was maintained. In this work, it is shown that temperature plays an important role in the kinetics of FeCO_3 film formation; however, a slight variation in pH has a significant effect on the CO_3^{2-} ions and subsequently the precipitation rate. Furthermore, it is observed that the FeCO_3 precipitation rate is surface dominated and there may be a significant difference between bulk and surface properties.

The next step in this work is the development of a FeCO_3 precipitation model that relates directly with the surface saturation ratio for varying conditions of pH and temperature. This requires an intensive knowledge on the kinetics of FeCO_3 precipitation over time at variable flow velocities. It is believed from the observed results that behaviour of FeCO_3 film formation varies for conditions of laminar and turbulent flow and a single model cannot account for all conditions. Furthermore, due to the time intensive nature, each study will have to be carried out independently. The following bullet points identify the next steps into further understanding the FeCO_3 formation kinetics in laminar flow at varying temperature and pH with the intent of working towards developing a novel FeCO_3 precipitation model.

- Develop flow cell to create a more efficient method of installation of samples within the flow path and removal for post surface analysis. The current method is limited due to wearing of cable gland thread and cable gland needs to be broken and disposed of to extract sample for post surface analysis.
- Carry out a sequence of experiments over variable time periods for a freely corroding system and determine how the precipitation rate changes over time from mass gain measurement. Identify what time period the predicted surface saturation ratio predicted by the combined MATLAB and COMSOL model can accurately relate to.
- Modify the flow cell apparatus for a once through flowing system as shown in schematic diagram in Figure 13.1. Control the surface SR across the surface of the sample by varying the Fe^{2+} ions added and determine the respective precipitation rate for varying conditions.

- Repeat experiments and determine a trend from the observed results. Where k_{CG} is the crystal growth rate constant and exponent y is the growth order that represents the growth mechanism of the crystal.
- Develop a novel approach to a mechanistic model for FeCO_3 precipitation.

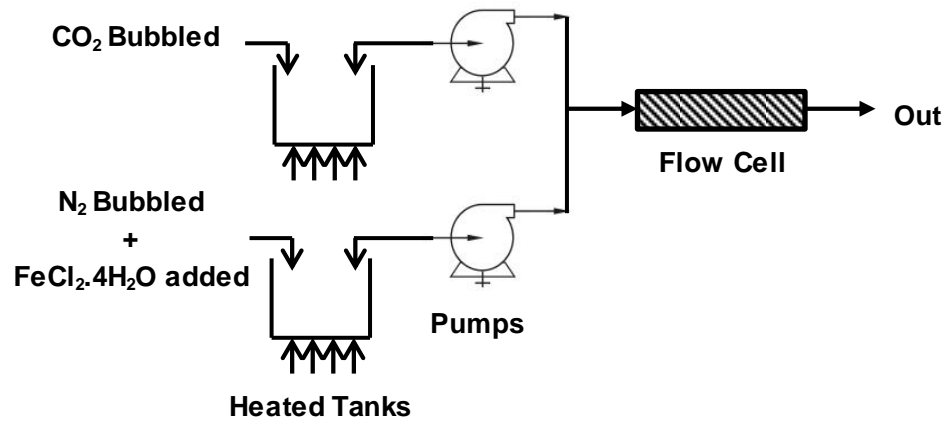


Figure 13.1 Schematic for once-through flow system for future work.

Bibliography

1. Garverick, L., *Corrosion in the petrochemical industry*. 1994: ASM international.
2. Kermani, M. and A. Morshed, *Carbon dioxide corrosion in oil and gas production-A compendium*. Corrosion, 2003. 59(8): p. 659-683.
3. Stansbury, E.E. and R.A. Buchanan, *Fundamentals of electrochemical corrosion*. 2000: ASM international.
4. Greenber, J.L., *High temperature kinetics of precipitation and dissolution of ferrous-carbonate*, 1987, Rice University.
5. Greenberg, J. and M. Tomson, *Precipitation and dissolution kinetics and equilibria of aqueous ferrous carbonate vs temperature*. Applied Geochemistry, 1992. 7(2): p. 185-190.
6. Johnson, M. and M. Tomson, *Ferrous carbonate precipitation kinetics and its impact CO2 corrosion*. M. L. Johnson, M. B. Tomson, CORROSION 91/268, NACE, Houston, TX., 1991.
7. Johnson, M.L., *Ferrous carbonate precipitation kinetics: A temperature ramped approach*, 1991, Rice University.
8. Van Hunnik, E., B.F. Pots, and E. Hendriksen, *The formation of protective FeCO₃ corrosion product layers in CO₂ corrosion*, 1996, NACE International, Houston, TX (United States).
9. Sun, W., *Kinetics of iron carbonate and iron sulfide scale formation in CO₂/H₂S corrosion*, 2006, Ohio University.
10. Sun, W. and S. Netic, *Basics revisited: kinetics of iron carbonate scale precipitation in CO₂ corrosion*. Corrosion/2006, paper, 2006(06365).
11. Papavinasam, S., *Corrosion control in the oil and gas industry*. 2013: Elsevier.
12. (IEA), I.E.A. *Oil*. 2016 25/10/16]; Available from: <http://www.iea.org/about/faqs/oil/>.
13. Fantini, A. *OPEC Annual Statistical Bulletin*. 2016.
14. Inc., P.E. *An Explanation of the Industry*. 2014 21/06/14]; Available from: <http://www.profireenergy.com/our-industry/>.
15. Roberge, P.R., *Handbook of corrosion engineering*. 2000: McGraw-Hill.
16. Speight, J.G., *The chemistry and technology of petroleum*. 2014: CRC press.
17. Kermani, M. and D. Harr. *The impact of corrosion on oil and gas industry*. in *Giornata di studio IGF S. Donato Milanese 1996*. 2008.
18. Borthwick, I., Balkau, F., Read, T. and Monopolis, J., *Environmental Management in Oil and Gas Exploration and Production*. UNEP Technical Publication, IE/PAC Technical Report, 1997. 37: p. 4-7.
19. Joshi, G.R., *Elucidating Sweet Corrosion Scales*. 2015.
20. Simmons, M.R. *Oil and Gas "Rust": An Evil Worse Than Depletion*. 2008 25/10/16]; Available from: <https://www.nace.org/Corrosion-Central/Industries/Oil---Gas-Production/>.
21. McCafferty, E., *Introduction to corrosion science*. 2010: Springer Science & Business Media.

22. Brondel, D., Edwards, R., Hayman, A., Hill, D., Mehta, S. and Semerad, T., *Corrosion in the oil industry*. Oilfield review, 1994. 6(2): p. 4-18.
23. Atkins, P. and J. De Paula, *Elements of physical chemistry*. 2013: Oxford University Press, USA.
24. Hu, X., *The corrosion and erosion-corrosion behaviour of high alloy stainless steels*, 2003, Heriot-Watt University.
25. Barker, R.J., *Erosion-corrosion of carbon steel pipework on an offshore oil and gas facility*. 2012: University of Leeds.
26. Bradford, S.A. and J.E. Bringas, *Corrosion control*. Vol. 115. 1993: Springer.
27. Tait, W.S., *An introduction to electrochemical corrosion testing for practicing engineers and scientists*. 1994: PairODocs Publications.
28. Stojek, Z., *The electrical double layer and its structure*, in *Electroanalytical methods*. 2010, Springer. p. 3-9.
29. Neville, A., S. Ramachandran, and V. Jovancicevic. *Erosion-Corrosion Mitigation Using Chemicals*. in *CORROSION 2003*. 2003. NACE International.
30. Obuka, N.S.P., Ikwu, O.N.C., Chukwumuanya, G.R.O. and Okechukwu, E., *Review of corrosion kinetics and thermodynamics of CO₂ and H₂S corrosion effects and associated prediction/evaluation on oil and gas pipeline system*. Int. J. Sci. Technol. Res, 2012. 1: p. 156-162.
31. Crow, D.R., *Principles and applications of electrochemistry*. 1994: CRC Press.
32. Scully, J.R., *Polarization resistance method for determination of instantaneous corrosion rates*. Corrosion, 2000. 56(2): p. 199-218.
33. Stern, M., *A method for determining corrosion rates from linear polarization data*. Corrosion, 1958. 14(9): p. 60-64.
34. De Waard, C. and D. Milliams, *Carbonic acid corrosion of steel*. Corrosion, 1975. 31(5): p. 177-181.
35. Nordsveen, M., et al., *A mechanistic model for carbon dioxide corrosion of mild steel in the presence of protective iron carbonate films-Part 1: Theory and verification*. Corrosion, 2003. 59(5): p. 443-456.
36. Woollam, R. C. and S. Nescic, *Review of Kinetics Models for Ferrous Carbonate (FeCO₃) Precipitation*, Institute for Corrosion and Multiphase Technology, Ohio University.
37. Arumugam, S., N. Tajallipour, and P.J. Teevens. *Modeling the Influence of Iron Carbonate Scale Morphology in Sweet Corrosion Prediction*. in *CORROSION 2014*. 2014. NACE International.
38. Dugstad, A. *Fundamental aspects of CO₂ metal loss corrosion-part 1: mechanism*. in *CORROSION 2006*. 2006. NACE International.
39. Lyon, S., *Corrosion in natural waters*. Shreir's Corros, 2009. 2: p. 1094-1106.
40. Mullin, J.W., *Crystallization*. 2001: Butterworth-Heinemann.
41. Markov, I.V., *Crystal growth for beginners: fundamentals of nucleation, crystal growth and epitaxy*. 2003: World Scientific.
42. Garside, J. and R. Davey, *From Molecules to Crystallizers—An Introduction to Crystallization Ch. 3*, 2000, Oxford Univ. Press.

43. Dugstad, A., L. Lunde, and S. Nesic. *Control of internal corrosion in multi-phase oil and gas pipelines*. in *Proceedings of the conference Prevention of Pipeline Corrosion*, Gulf Publishing Co. 1994.
44. Arumugam, S., N. Tajallipour, and P.J. Teevens. *Modeling the Nucleation and Growth of Corrosion Scales in Sour Petroleum Pipelines*. in *CORROSION 2014*. 2014. NACE International.
45. Nešić, S., *Key issues related to modelling of internal corrosion of oil and gas pipelines—A review*. *Corrosion Science*, 2007. 49(12): p. 4308-4338.
46. Bretherton, N., Robb, S., Richterova, K.G., Donaldson, D. and Smith, R.G., *Impact of acetic acid on weld corrosion and its mitigation*. *CORROSION 2009*. 2009. NACE International.
47. Schmitt, G. and M. Horstemeier. *Fundamental aspects of CO₂ metal loss corrosion-Part II: Influence of different parameters on CO₂ corrosion mechanisms*. in *CORROSION 2006*. 2006. NACE International.
48. De Waard, C., U. Lotz, and D. Williams, *Predictive model for CO₂ corrosion engineering in wet natural gas pipelines*. *Corrosion*, 1991. 47(12): p. 976-985.
49. Nešić, S. and K.-L. Lee, *A mechanistic model for carbon dioxide corrosion of mild steel in the presence of protective iron carbonate films-Part 3: Film growth model*. *Corrosion*, 2003. 59(7): p. 616-628.
50. Ikeda, A., M. Ueda, and S. Muka, *CO₂ behaviour of carbon and Cr steels in Hausler RH Giddard HP*. *Corrosion*, 1983. 39: p. 131-137.
51. Li, T., Yang, Y., Gao, K. and Lu, M., *Mechanism of protective film formation during CO₂ corrosion of X65 pipeline steel*. *Journal of University of Science and Technology Beijing, Mineral, Metallurgy, Material*, 2008. 15(6): p. 702-706.
52. Gao, M., X. Pang, and K. Gao, *The growth mechanism of CO₂ corrosion product films*. *Corrosion Science*, 2011. 53(2): p. 557-568.
53. Nešić, S., G.T. Solvi, and J. Enerhaug, *Comparison of the rotating cylinder and pipe flow tests for flow-sensitive carbon dioxide corrosion*. *Corrosion*, 1995. 51(10): p. 773-787.
54. Postlethwaite, J. and D. Wang. *Modeling Aqueous CO₂ Corrosion of Iron in Turbulent Pipe Flow*. in *CORROSION 2001*. 2001. NACE International.
55. Yang, Y., Brown, B., Nesic, S., Gennaro, M.E. and Molinas, B., *Mechanical strength and removal of a protective iron carbonate layer formed on mild steel in CO₂ corrosion*, 2010, National Association of Corrosion Engineers, P. O. Box 218340 Houston TX 77084 USA.
56. Fosbøl, P.L., K. Thomsen, and E.H. Stenby. *Improving mechanistic CO₂ corrosion models*. in *CORROSION 2009*. 2009. Nace International.
57. Newman, J., *Electrochemical Systems*, 1991, Prentice-Hall, Englewood Cliffs, New Jersey.
58. De Waard, C., U. Lotz, and A. Dugstad. *Influence of Liquid Flow Velocity on CO₂ Corrosion: A Semi-Empirical Model*. in *CORROSION-NATIONAL ASSOCIATION OF CORROSION ENGINEERS ANNUAL CONFERENCE*-. 1995. NACE.
59. Videm, K., A. Dugstad, and L. Lunde, *Parametric study of CO₂ corrosion of carbon steel*. *CORROSION/94*, paper, 1994(14).

60. Marie, A., K. Halvorsen, and T. Søntvedt, *CO₂ Corrosion Model for Carbon Steel Including a Wall Shear Stress Model for Multiphase Flow and Limits for Production to Avoid Mesa Attack*. CORROSION/99, paper, 1999(42).
61. Mishra, B., Al-Hassan, S., Olson, D.L. and Salama, M.M., *Development of a predictive model for activation-controlled corrosion of steel in solutions containing carbon dioxide*. Corrosion, 1997. 53(11): p. 852-859.
62. Nestic, S., Nordsveen, M., Maxwell, N. and Vrhovac, M., *Probabilistic modelling of CO₂ corrosion laboratory data using neural networks*. Corrosion science, 2001. 43(7): p. 1373-1392.
63. Nestic, S. and M. Vrhovac, *A neural network model for CO₂ corrosion of carbon steel*. JCSE: The Journal of Corrosion Science and Engineering, 1999. 1(April): p. 1-13.
64. Nyborg, R. *Overview of CO₂ corrosion models for wells and pipelines*. in *CORROSION 2002*. 2002. Nace International.
65. De Waard, C., Smith, L., Bartlett, P. and Cunningham, H., *Modelling corrosion rates in oil production tubing*. Eurocorr/2001, 2001. 254.
66. De Waard, C., L. Smith, and B. Craig, *The influence of crude oil on well tubing corrosion rates*. CORROSION/2003, Paper, 2001. 3629.
67. Gray, L.G., Anderson, B.G., Danysh, M.J. and Tremaine, P.R., *Effect of pH and temperature on the mechanism of carbon steel corrosion by aqueous carbon dioxide*. Corrosion/90, paper, 1990. 40.
68. Anderko, A. and R.D. Young. *Simulation of CO₂/H₂S Corrosion using Thermodynamic and Electrochemical Models*. in *CORROSION-NATIONAL ASSOCIATION OF CORROSION ENGINEERS ANNUAL CONFERENCE*-. 1999. NACE.
69. Nestic, S., M. Nordsveen, and A. Stangel, *A Mechanistic Model for CO₂ Corrosion with Protective Iron Carbonate Films*. 2001.
70. Nešić, S., Li, H., Huang, J. and Sormaz, D., *An open source mechanistic model for CO₂/H₂S corrosion of carbon steel*. in *NACE International Corrosion Conference & Expo*. 2009.
71. Zheng, Y., Ning, J., Brown, B. and Nešić, S., *Advancement in Predictive Modeling of Mild Steel Corrosion in CO₂-and H₂S-Containing Environments*. Corrosion, 2016. 72(5): p. 679-691.
72. Nestic, S., J. Postlethwaite, and S. Olsen, *An electrochemical model for prediction of corrosion of mild steel in aqueous carbon dioxide solutions*. Corrosion, 1996. 52(4): p. 280-294.
73. George, K., S. Nestic, and K. de Waard. *Electrochemical investigation and modeling of carbon dioxide corrosion of carbon steel in the presence of acetic acid*. in *CORROSION 2004*. 2004. Nace International.
74. Turgoose, S., R. Cottis, and K. Lawson, *Modeling of electrode processes and surface chemistry in carbon dioxide containing solutions*, in *Computer Modeling in Corrosion*. 1992, ASTM International.
75. Davis, M.E. and R.J. Davis, *Fundamentals of chemical reaction engineering*. 2012: Courier Corporation.
76. Dugstad, A., H. Hemmer, and M. Seiersten. *Effect of steel microstructure upon corrosion rate and protective iron carbonate film formation*. in *CORROSION 2000*. 2000. NACE International.

77. Han, J., J.W. Carey, and J. Zhang, *Effect of sodium chloride on corrosion of mild steel in CO₂-saturated brines*. Journal of Applied Electrochemistry, 2011. 41(6): p. 741-749.
78. Pessu, F., R. Barker, and A. Neville, *Understanding Pitting Corrosion Behaviour of X-65 (UNS K03014) Carbon Steel in CO₂ Saturated Environments: The Temperature Effect*. CORROSION, paper, 2014(4214).
79. Pessu, F., R. Barker, and A. Neville, *The influence of pH on localized corrosion behavior of X65 carbon steel in CO₂-saturated brines*. Corrosion, 2015. 71(12): p. 1452-1466.
80. Tanupabrungsun, T., B. Brown, and S. Nescic, *Effect of pH on CO₂ corrosion of mild steel at elevated temperatures*. CORROSION/2013, Paper, 2013(48).
81. Stern, M. and A.L. Geary, *Electrochemical polarization I. A theoretical analysis of the shape of polarization curves*. Journal of the electrochemical society, 1957. 104(1): p. 56-63.
82. Nafday, O.A., *Film Formation and CO₂ Corrosion in the presence of Acetic Acid*, 2004, Ohio University.
83. HACH. *Iron (II / III) cuvette test 0.2-6.0 mg/L Fe*. 2015 17/10/16]; Available from: <http://uk.hach.com/iron-ii-iii-cuvette-test-0-2-6-0-mg-l-fe/product?id=26370291418>.
84. Oddo, J.E. and M.B. Tomson, *Simplified calculation of CaCO₃ saturation at high temperatures and pressures in brine solutions*. Journal of Petroleum Technology, 1982. 34(07): p. 1,583-1,590.
85. Palmer, D.A. and R. Van Eldik, *The chemistry of metal carbonato and carbon dioxide complexes*. Chemical Reviews, 1983. 83(6): p. 651-731.
86. Corporation, H.H.-T. *Tabletop Microscope TM3030*. 2001; Available from: <http://www.hitachi-hightech.com/global/tm/products/>.
87. Davis, J.R., *Corrosion of weldments*. 2006: ASM International.
88. Krawitz, A.D., *Introduction to diffraction in materials science and engineering*. Introduction to Diffraction in Materials Science and Engineering, by Aaron D. Krawitz, pp. 424. ISBN 0-471-24724-3. Wiley-VCH, April 2001., 2001: p. 424.
89. Robinson, I. and D. Tweet, *Surface x-ray diffraction*. Reports on Progress in Physics, 1992. 55(5): p. 599.
90. Ingham, B., Ko, M., Kear, G., Kappen, P., Laycock, N., Kimpton, J.A. and Williams, D.E., *In situ synchrotron X-ray diffraction study of surface scale formation during CO₂ corrosion of carbon steel at temperatures up to 90 C*. Corrosion Science, 2010. 52(9): p. 3052-3061.
91. Nor, A.M., *The Effect of Turbulent Flow on Corrosion of Mild Steel in High Partial CO₂ Environments*, 2013, Ohio University.
92. Silverman, D., *The rotating cylinder electrode for examining velocity-sensitive corrosion-a review*. Corrosion, 2004. 60(11): p. 1003-1023.
93. Yang, Y., *Removal mechanisms of protective iron carbonate layer in flowing solutions*, 2012, Ohio University.
94. Revie, R.W. and H.H. Uhlig, *Uhlig's corrosion handbook*. Vol. 51. 2011: John Wiley & Sons.
95. Fang, H., *Low Temperature and High Salt Concentration Effects on General CO₂ Corrosion for Carbon Steel*, 2006, Ohio University.

96. Zeng, Z., R. Lillard, and H. Cong, *Effect of Salt Concentration on the Corrosion Behavior of Carbon Steel in CO₂ Environment*. Corrosion, 2016. 72(6): p. 805-823.
97. Asma, R., P. Yuli, and C. Mokhtar, *Study on the effect of surface finish on corrosion of carbon steel in CO₂ environment*. Journal of Applied Sciences, 2011. 11(11): p. 2053-2057.
98. Nešić, S., Nordsveen, M., Nyborg, R. and Stangeland, A., *A mechanistic model for carbon dioxide corrosion of mild steel in the presence of protective iron carbonate films-Part 2: A numerical experiment*. Corrosion, 2003. 59(6): p. 489-497.
99. Kharaka, Y.K., Gunter, W.D., Aggarwal, P.K., Perkins, E.H. and DeBraal, J.D., *SOLMINEQ. 88: A computer program for geochemical modeling of water-rock interactions*. US geological survey water-resources investigation report, 1988. 88: p. 4227.
100. Nor, A.M., Suhor, M.F., Mohamed, M.F., Singer, M. and Nesic, S., *Corrosion of Carbon Steel in High CO₂ Containing Environments-the Effect of High Flow Rate*. in *CORROSION 2012*. 2012. NACE International.
101. Perry, R.H. and D.W. Green, *Perry's chemical engineers' handbook*. 1999: McGraw-Hill Professional.
102. Kvarekvål, J., *A kinetic model for calculating concentration profiles and fluxes of CO₂ related species across the Nernst diffusion layer*, 1997, NACE International, Houston, TX (United States).
103. Newman, J.S., *Electrochemical Systems*. 2nd Edition ed. 1991, Englewood Cliffs, New Jersey: Prentice Hall
104. Zheng, Y., B. Brown, and S. Nešić, *Electrochemical study and modeling of H₂S corrosion of mild steel*. Corrosion, 2013. 70(4): p. 351-365.
105. Zheng, Y., Ning, J., Brown, B. and Nešić, S., *Electrochemical Model of Mild Steel Corrosion in a Mixed H₂S/CO₂ Aqueous Environment in the Absence of Protective Corrosion Product Layers*. Corrosion, 2014. 71(3): p. 316-325.
106. Sleicher, C.A. and M. Rouse, *A convenient correlation for heat transfer to constant and variable property fluids in turbulent pipe flow*. International Journal of Heat and Mass Transfer, 1975. 18(5): p. 677-683.
107. Cussler, E.L., *Diffusion: mass transfer in fluid systems*. 2009: Cambridge university press.
108. Lide, D.R., *CRC handbook of chemistry and physics*. Vol. 85. 2004: CRC press.